ELECTRON SPIN RESONANCE AND RESISTIVITY STUDIES OF Bi – MANGANITES

A thesis submitted for the degree of

DOCTORATE IN PHILOSOPHY

by

JOJI KURIAN

SCHOOL OF PHYSICS

UNIVERSITY OF HYDERABAD

HYDERABAD – 500046, INDIA

JUNE 2009

CERTIFICATE

This is to certify that the research work presented in the thesis entitled "**ELECTRON SPIN RESONANCE AND RESISTIVITY STUDIES OF Bi – MANGANITES"** is an original work carried out by **JOJI KURIAN.** This work has been carried out under my supervision. The thesis is submitted by **JOJI KURIAN** for the degree of **DOCTORATE IN PHILOSOPHY** in the School of Physics. This thesis work has not been submitted to any other university partially or fully for the award of any degree.

Prof. R. Singh
(Supervisor)

Dean
School of Physics

Date:

DECLARATION

I hereby declare that the thesis entitled "**ELECTRON SPIN RESONANCE AND RESISTIVITY STUDIES OF Bi – MANGANITES"** submitted to the University of Hyderabad for the award of Doctorate in Philosophy in Physics is a record of original research work done by me under the supervision of Professor Rajender Singh, School of Physics, University of Hyderabad, Hyderabad. This project has not been submitted partially or fully for any degree in any other university.

Date: Joji Kurian

Place:

ACKNOWLEDGEMENTS

This is one tough part – saying 'Thank You' !!!! Not that saying so is tough, but in itself it presents the risks of being misjudged, misinterpreted or even being considered as forgetful or one lacking modesty.

First, I thank my supervisor, Prof. R. Singh. I am grateful to him for teaching me, or showing me the way to learn by myself rather, the physics I know today through the subtle but beautifully expressive ways he did. I thank him for the opportunities I have had and still am being given for really 'experimenting' with my work and for him entrusting in me confidence in doing work myself. There are so many other qualities in him that I wish I could incorporate in my life and I am sure I would probably never be able to – the ease with which he tackles problems, the way he courageously stands his ground for the things he feels he is right in, and being a very patient and approachable person to anyone.

I thank the dean of the School of Physics Prof. Vipin Srivastava and the former dean of the School of Physics Prof. V.S.S. Sastry for providing me the facilities for the successful completion of my work. I also thank all the faculty members who have helped me throughout my stay here at the University of Hyderabad. The little discussions on physics, on life or even the small talks have always been interesting and very encouraging. I gratefully remember all my other teachers who taught me in school as well as in college, who have been constant sources of inspiration for me.

My sincere thanks to the staff of the CIL, Mr. C.S.Murthy, Mr. Suresh, Dr. S. Manjunath, Mr. Nageshwar Rao, Mr. Sudhakar, Mr. Illayaa, Mr. Kishta Reddy and Mr. Rajkumar for the technical support they provided (I know that I have been an irritant too many a time….but hope at the end of the day….all is forgiven). I also thank Mr. Sambasiva Rao, Mr. Mantoo Kumar and Giri Bahadur for the help they have provided me required for the low temperature experiments. I am grateful to the non teaching staff of the School of Physics especially Mr. Abraham and Mrs. Saramma for all the help they have provided regarding administrative matters.

And now…I come to the most tedious…..but most interesting part……MY FRIENDS…..

I first should….. and yes just SHOULD thank Abhilash. Abhi, for all these years in the last 14 years (now that’s a LONG period of time!), I thank you for just being there for me. With each passing year the bond of our friendship has grown to be stronger. You have been, and still will always remain, a wonderful friend…the long talks we have had…the immense support you have given me through the tough times I have had…and yes all the crazy things we have done together….these moments , I shall always cherish in my life ahead.

Santhosh and Saravanan…. I am not really sure how to thank you guys…because between us….its always been I ask and you give…be it regarding work, information or even about my personal life…whenever I have been in need I always knew that I could count on you to help me. But then, even without that I would have always been happy just to know all of you…for being the sweet natured people that you are. I am grateful to ….for all the help you have given me from my DAY 1 on the campus. Shinto, Rajesh K, Ajith and Biju A. R., I am really grateful to you guys for all the time we have spent together and surely for the interesting discussions we have always had, the leisurely time we have spent with each other and most of all for helping me understand many things on physics itself. Brahma (surely for the wonderful bike ride and DJ nites we had together!!!!), Sudheendran and Rohith for their companionship for the last few years. I would also like to mention some of the people I have known for a very short time but will probably take ages to forget – Dinesh, Azhar, Siraj, Anver, Rajesh K.P., Juby, Shalina, Amen, Rajesh P., Ajith, Shihab, Muneer, Srikanth, Ratheesh, Ren Gupta, Binoy, Vishnu, Varghese, Mochish, Anoop, Parameshwaran, Christy, Sumesh, Daughty, Rajitha, Shameema, Yasser, Rejina, Mini, Thushara, Sameera, Lekha, Susan, Priyanka, Asha, Sudarshan, Prabudha, Anitha, Bharathi, Anargha, Sreeja, Ramshina, Abhilash, Shamsheer, Anish, Abin, Rahul, Treasa, Anuraghi, Arathi, Reshma, Ghouse, Sherinmol Sonia, Neetu, Naveen, Anna, Eros, Sooraj, Geo and all my other friends in HCU.

I also thank my friends from my school and college days – Shony, who has been a great support to me all through these years, Sajeev, Mathew, Jerish, Roby, Reji, Prajesh, Sijo, Renit, Jimmy, Toms, Joe, Jeevan, Aagney, Anu, Jessy, Sophia , Anoop, Robin and all my other friends from St. Michaels School, Nirmalagiri College and Christ College. A few people I will never fail to mention, who have always been a source of inspiration to me, are Prashant, Rupert, Shefali and Fatima…my dear friends from Bangalore.

My lab mates….without them I guess my stay in the lab would have been so….lifeless! Sultan and Sandhya…thanks a million for being there with me through these years. You are two people whom I have probably spent the most time with on this campus. You have been great friends, listeners (especially whenever I've had my LONG talks trying to take out my frustrations on someone!), and probably some of my best critics, all which have helped me grow. I will always cherish the times we spent together…be it just sitting and whiling our time away or the time we spent for useful discussions and research work. I thank my former labmates Dhanya, Eswar, Lakshmikanth, Tali and Rajesh Babu who will always remain my good friends. I also thank the newest 'inductees' into our lab, Vijayan, Venkaiah and Sai Priya for being so understanding and caring and especially for putting up with me through one of the toughest periods of my life at HCU. I am very grateful to Harshan, my first lab mate, who introduced me to the low temperature experimental world and for remaining my well wisher.....…but more importantly.…for being a good friend.

I know I will always have very pleasant memories of my friends from the School of Physics. I thank my friends Uma, Lakshmi, Ravi, Gnanavel, Yugander, Basheed, Sathish N., Bari, Rizwan, Kiran, Prashant, Ashuthosh, Manoj, Sivakiran, Monisha, Thejal and Rajinikanth. My special thanks to Sathish A. for helping me with the SEM data.

And now……the most important people in my life…..my FAMILY! I thank my Daddy.….had it not been for him I would never even have thought of pursuing my higher studies…. and for all the support , love and care I have always got ..…….Amma…for being the constant moral support for me….for being the good listener….one whom I could ALWAYS talk to about anything and everything under the sun…Chettan, Isha and Unni……could I EVER ask for anything more when I have such wonderful siblings???? and oh yes….the new additions to our family…..Malu and Achu…….for being the darlings that they are…but then do I need to say a lot about my family……being a little more philosophical (if that is the right word to use)…….. without my family….I am just nothing…..or should I say that ' my life would touch the bottom of utmost nothingness?'

If there is a superpower above all of us…..the one we refer to as the Almighty……Creator……God…….this thesis is my humble offering

….because anything that I am…..I believe….its all part of a plan which has already been made for me……..

I have just named most of the people I could think of in one go…..I am sorry if I have left out to name any of my friends …..just want each one of my friends to know that you really have, in one way or another, made a difference to my life…..and moreover if I had to name all my friends, write everything they have done for me….well I guess that in itself would make a nice thesis! But to everyone who has been part of my life……I thank you all for everything…after all…just being someone dear to me itself makes a whole lot of a difference to my life!

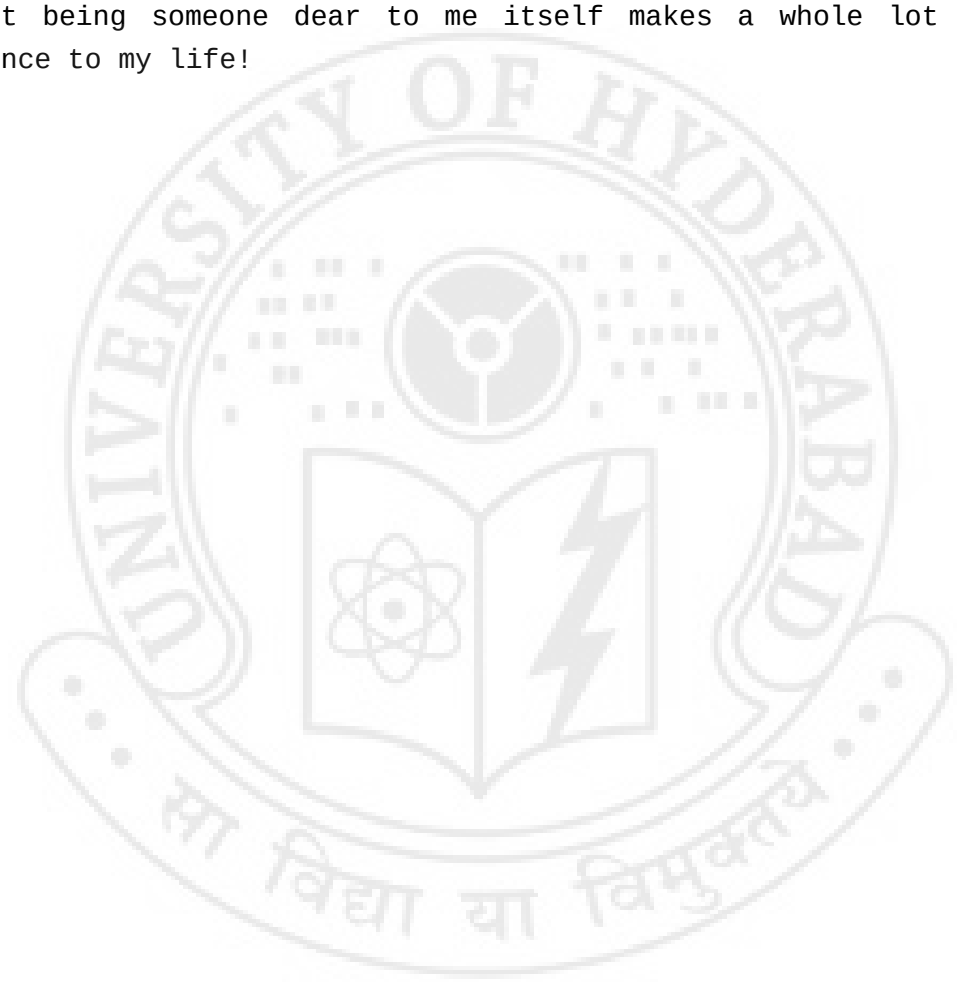

CONTENTS

1. INTRODUCTION

Superconductivity and Colossal Magnetoresistance (CMR) – two of the most exciting phenomena discovered in the 20^{th} century, paved way for a boost in research in the field of transition metal oxides. The last two decades of the 20^{th} century had seen an increase in activity in the field of high temperature superconductivity in cuprates, ferromagnetism in dilute magnetic semiconductors (DMS) and high spin polarization of conduction electrons in manganites. What made the discovery of these phenomena even more intriguing, but exciting, was the fact that it was observed in materials containing 3d transition metals. The properties of the 3d transition metal were, and still are, much less understood than that of the other metals, ionic oxide insulators and doped semiconductors. One of the main reasons of this was that these elements were considered to contain "almost localized" electrons in the 3d shell of the atoms. Though the transition metals present systems of rich physics, it turns out to be quite a difficult task for any one theoretical model to explain all the physical processes exhibited by them.

The latter part of the last decade saw enormous activity of research using metal oxide compounds, called manganites, which were basically manganese based compounds. This being because, no single theory or model could explain completely the mechanisms involved in the electric, magnetic, optical or any other physical property observed in these materials. The word manganites comes from the first publication by Jonker and Van Santen [1], where they mentioned the compounds which contained both tetravalent as well as trivalent Mn, as manganites, a convention that is still followed to this day!

In their first publication Jonker and Van Santen reported their results on (LaCa)MnO_3, (LaSr)MnO_3 and (LaBa)MnO_3. They conducted the magnetization studies on these materials, obtained the Curie temperature and observed the existence of ferromagnetism (FM). They attributed the existence of the FM phase to a positive indirect-exchange interaction. Later, that same year Van Santen and Jonker [2], in a subsequent paper, reported the conductivity in manganites, wherein they found anomalies at the Curie temperature. Volger [3] reported the magnetoresistance (MR) studies on manganites a few years later. In his work he had observed that when manganites are in the FM state the resistivity of these materials decrease when placed in a magnetic field. This was one of the very first reports of magnetoresistance in manganites.

The discoveries that triggered interest in these materials was the that of colossal magnetoresistance (CMR) effect by Jin *et. al.* [1] in strained annealed $La_{0.67}Ca_{0.33}MnO_3$ thin films and giant negative magnetoresistance (GMR) by Helmholt *et. al.* [5] in $La_{2/3}Ba_{1/3}MnO_3$ ferromagnetic films.

The study of manganites is one which has gained immense recognition owing to the vast range of applications these materials can be used in. Manganites are seen as prospective contributors in memory enhancement materials used in electronic devices. These materials are also used in solid oxide fuel cells (SOFCs) as cathodes. CMR oxides are seen to possess a possibility of a healthy balance between spin and charge transport. Thin films of perovskite manganites are also known to be used as protective coatings [6]. The low field magnetoresistance behaviour demonstrated in La manganite films [7] and isolated in artificial grain boundary devices [8] helps in making these materials good contenders for field sensor applications. The intrinsic CMR effect has been demonstrated at frequencies which can be used for microwave applications [9]. Perovskite manganite thin films find applications for bolometric devices [10]. Composites of lanthanum based manganites are known to be useful in the biomedical applications [11]. There are more recent works reported for the magnetoimpedence measurements and the manganite thin films which can be used for current limiter applications [12].

In spite of these possible applications there are still quite a few aspects about manganites which have not been fully understood. In later years it was noticed that these materials exhibited a lot more interesting properties than just magnetoresistance. The observation of spin, charge, lattice and orbital ordering in these materials intrigued scientists, especially since orbital ordering was not seen in the layered cuprate superconductors, and hence observing it in compound containing a transition metal oxide like manganese left many thinking. An informal presentation by Dagotto deals with an overall status of manganites [13], about the things that are known and accepted by researchers and those which still pose as intriguing problems.

One of the most highly acknowledged piece of work in manganites was the neutron scattering studies done on $La_{(1-x)}Ca_xMnO_3$ (LCMO) by Wollan and Koehler [14]. In these manganites they not only found FM phases present, but interestingly, antiferromagnetic (AFM) phases too which were, in some cases, accompanied along with charge ordering (CO). They also mentioned the different types of AFM ordering as shown in the figure 1.1. For example: A-type has FM planes with AFM coupling. B-type is a standard FM

arrangement while the C-type has AFM in two directions with an FM arrangement in one direction. The G-type shows AFM in all three directions.

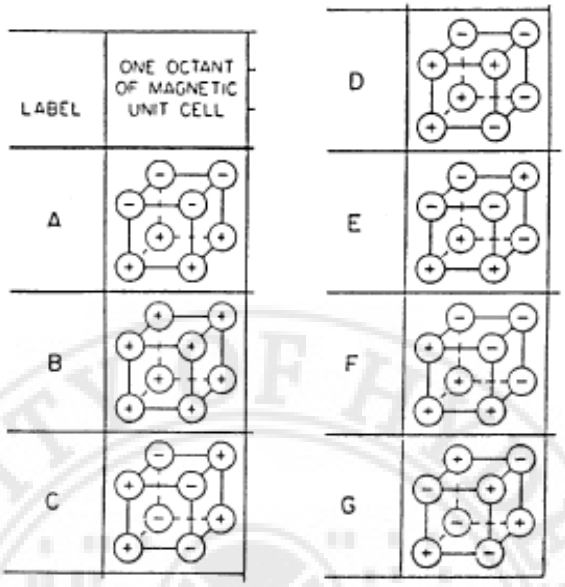

Fig.1.1 Different magnetic structures and the corresponding labels. Mn ions are depicted as circles and the signs within them are the orientations of the z-axis spin projection.

Apart from the AFM phases depicted in the figures there was one phase which stood out from the others and it was the CE phase, which is a mixture of the C-phase and E-phase. From the intensity of the peaks associated to the CE-phase they found that CO was present in the state. They also reported the mixtures of A-type AFM and FM phase and also CE- type AFM and FM phases. From the intensities of the peaks of the diffraction pattern corresponding to either A-, CE, C- or G-type of AFM states they also found the Neel temperatures (T_N).

Searle *et. al.* [15] studied the system (La,Pb)MnO_3 and found the Curie temperature (T_C) to occur well above room temperature. In the late 1970s, till the early 1990s, manganites other than La-based ones were not studied. Jirak *et. al.* [16] and Pollert *et. al.* [17] reported the structural and magnetic properties of $Pr_{(1-x)}Ca_xMnO_3$ (PCMO) using X-ray and neutron diffraction techniques. They found these materials to exhibit CO, unlike FM seen in other manganites studied earlier. They also observed deviations from the cubic structure (orthorhombic structure accompanied with an AF ordering and tetragonal structure).

As early as the 1950s MR was observed in manganites. Kusters *et. al.* [18] observed large MR in $Nd_{0.5}Pb_{0.5}MnO_3$ by applying different magnetic fields. Helmholt *et. al.* [2] also observed large MR in thin films of $La_{2/3}Ba_{1/3}MnO_3$ near room temperature (RT). Similarly Chahara *et. al.* [19] and Ju *et. al.* [20] also reported large MR near room temperature in thin films of $La_{(1-x)}Ca_xMnO_3$ and $La_{(1-x)}Sr_xMnO_3$ respectively. When Jin *et. al.* [1] reported results on their work on manganites it took the world by surprise, as the MR effect that they observed was of real colossal ratios. They had studied $La_{0.67}Ca_{0.33}MnO_x$ films. Defining MR as

$$\Delta R/R = (R_H - R_O)/ R_H,$$

where R_O is the resistance without a magnetic field and R_H is the resistance at any applied field (in their case 6T). They observed MR ratios close to 1500% at 200K and over 100,000% at 77K after optimizing the films! This one finding alone proved to open new doors to application oriented research work in manganites as these materials were suddenly looked upon as potential alternatives to systems showing giant magnetoresistance (GMR). This and the many other characteristics seen in manganites like CO, orbital ordering (OO), Jahn-Teller (J-T) effects, double exchange (DE) interactions, super exchange (SE) interactions, coexistence of different phases etc pushed research in the field of manganites again to the forefront as there did not seem to be a single model which alone could explain CMR and other properties in manganites.

One of the earliest theoretical works done in this regard, though not exclusively dealing with manganites, was by Zener [21]. In his paper the interactions of the d-shells in transition metals are talked about. This paper perhaps formed the basis of all theoretical work for Mn oxide based compounds. He had proposed that ferromagnetism occurred ‘from the indirect coupling of the incomplete d-shells via the conducting electrons’. In his following publication [22] he mentioned about manganites and concluded that the arguments he had put forth in his first work applied to manganites too. He went on to state that the transfer of carriers from one Mn ion to the other must occur through the oxygen ion, the process now known as double exchange (DE). DE is just the transfer of an electron in Mn-O-Mn from the Mn ion on the left to the Mn ion on the right through the connecting oxygen ion. Zener also had rightly stated that the process of DE was not to be mistaken for the superexchange (SE) interaction, which also happens with the oxygen ion acting as a passage between ions on either sides of it, as SE leads to antiferromagnetism.

Anderson and Hasegawa [23] tried to study the theory proposed by Zener in a more detailed manner. They purported that rather than the electrons moving simultaneously through the oxygen ion from one Mn to the other Mn ion, the electrons moved one by one. They also introduced a term called hopping amplitude, t, of the electrons. The effective hopping amplitude t_{eff} between two neighbouring Mn ions was given by a simple formula $t_{eff} = t\cos(\theta/2)$, where θ is the angle between the spins in the 'incomplete d- shells', which are the sites for electron transfer. Till recently this theory of t_{eff} was used extensively to explain different mechanisms in manganites. The presence of a spin-canted stable state was proposed by de Gennes [24]. But modern day work has not only questioned whether a stable spin canted state can be present in some manganites in the absence of a magnetic field, but also establishes a good alternative for this theory, which is, the coexistence of different magnetic phases. Goodenough [25] and later Kanamori [26] had introduced a more qualitative approach to analyze the work on manganites. In these papers the concept of DE is hardly used. Rather, his work is based on the concept of semicovalent bonds and elastic energy considerations. He proposed that the oxygen in manganites had a key role to play and so did the Coulomb interactions. Though the paper failed to give any clear cut idea on the stability of AFM states it is still accepted that he was the first to relate the 'CE-AFM state' with orbital and charge ordering.

Some important features of manganites

1.1 Basic Structure of Manganites

Manganites crystallize in a 'perovskite' structure as shown in the figure 1.2. The general formula of the perovskite is represented as ABO_3. Here A is a large cation and B a smaller cation. In manganites the A-site is occupied by La^{3+}, Bi^{3+}, Ca^{2+}, Sr^{2+} etc and the B-site by Mn ions. It contains a BO_6 vertex sharing network.

Ideal perovskites are known to be electric insulators. The strong ionic bonds keep the electrons in this structure from moving. They are also known to possess cubic symmetry and to be isotropic. Cation substitution and/or oxygen stochiometry can modify the structure of the perovskite from an ideal cubic structure to structures of lower symmetry by distorting and/or cooperatively rotating the BO_6 octahedra. As the magnitude of this distortion can be adjusted it helps in determining the correlation between the structural, magnetic and electric degrees of freedom of the compounds. In manganites, there are two factors which determine the distortion of the BO_6 octahedra:

(1) the influences of A-site cation mismatch called the Goldschmidt tolerance factor and (2) the electronic instability which is called the cooperative J-T distortion.

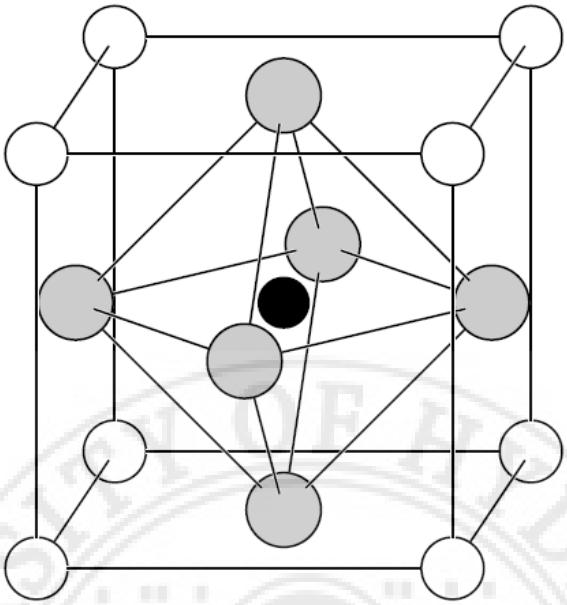

Figure 1.2. The perovskite structure with the A-cations occupying the unit cell corners. The oxygen anions are represented by the grey circles and the small B-cation is in the centre of the oxygen octahedral.

1.2 Tolerance Factor

The Goldschmidt tolerance factor is a geometrical factor which plays an important role in deciding the structure of perovskite manganites. It is define by the formula

$$t = (r_A + r_O) / [(r_B + r_O)\sqrt{2}]$$

where 'r' is the radius of the ion, $(r_A + r_O)$ is the distance between the A- site cation to the nearest oxygen ion and $(r_{\mathbf{B}} + r_O)$ is the distance between the B- site anion to the nearest oxygen ion. For an undistorted cubic structure the B-O-B link will be a straight one (in the case of a manganite an Mn-O-Mn bond), $(r_A + r_O) = \sqrt{2}$ and $(r_B + r_O) = 1$, i.e. for a perfect system the tolerance factor, t = 1. When there is a mismatch in the A-site cations there will be a distortion in the MnO_6 octahedra. This can change the amplitude of hopping of carriers between the Mn ions, which can determine the conductivity of the manganite. Distorted perovskite-like lattices exist approximately in the range of $0.89 < t < 1.02$.

The ABO_3 perovskite structure consists of a three dimensional vertex-sharing network of MO_6 octahedra and interstitial A cations as shown in figure 1.3. The perovskite properties are controlled by cation substitutions and/or oxygen stoichiometry. A distorted octahedra and/or a cooperatively rotated octahedral can cause structural modifications yielding lower symmetry structures. As the magnitude of these distortions can be tuned it is easy to probe the relation between the electrical, magnetic and structural properties. Due to the mismatch in the ionic sizes the bond lengths can also alter. This mismatch introduces a strain in the structure which is reflected in the tolerance factor. A tolerance factor of 1 characterizes an unstrained cubic system. On the other hand a tolerance factor of $t < 1$ or $t > 1$ represents a structure distorted from the cubic structure, which is specified depending on the value of t.

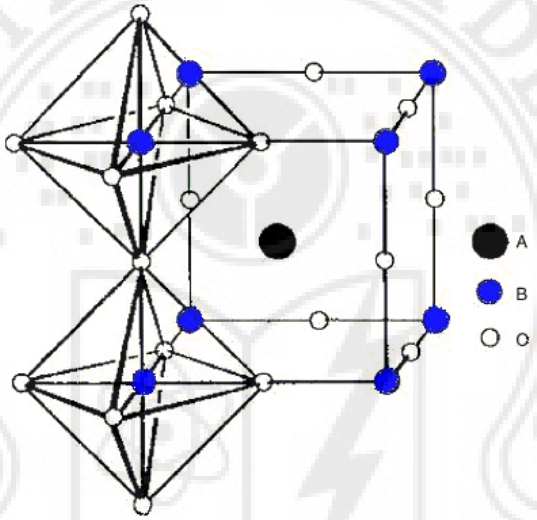

Figure 1.3. Ideal perovskite structure with the corner shared octahedral extending to three dimensions.

strain in the structure. This is relaxed by the distortion away from the ideal cubic structure which usually take the form of rigid rotations of the MO_6 octahedra (e.g. a $t < 1$ gives rise to an orthorhombic structure).

1.3 Crystal Field Splitting

Transition metal elements have an active d-shell with five degenerate levels. When these elements are part of a compound or near a ligand, the crystal axes orient to specific directions. There is an interaction between the ions of the metals and the non-bonding electrons of the ligand. As the ligand approaches the metal ions the degeneracy observed in these five levels is lost as the electrons of the ligand get closer to some orbitals of the

d-shell and are farther from the others, causing a difference in the energy. The electrons in the d-shell and those in the ligands repel; those closer to the ligands will have higher energy and farther from it lower energy. This is what causes the difference in energy. The magnitude of the energy difference is decided by the nature of the metal ions and their oxidations states, and the nature of ligands surrounding the metal ions.

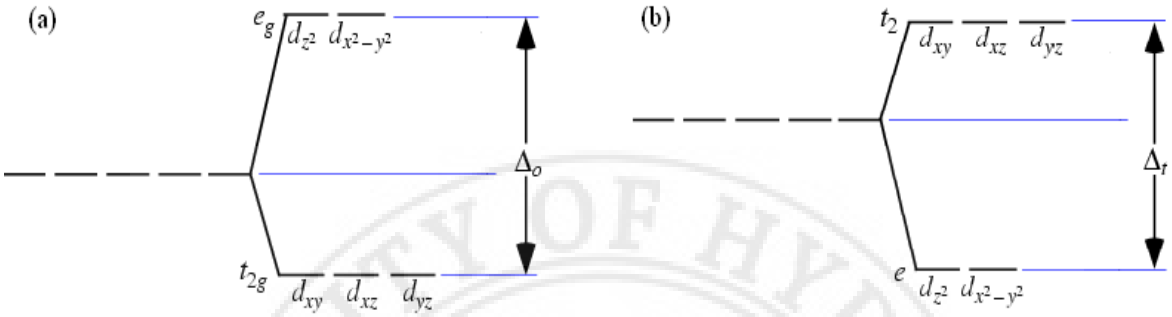

Figure 1.4. (a) Octahedral crystal field splitting (b) Tetrahedral crystal field splitting.

A more specific case is that of an octahedron structure which the ligands surrounding the metal ions form, which is of more interest to us. In the d-shells the orbitals split into two sets: the d_{xy}, d_{yz} and d_{xz} orbitals, which is of lower energy and the d_{z^2} and $d_{x^2-y^2}$, which is of higher energy. This energy difference (assigned as Δ_{oct}) occurs as the d_{xy}, d_{yz} and d_{xz} set of orbitals is farther away from the ligands and experiences lesser repulsion from the electrons of the ligands than the d_{z^2} and $d_{x^2-y^2}$ set of orbitals. Another common case is that pertaining to the tetrahedral structure. Here the d_{z^2} and $d_{x^2-y^2}$ orbitals are of lower energy and the d_{xy}, d_{yz} and d_{xz} orbitals are of higher energy. The crystal field splitting is given by the relation $\Delta \alpha \langle r^4 \rangle / R^5$ where 'r' is the radius of the orbital and R is the metal – ligand internuclear distance. The splitting in the case of the Mn ion is given as $\Delta = 10Dq$ [27]. Figure 1.4 represents the crystal field splitting pertaining to the octahedral and tetrahedral structures.

When the energy difference, Δ, is large it is more favourable for all the electrons to occupy the lower t_{2g} set of orbitals. Whereas when the energy difference, Δ, is small it is more favourable for the electrons to occupy both sets with as many parallel electron spins as possible.

In the case of Mn ions these splitting involve the d-orbitals of the central ion of the octahedral and the p-orbitals of the neighbouring ligands. Here the d_{z^2} and $d_{x^2-y^2}$ orbitals form σ – bonding orbitals and belong to the e_g symmetry category while the d_{xy}, d_{yz} and d_{xz} orbitals form π – bonding orbitals and belong to the t_{2g} symmetry category.

1.4 Jahn-Teller Effect

In the section above the effect of crystal field on the degenerate 3d orbitals to form two sets of degenerate orbitals called e_g (a doublet) and t_{2g} (a triplet) is explained. Further to this the ligands surrounding the transition metal ion, here oxygen surrounding the Mn ions, adjusts itself by a lattice motion causing an asymmetry in the different directions. This in turn removes the degeneracy of the doublet and triplet. This effect of removing the degeneracy through an orbital- lattice interaction is the Jahn Teller (J-T) effect. The famous theorem by Jahn and Teller [28] is stated as "any non-linear molecular system in a degenerate electronic state will be unstable and will undergo distortion to form a system of lower symmetry and lower energy thereby removing the degeneracy"

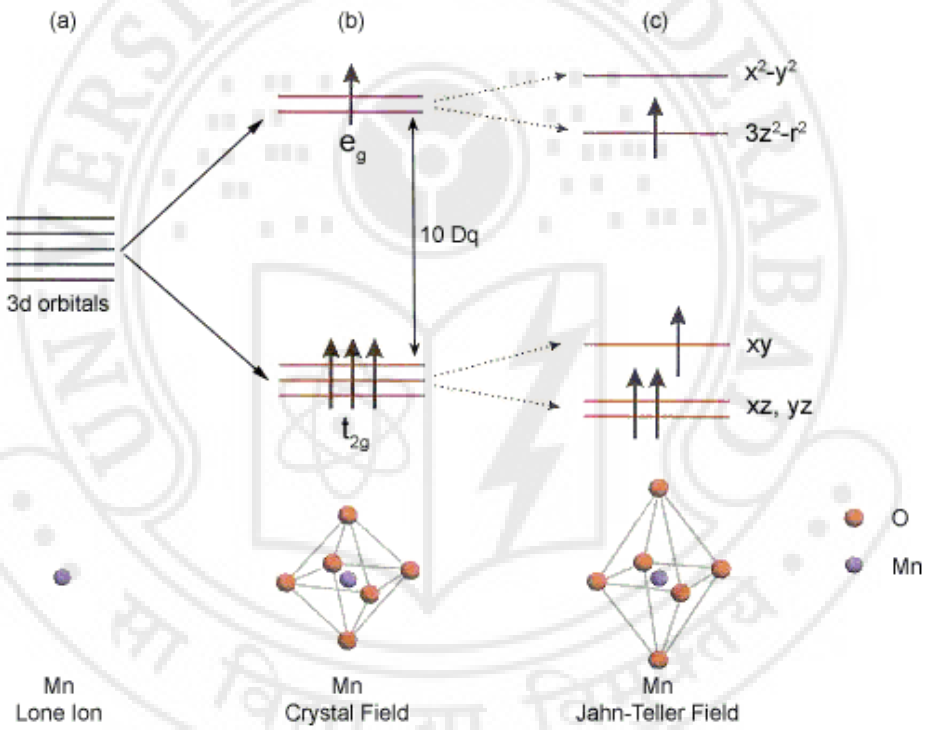

Figure 1.5: The Mn 3d energy levels for (a) the Mn ion alone with 5 degenerate d-orbitals. (b) Mn atom in the oxygen octahedron and the crystal field will split the 5 d-orbitals in 3 degenerate (xz, yz and xy) and 2 degenerate ($z^2 - r^2$ and $x^2 - y^2$) orbitals. The energy separation is termed 10Dq. (c) Jahn-Teller distortion of the MnO_6 octahedra lowers the energy of the system when the e_g orbitals have an uneven number of electrons.

The Mn^{3+} ions and the Mn^{4+} ions have configurations of $3d^4$ and $3d^3$ respectively. In the case of $3d^4$, with the Hund's rule and the exchange interaction J coming into play a high spin state is favoured, and due to the strong Coulomb repulsion between the d-

orbital electrons, there will be one electron in the e_g orbital. According to the Pauli's exclusion principle the orbitals first fill up with a single electron before double-occupancy takes place. For the $3d^4$ state, the system gains energy by lattice motion or distortion i.e. for the $z^2 - r^2$ orbital is further away from the oxygen p-orbitals the octahedron is elongated in the z-direction. The energy of the occupied $z^2 - r^2$ orbital will be lower, but the energy of the unoccupied $x^2 - y^2$ orbital will be higher as the octahedron is compressed in this direction. The electronic energy of the system is lowered when the e_g orbitals have an odd number of electrons. The $3d^3$ state does not exhibit such a distortion as there is no lowering of the energy. This distortion is called a J-T distortion and is important in manganites. The J-T distortion is represented in figure 1.5.

1.5 Effects of A-site cation, doping levels and variance factor

A general formula of manganites can be given as $A_xB_{(1-x)}MnO_3$, where A is a trivalent ion (e.g. La^{3+}, Bi^{3+}, Nd^{3+} etc) and B is a divalent rare earth metal ion (e.g. Sr^{2+}, Ca^{2+}, Ba^{2+} etc.) tetravalent (e.g. Ce^{4+}, Te^{4+} etc.) ion or a monovalent (e.g. K, Na etc.) ion. These non-trivalent ions act as dopants. There are a few parameters which play important roles in determining the physical properties of the perovskite structured manganites:

(1) the average size of the cation $\langle r_A \rangle$,
(2) the amount of doping *x*, which induces a mixed Mn valence state and hence charge carriers too
(3) doping at the Mn site, as Mn can be substituted by most of the 3d (e.g. Ti, Ga etc.) and some 4d (e.g. Ru) elements.
(4) enhancement or reduction of oxygen content.
(5) the variance factor define as $\sigma^2 = \langle r_A^2 \rangle - \langle r_A \rangle^2$, which is related to the degree of disorder of the system.

A change in the average size of the A- site cation can bring about changes in the crystallographic structure. This results in a deviation in the Mn-O-Mn bond angle from 180^o and the Mn-O bond length too. This in turn can alter movement of the carriers enhancing or hindering the charge conduction and therein other properties too. The variance factor too plays an important role in deciding the structure and structural distortions with the change in dopants [29]. For a mixed valence Mn state the magnetic ordering, which mainly occurs through the charge carriers, can be altered drastically. Enhancement of the amount of oxygen content can introduce metal vacancies and the

reduction of oxygen introduces oxygen vacancies, again which play important roles in defining different properties in these materials.

Work done in this accord highlights extensively the above mentioned parameters and the effects it plays on the structural, magnetic, optical and transport properties of manganites [30].

1.6 Exchange Interactions

The interactions between the spins of the Mn ions govern the magnetic properties of manganites. In manganites, the Mn ions are separated by an oxygen ion in between them. The extent of the overlap between the d-orbitals of the Mn ion and the p-orbitals of the oxygen ions control these interactions. These interactions are called exchange interactions as the electrons jump between the Mn^{3+}- O – Mn^{3+}, Mn^{4+}- O – Mn^{4+} or goes through a more interesting jump between Mn^{3+}- O – Mn^{4+}. The jumping of the electron between a Mn^{3+} and Mn^{4+} via the oxygen ion is called double exchange (DE).

1.7 Direct exchange

Direct exchange operates between moments, which are close enough to have sufficient overlap of their wavefunctions. As the ions are separated this strong but short range coupling decreases rapidly. A simple way of understanding direct exchange is to consider two atoms

Figure. 1.6. Antiparallel alignment of electrons for small interatomic distances.

with an electron each. When the atoms are closely spaced the Coulomb interaction between the electrons is minimal when the electrons spend most of their time in between the nuclei. The Pauli's exclusion principle requires these electrons possess opposite spins, to be at the same place in space at the same time. When the interatomic distance is small the electrons spend most of their time in between neighboring atoms and this gives rise to an antiparallel alignment and hence negative exchange (AFM) as depicted in figure 1.6.

Figure 1.7. Parallel alignment of electrons for large interatomic distances.

For atoms which are far apart the electrons spend their time away from each to minimize the electron-electron repulsion. This gives rise to parallel alignment or positive exchange (FM) as shown in figure 1.7.

1.8 Double exchange

The mechanism of DE was first proposed by Zener [21, 22]. Using a second order process involving an intermediate state (Mn^{3+}-O^{-}-Mn^{3+}), Anderson and Hasegawa [23] reformulated this model. Effective hopping amplitude was found to be dependent on the relative orientation of the magnetization on the two neighbouring Mn ions. Figure 1.8 shows

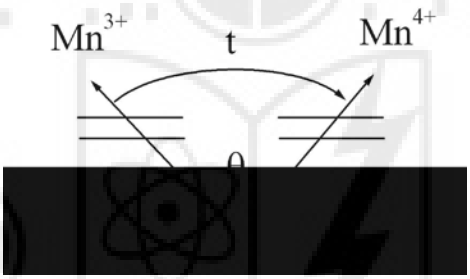

Figure 1.8. Schematic diagram depicting t

the effective hopping t, given by $t = t_0 \cos(\theta/2)$, where θ is the angle between the localised spins. de Gennes [24] introduced the DE lattice model by adding the super-exchange interaction and predicted canting of spins for a small doping in the parent manganite. As a result of the relative orientation of the Mn ions with respect to the bridging oxygen ion different phases occur in doped manganites. This is explained using the concept of semi-covalancy by Goodenough [25]. The so-called Goodenough-Kanamori [25, 26] rules allow qualitative understanding of the magnetic exchange between Mn ions in terms of the orientation of the orbitals.

The DE interaction process proposed by Zener was used to account for the mechanism explaining the FM phase that is formed as well as the conductivity in manganites. In the initial model it was proposed that a simultaneous transfer of one

electron from a manganese 3d e_g orbital to an oxygen 2p orbital and transfer from the same oxygen 2p to a manganese 3d e_g orbital on an adjacent ion takes place (depicted pictorially in Figure 1.9). In this way the e_g electrons are able to move throughout the lattice. Both electrons involved in the exchange must have the same spin (because of the Pauli Exclusion Principle). This leads to a ferromagnetic arrangement of the e_g electrons

The 2p orbitals of the O^{2-} are assumed to be completely filled. Hence DE is considered to take place in two steps. First, the e_g electron from the O^{2-} moves to the empty Mn^{4+} orbital. Then an e_g electron from the Mn^{3+} is transferred to the vacant O^{2-} 2p orbital. This could also

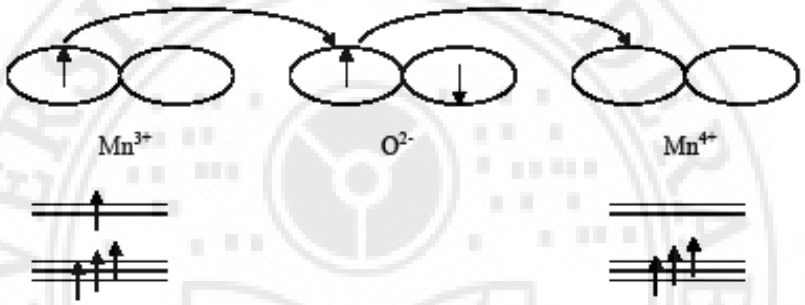

Figure 1.9. The schematic diagram of the DE mechanism depicting the simultaneous transfer of the electrons between adjacent atoms along with the Mn spins

happen in another manner where the holes from the Mn^{4+} can move instead of the electrons from the Mn^{3+}. A strong Hund's coupling between the localized t_{2g} and the itinerant e_g spins favours/hinders movement of electrons which have their spin parallel/antiparallel to the localized spin (figure 1.10). The result is high electrical conductivity (metallicity) and ferromagnetism as the hopping electron leads to the alignment of the spins of neighbouring Mn atoms. The electrons gain kinetic energy from these processes which is not possible if the spins are not aligned. With temperature the spins change their alignment.

Below T_C all the spins of Mn^{3+} as well as Mn^{4+} align in the same direction favouring FM. The hopping kinetic energy of the conduction electrons increases and the single e_g electrons of Mn^{3+} can hop back and forth between the Mn^{3+} and Mn^{4+} via the oxygen ion. When temperature is increased up to an ideal paramagnetic (PM) regime, all spins are completely disordered hampering electron hopping and producing a paramagnetic insulating (PMI) state. However at temperatures near T_C, an applied

magnetic field can align the spins, enhancing the effective electron hopping and thus decreasing the resistivity and as a result, the CMR-like effect seems to emerge.

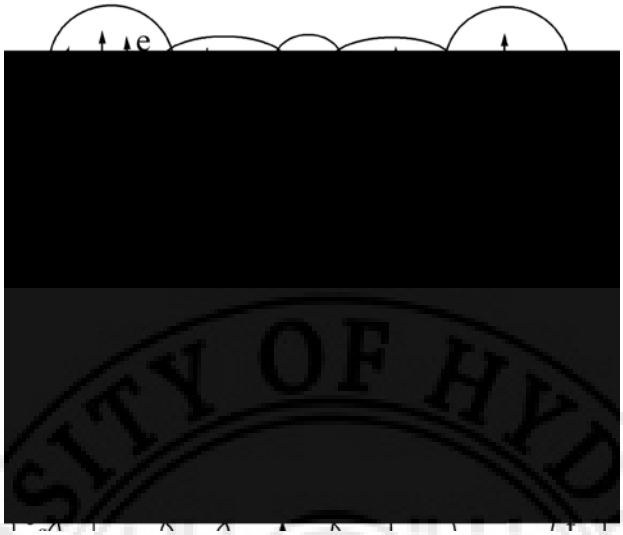

Figure 1.10. An illustration of DE for Mn ions with different valencies

A lot more theoretical modifications were brought about after Anderson and Hasegawa refined the original work of Zener. Millis *et. al.* considered the spin correlations and the electron-phonon coupling which arises from the J-T splitting of the Mn 3d levels [31] and Roder *et. al.* [32] brought the concept of the localized potential carriers due to the lattice distortions (self trapping polaron concept) while modifying the model proposed by Zener. Later it was also postulated that the FM occurs from the direct exchange between holes [33].

1.9 Superexchange

In DE, the effect of hopping of the e_g electrons between the Mn ions of different valencies is considered. The e_g electrons lie closest to the Fermi level and have the highest energy. Here the t_{2g} electrons are localized even in the metallic state. However, the t_{2g} electron can overlap with the oxygen 2p-states, which can also give rise to the superexchange (SE) interaction. Unlike DE, this mechanism traditionally applies to the neighbouring Mn ions with the same valency via intermediate O^{2-} ions, e.g. Mn^{2+}-O^{2-}-Mn^{2+}, Mn^{3+}-O^{2-}-Mn^{3+} and Mn^{4+}-O^{2-}-Mn^{4+}.

Superexchange (SE) describes the interaction between moments on ions too far apart to be connected by direct exchange, but coupled over a relatively long distance through a non-magnetic material. In SE, a non-magnetic ion with a closed shell acts as a mediator for the magnetic interaction between adjacent ions. In magnetic oxides this interaction takes place via the intermediate ion which is O^{2-}. If two orbitals on adjacent ions point towards each other, with one orbital fully occupied and the other orbital having

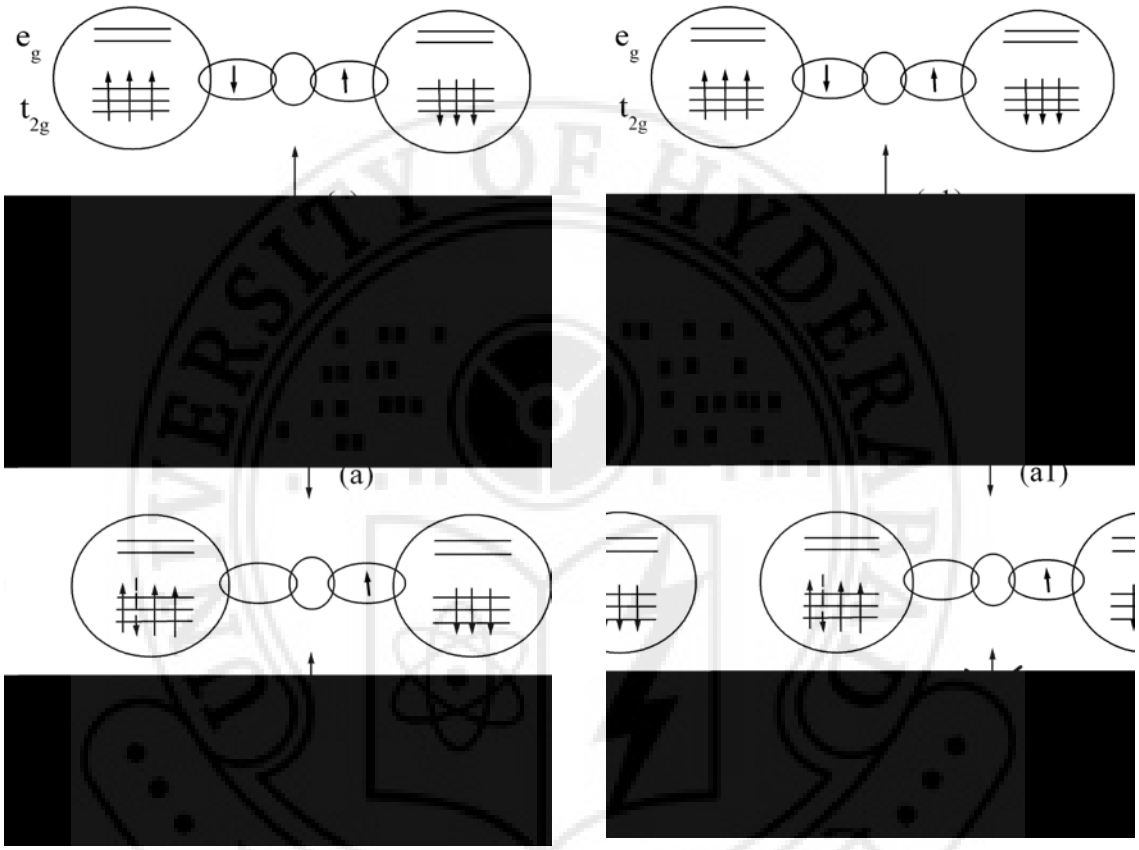

Figure 1.11. Illustration of the superexchange mechanism for Mn^{4+} ($3d^3$: $e_g^0 t_{2g}^3$) ions in the AFM state (left). FM (right) is rejected assuming non-orthogonal Mn^{4+} orbitals. It is stressed that the bottom configuration on the right is forbidden

a vacancy, then the electron will spend part of its time in the empty orbital on the other ion. In the case of the manganites, the orbitals involved are the vacant Mn e_g orbitals and the occupied O 2p orbitals, and so it is the O 2p electron that is 'shared' between the two ions. This virtual transfer of the electron is what characterizes superexchange. SE can lead to either an FM or an AFM type alignment of the spins, depending on the occupancy of the Mn orbitals, as depicted in figure 1.10. There is a strong Hund's coupling between the core Mn t_{2g} spins and any e_g electron(s). There are two cases to consider, namely when the Mn e_g orbital has one permanent electron (Mn^{3+}) and occasionally the virtual

electron, or only the virtual electron (Mn^{4+}). For Mn^{3+} the t_{2g} and permanent e_g electron will be spin-aligned (Hund's rules), so the spin of the transferred electron has to have the opposite sign, as required by the Pauli's principle. Conversely, for Mn^{4+}, the electrons in the Mn t_{2g} orbitals align with the virtual electron from the oxygen ion.

The different properties exhibited by manganites are related to the different strong couplings between the orbital, charge and spin ordering as well as between the lattice and spin, and between each other too. Below, the concepts of charge-ordering (CO), orbital-ordering (OO) and spin-ordering (SO) are discussed briefly.

1.10 Charge Ordering

Generally, the ordering of the metal ions in different oxidation states in specific lattice sites of a mixed valent material is termed as charge-ordering. Such ordering can localize the electrons/holes in the material, rendering it insulating or semiconducting. This occurs because the electrons/holes will not be able to hop from one cationic site to another in the material when the charges are localized. A very commonly cited CO state is that applied to the Verwey transition [34] that occurs in magnetite (Fe_3O_4) at 120 K.

In compounds with transition metals an incomplete doping with holes or electrons leads to a mixed-valence state for most of the transition metals (TMs) such as Cu, Mn, Ni, Fe, etc. For example, in manganites like in $LaMnO_3$ and $CaMnO_3$ the Mn ion has a valency of +3 and +4 respectively. When Ca is substituted in an La- manganite hole-doping occurs to give $La_{(1-x)}Ca_xMnO_3$. Similarly when La is substituted in a Ca-manganite, electron-doping occurs and $Ca_{(1-x)}La_xMnO_3$ is synthesized. In both these cases the Mn ion keeps both valence states and the ratio of Mn^{3+}/Mn^{4+} depends on the doping level and dopant. The relative long-distance chain of TM ions with the same valency in these kind of mixed-valence compounds, under certain conditions of doping level, temperature etc, is viewed as uniformly placed organized charge carriers with a specific pattern of valence states and this forms the charge-ordered state. Charge order including all charge carries of the conduction band leads to an insulating state as the ions are confined more to the lattices. Charge-ordering also favours AFM. CO competes with DE, giving rise to interesting properties which are sensitivity to factors like the A-site cation size, the doping level etc. The cooperative J-T effect induces other effects like lattice distortion and also adds to the electron localization in the CO state. On the other hand when distribution of valence states does not follow any specific pattern, the state is

called a charge disordered state. This facilitates mobility of charge carriers, which in turn favours a metallic state. Therefore the charge disorder-order transition usually accompanies the metal-insulator transition.

The CO- state can be destroyed or "melted" by the application of a magnetic field [35], pressure [36] or exposing the materials to x-ray photos [37]. Lots of work stating the occurrence of CO state in the manganite $A_{(1-x)}B_xMnO_3$ with $x = 0.5$ have been reported [14, 16, 38, 39], highlighting the equal amounts of Mn^{3+} and Mn^{4+} ions. But not all such systems with x = 0.5 exhibit CO. $Pr_{0.5}Sr_{0.5}MnO_3$ exhibits an A-type antiferromagnetic insulating ground state [39, 40], whereas $Pr_{0.7}Ca_{0.3}MnO_3$ has a CE- type antiferromagnetic structure and exhibits CO. Hence the equal amounts of Mn^{3+} and Mn^{4+} ions is not a pre requisite for CO. CO is a material dependent property alone.

1.11 Orbital ordering

Orbital degeneracy, through orbital ordering, helps to produce a rich structure of low energy excitations as seen above while considering the J-T effect. In manganites, the active orbitals are the Mn-O antibonding e_g orbitals, i.e. the $x^2 - y^2$ and $3z^2 - r^2$. The Mn^{3+} in an octahedral crystal field experiences a J-T instability due to the electronic instability implicit in the Mn^{3+} ions. This in turn gives rise to a bond length distortion of the MnO_6 octahedra.

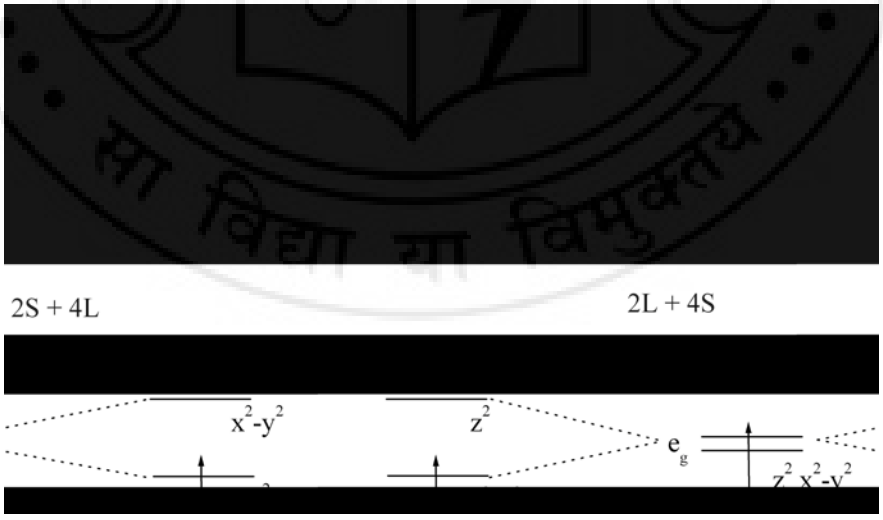

Figure 1.12. Effect of Jahn –Teller distortion on the partially occupied Mn^{3+} d orbitals.

The Mn^{3+} ion, which has 4 d-orbital electrons, experiences a weak crystal field. The non bonding t_{2g} orbital contains 3 electrons and the antibonding e_g orbital contains a

single electron (figure 1.12). The single electron results in an orbitally degenerate electronic state for the Mn^{3+} ion. This orbital degeneracy, is revoked as the orbitally degenerate state is unstable to a distortion along the vibronic coordinate (figure 1.13) [41]. Hence these orbitals in the octahedrally symmetric isolated MnO_6 unit are vulnerable to J-T distortions.

The occupied e_g orbital gets electronically stabilized as this distortion lowers the local symmetry to tetragonal or orthorhombic structure. When in a solid, the MnO_6 octahedra undergo J-T distortions which can be coherent or incoherent, static or dynamic. The coherent static J-T distortions are called cooperative J-T distortions or more generally they are known as 'orbital ordering' (OO). One of the earliest explanations for the orbital ordering was given

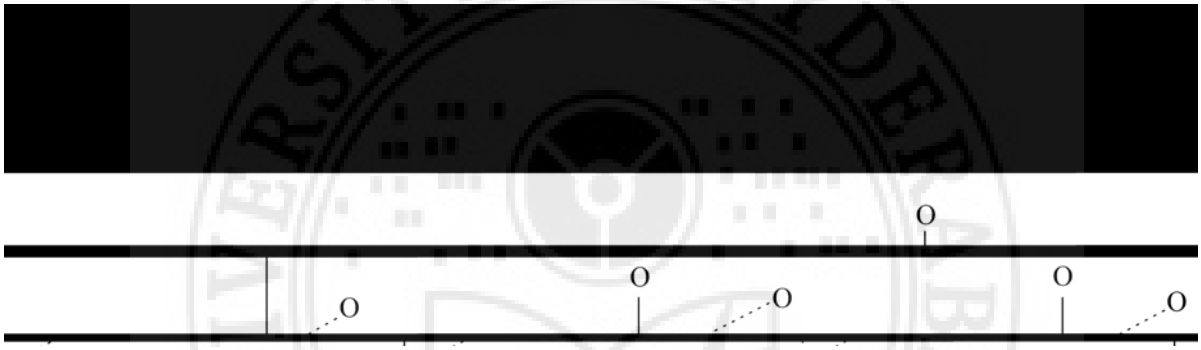

Figure 1.13. Distortion along the vibronic coordinates lifting the orbital degeneracy.

by Goodenough [25], arguing about the incoherency of the local strain induced by differing bond lengths, as seen in, figure 1.13, above some ordering temperature. The ordered arrangements of long and short Mn-O bonds which bring about the distortion, away from the cubic symmetry, are diluted as the distortions condense.

Goodenough [25] stated that OO can occur above the AFM ordering temperature, meaning that the magnetic ordering can depend on the OO that has already set in. With the addition of dopants the OO state disrupts as the interactions responsible for OO reduce or get replaced with other interactions. This could be due to the introduction of the different ratio of Mn^{4+} and Mn^{3+} ions in the material. The substitution at the A-site or the variation of the oxygen stoichiometry can play an important role in suppressing or enhancing the cooperative J- T ordered state.

The composition $A_{0.5}B_{0.5}MnO_3$ is particularly interesting as these materials should give the Mn^{3+}-Mn^{4+} ratio $Mn^{3+}/ Mn^{4+} = 1$. This would give equal numbers of J-T active as

well as inactive centres. The neutron and synchrotron x-ray diffraction studies by Radaelli *et. al.* [42] was the first to show the structure of Mn-O bond lengths coherent with the distinct Mn^{3+} and Mn^{4+} sites. The study also involved the detection of a "multi-phase" which was considered as a metastable phase with an assemblage of orbital orderings on the path to a stable ground state structure.

1.12 Spin ordering

The interplay of Coulomb's energy and the Pauli's exclusion principle affect the spin-spin interactions which form the basis for long range ordering. The Hund's rule, which is affected by the Pauli's exclusion principle and has parallel spins occupying different orbitals, also acts upon the arrangement of the orbitals.

The long range magnetic spin ordering seen in manganites is a result of the strong coupling of spin, charge, orbital and lattice degrees of freedom. DE and SE interactions and the interplay between the two interactions can be used well to explain most of these phenomena. The strength of the spin interactions is largely dependent on the doping level as well as the temperature.

DE involves real electron transfer from a filled e_g orbital to an empty one whereas SE involves only a 'virtual' electron transfer from the orbitally non-degenerate localized t_{2g} orbitals. Though SE is constrained by Pauli's exclusion principle DE is not. In SE the spin of the 'vitually' transferred electron is antiparallel to the spin of the t_{2g} configuration

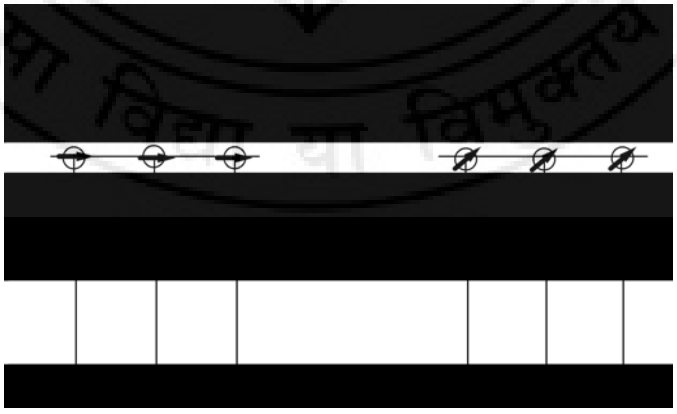

Figure 1.14. A Schematic diagram of (a) A-type AFM ordering and (b) canted A-type AFM ordering

of the acceptor atom. Pauli's exclusion principle does not affect DE. The spin of the transferred electron is parallel to the spin of both the donor as well as the acceptor due to strong intra-atomic exchange interactions.

The exchange interactions of DE and SE and the competition between them help in understanding spin-ordering in manganites. With the change in dopants and the doping levels the balance between DE and SE interactions can be tuned which in turn will reflect on the different properties of the manganites. For example a system with spin-ordering in the foreplay, doping into that system helps to change the AFM state to FM state as DE would play a more prominent role with increasing doping levels. de Gennes [24] and Goodenough [43] predicted that this kind of change goes through different phases like from the AFM phase to the canted AFM phase (figure 1.14) or even spiral magnetic structures before becoming FM.

The changes brought about in the preparation conditions like that of the oxygen pressure can introduce a structural transition in the system as shown by Mitchell *et. al.* [44]. The study highlights the magnetic transition in the absence of an electronic transition, hence focusing only on the spin- lattice coupling. Studies by Argyriou *et. al.* [45] reveal the anomalies in the lattice parameters and the Mn-O bond lengths as a function of temperature, near the magnetic transition temperature. Most importantly, the interaction of the spin ordering with the lattice reduces the ordered J-T state which sets in above the magnetic transition temperature.

1.13 Phase separation

A very interesting feature that has been reported in many manganite materials in recent times is that of phase separation. This emphasizes on the coexistence of different electronic and magnetic phases in structurally and chemically pure single phased samples. Examples are the existence of an FM phase in a PM matrix or FM phases embedded in an AFM background etc.

Zener was the first to qualitatively explain the correlation between transport and magnetic properties [21, 22] by explaining that the conduction electrons in $La_{(1-x)}Ca_xMnO_3$ move through the Mn^{4+} ions which are strongly ferromagnetically coupled to the spin of the ion carrier by the Hund's rule. Anderson and Hasegawa [23] proposed the concept of the hopping amplitude and the dependence of the kinetic energy on the angle between the sublattice moments. de gennes [24] suggested that this angle changes when

there is a change in the order from AFM to FM with different doping levels and the competition between the two states results in a homogeneous canted state, based on which the first phase diagram was plotted. Nagaev [46, 47] improved on this work by de Gennes by proving that an electron can move in an AFM ordered phase with a small hopping amplitude calculated to be t√2S + 1. Nagaev, Kasuya and Mott [46 - 49] proposed the concept of a kind of self trapped form of conduction electrons, an FM polaron, in an AFM matrix, in contrast to the homogeneous canted state. This was one of the first leads on phase separation. The concept of 'electronic' phase separation (PS) (finding FM regions in an AFM matrix) was first introduced by Nagaev in the late 1960s and early 1970s in semiconductors Later he remarked that if the two phases have opposite charges, the Coulombic forces will break the macroscopic clusters into microscopic ones, typically of nanometer-scale size.

In an effort to explain the CMR effect different arguments were made in terms of DE [50] alone, the consideration of J-T effect [31], percolation- type effects [51] etc. Dagotto *et. al.* [52] and Arovas *et. al.* [53] highlight the different calculations on different models exhibiting strong tendency to PS in a wide range of temperatures and concentrations. Thus phase competition and phase separation was considered to play an important role in explaining the CMR effect.

Earlier work by Moreo *et. al.* [54] and Burgy *et. al.* [55] used 'electronic phase separation' which is on a nanometer scale and 'disorder-induced inhomogeneity' (usually due to the random distribution of the A-site cations) which is on the micrometer scale to explain PS. Using two different scales to explain the same feature was something that was not plausible though. Mathur and Littlewood [56] used the Landau theory to explain phase separation on a mesoscopic scale, assuming the magnetic contribution to the overall free energy to be negligible. Ahn *et. al.* [57] put forth a model predicting a micron-scale coexistence of phases considering strain state to be the most important factor in determining the occurrence of PS, with the drawback of neglecting the magnetic and electronic interactions completely.

Using the one-orbital model [54] it was demonstrated that when certain electron densities are not stable the resulting ground state can be separated into two regions with different stable electron densities. This was observed as a separation as hole-undoped AFM and hole-rich FM regions [58]. The two-orbital model on the other hand took into account the J-T distortions as well as the electron phonon coupling strength [59], which

also helped in predicting the phase separated regions in electron poor and rich regions [60]. Taking into account the Coulomb interactions due to different electron densities and hence charges, a stable state is formed when a cluster of one phase gets embedded in the matrix of the other. The competition between the attractive DE and repulsive Coulomb interactions determine the size of the 'cluster'. This state can be termed as a charge inhomogeneous state. The charge carriers cannot hop between antiparallel spins in charge inhomogeneous states. The insulating state, which cannot be explained by double-exchange alone, then arises from the cluster formation, which is dynamical at high temperatures. The metallic state is then obtained if the clusters grow in size as the temperature is lowered and eventually reaches a limit where the percolation between the clusters is possible. At this stage the carriers can move over long distances and a metallic state is formed.

The theoretical predictions were followed by experimental reports on phase separation. Perring *et. al.* [61] reported AFM clusters of C-type coupled in the MnO_2 plane within FM fluctuations of $La_{1.2}Sr_{1.8}Mn_2O_7$. Below T_C the AFM fluctuations rapidly decrease as the FM metallic state is reached. Hence the charge carriers in the PM phase hop in a medium with mixed FM and AFM correlations. Using DE the resistivity in the PM phase can be explained with the hopping across FM bonds allowed and those across AFM bonds suppressed.

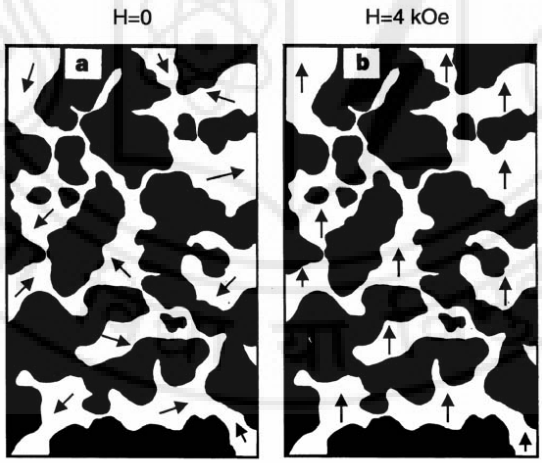

Figure 1.15. A schematic diagram representing the phase coexistence observed at low temperature. The white regions represent the FM metallic phase and the dark regions the CO insulating phase. The magnetic moments (represented by arrows) align when a magnetic field of 4kOe is applied. Taken from [65].

First order transitions that occur at low temperatures between FM and CO states are one of the most studied features while probing the phenomenon of PS. Electrical and

magnetic properties studied on polycrystalline samples of $La_{0.5}Ca_{0.5}MnO_3$ [62, 63] with different grain sizes have been reported; for larger grain sizes CO is observed at 140K but for sizes lesser than 450nm no such feature is observed. The magnetic moment for particle sizes > 450nm is seen to drop below a temperature of 140K whereas for grain sizes < 450nm there is no such drop in the magnetic moment. On the contrary the moment continues to decrease with decreasing temperature. As the sample goes into the CO state with decreasing temperature a residual magnetic moment is still present even at 20K which indicates that FM clusters still exist in the system. The increase of the residual moment with decrease in temperature suggests that the grain boundaries which introduce structural defects and variation in the strain state hinder the CO state from setting in. A schematic diagram of phase coexistence at low temperatures is shown in figure 1.15.

TEM and holography studies on polycrystalline $La_{0.5}Ca_{0.5}MnO_3$ revealed a micron-sized region that was both ferromagnetic and charge ordered [65], which was different from the conventional idea of phase separation with separate CO and FM clusters, though charge ordering and ferromagnetism can coexist. The magnetic moment in this region was measured to be $3.5\pm0.2\ \mu_B$ per manganese ion, which was in excellent agreement with the fully spin-aligned value of $3.5\ \mu_B$/Mn ion.

The above mentioned are results keeping in view of the fact that these results do not vary with time. Levy *et. al.* reported variation of resistivity with time and the magnetic history of $La_{0.5}Ca_{0.5}Mn_{0.95}Fe_{0.05}O_3$ [66]. The resistivity studies of $La_{0.5}Ca_{0.5}Mn_{0.95}Fe_{0.05}O_3$ later reported was seen to depend on the cooling rate, though the metal to insulator transition temperature remained the same. In the temperature range $T< T_C$, at a constant temperature the resistance undergoes a time dependent logarithmic decrease. The authors attributed this relaxation to the continued expansion of FM clusters within a non-FM matrix. On resumption of cooling, the resistance was 'rejuvenated' and merged smoothly with the curve obtained with cooling at a constant rate. A phenomenological model was proposed in which the expansion of the FM regions against the host material proceeded via a step-wise movement of phase boundaries through energy barriers. In this model, the slope of the resistivity curve had a static contribution from $d\rho/dT$ for fixed fractions of each type of phase, and a dynamical term related to the change in size of the FM clusters.

In recent years, coexistence of FM and AFM domains in different types of manganites has been treated in terms of the Griffiths phase (GP) concept. According to

the Griffiths theory [67], there is a finite probability of finding FM clusters for a system with randomly distributed spins in the temperature range of $T_C(p) < T < T_G$ between the random transition temperature $T_C(p)$ and the pure transition temperature T_G. This feature is dealt with and looked into more intently in chapter 4.

LITERATURE REVIEW.

The electronic transport properties of the transition metal oxides strongly interact with the magnetic properties and with the crystal lattice. Many properties and transitions cannot be described by simple one electron models. This holds well in the case of manganites too. Thus manganites are also part of the strongly correlated electron systems. A few obvious reasons, from what has been discussed in reference 4, which motivate physicists towards extensive research in manganites, can be stated: "In an applied magnetic field the transport carriers move in a helical path tending to have more collisions, thereby increasing the resistance. But in the case of manganites, in the presence of a magnetic field, the resistivity of the material drops by many orders of magnitude leading to the CMR effect." The CMR-effect was initially understood in the framework of the DE [21] theory, which intuitively explains the coupling between the magnetic and resistive transitions. Later, however, it was recognized by Millis *et. al.* [31] that double-exchange fails to explain the quantitative change in resistivity and the low T_C and additional physics must be taken into account. The authors also argued, in a separate publication, that there is an unusually strong interaction between the electrons and lattice vibrations (phonons) [68] and that this coupling of the electrons to the lattice might explain the quantitative change in resistivity. The theories of DE and Anderson's localization [23] alone do not explain CMR in manganites. Moreover, it is difficult to understand CMR, when Coulomb based interactions as well as electron phonon couplings occur simultaneously. These are only a few of the difficulties faced in understanding the phenomenon of CMR that occurs in different kinds of manganites.

Manganites are intrinsically inhomogeneous materials i.e. clusters of competing phases coexist in these compounds. These inhomogeneities, it has been argued (with due experimental evidence too), cause the CMR effects [66]. The large resistivity in the PM insulating phase is also caused by these inhomogeneities [66]. Manganites exhibit different degrees of freedom in the form of spin, charge, lattice and orbital order. This gives manganites a rich phase diagram which can be immensely helpful in not only observing the systematic changes in these materials by changing these degrees of freedom but can also assist in trying to predict properties of different manganites.

There are many more specific issues that need to be studied more keenly for the better understanding of the different mechanisms in manganites, of which a few can be

stated. Different studies have been carried out to evidence and explain the existence of CO nanoclusters above T_C [70-74]. The concept of the FM insulating phase and glassy phases in manganites still fascinates physicists and chemists alike. Similarly there are lots of unsolved problems which keep the theoreticians also bustling about for answers. The conduction via the percolation of carriers cannot be explained by phase separation alone as the concept of inhomogeneities also is to be considered. Likewise the theories of phase separation have been built with a dimensionality of 2 in picture. Work done for accommodating a three dimensional picture [55] has yielded good results but a more realistic Hamiltonian regarding the same is yet to be arrived at.

1.14 Studies on $BiMnO_3$

Study on the various properties using different kinds of manganites can help in shedding light over a lot of unsettled issues and unanswered questions. Manganites which have similar kinds of A-site ions too vary a great deal in their properties. A typical example is the difference exhibited by $LaMnO_3$ and $BiMnO_3$. Though the ionic radii of lanthanum ($1.22A^o$) and bismuth ($1.24A^o$) are almost similar the properties of the two materials vary (the radii given is for a coordination number 9). $BiMnO_3$ has a triclinic structure, which is a more distorted structure, whereas $LaMnO_3$ has a monoclinic structure. In a similar manner there are many other systems which yield results different from the expected, which make the research on manganites all the more exciting. $LaMnO_3$ is an antiferromagnetic insulator whereas $BiMnO_3$ exhibits ferromagnetism with a T_C around 105K [74]. Investigation of polycrystalline and thin films of $BiMnO_3$ by Santos *et. al* [75] suggest it to be FM with a T_C of 105K and ferroelectric with a Curie temperature of 450K, remaining ferroelectric to low temperatures through the ferromagnetic transition.

Bismuth based manganites have not been studied as extensively as their La, Pr or Nd based counterparts. Till date there have been no reports on applications in which these materials are being used. The earliest works recorded on Bi based manganites was the study of $BiMnO_3$ highlighting the FM property with a $T_C \sim 105K - 110K$ and presenting other magnetic properties of perovskite $BiMnO_3$ [76 – 81]. The structure is analyzed to be a distorted triclinic which is explained by the highly polarizable Bi^{3+} $6s^2$ lone pair of electrons. Tomashpol'skii *et. al.* [78] reported that polycrystalline $BiMnO_3$ shows a transition at ~ 483K in relation to the change of the superstructure. Beyond ~ 873K it begins to decompose. Atou *et. al.* [80] ascertain the structure of ferromagnetic $BiMnO_3$

by electron diffraction and neutron powder diffraction. The structure is reported to be related to distorted perovskite structure with a monoclinic symmetry, space group C2, the distortion being caused by a polarized Bi $6s^2$ lone pair. A J-T distortion is seen in the Mn^{3+} ions and the ordering of a vacant $d_{x^2-y^2}$ orbital plays an important role for exhibiting ferromagnetism. Fakir *et. al.* [81] reports high pressure synthesized $BiMnO_3$ with a triclinically distorted perovskite structure being ferromagnetic (T_C ~ 108 K). The stability and melting sequence of $BiMnO_3$ in air is determined from high-temperature x-ray diffraction analysis, thermal analysis, thermogravimetry, and magnetic measurements. Structural phase transition from triclinic to tetragonal structure has been determined at 490^{o}C in air for a polycrystalline $BiMnO_3$ perovskite. Two phases form immediately at the decomposition temperature of 600^{o}C, namely Bi_2O_3 and $Bi_2O_3 \cdot 2Mn_2O_{3-\delta}$.

Hill *et. al.* [82] present results of local spin density approximation (LSDA) pseudopotential calculations $BiMnO_3$. The origin of the differences between bismuth manganite and other perovskite manganites is determined by first calculating total energies and band structures of the high symmetry cubic phase, then sequentially lowering the magnetic and structural symmetry. The results indicate that covalent bonding between bismuth cations and oxygen anions stabilizes different magnetic and structural phases compared with the rare earth manganites, which is consistent with experimental results showing enhancement of charge ordering in doped bismuth manganite.

Results of first-principles electronic structure calculations on the low-temperature monoclinic phase of $BiMnO_3$ have been reported by Seshadri *et. al* [83] too. In agreement with experimental results, the calculations obtain an ferromagnetic insulating (FMI) ground state for the system. The role of Bi 6s “lone pairs” in stabilizing the highly distorted perovskite structure using real-space visualization of the electronic structure is mentioned. Comparisons are drawn with the electronic structures of hypothetical cubic $BiMnO_3$ and with the electronic structure of the prototypical perovskite manganite, $LaMnO_3$. The exploitation of the ‘s’ electron lone pairs in the design of new ferroic materials is suggested.

Baettig *et. al.* [84] use the local density approximation and Hubbard’s (LDA+*U*) method of density functional theory to compare the structure and properties of the calculated lowest energy structure of $BiMnO_3$ to the experimentally reported structures. Though the two works reported that C2 structures are polar, they are also found to be

higher in energy than a closely related centrosymmetric C2/c structure with zero polarization. As the ferroelectric hysteresis loops or second harmonic signals of work on polycrystalline bulk samples cannot be explained these calculations suggest that the ground state of perovskite-structure $BiMnO_3$ is centrosymmetric with space group C2/c and zero ferroelectric polarization. These calculations are robust and consistent with experimental values for stoichiometric $BiMnO_3$ (which may not be achieved always).

One of the more recent works by Santos *et. al.* [85] revealed similar structural results as reported earlier. They report the ferromagnetic structure of $BiMnO_3$ with T_C ~105K, determined from powder neutron-diffraction data collected at 20K. $BiMnO_3$ is a distorted perovskite that crystallizes in the monoclinic space group C2. Data analysis reveals a collinear FM structure with a magnetic moment of $3.2\mu_B$. It is believed that ferromagnetism and ferroelectricity coexist in $BiMnO_3$ as there is no crystallographic phase transition on cooling the polar room temperature structure to 20K. The six unique Mn–O–Mn superexchange pathways between the three crystallographically independent Mn^{3+} sites show that four are ferromagnetic and two are antiferromagnetic, confirming orbital ordering the cause of ferromagnetism of $BiMnO_3$.

Kimura *et. al.* [86] describe ferroelectricity in $BiMnO_3$ at $T_E \approx 750 – 770$ K due to a centrosymmetric to non-centrosymmetric structural transition. Magnetic ordering (T_M ~ 100K) as well as application of magnetic fields near T_M induces changes in the dielectric constant. These features are attributed to the inherent coupling between the ferroelectric and ferromagnetic orders in the multiferroic system.

The structural evolution of biferroic $BiMnO_3$ caused by electron-beam irradiation has been studied by means of electron diffraction (ED), HRTEM, EELS and EDAX techniques [87]. The ED and HRTEM observations demonstrate that the C2 monoclinic form of $BiMnO_3$ irreversibly transforms to another modulated form by electron-beam irradiation. This irradiation-induced form shows a higher symmetry and can be described by a body-centered pseudocubic superstructure. The EELS and EDX measurements reveal a small decrease of O/Mn ratio, but no change of Bi/Mn ratio in the irradiation-induced form as compared with the *C*2 monoclinic form. From the decrease of the O/Mn ratio, it is concluded that the irradiation-induced form is produced from ordered oxygen deficiencies and a possible structure model is proposed.

Montanari *et. al.* [88] reports a metastable state in $BiMnO_3$ synthesized at high pressure and temperature at ambient conditions. They evidence polymorphism by observing the coexistence of a minor phase with the well-known C2 monoclinic form, which can be described by a triclinic (pseudorhombohedral) superstructure which is mostly segregated at the grain surface, from the electron diffraction and high-resolution electron microscopy results of the samples. Magnetic characterizations revealed for this second minor phase a critical temperature of 107 K, a few degrees above the ferromagnetic transition of the monoclinic C2 form measured at 99 K. The new phase disappears by reheating the samples at ambient pressure, suggesting the idea of a higher energy polymorph, which kinetically converts in the usual phase once a sufficient temperature is achieved. In another report Montanari *et. al.* [88] describe their work on high-pressure synthesized $BiMnO_3$, which decomposes if heated at room-pressure in the temperature range of 500 - 650°C. Comparative studies by high-temperature x-ray diffraction, electron diffraction, thermal analysis, and magnetic investigation revealed the existence of a complex pathway to decomposition, depending on the heating rate, pressure, and atmosphere that involves different metastable phases. In particular the as-prepared monoclinic phase (I) transforms to a second monoclinic form (II) at 210 °C and then to an orthorhombic phase (III) at 490°C. These phase transitions occuring on heating are moved at higher temperatures when pressure is decreased. The transition from II to III, typically observed in inert atmosphere, can be also detected in air when the heating rate is kept sufficiently high. When III is heated in an oxygen-containing atmosphere a slow irreversible transition to variants IV and then V takes place with kinetics depending on temperature, heating rate and oxygen partial pressure. Both IV and V are oxidized FM phases containing Mn^{4+} characterized by a modulated structure based on fundamental triclinic perovskite cells. Their magnetic behavior shows a strong analogy with thin films of $BiMnO_3$, suggesting for the latter an oxidized nature and for the former a possible multiferroic behaviour. Montanari *et. al.* [88] report the structural properties of $BiMnO_3$ from neutron powder diffraction data as a function of temperature and magnetic field. The structure at all temperatures is found to be centrosymmetric with space group C2/c, which is incompatible with ferroelectricity. Both the magnetodielectric anomalies and the large magnetoelastic strain ($T_C \approx 100K$) is proportional to the square of the magnetization and hence to each other. From the data above and below the magnetic transition the authors confirm that the structure of $BiMnO_3$ retains a center of inversion, and is therefore unlikely to be ferroelectric

The studies on the electronic structure, magnetic and electric properties, and lattice stability of multiferroic $BiMnO_3$ using first principles are presented by Shishidou *et. al* [89]. Consistent with crystallographic data, it is demonstrated theoretically that orbital ordering within the Mn e_g orbitals is realized in $BiMnO_3$ and plays a crucial role in the appearance of ferromagnetism. Total-energy calculation shows a stabilized FM state. Electrical polarization of $BiMnO_3$ is estimated based on the Berry phase theory. They report lattice instability to off-centred displacement, which is driven by strong covalent bonding between Bi 6p and O 2p states, to be common in the $BiMO_3$ series.

Structural properties of polycrystalline single-phased $BiMnO_3$ samples prepared at 6 GPa and 1383 K have been studied by selected area electron diffraction (SAED), convergent beam electron diffraction (CBED), and the Rietveld method using neutron diffraction data measured at 300 and 550K [90]. The SAED and CBED data showed that $BiMnO_3$ crystallizes in the centrosymmetric space group C2/c at 300K. The analysis of Mn-O bond lengths suggested that the orbital order present in $BiMnO_3$ at 300K melts above $T_{OO} \approx 474K$. The phase transition at 474K is of the first order and accompanied by a jump of magnetization and small changes of the effective magnetic moment and Weiss temperature, $\mu_{eff} = 4.69\mu_B$ and $\theta = 138.0K$ at 300 - 450K and $\mu_{eff} = 4.79\mu B$ and $\theta = 132.6$ K at 480 - 600K. Similarly in a later work Yokosawa *et. al.* [90] report CBED and SAED results of $BiMnO_3$. CBED results show it to belong to point group 2/m with the c-glide plane perpendicular to the b axis, resulting in space group C2/c while SAED patterns indicate the noncentrosymmetric long-range (space group C2) and short-range ordered structures (P2 or $P2_1$), respectively implying little influence of the weak reflections on CBED patterns. By substituting Sc for Mn, the long-range ordered structure persisted up to $BiMn_{0.6}Sc_{0.4}O_3$ at 300K, but short-range ordered structure disappeared already in $BiMn_{0.9}Sc_{0.1}O_3$. In $BiMnO_3$ at 673K, the long-range ordered structure persisted while the short-range ordered structure disappeared. Analyzing the data suggests the noncentrosymmetric long-range ordered structure (C2) of $BiMnO_3$ to be attributed not only to Bi^{3+} ions with lone electron pair but also to Mn^{3+} ions, implying a correlation between Bi^{3+} and Mn^{3+} ions. These results help in understanding multiferroic properties of $BiMnO_3$.

1.15 Studies on Bi(Ca,Sr)MnO_3 systems.

1.15a BiCaMnO (BCMO)

One of the first extensive works reported on doped Bi-manganites was by Bokov and his group [91]. In their work the structural, magnetic and conductivity studies were carried out on $Bi_{(1-x)}Ca_xMnO_3$ (BCMO) and these studies were correlated to one another. They suggested a modification of the Zener DE [22] mechanism to explain the magnetic ordering. The change in the structure in connection with ordering of electrons and the change in the Curie temperature T_C with respect to the structural changes was also proposed in their work.

Chiba *et. al.* [92] present the magnetic and electronic properties examined down to 5K of polycrystalline perovskite manganites $Bi_{(1-x)}Ca_xMnO_3$ ($x \geq 0.8$). $Bi_{(1-x)}Ca_xMnO_3$ ($x \geq 0.875$) exhibits FM moment, reduces resistivity and large negative magnetoresistance appears below T_C. The system $Bi_{(1-x)}AE_xMnO_3$ (AE = Ca, Sr) has been investigated for the electric, magnetic and magnetoresistive properties. By continuous increase of the substituant Bi^{3+} in place of Ca^{2+} in the system $CaMnO_3$ the FM magnetic moment and resistivity decreases at low temperatures. But an insulator to metal transition (I-M) was not observed around T_C. The comparison with the La counterparts showed similar crystal symmetry for both the La as well as Bi manganites but the magnetic moments were found to be higher for the Bi manganites than that of the La manganites for the same value of *x*. They suggest this difference to be associated with the Bi $6s^2$ lone pair of electrons. The FM is suppressed with increase in Bi content due to the increase in CO. Chiba *et. al.* [92], in a later communication, investigated the effects of electron lone pairs of Bi^{3+} ions on the crystal structure and magnetic properties in polycrystalline $Bi_{1-x}AE_xMnO_3$ (AE=Ca, Sr). Perovskites with triclinic, monoclinic, and tetragonal distortions were found in $Bi_{1-x}Sr_xMnO_3$ from x-ray powder diffraction. The superlattice reflections found in $BiMnO_3$ by electron diffraction revealed existence of polymorphism and these structures reflected the Bi^{3+} lone pair character. $Bi_{1-x}Ca_xMnO_3$ (BCMO) and $La_{1-x}Ca_xMnO_3$ (LCMO) show the same crystal symmetry and weak ferromagnetism in the Ca-rich region. However, the magnetic moment of BCMO is found to be larger than that of LCMO for the same value of *x*. The ferromagnetism is suppressed by CO with further substitution of trivalent cations, although the T_{CO} of LCMO is higher than that of the BCMO system. The difference is attributed to the Bi $6s^2$ lone pair of electrons.

Pal *et. al.* [93] have compared the electrical transport properties of $Bi_{0.1}A_{0.9}MnO_3$ (A = Ca, Sr and Pb) over a wide range of temperatures (80 – 375K). XRD data show changes of structure with the dopants of different ionic radii (r_i). The dc conductivity of the Sr- and Pb-doped samples, which have larger r_i than Ca, is lower than that of the Ca-

doped sample. A negative magnetoresistance is observed in the Ca-doped sample (T < 115 K at 1.5 T field). The high temperature conductivity fits well with the nearest neighbour small polaron hopping model for $T > \theta_D/2$, where θ_D is the debye temperature, while the low temperature data fits well with the Mott's variable range hopping model for $T < \theta_D/2$. The condition of non adiabatic small polaron hopping mechanism is valid for all samples. The estimated electron–phonon interaction constant γ_p of Sr- and Pb-doped samples are much higher than those of the Ca-doped sample. The large values of γ_p destroy spin ordering in the Sr- and Pb-doped samples, while for the lower value of γ_p in the Ca-doped sample spin ordering favours high conductivity and show a negative magnetoresistance. For $T < \theta_D/2$, frequency-dependent ac conductivity data indicate that the conduction mechanism in the Sr- and Pb-doped samples is primarily due to hopping of Anderson-localized charge carriers.

Structural, magnetic and electrical properties studied on Ca – rich BCMO system by Santhosh *et. al.* [94] renders three distinct phases at low temperatures for different doping levels. From the ground state G-type AFM state for $x \leq 0.03$, $Ca_{(1-x)}Bi_xMnO_3$ changes to a canted G-type AFM state for $0.03 \leq x \leq 0.09$. For $0.09 \leq x \leq 0.18$ phase separation into a conducting, canted G-type and an insulating, AFM C-type phase is evident. The low temperature phase diagram is also realized where a wide compositional range over which low temperature phase separation is observed.

Raman scattering studies on $Bi_{(1-x)}Ca_xMnO_3$ ($x > 0.5$) describes the influence of CO and OO on the lattice, charge and spin dynamics of the system [95]. These studies reveal the development of a fluctuational response with the distinctive symmetry of the spin-chirality operator, which is consistent with the fluctuating chiral state at finite temperatures in the CO/AFM state. The usability of Raman scattering to probe chiral phases in other correlated systems like CMR in phase manganites is well highlighted in this work.

The scanning tunneling microscopy (STM) results on $Bi_{(1-x)}Ca_xMnO_3$ presented by Renner *et. al.* [96] show that charge ordering and phase separation can be resolved in real space with atomic-scale resolution. The STM images and the current – voltage spectroscopy data show the charge order to be related to both structural order and the local conductive state (either metallic or insulating) and this serves in providing descriptions of manganites as mixtures of electronically and structurally distinct phases. Varela *et. al.* [96] report on the scanning electron transmission microscopy (STEM)

images recorded on the BCMO system. The Z-contrast image formed by collecting the electrons scattered out to high angles on a high-angle annular dark field (HAADF) detector relates to the sample structure. The columns with a higher Bi concentration are found to be brighter, whereas the Ca-rich columns are darker. No chemical ordering is observed from these images. But it is observed that the resulting mixed-valence state within the Mn sublattice produces a complex electronic structure that can be imaged using electron energy loss spectroscopy (EELS). They also report that the charge ordered as well as disordered state can be detected from these studies as the CO state is believed to arise as a spatial stabilization of the e_g orbital distribution. The authors highlight on the strong valence modulations corresponding to Mn^{3+} and Mn^{4+} scanning along the pseudocubic [100] direction and no modulation in the pseudocubic [001] direction.

The magnetization and resistivity measurements as well as x-ray absorption and diffraction measurements are reported on the BCMO system for $x \geq 0.4$ by Woo *et. al.* [97]. They find the charge-ordering temperature (T_{CO}) as well as the Neel temperature (T_N) and give a summary phase diagram for the specified range. The low temperature electrical and magnetization studies uncover an insulating antiferromagnetic behaviour with increasing Ca, except for $x = 0.9$, where a canted spin arrangement with approximately one Bohr magneton per Mn site is observed. The net magnetic moment as a function of x is obtained from the magnetization measurements performed as a function of field and temperature and reveal the T_{CO} and T_N. The x-ray absorption studies reveal the Bi dependency of the crystal structure and transition temperatures. With increasing amount of Bi the system changes from an FM- metal to a highly stabilized CO-insulator. The x-ray diffraction data reveal peak splittings consistent with lower-symmetry cells as Bi content increases. The structural-magnetic correlations are conclusive of the importance of Mn-O distortions in stabilizing the charge-ordered state in the manganites. In a later communication Woo *et. al.* [97] also reported detailed magnetic and transport properties of Ca–rich Bi-manganite. The low field measurements show FM Curie Weiss behaviour at high temperature and an AFM state, supporting an FM component and low temperature and high field measurements show a non linear field response both above as well as below ordering temperatures. The residual magnetic moment and coercive field, in the ordered state of the material, is found to be small. The possibility of FM spin clusters coupling with the AF staggered magnetization below T_N and AF fluctuations above T_N is investigated to analyze the results. The high field magnetoresistance (up to 30 T) appears to be governed by a field-induced reduction in the doped carrier localization. The observed glassy character of the cluster magnetic response is discussed

by measuring the frequency dependent AC susceptibility and time/history evolution of the low field magnetization and the authors try to differentiate it with canted AFM state but ultimately leaves more open questions to be pondered over.

Munoz *et. al.* [98] performed high-resolution synchrotron x-ray and neutron powder diffraction of $Bi_{(1-x)}Ca_xMnO_3$ ($x \geq 0.75$) and showed that these systems present a phase segregation coinciding with the electronic localization of the electrons. The very precise results obtained provide evidence of a mechanism for phase segregation based on subtle compositional heterogeneity effects.

Munoz *et. al.* [99] studies the effects of Ca and Sr substitution at the Bi site in $BiMnO_3$. A high $T_{CO} \approx 475K$ is reported for $Bi_{0.5}Sr_{0.5}MnO_3$. The charges order at ~ 350K above the temperature predicted by the bandwidth tuning mechanism in the $Ln_{0.5}(Ca,Sr)_{0.5}MnO_3$ family and ~ 150K above that of $Bi_{0.5}Ca_{0.5}MnO_3$. Using the neutron and synchrotron diffraction techniques and magnetization data they study the changes in the T_{CO} with respect to the different doping levels in the system $Bi_{0.5}(Ca_{(1-y)}Sr_y)_{0.5}MnO_3$. The T_{CO} for $y < 0.5$ is ~ 300K-330K. The change in T_{CO} with varying doping levels is not monotonous as at $y \approx 0.5$ there is a sudden jump in the value of T_{CO}. This is presumed to be due to the dominant character of the lone pair of $6s^2$ electrons of Bi^{3+} in the system with more effective contribution of Sr to the A-site average ionic size.

The system $Bi_{0.75}Ca_{0.25}MnO_3$ was investigated for its magnetic, structural and electronic properties using magnetometry, diffraction and muon spin relaxation data [99]. Unlike $Bi_{0.75}Sr_{0.25}MnO_3$, which has a T_{CO} closer to 600K, $Bi_{0.75}Ca_{0.25}MnO_3$ has a T_{CO} closer to 300K. The ground state of $Bi_{0.75}Ca_{0.25}MnO_3$ is characterized by a high degree of spin disorder and frustrated interactions. But neither of these samples show an FM component (which rules out the possibility of spontaneous magnetization). The application of a small magnetic field produces a continuous progressive polarization of the Mn moments (≈ 2 μB/Mn at 5T, ZFC, 5K). The differences between Ca and Sr manganties with $x = 0.25$ are greater than that for the $x = 0.5$ counterparts, and point to distinct ground states and charge/orbital configurations. $Bi_{0.75}Ca_{0.25}MnO_3$ exhibits short range magnetic order and spin disorder at low temperatures with a few regions of pseudo charge exchange (CE) type order while $Bi_{0.75}Sr_{0.25}MnO_3$ exhibits long range order.

There have been various other studies on Bi based manganites, especially the BCMO and BSMO systems. Substitution at the Mn site has also been studied, though not as extensively as the afore mentioned systems. For Bi rich samples in the BCMO system

phase transformations from FM to spin-glass (SG) to a CO AFM phase is observed, with the SG and CO AFM phase seen to coexist at slightly higher Ca content due to the charge order-disorder phase transformation being martensitic in nature [100].

X-ray scattering results of CO and OO in the electron doped manganite $Bi_{0.24}Ca_{0.76}MnO_3$ are presented by Wilkins *et. al.* [101]. Using High Energy X-ray Scattering (HEXS) charge ordering, structural modulation due to the J–T ordering and the harmonic of the structural modulation are observed and the superlattice reflections due to the J–T ordering are found to maximize in intensity at the Neel point. Using resonant x-ray scattering at the K-edge of manganese and the anisotropic tensor of susceptibility technique (ATS) they confirm that superlattice reflections occurring at a modulation wave vector of (0.5, 0, 0) are due to charge ordering in a Mn^{3+}/Mn^{4+} ordering pattern. Superlattice reflections corresponding to the orbital order are also measured, at a modulation wave vector of (0.25, 0, 0). It is concluded from the temperature dependence of the OO and CO that orbital ordering is driven by charge ordering.

Lu *et. al.* [102] reported the effect of intrinsic strain on the coexistence of charge ordered and charge-disordered (CD) phases in $Bi_{0.4}Ca_{0.6}MnO_3$. The electronic transport measurements show that a CO phase forms below T_{CO} ~ 320K, accompanied by a distinct maxima in magnetization. The softening of shear modulus in the vicinity of T_{CO} is suggestive of strong coupling of electrons and phonons in this compound. Two internal friction peaks at temperatures ~ 320K (originating from the CO phase transition with typical signatures of a martensitic transformation) and ~ 260K (related to a relaxation mechanism is ascribed to the motion of CO and CD domains) are observed in the mechanical energy dissipation spectra. The presence of an intrinsic inhomogenous martensitic accommodation strain causes the coexistence of CO and CD phases. This strain is thought to stabilize the large scale phase separation in manganites.

Resonant x-ray diffraction studies at the oxygen K edge to detect the electronic superstructures of the 2p states near Fermi level, εF, in $Bi_{0.31}Ca_{0.69}MnO_3$ were reported by Grenier *et. al.* [103]. In the stripe order system $Bi_{0:31}Ca_{0:69}MnO_3$, hole-doped O states are orbitally ordered, at the same propagation vector as the Mn orbital ordering, but no oxygen charge stripes are found at this periodicity. This provides an evidence of orbital ordering of hole-doped hybridized 2p–3d, and contradicted O charge stripes with the same propagation vector as the Mn orbital ordering. The characterization of OO and the associated lattice distortions in highly doped $Bi_{(1-x)}Ca_xMnO_3$ is reported by Grenier *et. al.* [104]. The ordered localized states and the sensitivity to the distortions of the manganese oxygen octahedra is directly observed using the resonant x-ray diffraction at the Mn L-

edge and at the Mn K-edge respectively. The OO on Mn atoms is directly observed at x = 0.69 while from the analysis and the numerical simulations of the K-edge spectra the pattern of the distorted octahedra at x = 4/5 is characterized. These observations support the Wigner-crystal-type model at both dopings and rules out the bi-stripe model at x = 0.69.

Qin *et. al.* [105] conducted temperature and magnetic field dependent small-angle neutron scattering measurements on $Bi_{0.125}Ca_{0.875}MnO_3$ with the objective of understanding the magnetic properties of this system. Non-trivial spin structure is revealed. FM spin clusters form in the antiferromagnetic background (giving rise to a phase separated system) when temperature is decreased to $T_C \sim 108$ K. On further decrease of temperature or application of external magnetic field, the clusters begin to form in larger numbers, giving an overall enhancement of magnetization below T_C.

Shimizu *et. al.* [106] report the ^{55}Mn NMR measurements on $Bi_{0.125}Ca_{0.875}MnO_3$. NMR signals recorded at 4.2 K at 100 MHz and 605 MHz are ascribed to regions with FM spin structure. The main resonance line observed at ~ 320 MHz has two peaks, one at ~ 298MHz and the other at ~ 318 MHz. The magnetic field dependence of the lines up to 4 T show that they originate from regions with AFM spin structure. This is consistent with the observed lack of saturation of the magnetization at high magnetic fields suggesting coexistence of different magnetic phases.

1.15b BiSrMnO (BSMO)

The system $Bi_{(1-x)}Sr_xMnO_3$ is studied for the structural, electrical and magnetic properties by Chiba *et. al.* [107]. The x-ray diffraction (XRD) studies reveal a structural transition from triclinic (~monoclinic) to monoclinic (~orthorhombic) to tetragonal with increasing amount of Sr. $BiMnO_3$ exhibits a PM-FM transition and obeys the Curie-Weiss law above the T_C. With increasing amount of Sr the T_C becomes ambiguous and the FM exchange seems to get weaker. No insulator to metal (I – M) transition is observed but with increasing Sr content the resistivity decreases till x = 0.5, due to the excess of hole doping, beyond which a reversal is observed and the resistivity begins to increase again.

Munoz *et. al.* [108] report a comparative investigation of the charge modulation tendencies in R–M–MnO_3 and Bi–Sr–MnO_3 manganites by means of magnetic, magnetotransport, synchrotron x-ray and neutron diffraction. The remarkable differences

observed in the properties of these systems are rationalized in terms of the role that the different electronic structure of bismuth and rare earth elements play. Real space and charge order is observed in half doped R–Ca manganites. Changing the doping level to lower (or higher) values (unbalance of electrons and holes) decreases T_{CO} or suppresses CO as it happens in R–Sr compounds. The excess electrons are found to weaken the CO state: The higher stability of CO in half doped samples is usually attributed to the maximal Coulomb energy gain due to CO and the strain energy gain due to OO for a Mn^{3+}/Mn^{4+} ratio of 1. In Bi-manganites an off-stoichiometry corresponding to a Mn^{3+}/Mn^{4+} ratio of 3 in underdoped $Bi_{0.75}Sr_{0.25}MnO_3$ increases T_{CO} by ~75K with respect to the half-doped sample. They attribute this unusual behaviour to the increase in concentration of bismuth, and confirm the key role of Bi^{3+} ions in the CO phenomena of $Bi_{(1-x)}Sr_xMnO_3$. These results suggest that the $6s^2$ lone pair of Bi^{3+} is weakly screened in $(Bi,Sr)MnO_3$ compounds. An orientation of the $6s^2$ lone pair toward a surrounding anion (O^{2-}) can produce a local distortion or a hybridization between 6s-Bi-orbitals and 2p-O-orbitals reducing the movement of e_g electrons through the Mn–O–Mn bridges and favouring CO. The magnetic field induced coexistence of ferromagnetism and charge/orbital order in $Bi_{0.75}Sr_{0.25}MnO_3$ is also reported by Munoz *et. al*. [108]. The long-range modulation with double periodicity along the *a* and *c* axes and unusual anisotropic evolution of the lattice parameters in this system is produced by the electronic transition at $T_{CO} \approx 600$ K. In zero field the magnetic structure is AFM in nature, ruling out the apparition of spontaneous FM. At relatively small fields (H < 1T) a continuous progressive canting of the moments, inducing a ferromagnetic phase, is observed. It is also found that application of pulsed high magnetic fields produces reversible spin polarization confirming the coexistence of ferromagnetism and charge/orbital order.

The structural, magnetic and transport properties in strontium rich $Bi_{(1-x)}Sr_xMnO_3$ solid solution ($0.5 \leq x \leq 1$) examined by X-ray powder diffraction, DC susceptibility, thermopower, resistivity and thermal conductivity measurements are described by Sedmidubsky *et. al.* [109]. A change in material properties at T_{CO} (which gradually decreases from ~ 550K for $x = 0.5$ to almost 0K at $x = 0.9$) is reported. The temperature independent thermopower (the absolute value of which increases with x) above T_{CO} indicates polaronic transport. Below T_{CO} an activated transport mechanism of localized charge carriers is observed. The Weiss temperature decreases with x and becomes negative for $x = 0.8$ suggesting AFM interactions at high temperatures. The progressive decrease of orthorhombic distortion at room temperature along with the above mentioned features is also remarked upon in the report.

The temperature dependence of inverse susceptibility, resistivity, and thermoelectric power (TEP) for $Bi_{(1-x)}Sr_xMnO_3$ (BSMO) from 300K to 700K give information on the CO transitions [110]. At high temperatures susceptibility and resistivity follow a Curie–Weiss law and variable range hopping behaviour, respectively. The value of TEP is negative and has a weak temperature-dependence in the high temperature regime. The increase of energy gap due to CO is indicated from the change of slope in the TEP data. The martensitic transition of the CO phenomena is confirmed from the thermal hysteresis observed in TEP and resistivity data in the vicinity of T_{CO}. As x increases T_{CO} shifts from $\sim$ 490K for $x = 0.45$ to $\sim$ 435K for $x = 0.8$, and the thermal hysteretic behaviour becomes less pronounced. Kim *et. al.* discuss the electrical transport properties in terms of carrier localization accompanied by the local lattice distortions due to Bi^{3+} lone pairs.

The relation between the TEP and magnetic susceptibility for $Bi_{(1-x)}Sr_xMnO_3$ ($0.5 \leq x \leq 0.8$) has been established empirically by Kim *et. al.* [111]. They deduce a linear equation for the relation between the two transport coefficients. From this relation the Peltier heat and TEP is extracted for this material which consist of two terms: one which has a magnetic origin and the other originating from the configuration entropy. They establish the universality of the relation by applying it to other magnetically interacting systems including colossal magnetoresistance materials and high T_C cuprates.

A study of the effect of CO and OO on the magnetic properties of the BSMO system is accounted by Mantytskaya *et. al.* [112]. The study of the crystal structure and the magnetic and elastic properties of $Bi_{(1-x)}Sr_xMnO_3$ reveals the following phase transformations: FM ($x \geq 0.15$) – SG ($0.15 < x < 0.25$) – CO AFM ($0.35 < x < 0.8$). The FM state corresponds to ordering of the orbitals of the Mn^{3+} ions. For $Bi_{(1-x)}Sr_xMnO_3$, in the concentration interval $0.15 < x < 0.35$, it is assumed that the orbitally disordered phase is not realized. Samples with $0.25 < x < 0.8$ undergo a first-order transition of the crystal structure, attributed to ordering of the Mn^{3+} and Mn^{4+} ions in the ratios 1:1 ($x \leq 0.6$) and 1:3 ($x \geq 0.7$). The possibility of the martensitic character of the charge order–disorder phase transformation causing the AFM CO and SG phases to coexist in samples with $0.25 < x < 0.35$ is cited. The authors construct a hypothetical magnetic phase diagram.

Rebello *et. al.* [113] report pulsed as well as direct current/voltage induced electroresistance in $Bi_{0.8}Sr_{0.2}MnO_3$ at room temperature. They observe that bilevel and multilevel resistivity switching can be induced by a sequence of pulses of varying pulse

width at a fixed voltage amplitude. Resistivity increases abruptly (≈ 55% at 300K) upon reducing pulse width from 100 to 25 ms for a fixed electric field (E = 2 V/cm^2) of 200 ms pulse period. But it is inferred that the periodic change in temperature which accompanies the resistivity switching alone cannot explain the magnitude of the resistivity change.

Frontera *et. al.* [114] performed the room temperature (RT) and low temperature (LT) neutron and synchrotron powder diffraction studies on $Bi_{0.5}Sr_{0.5}MnO_3$. These studies provide a confirmation to the coexistence of two phases in these materials. Below 350K the majority phase exhibits charge as well as orbital ordering. The existence and stability of charge order up to this high temperature agrees with the fact that magnetic fields higher than 45 T are not sufficient to melt the charge-ordered state at 4K. This is in great contrast with the behaviour of non-Bi-based $Ln_{0.5}Sr_{0.5}MnO_3$ isostructural oxides. The OO is responsible for AFM correlations. The two orthorhombic phases which exist are found to have two different magnetic structures: one, a distorted CE magnetic structure with which CO is associated while the other, existing with an A-type order, which is also insulating due to the low mobility of the e_g electrons, with which OO is associated. Both these phases are stable up to high temperatures ≈ 525K. Here too the importance of the Bi lone pair of electrons is highlighted in decreasing the mobility of the e_g electron. The $6s^2$ lone pair effect and some structural and magnetotransport results, indicate that the A-phase is quite different from previous A phases found in manganites and it cannot be described as a ‘‘metallic antiferromagnet.’’ They examine a possible ordered arrangement of the Mn^{3+}/Mn^{4+} ions in this phase.

Kirste *et. al.* [115] study the effect of high magnetic field on CO. It turns out that a very high field of ~ 50 T is required on both the BSMO as well as the BCMO systems to induce an FM state. This is far above that estimated from values obtained by studying the Mn – O – Mn bond angle and hence is concluded that the bond angle does not decide the field required to induce FM in these materials. But their studies do not conclusively say whether the CO state melts at high magnetic field or whether the AFM coupling between the FM chains of the localized Zener polarons breaks. Comparing the results with other rare earth manganites it is found that if the AFM coupling breaks, the mobility region of the e_g electrons will not change and hence the FM state will be insulating.

The structural phase diagram of $Bi_{0.5}Sr_{0.5-x}Ca_xMnO_3$ studied by Beran *et. al.* [116] presents quite interesting results. The samples have two domains separated by a biphasic region (where the monophases are in the AFM state below T_N ~ 140K and in the PM state above this temperature, the samples being in the CO state till the T_{CO} is reached). But

apart from these similarities the properties of samples in the system vary with difference in the value of *x*. The Sr- rich samples, which belong to the Imma subgroup, have a T_{CO} ranging from 460K – 520K, where T_{CO} decreases with the size of the A-site cation. The Ca- rich samples (which belong to the Pnma subgroup), on the other hand, have smaller T_{CO} values ranging from 300K–340K where the T_{CO} increases as the size of the A-site cation decreases. The opposite A-site size effect on the T_{CO} is due to the increased influence of interaction of Bi 6p with p-type atomic orbital of the A-site atoms with increasing of their radius. This interaction reduces the Mn-O hybridization and stabilizes the OO/CO state.

Lu *et. al.* [117] reported XRD, magnetic, electronic transport, and elastic studies performed on polycrystalline $Bi_{0.5}Ca_{0.4}Sr_{0.1}MnO_3$. The T_{CO} of the sample occurs at ~304K, which is accompanied by a distinct maximum in magnetization. The strong coupling of electron–phonon due to J–T effect is evidenced in the form of softening of Young's modulus in the vicinity of T_{CO}. The dynamic FM spin correlations observed at high temperatures above T_{CO} are replaced by AFM spin fluctuations at a concomitant CO transition. A SG state dominates below 32 K. The voltage – current (V–I) characteristics measurements indicate the non-linear conduction above a threshold current, giving rise to a region of negative differential resistance (NDR). The origin of the non-linear conduction is discussed in view of current induced collapse of CO state associated with phase-separation mechanism. Similarly, Loudon *et. al.* [117] investigate the microscopic nature of the CO modulation in $Bi_{0.5}Sr_{0.4}Ca_{0.1}MnO_3$ in real space using STEM. The modulation is found to have a uniform periodicity appearing as stripes in HAADF images. Geometric phase analysis shows the modulation to be a displacement wave with transverse amplitude $(0.008 \pm 0.001)a$ and longitudinal amplitude $(0.003 \pm 0.001)a$. The energy loss spectra taken across the stripes show no periodic changes and place an upper bound of ± 0.04 on any valence changes of the Mn ions.

1.16 Studies on single crystals of Bi- manganites

Bao *et. al.* [118] investigate single crystalline $Bi_{(1-x)}Ca_xMnO_3$ $(0.74 \leq x \leq 0.82)$ using neutron scattering, electron diffraction, and bulk magnetic measurements. Dynamic FM spin correlations are found at high temperatures, which are replaced by AFM spin fluctuations at a concomitant CO and structural transition. The results indicate that thermal-activated hopping of the J-T active e_g electrons in these insulating materials

induces FM interaction through the DE mechanism. It is concluded that it is the ordering of charges which competes with the DE FM metallic state.

Liu *et. al.* [119] reported optical reflectivity studies on $Bi_{(1-x)}Ca_xMnO_3$ (x = 0.74 and 0.82) single crystals. In the high temperature phase, $T > T_{CO}$, which is characterized by FM correlations, the low-energy contribution to the optical conductivity $\sigma_1(\omega)$ is dominated by small polaron dynamics. For $T_{CO} > T > T_N$, the presence of both small polaron and charge-gap-like features signifies PS behaviour in which domains of FM and AFM order coexist. Below T_N, the polaron response is completely suppressed, and a complete charge gap develops, coincident with the onset of long-range AFM order.

Rubhausen *et. al.* [120], in their spectroscopic ellipsometry studies of the optical properties of $Bi_{(1-x)}Ca_xMnO_3$ single crystal, identify two energy ranges reflecting two physical processes, charge ordering and orbital ordering. They found that in the low frequency region features reflecting the development of a highly anisotropic charge gap is observable whereas in the higher frequency range the orbital effects associated with the charge transfer band features reflecting short range orbital ordering, which precedes charge ordering at T_{CO}, are observed.

The superstructure of $Bi_{(1-x)}Ca_xMnO_3$ (x = 0.4 or 0.45), which exhibits CO/OO at room temperature ($T_{CO} \approx 330K$), determined at different temperatures using single-crystal x-ray diffraction data and the superspace formalism was reported by Giot *et. al.* [121]. The structural model of the ordered state has been confirmed using data from other techniques like electron diffraction, HREM and synchrotron high-resolution x-ray powder diffraction. It is compatible with an orthorhombic cell and the space group $Pnm2_1$. The structural model is based on the alternation of one double band of $Mn(1)O_6$ octahedra and one double band of $Mn(2)O_6$ octahedra, the two octahedron types exhibiting almost similar distortion. The simulated HREM images (using the refined atomic positions) are in good agreement with the experimental images, confirming the model. The authors also investigate the relationship between structural characterizations and magnetic properties of these compounds. Giot *et. al.* [121], in a later work, presented evidence of an unprecedented ordering in the Bi-rich part of the Bi–Ca–Mn–O diagram, where the SG state is observed at low temperature. The $\chi^{-1}(T)$ curves of three compounds, corresponding to different Ca/Bi + Ca ratio varying between 0.37 and 0.25, are discussed in correlation with the structural transitions as a function of T. The anomalies in the $\chi^{-1}(T)$ curves of $Bi_{0.71}Ca_{0.24}MnO_{3-\delta}$ and $Bi_{0.63}Ca_{0.37}MnO_3$ are associated with two different

mechanisms which are not observed in the intermediate $Bi_{0.67}Ca_{0.33}MnO_3$. For the Bi-rich compound, an unprecedented [111] p-type ordering of the perovskite cell associated to a change of the slope in the magnetic curve, is reported. $Bi_{0.71}Ca_{0.24}MnO_{3-\delta}$ appears at the convergence point of a complex competition between the complementary lone pair ordering/orbital ordering of the FM $BiMnO_3$ and the CO/OO of the pseudo CE AFM $Bi_{0.63}Ca_{0.37}MnO_3$.

Su *et. al.* [122] present synchrotron radiation x-ray scattering studies on single crystals of $Bi_{0.24}Ca_{0.76}MnO_3$. The formation of charge stripes associated with the low-temperature structural phase transition using x-ray techniques is reported. Weak satellite peaks with a modulation wave vector $\mathbf{q} \approx (0.24, 0.24, 0)$ observed below the transition temperature are associated with the charge ordering of Mn^{3+} and Mn^{4+} ions into charge (and spin) stripes within the perovskite structure. Temperature dependence of the intensity and width of the CO satellites over the temperature range 10 – 240K demonstrate the first-order structural phase transition that accompanies the formation of CO and spin ordering (SO). The authors conclude from the width of the CO satellites that the correlation length of the CO is long range at all temperatures, and in all directions, below the structural phase transition.

The near-field and far-field optical microscopic studies of photoinduced effects in charge ordered $Bi_{0.3}Ca_{0.7}MnO_3$ are reported by Smolyaninov *et. al.* [123]. Permanent reflectivity changes following local sample illumination with 488 nm light have been observed in this study. High-resolution images of exposed regions reveal optical contrast on a submicrometer scale indicating that photonic band-gap structures may be created using holographic recording in manganites. Images of photoinduced CO domain switching in $Bi_{0.3}Ca_{0.7}MnO_3$ are also presented.

Single crystals of the BSMO system behave differently from the polycrystalline sample of the same. Hejtmanek *et. al.* [124] have reported measurements of the electrical and thermal conductivities, thermopower, and paramagnetic susceptibility and x-ray powder diffraction performed on single-crystals of $Bi_{0.5}Sr_{0.5}MnO_3$. The hysteretic behaviour, observed below the cubic-to-orthorhombic transition at $T_{crit} \approx 535K$, is related to the onset of long-range CO at $T_{CO} \approx 450K$ and its further evolution down to about 330K. That the CO state is formed by Zener pairs, represented by Mn^{4+} dimers linked by one extra e_g electron, and is possibly stabilized by cooperative Bi,Sr displacements, is understood from the diffraction data. The system is found to have low thermal

conductivity down to the lowest temperatures without any recovery at the AFM ordering temperature $T_N \approx 150K$. These observations point to the presence of strong scatterers of phonons, the origin of which can be linked to ‘‘optical-like’’ oscillations that are associated with fluctuating charges within the Zener pairs.

Yamada *et. al.* [125] investigated anisotropic properties of a single – domain crystal of $Bi_{(1-x)}Sr_xMnO_3$ with $x = 0.47$. Temperature dependence of resistivity and magnetization are seen to exhibit an anomaly which is accompanied by a hysteresis at 400 – 550 K and a kink near 600 K. They attribute the hysteresis and the kink to the CO – CD transition which is accompanied with orbital commensurate – incommensurate phenomenon, and orbital order–disorder transition, respectively. The magnetization measurements show an AFM transition near 150K. Below 150K, the magnetization for a magnetic field in the ab-plane is found to be larger than that along the c-axis. This magnetic anisotropy indicates that the Mn spin moments direct to the c-axis. In the CO phase, anisotropy of the resistivity is approximately $\rho_{ab}/\rho_c \approx 10$ indicating that e_g electrons on excess Mn^{3+} ions have easier movement along the c-axis than in ab-plane. In a separate study Yamada *et. al.* [125] extended the same study to a wider range of substitutions and reported measurements of magnetization, electrical resistivity and synchrotron x-ray diffraction on single crystals of $Bi_{(1-x)}Sr_xMnO_3$ ($0.35 \geq x \geq 0.64$). The resistivity and magnetization curves show a kink near 570K and an anomaly which is accompanied by a hysteresis at 400 – 500K for all samples. Synchrotron x-ray diffraction of a sample with $x = 0.47$ indicates that the kink and the anomaly are ascribed to an OO and a CO phase transition, respectively. Orbital ordering becomes incommensurate above T_{CO}, which is not reported in other perovskite manganese oxides. Magnetization measurements show an AFM transition near 150K. Below 40K, an SG-like behaviour is observed for $0.35 \geq x \geq 0.53$. The anisotropic properties of a single-domain crystal with $x = 0.47$ are also investigated. Magnetic anisotropy below T_N implies that the Mn spin moments orient themselves along the *c*-axis. Anisotropic electrical conduction starts appearing below the OO transition temperature at 570K.

Studies on single crystals of $Bi_{0.63}Sr_{0.37}MnO_3$ using resonant x-ray scattering at the Mn K edge have been carried out by Subias *et. al.* [126]. The compound undergoes a metal–insulator (M-I) phase transition to the CO state at about 530K. Strong resonance signals are observed at room temperature as the energy was tuned through the Mn K edge for several superstructures of the CO phase. The energy, polarization and azimuth angle dependences agree with a checkerboard ordering in the *ab* plane of manganese atoms of two types, in terms of their different local geometrical structures. One of the sites is

anisotropic, a tetragonally distorted oxygen octahedron, and the other is isotropic, a nearly undistorted one, as observed for $Bi_{0.5}Sr_{0.5}MnO_3$ and other half-doped manganites. This result indicates that the checkerboard pattern is strongly stable and extends to doping concentrations of $x < 0.5$. No superstructures corresponding to the doubling of the *c* axis are detected. Intermediate valence states lower than 3.5, according to the fractional charge segregation, were deduced for the two non-equivalent Mn atoms, i.e. $Mn^{3.30+}$ and $Mn^{3.44+}$.

1.17 Thin films of Bi- manganites

Reports on thin films of Bi manganites are very few. Chen *et. al.* [127] performed hall measurements on $Bi_{0.4}Ca_{0.6}MnO_3$ thin films grown on $SrTiO_3$ substrates. They found that, around the CO transition, the charge carriers are electron like, the carrier density being nearly constant above T_{CO} ~ 0.36 electrons/Mn and decreasing on cooling below T_{CO} following the formula $n \propto \exp(-E_H/k_BT)$ with activation energy E_H ~ 0.13eV. The films exhibit no signatures of thermal activation of Hall mobility. The resistivity exhibits a semiconducting behaviour with the T_{CO} observed at ~ 270K compared to the bulk material value of ~ 330K. Application of magnetic field enhances the carrier mobility, becoming relatively highest at the temperature where the strongest MR is observed. Chen *et. al.* [127] also account separately the effects of substrate induced anisotropic strain on the CO transition and surface morphology in $Bi_{0.4}Ca_{0.6}MnO_3$ films deposited on (110) and (111) - oriented $SrTiO_3$ substrates. Effects of film thickness, *t*, on the CO transition are also reported. The T_{CO} is found to appear when *t* exceeds 50 nm, and develops rapidly to an excellent state as *t* reaches 100 nm. The distinctive thickness-dependent CO transition is closely related with the anisotropic strain relaxation process.

The effect of pressure on T_{CO} of thin films of $Bi_{0.4}Ca_{0.6}MnO_3$ grown on (110) and (111) $SrTiO_3$ substrates of different orientations have also been reported [128]. X-ray analysis on these films shows the occurrence of differently deformed structures. The decrease in T_{CO} as well as the rate of CO melting with pressure is different for the two films. Analysis of the relative volume fraction of the CO phase, obtained based on the effective medium theory, shows that the CO collapsing occurs in a wide pressure range, typically ~ 1.2GPa in width, and there will be no long–range CO phase above the pressure of ~ 2/2.3GPa for the (111)/(110) – film. The study also shows the correspondence between CO melting and the pressure-driven upturn of resistivity above T_{CO} suggesting the simultaneous occurrence of CO melting and shear–type lattice

distortion. Different lattice strains are believed to be the reason for the dissimilar behaviours of the two films.

Studies by Gajek *et. al.* [129] by experiments of spin filtering through ultrathin single–crystal layers of the FMI $BiMnO_3$ (BMO), highlight the potential of using FMI oxides for spin filtering and injection. The spin polarization of the electrons tunneling from a gold electrode through BMO is analyzed with a counter electrode of the half-metallic oxide $La_{2/3}Sr_{1/3}MnO_3$ (LSMO). The spin-filtering efficiency of up to 22% at 3K is attributed to the 50% change of the tunnel resistances according to whether the magnetizations of BMO and LSMO are parallel or opposite.

The dynamics of the CO state under non – equilibrium conditions created by strong dielectric fields ($\leq 10^6$V/cm) and photoillumination with short ($\approx$ 6 ns) laser pulses is investigated in $Bi_{1-x}Ca_xMnO_3$ ($x > 0.5$) epitaxial films by Chaudhuri and Budhani [130]. A pulsed laser deposition method was used to synthesize films on (100) $LaAlO_3$ (LAO) and (100) $SrTiO_3$ (STO) substrates. The crystallographic structure, temperature dependence of electrical resistivity and magnetization of the samples of different composition prepared under different oxygen partial pressure (pO_2) and deposition temperature (T_D) are presented. A clear signature of T_{CO} is seen in the magnetization at ~ 270K and in the resistivity data at ~ 260K for the x = 0.6 sample grown on LAO. The same sample grown on STO revealed T_{CO} at ~ 300K, T_N at ~ 150K and a weak FM phase below 50K. A strong correlation between T_{CO} and the *c*-axis lattice parameter (c) of the type ($dT_{CO}/dc \approx -350$K/A^o) emerges from measurements on films deposited under different growth conditions. Since the out–of–plane lattice parameter (c) increases with in-plane compressive strain, this effect directly shows a compressive strain induced suppression of the T_{CO}. The I-V characteristics of the samples at $T < T_{CO}$ show hysteresis due to a compound effect of joule heating and collapse of the CO state. Transient changes in conductivity of lifetime ranging from nanoseconds to microseconds are seen at $T < T_{CO}$ on illumination with pulsed UV (355 nm) radiation. The authors explain these observations on the basis of the topological and electronic changes in the CO phase.

Bi ions of multiferroic $BiMnO_3$, when replaced with La ions, induce an overlap of the ferroelectric and ferromagnetic transitions in temperature and thus enhance the interproperty coupling. Yang *et. al.* [131] found that 20% La-doped $BiMnO_3$ in thin-films show a broad ferroelectric transition below 150K and spontaneous magnetization to develop in the transition region. The saturation magnetization and polarization are found

to reach 1.6μ_B/Mn and 12μC/cm^2 at 5K respectively. This new magnetic ferroelectric shows a greatly enhanced magnetodielectric effect in the transition region with maximum 45% at 9 T, which is a 70-fold increase compared to that of the pure bulk compound. It is demonstrated that a phenomenon of magnetic-field controlled electric relaxations dynamically enhances the magnetodielectric effect.

Magnetic properties of thin films of $BiMnO_3$ synthesized by a pulsed laser deposition method on a $SrTiO_3$ single crystal substrate is presented by Ohshima *et. al.* [132]. The Curie temperature (T_C) is found to be ~ 105K, consistent with that for $BiMnO_3$ bulk, prepared under high pressure but the saturation magnetic moment is 2.8μB, which is smaller than that of the bulk (3.6μB). Effect of Sr substitution for the Bi site is also investigated.

Sharan *et. al.* [133] reported evidence for ferroelectricity in bismuth manganite epitaxial films from optical second–harmonic generation (SHG). They correlate the change in the polar symmetry of SHG signals under external electric fields to specific changes in the ferroelectric domain microstructures. A giant enhancement of SHG by 3 to 4 orders of magnitude with effective *df* ~ 193 pm/V under electric fields of ~ 707 V/mm is observed. The material also exhibits a large third-order nonlinear optical response with nonlinear absorption coefficient α_I ~ -0.08 cm/kW and nonlinear refractive index n_I ~ -0.53 x 10^{-9} cm^2/W.

The influence of deposition temperature and the deposition rate on the growth of the ternary Bi–Mn–O system onto (0 0 1) $SrTiO_3$ substrates by pulsed laser deposition has been explored by Langenberg *et. al.* [134]. The films are obtained from non-stoichiometric targets with 10 and 15% Bi excess in order to compensate for Bi volatility and studies are performed with a fixed oxygen pressure of 10 Pa (0.1 mbar) and substrate temperatures between 600 and 680^{o}C. The compound being metastable together with the high volatility of Bi induces different Bi and Mn oxides apart from $BiMnO_3$. Stabilization of epitaxial $BiMnO_3$ is elusive and only in a narrow temperature window (~ 630^{o}C) is the presence of spurious phases reduced to traces. X-ray diffraction results reveal a correlation between the Bi–Mn–O compounds and the deposition temperature. Reciprocal space maps show that the $BiMnO_3$ grows completely strained on $SrTiO_3$ substrates. The reduced volume in the unit cell hints at the presence of Bi vacancies. The surface of the films is rough, but flatten when the films are obtained at lower deposition rates.

The study of the microstructure of an interfacial epitaxial $BiMnO_3$ layer fabricated by chemical solution deposition on $SrTiO_3$ (100) substrate analyzed by XRD and cross-sectional TEM is presented by Naganuma *et. al.* [135]. The TEM observation reveals the epitaxial growth of $BiMnO_3$ on the $SrTiO_3$ substrate as follows: ([110](001))$BiMnO_3$‖[0-10] x (001) $SrTiO_3$. XRD and TEM analyses reveal the mismatch between the epitaxial $BiMnO_3$ and the $SrTiO_3$ substrate causing a distortion in lattice parameters of $BiMnO_3$ and consequently a large compressive strain in the $BiMnO_3$ layer.

1.18 Studies of 3d transition ion doping at Mn-Site in Bi- manganites

The effect of substituting Mn with other 3d transition ions like Cr, Fe, Zn etc on various properties of Bi- manganites has been explored. Xiong *et. al.* [136] investigate the structure, magnetic, and transport properties of the compounds $Bi_{0.5}Ca_{0.5}Mn_{(1-x)}Cr_xO_3$ (BCMCO) with $0 < x < 0.15$. The substitution of Cr^{3+} ion for Mn^{3+} ion suppresses the CO state, leading to a gradual reduction of the T_{CO}. The AFM ordering temperature remains unaffected until $x = 0.024$. An SG like behaviour appears above $x = 0.024$ due to the competition between the AFM and FM correlations. The latter emerges and develops with the incorporation of Cr. The AFM phase disappear completely for $x > 0.1$, whereas the CO phase is still perceptible for $x = 0.15$. Cr doping produces a similar effect on T_{CO} for the Bi-based and lanthanide-based manganites. The T_{CO} decreases at the same rate of ~ 8 K for 1% Cr, despite the different initial values of T_{CO}. Below a characteristic temperature $T_{CO} < 180$ K the CO state is unstable. As a result, a heavier Cr doping is required to completely destroy the CO phase with a higher T_{CO} . For BCMCO, the critical Cr content is estimated to be about 0.2. Electrical studies show that the conduction of BCMCO proceeds via variable–range hopping of charge carriers, and a huge magnetoresistance can be produced by Cr doping.

Luan *et. al.* [137] investigated the resistivity, magnetization and electron spin resonance (ESR) properties of two series of samples, $Bi_{0.6}Ca_{0.4}Mn_{(1-x)}Cr_xO_3$ ($0 \leq x \leq 0.05$) and $Bi_{0.24}Ca_{0.76}Mn_{(1-x)}Cr_xO_3$ ($0 \leq x \leq 0.24$). The evolution of CO with change in Cr content is drastically different between Bi-rich and Bi-poor samples. CO is found to melt gradually with increasing Cr content in Bi-rich system while it collapses when $x \geq 0.03$ in Bi-poor samples. It is found that understanding the evolution of Mn^{3+}/Mn^{4+} ratio with Cr doping in different systems helps in interpreting the various results. Using the concept of phase separation the complex magnetic properties observed in Bi-poor series is discussed.

The effect of Cr-doping on electrical and magnetic properties of high-temperature CO manganites $Bi_{(1-x)}Sr_xMn_{(1-y)}Cr_yO_3$ (x = 0.25, 0.3, 0.4; $0 \leq y \leq 0.1$) is explored by Yamada *et. al*. [138]. In the absence of Cr doping they observe a CD to CO transition at T_{CO} and an AFM phase transition at T_N near 500 and 150 K, respectively. The CO phase transition broadens, but does not disappear upon Cr-doping up to y = 0.1. The AFM phase disappears upon 10% of Cr-doping, transforming into a PM phase, rather than into a DE FM metal, in contrast to the case of $Pr_{(1-x)}Ca_xMn_{(1-y)}Cr_yO_3$.

Room temperature x-ray powder diffraction and neutron diffraction studies on $Bi_{0.5}Ca_{0.5}Fe_xMn_{(1-x)}O_3$ ($0 \leq x \leq 0.6$) synthesized by the solid state reaction method are reported by Tzankov *et. al.* [139]. With increase in Fe content the crystal lattice parameters are found to change monotonically. From the magnetic properties studied between 5 and 1300K, in fields up to 16 kOe, all compounds are found to exhibit AFM properties below a certain temperature, which decreases with increasing Fe substitution. For $x \geq 0.1$ the AFM is accompanied by weak FM. The CO/OO order exists in the pure form for the compounds with or without very low Fe substitution (x = 0 and 0.05). In the presence of a magnetic field a new magnetic cluster state is seen to exist in the PM region of manganites with Fe substitution $x \geq 0.3$. The conductivity of compounds measured between 100 and 600K is of semiconducting type, and no MR is observed in fields up to 7kOe.

Three $Bi_{0.5}Ca_{0.5}MnO_{3-\delta}$ compounds synthesized by three different methods (solid state reaction method, liquid method and Pechini method) are characterized and analyzed by Toulemonde *et. al.* [140]. Large magnetic Mn_x clusters ($x \geq 4$) are considered to explain the high value of the Curie-Weiss constant. The authors analyzed the data in view of Goodenough ionic model and Zener polaron model and found them unsuitable to explain the observed results. The cluster behaviour is observed at low field and at low temperature in all cases. The authors also discussed the influence of the oxygen stoichiometry and the homogeneity of the cation distribution depending on the method of synthesis employed. Studying the effects of nickel doping on the magnetic properties the cluster behaviour in these samples is confirmed and it is found that the distribution in cluster size depends on the amount of nickel and it induces a glassy magnetic behaviour.

Zhang *et. al.* [141] explored the structural, magnetic and transport properties of $Bi_{0.3}Ca_{0.7}Mn_{(1-x)}V_xO_3$ ($0 \leq x \leq 0.1$). Introduction of a non-magnetic dopant like V^{5+}

($3d^0 4S^0$, S=0) in the Mn – O – Mn network results in the variation of the Mn^{3+}/Mn^{4+} ratio. The authors suggest that Mn^{4+} ions are substituted by V^{5+} ions giving rise to the increase of Mn^{3+} ions. The electronic transport and magnetization results show that the T_{CO} increases with increasing *x*. The conduction mechanism in the temperature range $T > T_{CO}$ is attributed to the adiabatic hopping of small polarons while that for $T < T_{CO}$ to Mott's variable range hopping. The enhanced charge ordering caused by V-doping is suggested to originate from the enhanced J-T distortion of the MnO_6 octahedrons due to increased Mn^{3+} ions.

1.19 Studies on Bi- manganite nanoparticles

There are only two reports on the properties of Bi – manganite nanoparticles. Rao and Bhat [142] synthesized $Bi_{0.5}X_{0.5}MnO_3$ (X = Ca, Sr) nanoparticles (diameter ~ 5 - 7 nm) by polymer assisted sol-gel method. The HREM data showed the crystalline nature of the nanoparticles. Magnetic measurements from 10K to 300K using SQUID showed that the nanomanganites retain the CO nature unlike Pr and Nd based nanomanganites. The CO in Bi manganites is found to be robust, consistent with the observation that magnetic field of the order of 130 T are necessary to melt the CO in these compounds.

Fang *et. al.* [143] report the dc magnetization, ac susceptibility and ESR measurements on a series of $Bi_{0.2}Ca_{0.8}MnO_3$ samples with different particle sizes ranging from 60 to 1500 nm synthesized by the sol-gel method. It is found that the reduction in particle size suppresses the T_{CO} in this composition, resulting in the occurrence of the SG state at low temperatures. The observations are interpreted in terms of martensitic strain and surface effect. Moreover a scenario has been posed for the waning process of the CO transition. With the reduction in the particle size, the CO phase transition survives only in the core regions until its complete disappearance, and connected with this, the magnetic cluster phenomenon becomes more pronounced.

The studies summarized above highlight the significance of the Mn^{3+} – O – Mn^{4+} network in the properties of these materials. Much still remains to be understood about the structure – property correlations in these materials, especially the complex nature of the interplay of the spin, charge and lattice systems. The lattice strain and deformations, which affect the Mn^{3+} – O – Mn^{4+} bond angle and length have strong influence on the properties of these systems.

OBJECTIVES OF THE PRESENT WORK

In recent years there have been a number of studies on Bi – manganites, as listed in the previous pages, to understand the structure and properties of these materials. Electron spin resonance (ESR) is known to be a powerful technique for understanding the spin structure and its dynamics. The changes in short–range magnetic interactions and micro-magnetic phases can be easily detected because of its high sensitivity. There are very few ESR studies on Bi– manganites. Similarly there are no systematic transport measurements to understand the conduction mechanisms in Bi – manganites.

In this thesis, the detailed temperature dependent ESR studies on different compositions of Bi – manganites are reported. The detailed study on temperature dependence of resistivity for all the compositions was also carried out with the objective of understanding the conduction mechanisms in these materials and possible correlation with the ESR data. In the recent years the phenomena of phase separation (PS) has been intensely studied in various manganites. The recent theoretical models of this phenomenon predict the formation of nanometer size domains with different electronic and magnetic properties. The coexistence of FM and AFM domains in different types of manganites has been treated in terms of Griffiths Phase (GP) concept. The emphasis in the present study is on understanding the changes in the magnetic phase separation/competitions and CO with different dopants at different sites of Bi – manganites using temperature dependent ESR and resistivity studies.

The different series of Bi-manganite samples studied are:

1. $Bi_{(1-x)}Ca_xMnO_3$ $(0.4 \leq x \leq 0.75)$ (BCMO)
2. $Bi_{(1-x)}Sr_xMnO_3$ $(0.3 \leq x \leq 0.5)$ (BSMO)
3. $Bi_{0.6}Ca_{(0.4-x)}Sr_xMnO_3$ $(0 \leq x \leq 0.4)$ (BCSMO)
4. $Bi_{0.5}Sr_{(0.5-x)}Ce_xMnO_3$ $(0 \leq x \leq 0.2)$ (BSCMO)
5. $Bi_{0.5}Ca_{0.5}Mn_{(1-x)}Cr_xO_3$ $(0 \leq x \leq 0.05)$ (BCMCO)
6. $Bi_{0.55}Ca_{0.45}MnO_3$ nanoparticles.

The Mn^{3+}/Mn^{4+} ratio has a very decisive role in determining the properties of manganites. Varying the concentrations of Mn gives rise to differences in Mn^{3+}/Mn^{4+} ratio, changing the properties of the system. Temperature dependent ESR studies on Ca doped $BiMnO_3$ are undertaken in view of understanding the different micromagnetic phases that are formed in the sample with varying Ca content. The detailed temperature dependence of resistivity for the samples is carried out with the objective of understanding the conduction mechanisms in these materials. A possible correlation between the ESR and resistivity data is explored. This kind of study helps in the better understanding of the magnetic and electrical properties of the system.

The ionic radius of Sr is larger than that of Ca. The BSMO systems shows high T_{CO} compared to the Ca doped system. The studies on temperature dependent ESR and transport properties is taken up to explore and understand the different micromagnetic phases formed in the samples and the transitions as a function of Sr content. The possible reasons for high T_{CO} are explored from the ESR and transport studies.

The BCSMO manganite is a complex system. There are no ESR studies reported in the literature on this system. The objective of the present study is to examine the effect of substitution of two ions of different radii at Bi sites on the magnetic phase formation and transport properties. There are possibilities of formation of different correlated entities due to Ca, Sr and mixed (Ca,Sr) phases leading to the change in properties of the bulk samples. The possibility of the Bi^{3+} $6s^2$ lone pairs of electrons becoming a deciding factor in altering the properties of the samples at lower concentrations of Sr is explored.

The studies on cerium doped BSMO system were taken up keeping in view that cerium has two stable valencies of +3 and +4 and large ionic radii. This can bring about a change in the Mn^{3+}/Mn^{4+} ratio and affect the $6s^2$ lone pair of electrons and consequently the magnetic and electrical properties of the materials.

Chromium is a magnetic ion with a variety of valence states of which the +3 state is the most stable one. It is isoelectronic with Mn^{4+} making it viable to FM DE interactions with the Mn^{3+} ion. The objective of the temperature dependent ESR and resistivity studies on the BCMCO system is to probe the effect of Cr doping at the Mn site on the magnetic

phase formations and transport properties. Doping at the Mn site modifies the crucial $Mn^{3+} – O – Mn^{4+}$ network and in turn affect the structure and properties of the manganite.

The ESR studies on $Bi_{0.55}Ca_{0.45}MnO_3$ nanoparticles were carried out to understand the effect of particle size on the T_{CO} and T_N.

The details of the material synthesis methods and characterization techniques are presented in this chapter.

2.1 Material Synthesis Methods

2.1a Solid State Reaction Method

One of the most common methods of materials preparation is the solid state reaction method. Stochiometric amounts of powders of the compounds containing the required materials are taken and mixed. This mixture is calcined at lower temperatures to eliminate the impurities like carbonates and then sintered at higher temperatures for phase formation. Intermediate grinding of the mixture is performed for better mixing of the powders.

The Bi-manganite samples were synthesized by using high purity (99.99% pure) powders of Bi_2O_3, $SrCO_3$, $CaCO_3$, CeO_2, MnO_2 and Cr_2O_3 as starting materials for the respective samples. Stochiometric amounts were taken by weighing required amounts, calculated from the molecular weight of the compound. Powders of these samples were mixed and ground using an agate mortar. The mixtures obtained were then placed in a porcelain crucible and calcined at 600^{o}C for 6 hours in an electric furnace which is connected to a temperature controller. The furnace was then switched off and allowed to cool slowly. The calcined samples showed a yellowish to black colour, indicating the reaction to have taken place. The samples were ground and sintered at high temperatures (increasing from 800^{o}C to 950^{o}C) for 30 hours with intermediate grinding. The single phase formation of the black powders obtained was checked. The single phase materials were then pressed into pellets and sintered at 950^{o}C for 6 hours. An extra 5-10% of bismuth oxide was added in order to compensate for the loss of bismuth which can occur due to its sublimation at high temperatures (greater than 820^{o}C).

2.1b Sol-Gel Method

Sol-gel process is a method of synthesis of compounds via the chemical route [144]. The sintering temperature used and the duration of sintering can be lowered considerably compared to that used for the solid state reaction method. The size of the particles can be monitored and tuned (the particle size of the as prepared samples is usually well below 100nm) and the samples will be homogeneous.

$Bi_{0.55}Ca_{0.45}MnO_3$ nanoparticles were synthesized by the sol-gel process using urea ($(NH_2)_2CO$) as the gelification agent. Nitrates of Bi and Ca, i.e. $Bi(NO_3)_3.5H_2O$ and $Ca(NO_3)_2.4H_2O$ respectively, and chlorides of Mn, i.e. $MnCl_2{\cdot}4H_2O$, were used as starting materials. Nitrates and chlorides of the materials were used owing to their high solubility in water. Stoichiometric amounts of these materials were dissolved and mixed in distilled water. The concentration of urea was decided such that $\psi = 10$, where ψ = (urea)/{[Bi]+[Ca]+[Mn]}[145]. The solvent was heated in an oven, raising the temperature from 80°C to 140°C, which is above the melting temperature of urea. The pink gel formed was decomposed by heating at 250°C giving a porous precursor. This precursor was sintered at 900°C for 6 hours with intermediate grindings. The powders obtained were then checked for the single phase formation.

The mechanism of the gel formation is as follows:

Urea plays an important role in the formation of the gel. When an aqueous solution of urea is heated to temperatures≥ 75 °C it decomposes into CO_3^{2-} and NH_3 along with the release of hydroxide ions. The decomposition of urea can be represented as follows:

$$\text{Urea} \longrightarrow NH_4^+ + CNO^-$$

in a non-acidic media. When it is in an acidic medium the cyanate ion immediately converts into an ammonium ion [146].

$$CNO^- + 2H^+ + 2H_2O \longrightarrow NH_4^+ + H_2CO_3.$$

Some new ligands which can substitute water molecules in their coordination positions around the metal ions (NH^{4+}, OH^-, CO_3^{2-}) appear in the solution. The concentration of urea and the temperature decides the rate of decomposition of urea. The nature and the concentration of the metallic ions and ligands decide the degree of substitution of water by other ligands.

The water ligands are substituted during the evaporation of water. This can be represented by

$$[M(H_2O)_m]^{n+} + xL^{q-} \longrightarrow [M(H_2O)_{m-x}{\cdot}L_x]^{p+} + xH_2O$$

where M can be Bi, Mn or Ca and L can be NH_3, OH^-, CO_3^{2-} or urea. The metallic ions are coordinated by urea through the carbonyl or amino group whereas the Mn^{II} coordination happens through the oxygen of the urea used. The pH value of the aqueous solution is observed to be acidic. This state may prevail for most part of the evaporation process. As the water gets removed due to the decomposition of urea with increase in temperature, the pH value also increases slightly. A small amount of precipitate forms as the decomposition of urea leads to the release of hydroxide ions which favours the hydrolysis of cations [147]. On further heating the volume of the solution decreases considerably and the pH value increases, giving a basic solution. The precipitate completely redissolves. On cooling the solution a gel is formed. This is because of the condensation of the monomers through the hydroxide ligands which forms long chains. The metallic ions are located in the gel network. The final stochiometry of the product is decided by the complexation rate of the metal ions and the concentration of the metallic ions and urea. (It should be noted that there is an optimum value of ψ for which the complexation occurs in appropriate proportions to form the desired compound).

When the mixture becomes sufficiently concentrated the temperature rises to the melting point of urea, which is 137^oC [148]. At this temperature a large amount of urea decomposes. The decomposition is easily identified by the smell of ammonia and the bubbles viewed in the mixture. This leads to a sudden increase in the pH value due to the release of a large amount of hydroxide. The hot mixture is then cooled. An increase in the viscosity of the mixture is observed which leads to the formation of a gel. The metallic ions are located within the gel with a statistical distribution of the stoichiometric amounts of the ions used as the starting materials.

2.2 Characterization Techniques

The synthesized samples are characterized by X-ray Diffraction (XRD), Scanning Electron Microscopy (SEM) and Energy Dispersive X-ray Spectroscopy (EDAX).

2.2a X-ray Diffractometer (XRD)

X-rays are electromagnetic radiation with typical photon energies in the range of 100 eV - 100 keV. X-rays of short wavelength in the range of a few angstroms to 0.1 angstrom (1 keV - 120 keV), also called hard x-rays, are used for diffraction studies. A

diffraction pattern is observed only when Braggs law is satisfied. The Bragg equation for diffraction that works for basic calculations is given by:

$$2dsin\theta = n\lambda \quad (2.1)$$

where *n* is an integer, λ is the wavelength of the X-ray, *d* is the interplanar spacing in the crystalline material and θ is the angle between the incident beam and lattice plane diffracted angle. The maximum intensity of 2θ, which is called the Bragg angle, is the angle between incident and scattered beam. A schematic diagram is shown in figure 2.1

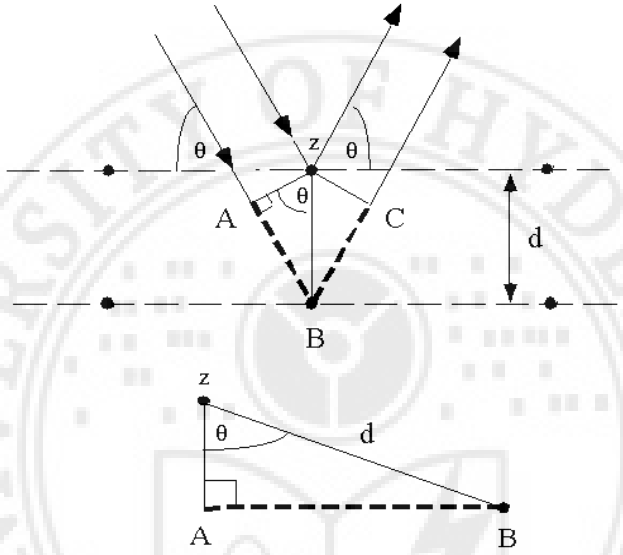

Figure 2.1Schematic diagram of the Bragg's Law.

Consider two parallel waves of the incident beam which are always in phase. The first beam strikes the top layer at atom z. The second beam continues to the next layer and gets scattered by atom B. The second beam must travel the extra distance AB + BC. The diffracted beam will be observed in the direction for which this extra distance is an integer (n) multiple of the wavelength λ i.e. nλ = AB + BC, which satisfies the condition of constructive interference. From the triangle AB = dsinθ and as AB = BC, nλ = 2AB = 2dsinθ, which is the Braggs law.

The XRD patterns of the samples were recorded using a PHILIPS X–ray diffractometer. Cu K_α X-radiation is used as the X-ray source which has a characteristic wavelength of 1.5405A^o and which operates at 40kV and 30mA. X – rays filters, monochromators, detectors like lithium drifted silicon etc. can be used to obtain monochromatic high intensity x-rays. A Ni filter is used to filter the CuK_α radiation. During diffraction the intensity of undesirable components are also eliminated through

filters [149]. The XRD patterns are recorded in the range 10-80^{o}, with the step size of 0.02^{o}, and at the rate of 1^{o} per minute. The data is collected using a counter proportional detector

The single phase formation of the materials synthesized is confirmed from the XRD plots by comparing it with existing data on similar samples. From the obtained XRD patterns the d-spacings can be estimated, the lattice parameters and angles can be calculated and the structure of the samples is determined.

2.2b Scanning Electron Microscope (SEM)

The scanning electron microscope (SEM), shown schematically in figure 2.2, scans the surface of the sample with a high-energy beam of electrons and depicts the surface morphology of the sample. Information about the sample's surface topography, composition etc. is obtained by the signals produced by the interaction of the electrons with the atoms of the sample material. These signals include secondary electrons (SE), back scattered electrons (BSE), light, transmitted electrons etc. The most common signals that are detected are the secondary electrons. The three dimensional images obtained in the SEM micrographs help to understand the surface structure of the sample as measurements of the order of a few nanometers can be accurately reached. Depending on the instrument magnification capability, images can be magnified 25 times to 250,000 times the original size can be obtained.

In an SEM the electron source can be a tungsten filament cathode, LaB_6 or field emission guns which emits electrons, via thermionic emission. The emitted electrons are attracted to a positive anode, which also accelerates it. The velocity of the attracted electrons can be so high that it can move right past the anode up to the sample.

The interactions between the beam electrons and the weakly bonded conduction-band electrons in metals or the valence electrons of insulators and semiconductors yield secondary electrons. The kinetic energy of the secondary electrons will be very less as the difference in energy between that contained by the beam electrons and the specimen electrons is large. As there is energy transfer from the beam electron to the electrons surrounding the atoms the scattering is inelastic. An electron detector (e.g. Everhart-Thornley (E-T) detector which is of a scintillator-photomultiplier type) is used with the SEM to convert the radiation of interest into an electrical signal for manipulation and display. Typically, elastic scattering occurs between the negative electron and the positive

nucleus, which is Rutherford scattering. The backscattered electrons are used to detect contrast between areas with different chemical compositions. BSE detectors are usually either of scintillator or semiconductor types.

The beam of electrons generated by the electron gun has an energy typically ranging from a few hundred eV to the order of keV. This beam is focused at a spot of a few nanometers in diameter by the condenser lenses. The beam passes through the scan coils which deflect the beam in the x and y axes in a raster manner and is focused on the sample through the objective lens. Secondary electrons are produced from the sample when the electron beam hits it. These electrons are collected by a secondary detector or a backscatter detector, converted to a voltage and amplified. The amplified voltage appears as variations in the brightness when it is applied to the grid of the cathode ray tube and the resulting image is hence, a distribution map of the intensity of the signal that is being emitted from the scanned area of the sample.

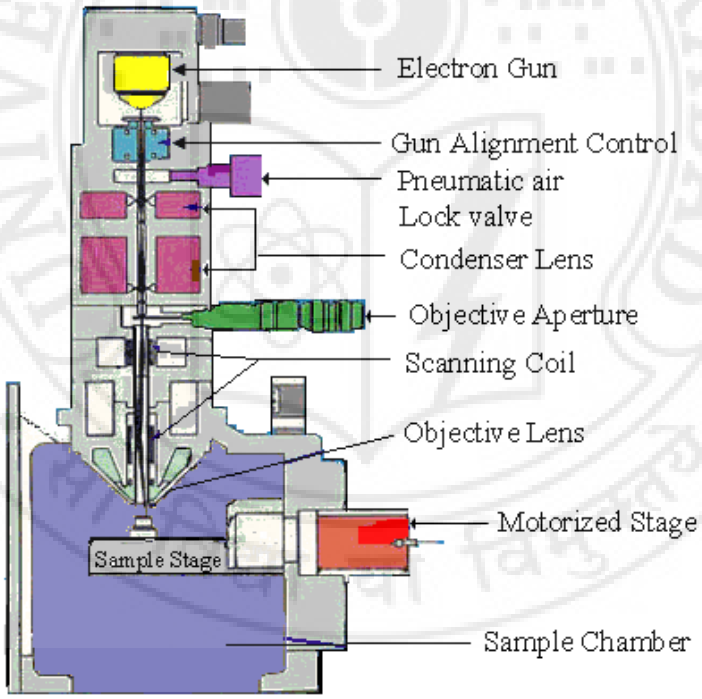

Figure 2.2 Schematic diagram of an SEM

To analyze the surface morphology of the samples, a PHILPS XL 30 SERIES scanning electron microscope was used. The voltage at the cathode for the acceleration of electrons was 20kV. The samples used in an SEM must be electrically conductive, at least at the surface, and electrically grounded to avoid the accumulation of charges on the

surfaces. The Bi-manganite samples were coated with a very thin film of gold (which is electrically-conducting) which intensifies the signal and improves the spatial resolution. Coating with a high atomic number material such as gold maximizes secondary electron yield from within a surface layer of the order of the beam diameter, so that the signal is derived from locations closer to the specimen surface and hence will enhance reliability. The spot size, contrast and brightness is adjusted to obtain clear images of the sample surface. Images at different regions of the same sample is taken for different magnifications to get more information about the sample morphology.

2.2c Energy Dispersive X-ray Spectroscopy (EDAX)

Energy dispersive x-ray spectroscopy (EDAX) is a technique used for the elemental analysis of a sample by analyzing the x-rays that are emitted when matter is bombarded with charged particles. It is usually coupled along with the SEM. The principle it works on is that each element has a unique atomic structure; x-rays that are characteristic of an element's atomic structure can be distinguished and identified from each other.

When a high energy beam of charged particles is focused on the sample to be studied characteristic x-rays from the samples are emitted. An atom within the sample contains ground state (or unexcited) electrons in discrete energy levels or electron shells bound to the nucleus. The incident high energy beam excites an electron in an inner shell. A hole is created in the shell as the beam ejects the electron from the shell. An electron from an outer, higher-energy shell then fills the hole, and an x-ray is released as a result of the difference in energy between the higher-energy shell and the lower energy shell. The number and energy of the X-rays emitted from a specimen can be measured by an energy dispersive spectrometer and the elemental composition of the specimen is measured by analyzing the characteristic x-rays emitted from the specimen. The elastic scattering of the high-energy electron beam that occurs by the atoms of the sample gives rise to the back-scattered electrons. As the intensity of BSE is dependent on the atomic number (Z) of the sample they are used in obtaining information of different elements in the sample.

2.3 Material Properties Measurements

The magnetic properties of the materials were studied by electron spin resonance (ESR) and magnetization measurements using the vibrating sample magnetometer. The

transport properties were studied by resistivity measurements employing the four probe method and using the closed cycle refrigerator to attain low temperatures. The following sections describe the of the experimental techniques.

2.3a Electron Spin Resonance (ESR)

Electron spin resonance (ESR) spectroscopy deals with the interaction of electromagnetic radiation with the intrinsic magnetic moment of electrons arising from their spin. A material which does not have a net magnetic moment may acquire one when placed in an external magnetic field. This results in an internal magnetic field in the material, which is different from the external applied magnetic field. Because an electron has an intrinsic spin and magnetic moment, it may be used as a probe of local magnetic fields on an atomic scale, which forms the basis of ESR. Important information about the physics of the material may be obtained by probing the internal field.

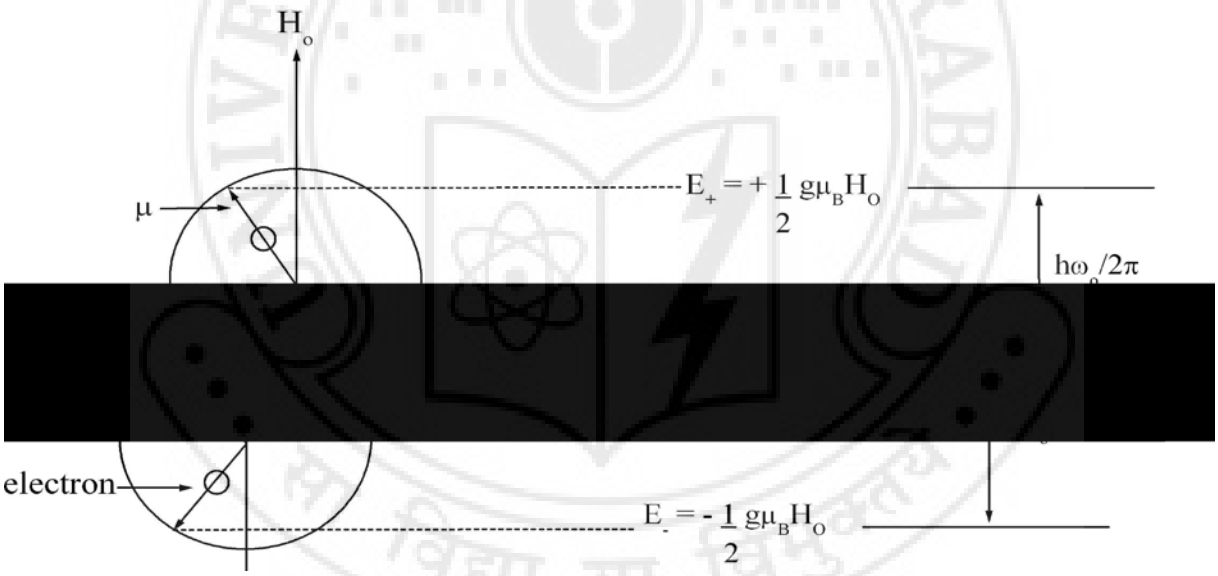

Figure 2.3 Schematic representation of a single electron spin in a steady magnetic field H_o.

According to quantum theory an electron has a spin which is understood as an angular momentum. This leads to a magnetic moment. Consequently, the negative charge that the electron carries is also spinning and constitutes a circulating electric current. The circulating current induces a magnetic moment μ_s. If the electron is subjected to a steady magnetic field $H_o \parallel z$, the magnetic moment μ_s causes the electron to experience a torque tending to align the magnetic moment with the field. The relation between the magnetic moment and the spin vector is

$$\mu_s = \frac{2\pi g \mu_B}{h} S \qquad (2.2)$$

where μ_B is the Bohr magneton, h is the Planks constant and g is the Lande factor. The value of μ_B is given as $\mu_B = \frac{eh}{4\pi m}$ and has a value of 9.274 x 10^{-24}JT^{-1} and the value of g for a free electron is 2.0023. The g-factor gives information about a paramagnetic centre's electronic structure. The energy of the system is determined by the projection of the spin vector along the applied field H_o which is along the z-axis. According to the quantum theory only two values are permitted for an electron namely $S_z = \pm\frac{h}{4\pi}$. The magnetic moment of the electron can hence assume only two projections onto the applied magnetic field. The degeneracy of the electron placed in a magnetic field is lifted as shown in the figure 2.3.

Hence the two values of energy are given as:

$$E_{\pm} = \pm\frac{1}{2} g \mu_B H_o \qquad (2.3)$$

When the applied electromagnetic radiation is at a frequency that corresponds to the separation between the permitted energies levels, the difference in energy levels is equal to

$$\Delta E = E_+ - E_- = g\mu_B H_o = \frac{h\omega_o}{2\pi} = h\vartheta \qquad (2.4)$$

When the equation 2.4 is obeyed energy is absorbed which leads to resonance. This is the basic theory of ESR [150].

Figure 2.4 gives a pictorial idea of the ESR. The test sample which is placed in a uniform magnetic field is wrapped within a coil which is connected to an RF oscillator. The smaller magnetic field induced in the coil by the oscillations of the oscillator is at right angles to the uniform magnetic field. Consider a single electron within the test sample. It will have a magnetic dipole moment (μ_s) that is related to its intrinsic angular momentum, or spin, by the vector equation

$$\mu_S = \frac{2\pi g_S \mu_B S}{h} \qquad (2.5)$$

where g_s is the electron spin factor and S is the magnitude of the spin angular momentum of the electron. Associated with the electron there are other magnetic moments coming from the orbital angular momentum given by the equation

$$\mu_L = \frac{2\pi g_L \mu_B L}{h} \tag{2.6}$$

where μ_L is the total magnetic moment resulting from the orbital angular momentum of an electron, L is the magnitude of its orbital angular momentum and total angular momentum is obtained from the equation

$$\mu = \frac{2\pi g_J \mu_B J}{h} \tag{2.7}$$

where where $\boldsymbol{\mu}$ is the total magnetic moment resulting from both spin and orbital angular momentum of an electron, $\boldsymbol{J} = \boldsymbol{L}+\boldsymbol{S}$ is its total angular momentum. The magnetic dipole moment of the electron and the uniform magnetic field interact with each other. Due to its quantum nature, the electron can orient itself in one of only two ways, with the value of energy as given in equation 2.3. When the RF oscillator is tuned to a frequency ν and the

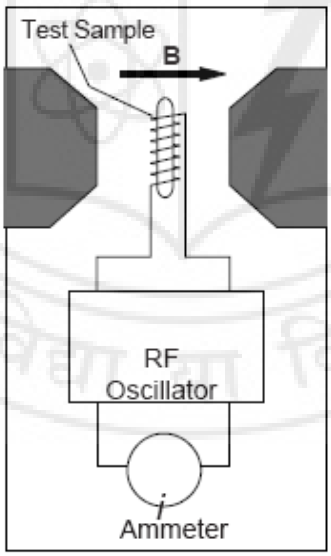

Figure 2.4 Depiction of the mounted samples in an ESR Spectrometer.

energy of the irradiated photons, hν, is equal to the difference between the two possible energy states of the electron, resonance occurs. The absorption of energy affects the permeability of the test sample, which affects the inductance of the coil and thereby the

oscillations of the RF oscillator. The result is an observable change in the current flowing through the oscillator. The condition for resonance, therefore, is that the energy of the photons emitted by the oscillator match the energy difference between the spin states of the electrons in the test sample which is mathematically stated in equation 2.4.

The temperature dependent ESR spectra of the samples were recorded on a JEOL JES-FA SERIES X-Band ESR spectrometer. A compressor is used to supply a continuous column of hot air through a hot heat blast pipe attached to the dewar adapter through which the gas flows, for the high temperature measurements in the temperature range 330K – 473K (±0.5 K). A continuous gas-flow cryostat for liquid nitrogen is used for the low temperature measurements in the temperature range 100K – 330K (±0.5 K). The electromagnet used has a low impedence, water cooled main coil which gives a magnetic field homogeneity of ± 5μT

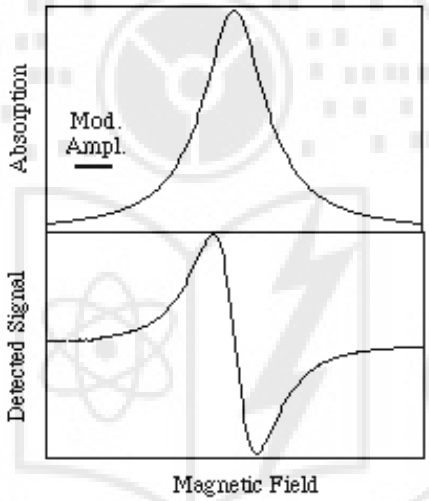

Figure 2.5 Absorption curve (above) and corresponding first derivative detected signal (below). Taking first-derivative spectra has a much better apparent resolution than the absorption spectra. Indeed, second-derivative spectra are even better resolved (though the signal-to-noise ratio decreases on further differentiation).

per effective volume at a field of 330mT. The instrument is operated at a frequency of ~ 9GHz. The cavity resonator is used in the TE mode. Thoroughly ground samples weighing a few milligrams are mounted in quartz tubes of diameter 5mm and length 270mm under optimized conditions of modulation amplitude, receiver gain, time-constant and scan time. The instrument is interfaced with a computer and data was

obtained for more detailed analysis. The dc magnetic field is ramped to 800mT and the ESR spectra for the samples are recorded.

The ESR spectrum recorded is the first derivative of spectral trace as shown in figure 2.5, as it has advantages over recording the direct signal. It indicates the centre of the broad resonance peak more precisely than the direct signal and the width of the peak (taken as half width) is often more accurately measured from the derivative curve [151].

2.3b Magnetization Measurements

The magnetization studies on the materials were performed using a vibrating sample magnetometer (VSM). The M-H curves and hysteresis loops give information on the magnetic properties of the materials. Apart from this basic measurement performed to obtain the hysteresis loops, the M-H curves or measuring the magnetic moment of materials, most

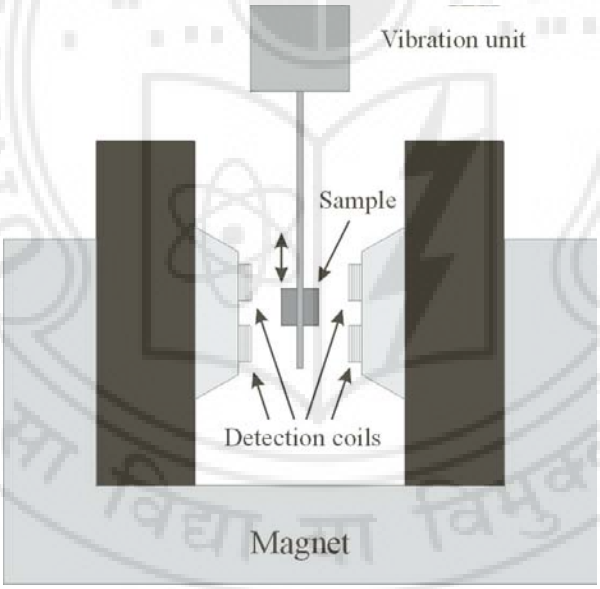

Figure 2.6. A Schematic diagram of a VSM

modern day VSMs have the versatility to be used for different magnetic studies like the temperature dependent magnetization studies, magnetoresistance measurements of bulk as well as thin film samples as a function of temperature, field and angle and measurements of magnetization in the X and Y directions simultaneously using vector measurements. Using an add-on facility of a torque system the VSM can be used as a

torque magnetometer to measure magnetic anisotropies, rotational hysteresis, and anisotropy field distributions.

The Vibrating Sample Magnetometer (figure 2.6) works on the basic principle of Faraday's Law of magnetic induction. When a sample is placed in a uniform magnetic field, a dipole moment proportional to the product of the sample susceptibility and the applied field is induced in the sample. The sample holder placed at the tip of a long slender vertical rod, is connected to a vibration unit. This is a transducer assembly which is placed above the magnet. This is the vibration unit, which vibrates the sample centred in between the pole pieces. The sample undergoing sinusoidal motion as well induces an electric signal in suitably located stationary pick-up coils. This signal, which is at the vibration frequency, is proportional to the magnetic moment, vibration amplitude and the vibration frequency.

A vibrating capacitor is located below the transducer. This generates an AC control signal which varies with the vibration amplitude and frequency. The signal is fed back to the oscillator where it is compared with the drive signal to maintain constant output drive signal. It is also phase adjusted and routed to a signal demodulator where it functions as the reference drive signal. A signal from the sample is developed in the pickup coils, buffered, amplified and applied to the demodulator where it is synchronously demodulated with respect to the reference signal derived from the moving capacitor assembly. The resulting DC output is an analog of the moment magnitude alone, uninfluenced by the vibration amplitude changes and frequency drift.

The room temperature magnetization experiment was carried out on a Lakeshore 7400 series VSM, Model 7407. The sensitivity of the instrument is high enough to measure magnetic moments ranging from 5μemu to 10^3emu. The gaussmeter is used in the transverse probe mode. The water cooled electromagnet has a maximum field strength of ±10kG in a 2 inch air gap with a 6-inch pole face or ±21kG in a 0.9-inch air gap with a 3-inch pole face, having a field accuracy of 1%.

2.3c Resistivity Measurements

The Closed Cycle Refrigerator (CCR) (figure 2.7) was used to conduct the temperature dependent resistivity studies of the samples.

The CCR operates on the Gifford-McMahon (GM) principle using a closed helium gas cycle, where helium gas is used as the refrigerant. Self-sealing screw-couplings are used to make the connection of the flexible or rigid pressure tubings, which are used to connect the compressor unit and the cold head to each other. This virtually avoids almost any loss of helium gas when screwed on and off repeatedly. Keeping the compressor and the cold head separate is more flexible as the cold head (which is lighter) can be operated in any mounting position. By means of a valve control either high-pressure or low-pressure helium gas is led to the expansion volume via the regenerator. The regenerator is a heat exchanger where the entering warm helium gas is precooled to the temperature to which the regenerator was cooled by the expanded gas leaving the expansion chamber.

Room temperature helium gas is first compressed, and then supplied to the refrigerator via flexible gas lines. The compressed helium is cooled by expansion, and provides cooling to

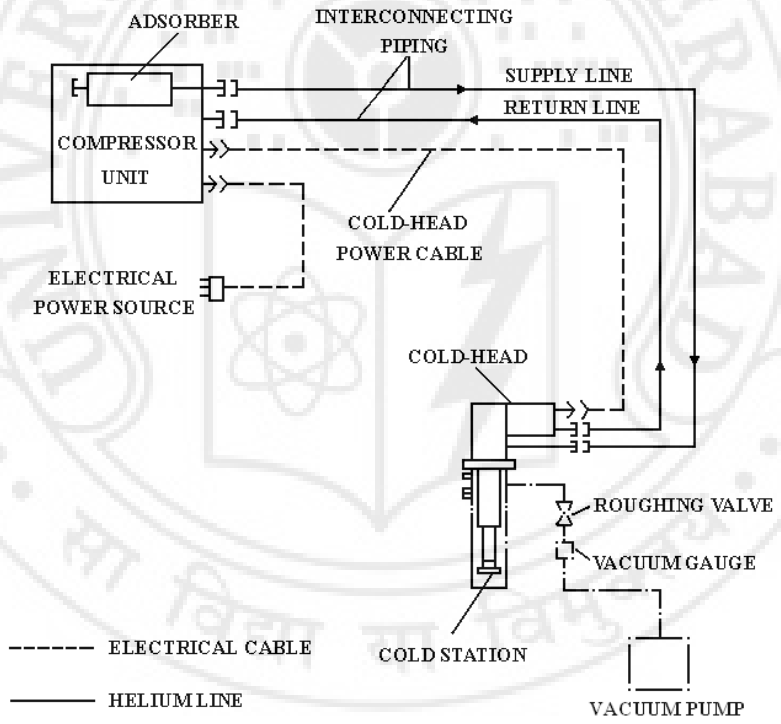

Figure 2.7 Schematic diagram of a Closed Cycle Refrigerator.

the heat station on the refrigerator. After cooling the refrigerator, the gas is returned to the compressor to repeat the cycle. Low temperature at the cold head is attained in this manner.

Electrical resistivity measurements were carried out by the four probe method. The samples were cut into rectangular pieces. Electrical contacts were made by pressing the copper wires onto the sample surface. The wires were fixed on the sample by applying silver paste, which also decreases the contact resistance. The sample was fixed on the cold head by thermally insulating it. The chamber was evacuated to the pressure of the order of 10^{-5} torrs. The typical four-probe set up is shown as in the figure 2.8.

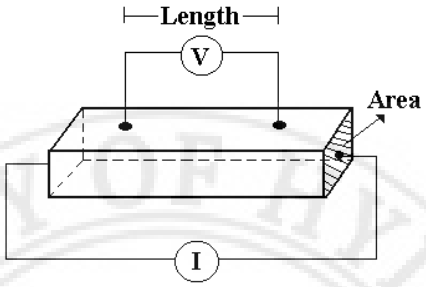

Figure 2.8 Schematic four probe setup for temperature dependent resistivity measurements

The linear voltage dependence of current showed that the contacts were ohmic. A Keithley D.C. and A.C. current source (model 6221) was used as the current source, for varying the applied current in the range 1μA to 1mA. Voltage across the terminals was measured using Keithley nanovoltmeter (model 2182A). The temperature is controlled using a Lakeshore (model 332) temperature controller. The D.C resistivity is calculated using the relation

$$\rho = \frac{V.A}{I.L} \qquad (2.8)$$

where V is the voltage measured across the terminals, I the current supplied to the sample, A the cross section area of the sample and L the length between the voltage terminals. By reversing the direction of the current the non-rectifying nature of the junctions is checked.

The basic structure of manganites is perovskite structure. The study of the structure of the parent compound of $BiMnO_3$ has yielded slightly varying results. $BiMnO_3$ is said to have a triclinically distorted perovskite structure using XRD studies [92]. The neutron diffraction studies and the electron diffraction studies have led to conclusions that $BiMnO_3$ has a structure which is related to a heavily distorted perovskite structure, having monoclinic symmetry [76 - 78], which becomes cubic at lower temperatures [83]. This difference in the determination of the structure can be attributed to the variation of lattice parameters which depend on the sensitivity of the technique assorted to.

One of the earliest structural studies on the system $Bi_{(1-x)}Ca_xMnO_3$ (BCMO) was done by Bokov *et. al.* [91]. The temperature dependent studies performed revealed two monoclinic phases and an orthorhombic phase for the values $x < 0.4$. The high temperature studies in the range $0.4 < x < 0.83$ reveals a cubic phase, which transforms to a monoclinic phase at low temperature. Above $x < 0.83$ an orthorhombic structure is observed. Woo *et. al.* [97] reported the structural transitions of the BCMO system, from XRD studies, for $0.4 < x < 0.9$. In this work the $x = 0.4$ sample is indexed with a triclinic cell. It is also considered as nearly monoclinic as the lattice parameters vary slightly from that of a triclinic one. The $x = 0.9$ sample is indexed with the orthorhombic perovskite structure. The samples with $x = 0.6$ and $x = 0.8$ exhibit structures similar to the $x = 0.4$ and $x = 0.9$ samples respectively. It is concluded that with increasing Ca content the space-group symmetry reduces. Other neutron scattering experiments on doped Bi-manganites also ascertained the distorted orthorhombic structure for samples with higher Ca content [118]. The XRD results on $Bi_{0.4}Ca_{0.6}MnO_3$ yielded the distorted perovskite structure indexed with an orthorhombic structure with lattice parameters quite similar to an orthorhombic structure or a tetragonal structure [102]. From high resolution electron microscopy studies it is known that the half doped BCMO system exhibits a Pnma subcell [116].

Figure 3.1 shows the XRD patterns of the $Bi_{(1-x)}Ca_xMnO_3$ ($x = 0.4 – 0.75$). The $x = 0.4$ system is indexed with a triclinic (~ monoclinic) structure as reported by Woo *et. al.* [97]. With increasing Ca content the system tends towards an orthorhombic (~ tetragonal) structure. The change in lattice parameters of the Ca – rich samples is such that they become similar to that of a tetragonal structure and hence the tag as mentioned above. The triclinic splitting visible in the XRD spectra of samples with low Ca content decreases with increasing Ca content indicative of the structure changing to a more symmetric one. The lattice parameters are estimated from the XRD patterns and are found to change from $a \approx 3.8$ A^o, $b \approx 7.5$ A^o and $c \approx 3.8$ A^o for $x = 0.4$ to $a \approx 5.3$ A^o, $b \approx 7.5$

A^o and c≈ 5.3 A^o for the x = 0.75 sample. These values are comparable to the values reported in literature [94, 97]. The change in the structure is almost in line with the studies reported by Bokov *et. al.* [91]. Figure 3.2 shows the variation of the cell parameters with composition of the system, at 600°C, which is the paramagnetic state of the samples, as given by Bokov *et. al*. The system exhibits an orthorhombic structure for a wide range of compositions and changes to a cubic structure just above x = 0.8.

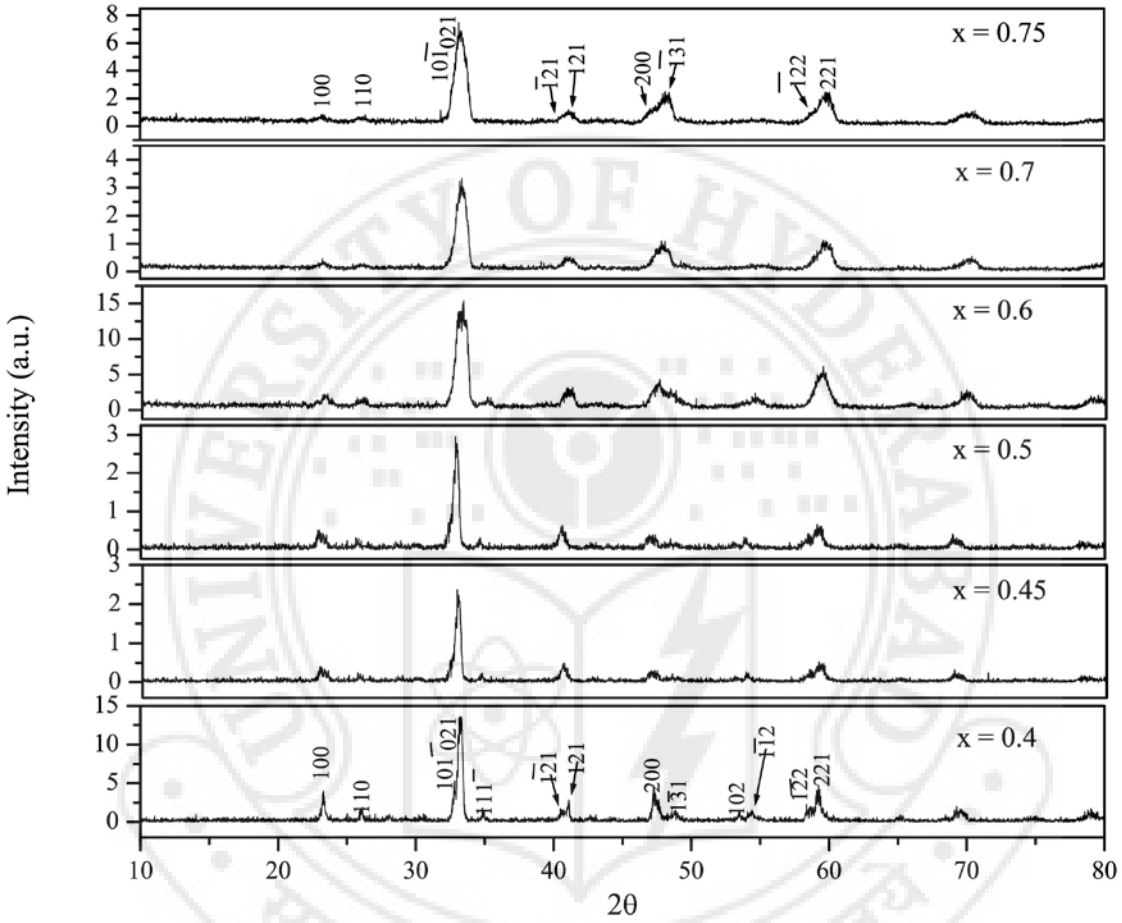

Figure 3.1 XRD plots of $Bi_{(1-x)}Ca_xMnO_3$

The SEM images recorded for the system are represented in figure 3.3. The x = 0.4 sample shows grains of ~ 1μm size and agglomerates of sizes ranging up to ~ 30 μm. With the increase in the value of x the concentration of the smaller grains increase. The increase in Ca content also helps in measuring the size of the smaller grains as the boundaries do not get defused. The sizes of the smaller grains range from ~ 400nm to ~ 1μm. With the increase in x the concentration of the agglomerates also decreases. This is typical of the fact that with the smaller value of x the Bi content is high, which promotes agglomeration. The EDAX on select samples were done for the analysis of the

composition of the samples. The composition of the samples were found to be within ~ 3% error of the starting materials.

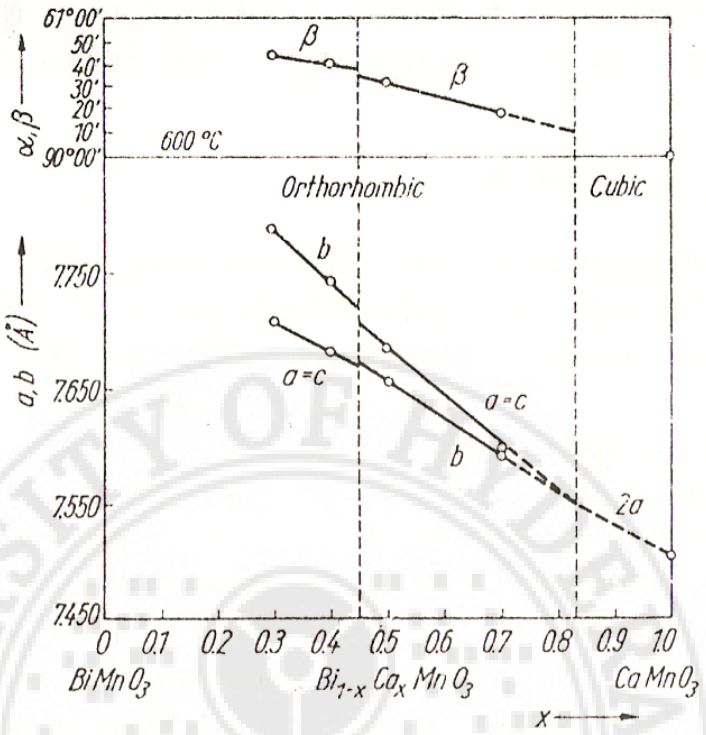

Figure 3.2 Composition dependence of the cell parameters of the $Bi_{(1-x)}Ca_xMnO_3$ system in the PM state at 600°C [91].

There are several reports of the structural studies on $Bi_{(1-x)}Sr_xMnO_3$ using techniques like XRD, neutron powder diffraction (NPD), Synchrotron powder X-ray diffraction (SXRPD) etc [92, 108, 112]. Chiba *et. al.* reported the change in structure with the change in x value from triclinic ($0 < x < 0.2$) to monoclinic ($0.2 < x < 0.4$) to tetragonal ($0.4 < x < 0.7$); the symmetry, though, was found to be higher which could also give the structure variation as monoclinic to orthorhombic to tetragonal respectively with the increase in the value of x. Mantytskaya *et. al*., on the other hand reported the structure for this system as being triclinic for $x = 0$, monoclinic for $x = 0.25$ and tetragonal for $0.35 < x < 0.8$. The structure of $Bi_{0.5}Sr_{0.5}MnO_3$ has been given as orthorhombic by Munoz *et. al.* using NPD and SXRPD, whereas Kim *et. al.* [110] reported a tetragonal structure for the same owing to the lower resolution of the measurement technique adopted. Electron diffraction studies on this composition proved the samples to have an orthorhombic structure [152]. The high resolution electron microscopy study on half doped BSMO system revealed the Imma type of subcell it exhibits [152].

Figure 3.4 shows the XRD plots of the series $Bi_{(1-x)}Sr_xMnO_3$ (x = 0.3, 0.4, 0.45, 0.5). The peaks are indexed in view of the perovskite structure. The lattice parameters for

a perovskite structure is given as a = c ≈ b ≈ a $_p$, where a_p is a lattice parameter of the cubic perovskite structure. The x-ray diffractograms are analyzed for a tetragonal structure (~ orthorhombic) as the lattice parameters are obtained as a≈ c ≠ b. Chiba *et. al.* [107] established the structure of $x = 0.3$ as monoclinic. The double peaks at $2\theta = 33^o$ in the $x = 0.5$ sample, which are characteristic of the tetragonal structure, are not observed in the $x = 0.3$ sample. This manifests the beginning of the change in the structure with decreasing value of x

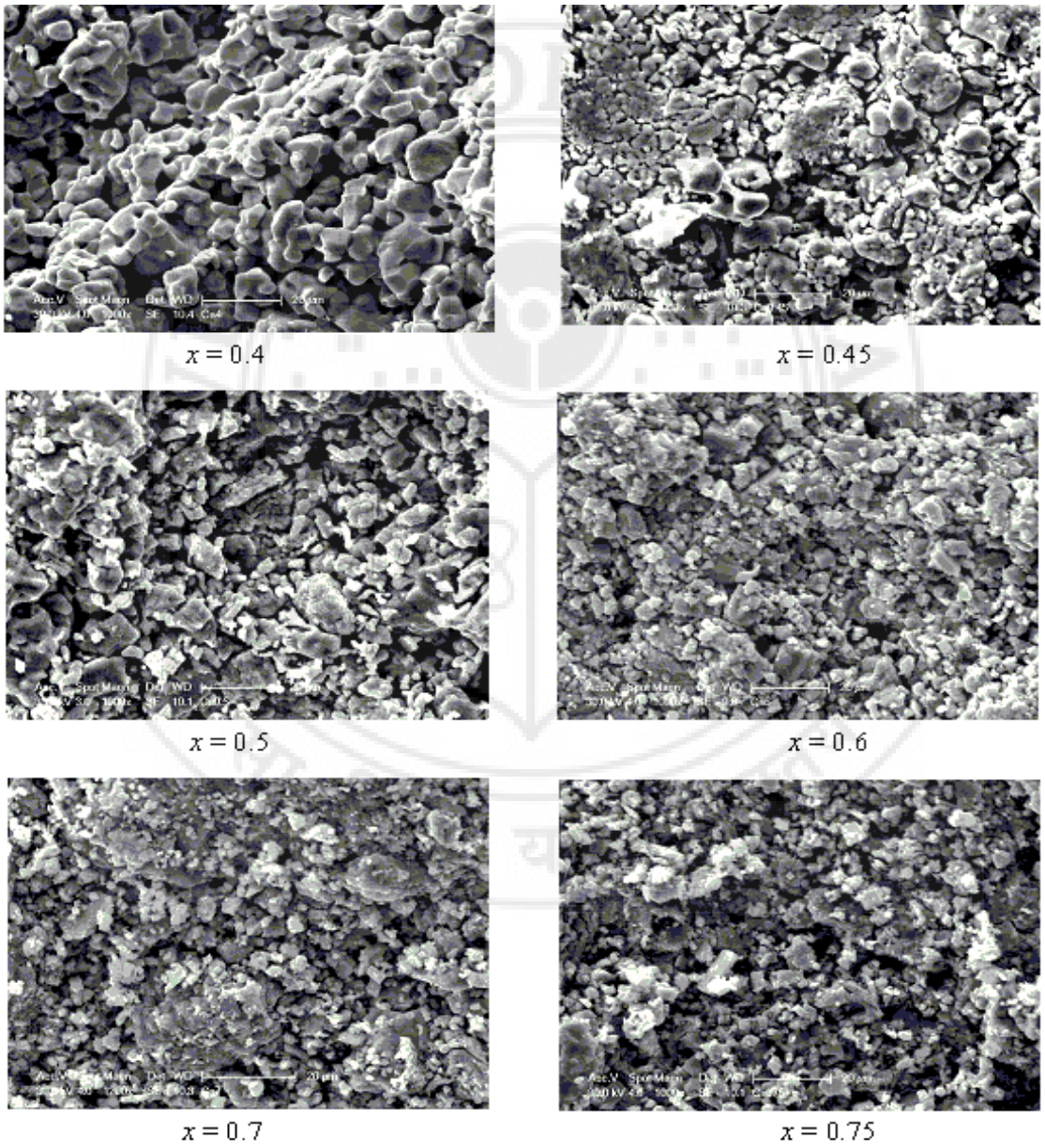

Figure 3.3. The SEM images of $Bi_{(1-x)}Ca_xMnO_3$

to a more asymmetrical structure. These samples undergo a first order transition of the crystal structure which can be attributed to the difference in the Mn^{3+} (ionic radius 0.645A^o) and Mn^{4+} (ionic radius 0.53A^o) ratios. The lattice parameters estimated from the XRD patterns are a ≈ c ≈ 3.92 A^o and b ≈ 3.88 A^o for x = 0.3, indicative of a ~ tetragonal structure, which changes gradually to a≈ c ≈ 3.9 A^o and b ≈ 3.78 A^o for x = 0.5 samples, indicative of a ~ monoclinic structure.

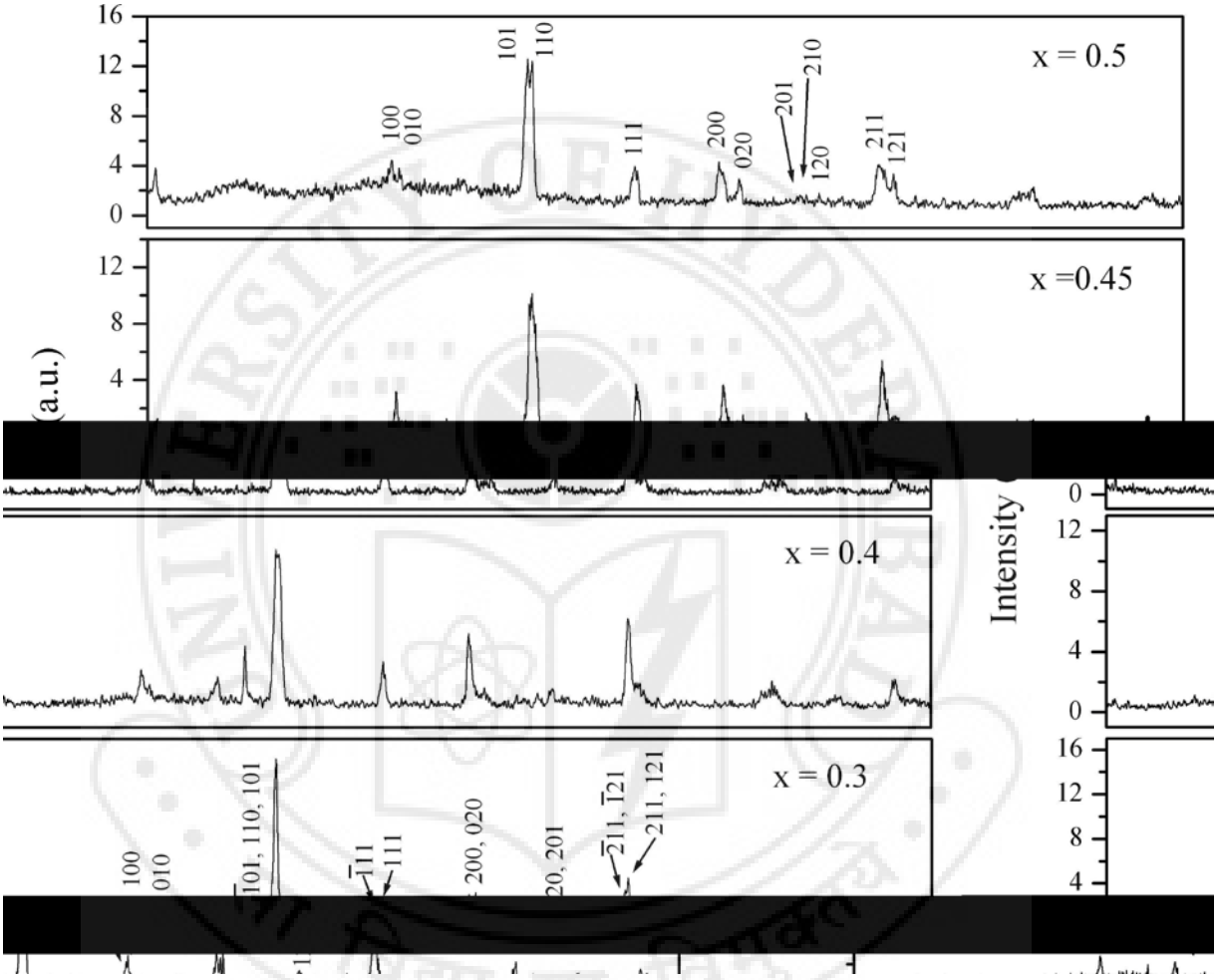

Figure 3.4 XRD plots of $Bi_{(1-x)}Sr_xMnO_3$

Figure 3.5 shows the compositional changes of the lattice parameters for the $Bi_{(1-x)}Sr_xMnO_3$ system for x = 0 to 0.7 [92]. The structure of the system changes from a triclinic one at x = 0 to monoclinic one just above x = 0.1 and then to a tetragonal structure for x ≈ 0.35. The values of the cell parameters are also depicted in the figure giving a clear picture of the variation of the structure of the BSMO system with composition.

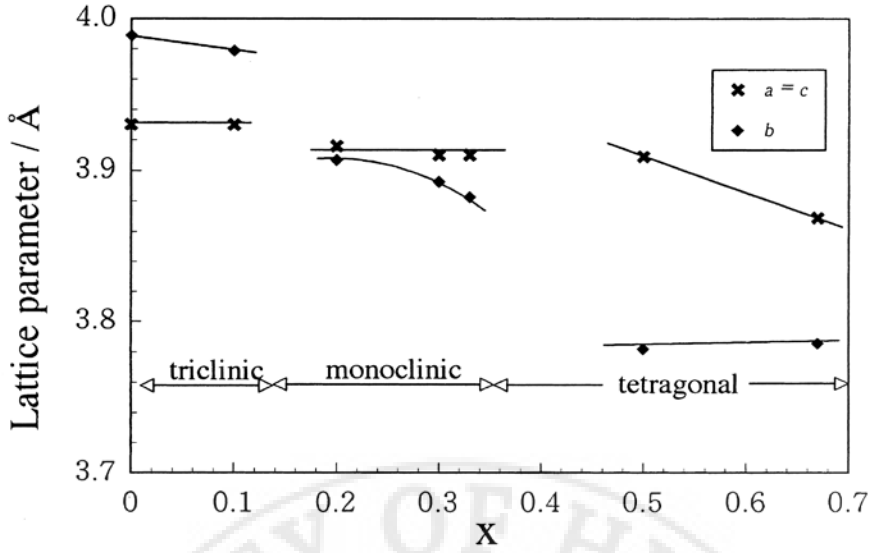

Figure 3.5.Compositional changes of lattice parameters at room temperature in the $Bi_{(1-x)}Sr_xMnO_3$ sample. Figure taken from reference 92.

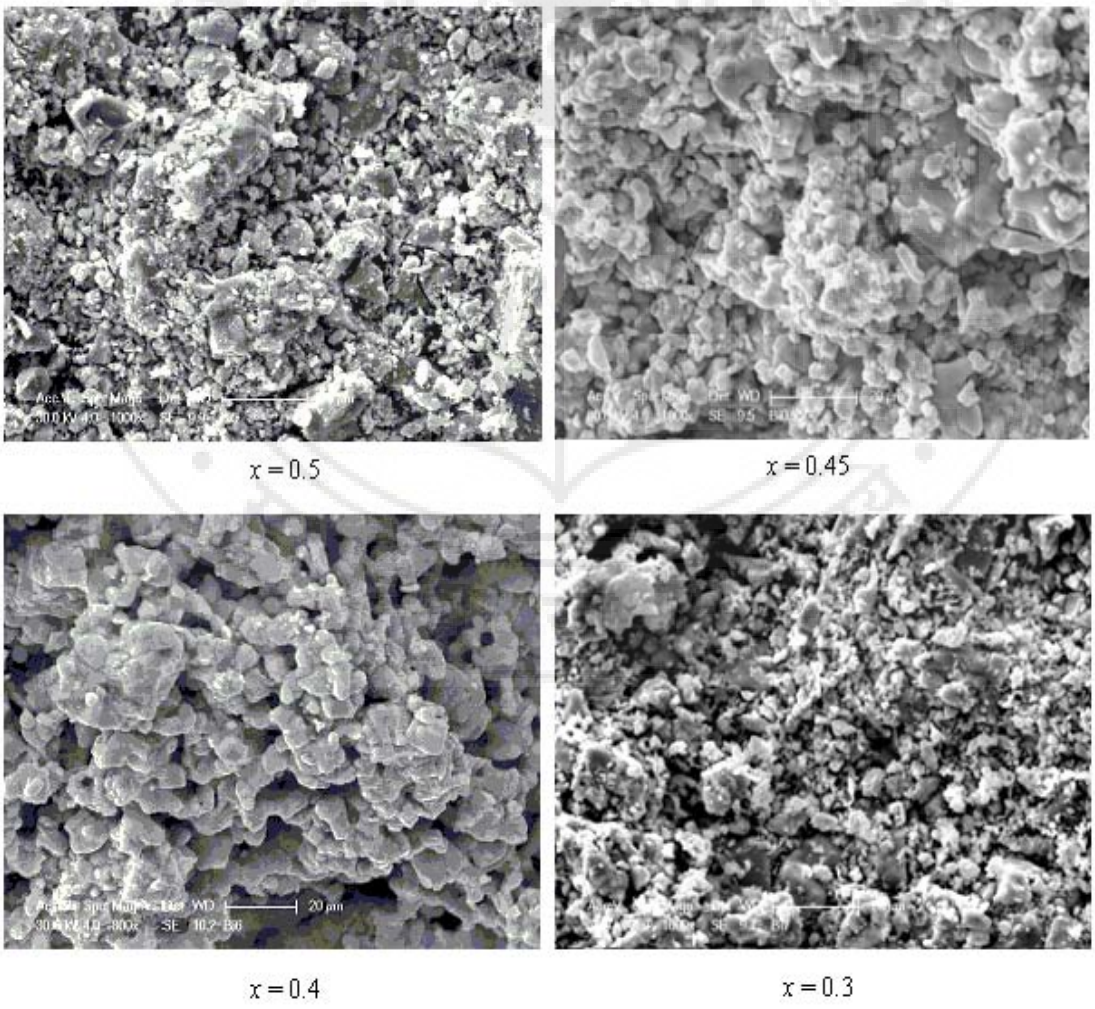

Figure 3.6. The SEM images of $Bi_{(1-x)}Sr_xMnO_3$

The SEM images can give information on the microstructure and particle distribution. The information regarding the grain size and porosity too can be extracted from the micrographs. Figure 3.6 gives the SEM images of the $Bi_{(1-x)}Sr_xMnO_3$ samples. The samples are characterized by a porous structure and with grains sizes extending from those in the range of a few hundred nanometers to a few microns. These samples also show multi-grain agglomeration with the sizes of these agglomerates ranging from ~ 20μm for the $x = 0.5$ sample to ~ 40μm for the $x = 0.3$ sample. The size of the pores could not be measured as they are intergranular and remain interconnected throughout the sample forming channels of small pores. Hence these pores do not form any kind of a particular well-defined shape making it difficult to give any particular dimension to the pores. The formation of the agglomerates can be due to the low melting point of the starting material of Bi_2O_3. The EDAX on select samples were performed to analyze the composition of the samples. The compositions were found to be within ~ 3% error of the starting materials.

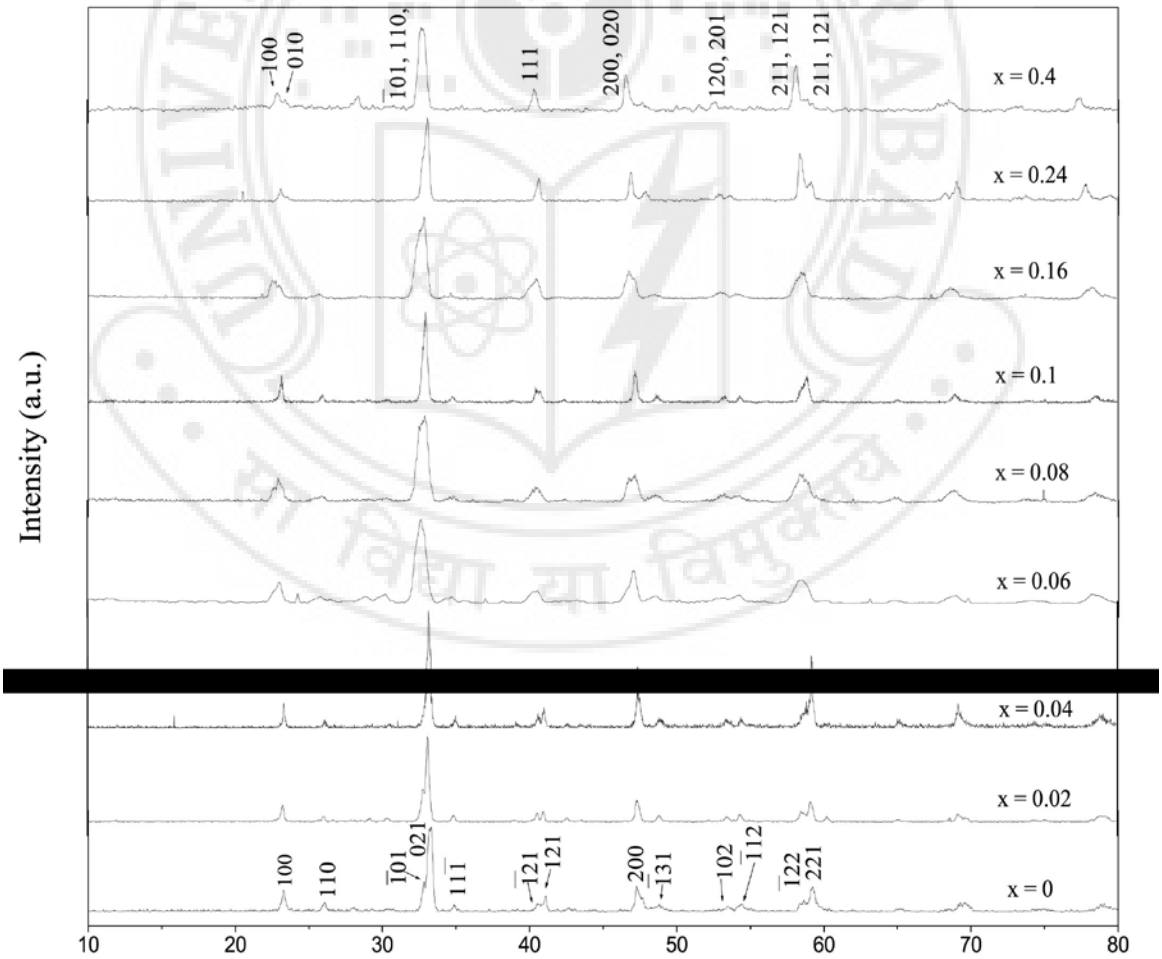

Figure 3.7 XRD plots of $Bi_{0.6}Ca_{(0.4-x)}Sr_xMnO_3$

The XRD data of the $Bi_{0.6}Ca_{(0.4-x)}Sr_xMnO_3$ (x = 0, 0.02, 0.04, 0.06, 0.08, 0.1, 0.16, 0.24, 0.4) system is seen in figure 3.7. As stated before the x = 0 sample is of a triclinic (~monoclinic) structure and the x = 0.4 system shows an tetragonal (~ orthorhombic) structure. The structure of the sample $Bi_{0.6}Ca_{(0.4-x)}Sr_xMnO_3$ undergoes a change with increasing content of Sr. The lattice parameters are estimated from the XRD patterns and are found to change from a≈ 3.8 A^o, b ≈ 7.5 A^o and c ≈ 3.8 A^o for $Bi_{0.6}Ca_{0.4}MnO_3$ to a ≈ c ≈ 3.91 A^o and b ≈ 3.79 A^o for $Bi_{0.6}Sr_{0.4}MnO_3$. The average A-site cationic size, $<r_A>$, increases with increase in the Sr content. But as is known the effect of the difference in the $<r_A>$ on the different properties of Bi- manganites is not as prominent as the lone pair of Bi^{3+} $6s^2$ electrons, which is a deciding factor for the properties. In the BCMO system the $6s^2$ lone pair of electrons has a constrained effect and the ionic radius of Bi^{3+} is ≈ 1.16 A^o and the ionic radius of Ca^{2+} is 1.12 A^o [213]. In the BSMO system the ionic radius of Bi^{3+} is ≈ 1.24 A^o and the ionic radius of the Sr^{2+} ion is 1.32 A^o and the lone pair effect is dominant [99, 213]. At x = 0.06 the triclinic splitting begins to decrease till x = 0.16. At x = 0.24 the splitting seems to diminish completely. This could be seen as the complete transition from a ~ triclinic structure at x < 50% to an ~ orthorhombic structure for x > 50%. There are reports of electron diffraction studies on the coexistence of monophasic and biphasic domains in different systems for a small range of substitution at the A-site [153]. But for the Bi manganites the emergence of a biphasic domain is observed for a larger compositional range [116]. In the range x = 0.06 to x = 0.16, the values of T_{CO} and T_N shift and spread out over a larger range of temperatures making the exact values unclear, which are typical of the changes in the structure. At x = 0.24 the sample shows an orthorhombic (~ tetragonal) structure reflected in the transport as well as magnetic properties too. A direct analysis of the evolution of the room temperature lattice parameters is not easy.

Figure 3.8 shows the SEM images of the $Bi_{0.6}Ca_{(0.4-x)}Sr_xMnO_3$ system. Similar to that seen in the previous two samples the grains sizes varies from ~ 700nm to ~ 20μm. The agglomerates of grains are of the size ~ 30μm, which are visible in all the samples. The samples were scanned at different areas and the morphology was confirmed to be similar throughout the sample surface. The end products with x = 0 and x = 0.4 give grains of almost similar sizes whereas the difference in the grains sizes is observed more

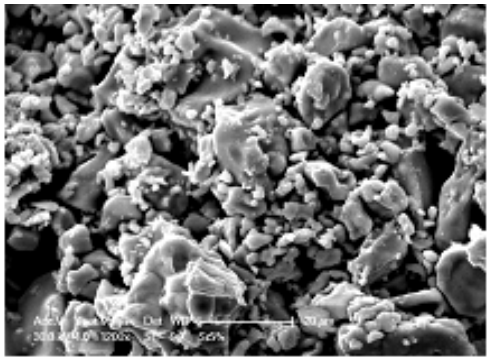

$x = 0.02$

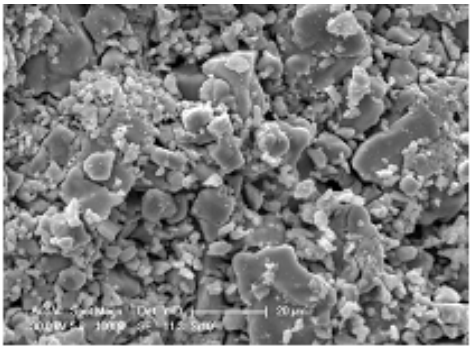

$x = 0.04$

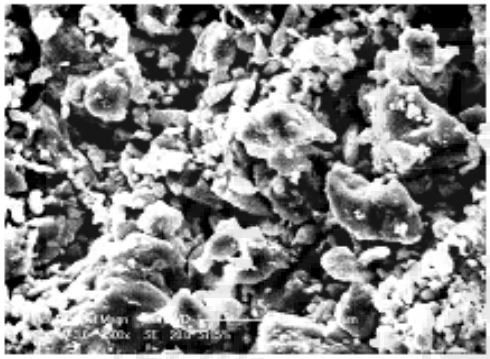

$x = 0.06$

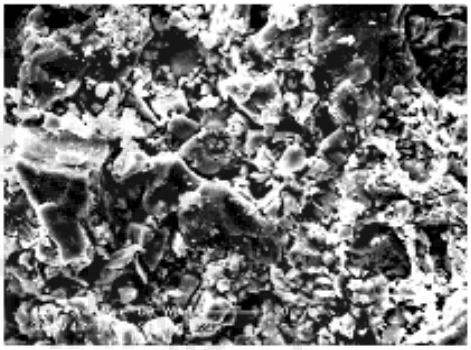

$x = 0.08$

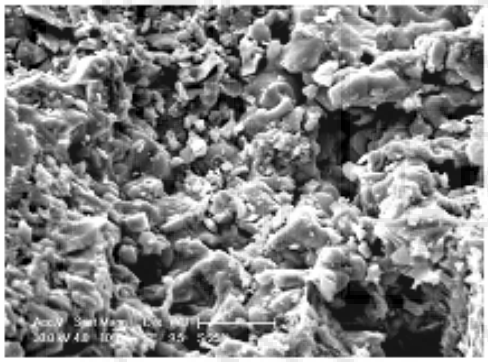

$x = 0.1$

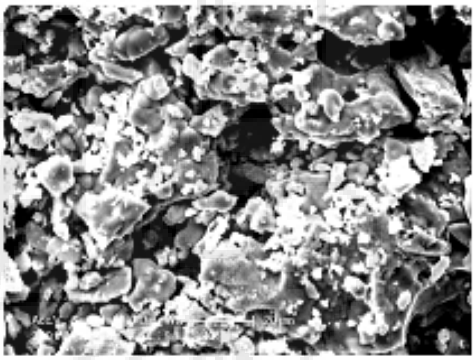

$x = 0.16$

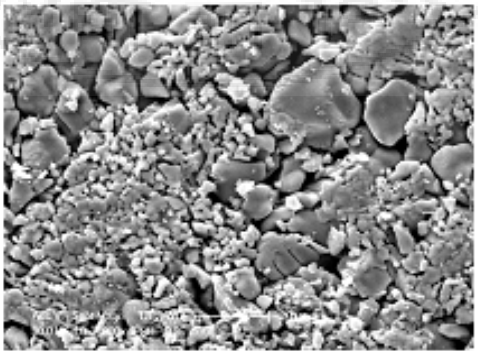

$x = 0.24$

Figure 3.8. SEM images of $Bi_{0.6}Ca_{(0.4-x)}Sr_xMnO_3$

prominently in the range $x = 0.06$ to $x = 0.16$. This could be a reflection on the phases that are formed as seen from the XRD studies, where the $x = 0$ sample has a triclinic (~ monoclinic) structure and $x = 0.4$ an orthorhombic (~ tetragonal) structure while the samples with a mixture of Ca and Sr exhibit a kind of transition phase attesting the results found from the XRD studies.

Cerium doped BSMO system was studied for its structural properties. The x-ray diffractograms of the samples $Bi_{0.5}Sr_{(0.5-x)}Ce_xMnO_3$ ($x = 0$, 0.1, 0.2) are shown in figure 3.9. The samples crystallize in the tetragonal structure. Though majority of the Cerium becomes part of the single phase material, an impurity phase of CeO_2 indicating the segregation of cerium oxide, is visible. Earlier reports on Ce doped manganites [154 – 157] have also shown that the samples are not single phased but are multiphase mixtures comprising hole – doped trivalent ion deficient manganite phases, and cerium oxide, CeO_2. This may probably be related to the presence of Ce^{4+} cations. The most stable valence state for air – prepared samples is +4. Charge neutralization is attained by the formation of Mn^{2+} (ionic radius 0.83A^o) ions. The ionic size of Mn^{2+} is much larger

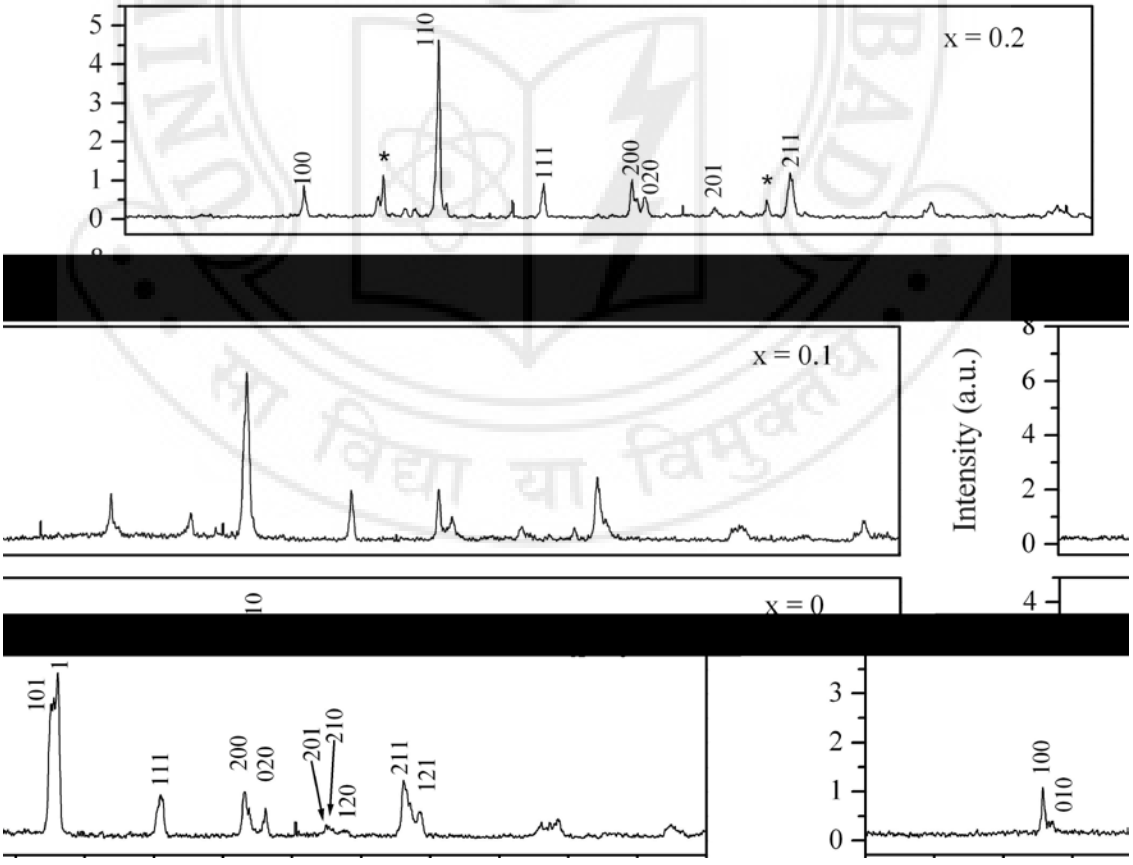

Figure 3.9 XRD plots of $Bi_{0.5}Sr_{(0.5-x)}Ce_xMnO_3$. The stars shown in the x = 0.2 plot designates the CeO_2 impurity phase.

compared to that of Mn^{3+} and Mn^{4+}, whereas Ce^{4+} (ionic radius 0.97A^o) is a much smaller ion than Bi^{3+} or Ce^{3+} (ionic radius 1.143A^o) ions [213]. This can make the cerium-doped structure very unstable and lead to segregation of CeO_2 [158]. With increasing content of Ce the lattice parameters change to give a tetragonal (~ orthorhombic) structure. Figure 3.10 shows the SEM images of the $Bi_{0.5}Sr_{(0.5-x)}Ce_xMnO_3$ system. The x = 0 sample shows grains of different sizes ranging from just below ~ 1μm to around 15μm. The SEM images show two different parts of the x = 0.1 and the x = 0.2 samples. The right hand side of the figure is the micrograph of the surface of the x = 0.1 sample. Rod-like growths are observed in this image. This is analyzed to be Ce rich from the EDAX results.

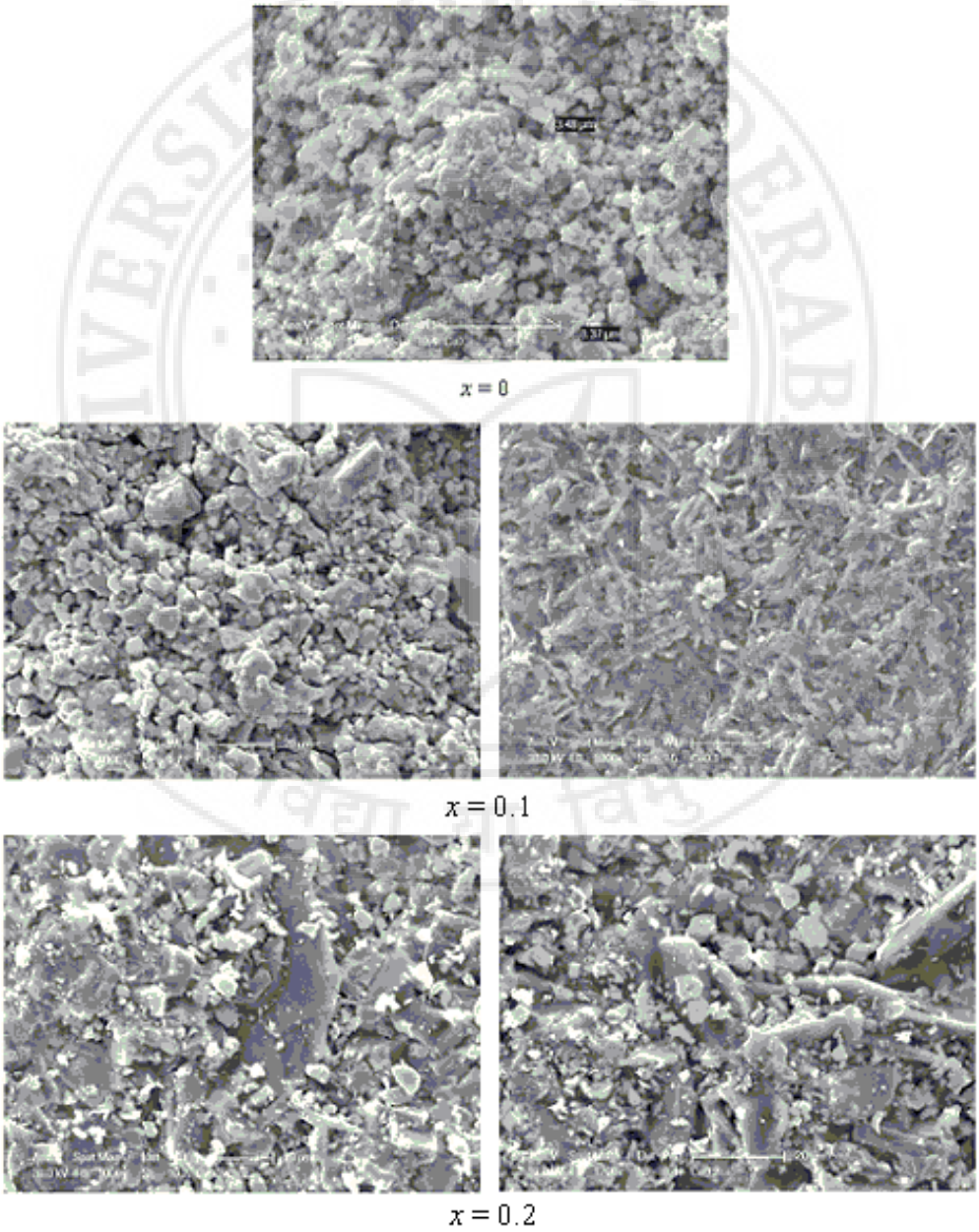

Figure 3.10 SEM images for the system $Bi_{0.5}Sr_{(0.5-x)}Ce_xMnO_3$

The large sized grains typical of Bi and Sr was hardly visible in this image. On the other hand the image on the left hand side of this figure shows grains of different sizes and almost similar shapes, with the rod-like feature quite less. The surface shows difference in the concentration of the starting material ratio or phase segregation (multi phase formation) which has occurred at the grain boundaries and can be considered as an inhomogeneity visible on the surface of the system. The images of the x = 0.2 sample too show the rod – like growth in the micrographs and other different sized grains representative of expected Bi, Mn and Sr content as well in the inner part of the sample. The length of the rod like features is ~ 25 μm. The presence of unreacted CeO_2 impurity phase has been reported earlier too for different manganites [159 - 161].

The powder XRD patterns of $Bi_{0.5}Ca_{0.5}Mn_{(1-x)}Cr_xO_3$ (x = 0, 0.01, 0.03, 0.05) is shown in figure 3.11. Chromium, which has multiple valencies, exists predominantly in the +3 state (with an ionic radius of 0.615A^o [213]) as it is the most stable ion. The patterns are indexed with distorted perovskite structure. The samples have been analyzed for an orthorhombic structure (~ tetragonal). The lattice parameters begin to change with the addition of chromium. This shows the tendency of the samples to crystallize in the tetragonal structure.

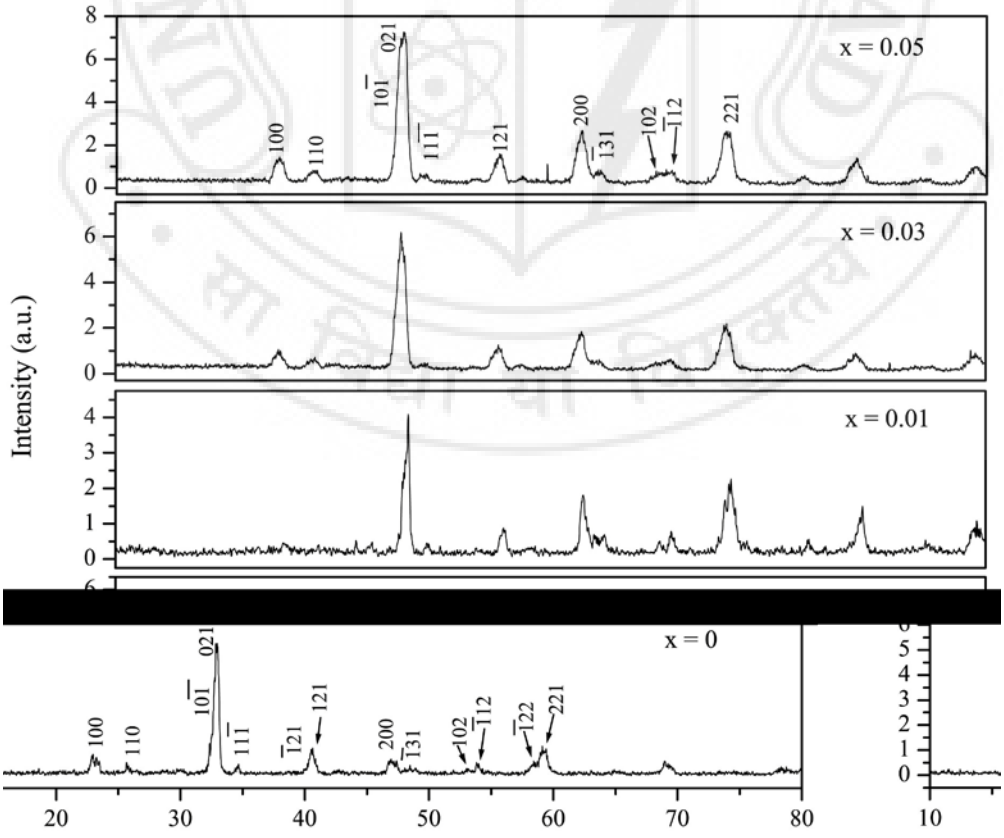

Figure 3.11. XRD plots of $Bi_{0.5}Ca_{0.5}Mn_{(1-x)}Cr_xO_3$

The lattice parameters vary from a ≈ 5.42A^o b ≈ 5.47A^o and c ≈ 5.32A^o for x = 0 to a ≈ c ≈ 5.37A^o and b ≈ 5.44A^o for x = 0.05. The lattice parameters are similar to that reported from earlier similar studies [136]. There are other studies on Cr doped BCMO systems with different ratios of Bi and Ca showing the samples to crystallize in the monoclinic structure. This confirms that it is rather the Ca content which can possibly alter the structure of the system than the addition of chromium. It is observed that with the addition of Cr the splitting in the XRD peaks decreases.

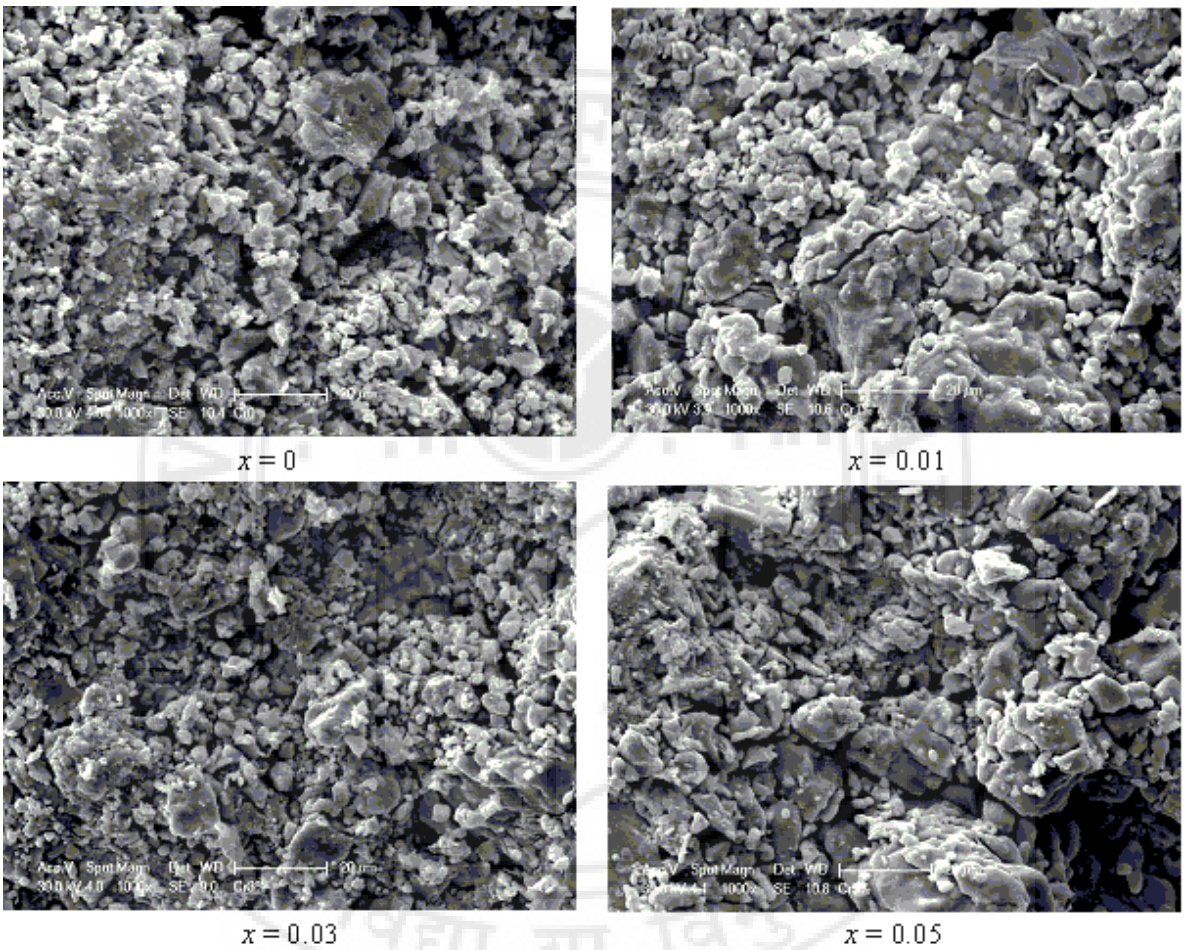

Figure 3.12 SEM images for the system $Bi_{0.5}Ca_{0.5}Mn_{(1-x)}Cr_xO_3$

The SEM images of $Bi_{0.5}Ca_{0.5}Mn_{(1-x)}Cr_xO_3$ are shown in figure 3.12. There are no prominent changes in the overall morphology of the samples from that of the pure $Bi_{0.5}Ca_{0.5}MnO_3$ observed. The size of the grains are of the order of a few micrometer while the agglomerates are of sizes ranging up to ~ 30 μm. The size of the grains range from ~ 400nm to ~ 1μm. One of the prominent differences in this series of samples from the BCMO system is that, with the increase in Cr content the agglomerates formed are

found to be more fractured. This is a unique feature which is not observed in any of the other series of samples.

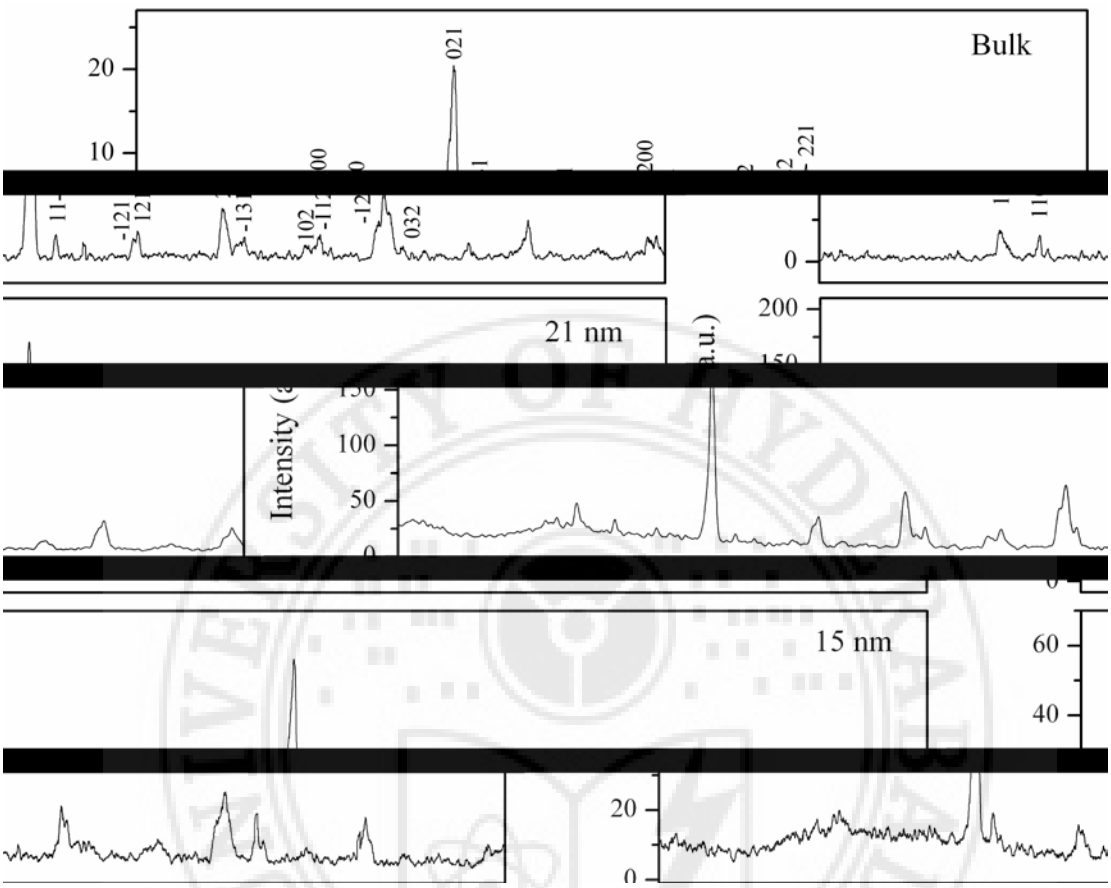

Figure 3.13 XRD plots of bulk and nanoparticle $Bi_{0.55}Ca_{0.45}MnO_3$.

Figure 3.13 depicts the XRD plots of the bulk and nano particle sized samples. All the samples are analyzed to have a triclinic (~ monoclinic) structure. The average grain size of the nanoparticle sized materials is calculated using the Scherrer's formula

$$t = \frac{k\lambda}{\beta cos\theta} \qquad (3.1)$$

where k is a constant (shape factor about 0.9), λ the X-ray wavelength, β the full width at half maxima of the diffraction line and θ the diffraction angle. It is found that the nanoparticle sample sintered for 6 hours had a particle size of 21nm while that sintered for 3 hours had a particle size of 15nm.

The SEM images of bulk and nanoparticle $Bi_{0.55}Ca_{0.45}MnO_3$ is shown in figure 3.14. It is observed that the bulk sample possesses agglomerates of sizes upto ~ 30 μm. The sizes of the agglomerates in the sample of particle size 21nm ranges from ~ 500nm to ~ 2 μm while the 15nm sized samples have agglomerates within the range of 200nm to 1μm. The boundaries of the grains of the 15nm sized grains are more well defined than those of the 21nm sized grains, which can be attributed to the shorter duration of sintering. The sol – gel method of sample preparation adopted gives better homogeneity of the samples as indicated by the uniform spread of grains.

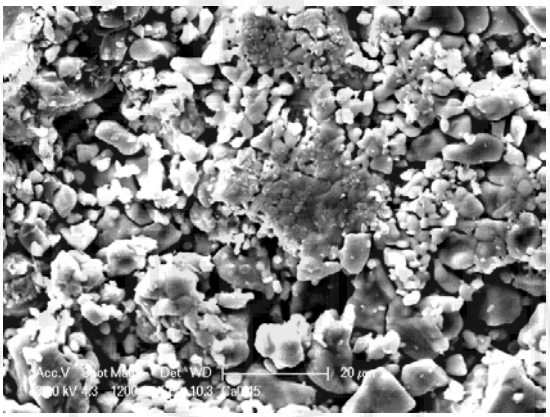

Bulk

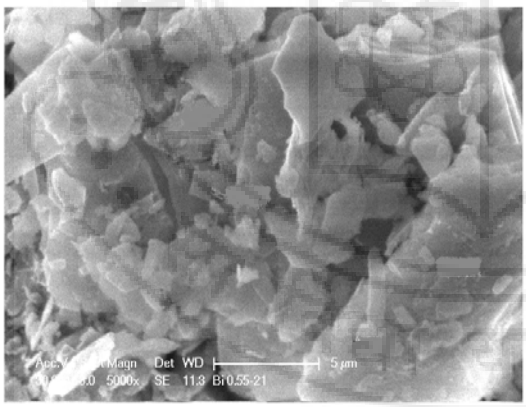

21nm

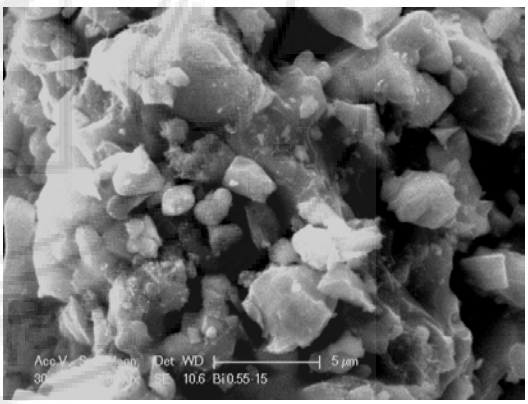

15nm

Figure 3.14 SEM images for the system $Bi_{0.55}Ca_{0.45}MnO_3$ bulk and nanoparticles.

This chapter describes the temperature dependent electron spin resonance (ESR) studies on various synthesized compositions. The ESR studies were performed on the samples to obtain information on the spin structure and its dynamics. The ESR data was taken on a few milligrams of powdered sample in a quartz tube.

4.1 The ESR parameters:

The parameters that are derived from the ESR resonance spectra to obtain information on the magnetic properties of the system are the line shape, double integrated intensity of the resonance line (DIN), peak to peak line width (ΔH) and the g-factor of the resonance peaks.

4.1a Intensity and Double Integrated Intensity (DI) of ESR:

The line intensity depends on experimental factors like power level, detector sensitivity, amplifier settings, sample composition and temperature. The intensity is representative of the amount of power absorbed per unit field applied. This is indicative of the number of ESR active centres in the sample. The intensity of the ESR line is proportional to the population difference between the two states involved in the transition and to the number of spins in the sample. Information on the nature of the magnetic ions and about the spin environment of the samples is obtained from the line intensity. Electron spin exchange between identical and non identical molecules, chemical exchange between the PM molecule and its environment, and the interaction of nearby molecules with unpaired spins are some examples of environmental effects which can influence line width and intensity in the ESR spectrum. Figure 4.1 shows the line intensity of a resonance line.

From the ESR experiments double integrated intensity (DI) can be measured. If magnetization (M) varies linearly with field (H) the DI of the resonance line is proportional to the magnetization, which in turn is proportional to the ESR susceptibility. The DI value is estimated by finding the area under the ESR resonance curve, by multiplying the peak to peak amplitude or intensity (ΔI_{PP}) and the peak to peak linewidth (ΔH_{PP}) of an ESR line. Figure 4.1 shows the parameters ΔI_{PP} and ΔH_{PP}. It should be noted that the amplitude or peak to peak intensity depends on the number of spins within the microwave cavity of the ESR spectrometer, which is proportional to the mass and the

density of the material used. Hence, DI is directly proportional to the ESR susceptibility χ_{ESR}, which is proportional to M.

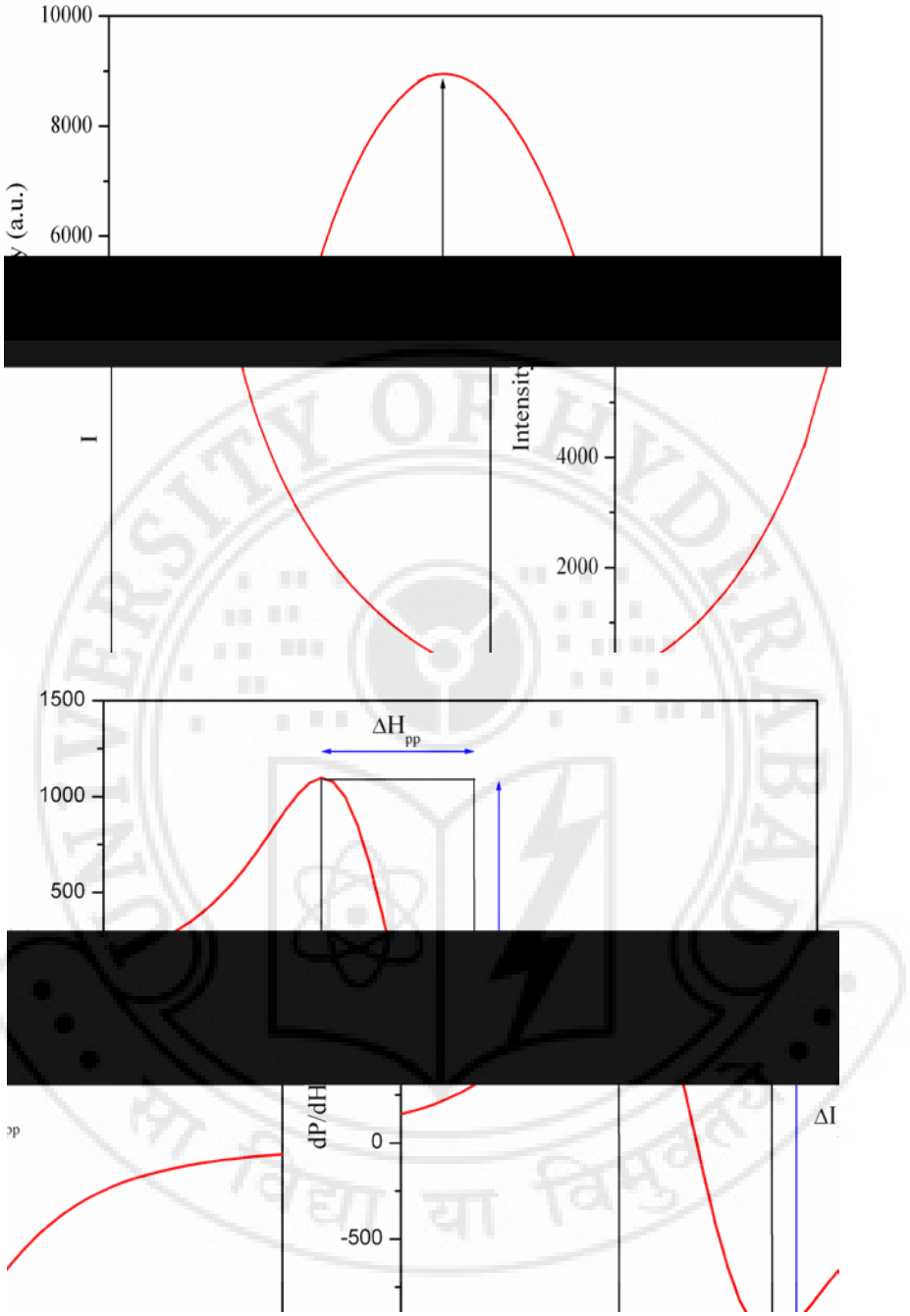

Figure 4.1. Diagram of the resonance line (top) and the derivative of an absorption curve (bottom)as obtained from the ESR, depicting parameters of ΔI_{PP} and ΔH_{PP}

4.1b Lande g factor :

The g-factor (or g-value) is a dimensionless quantity, which is essentially a proportionality constant relating the magnetic moment of the particle μ, the angular

momentum and the Bohr/nuclear magneton. Knowledge of the g–factor can give information about the paramagnetic centre's electronic structure. An unpaired electron responds to the magnetic field applied, H_o, in the spectrometer. It also experiences local magnetic fields due to the other particles in its vicinity, which should also be taken into account when the field experienced by the electron is calculated. Hence the net effective field, H_{eff}, experienced by the unpaired electron is given as

$$H_{eff} = H_O(1-\sigma) \tag{4.1}$$

where σ represents the effects of all the local fields and it can be either positive or negative. Therefore the resonance condition can be written as

$$h\vartheta = g_e\mu_B H_{eff} \tag{4.2}$$

which can be also represented as

$$h\vartheta = g_e\mu_B H_O(1-\sigma) \tag{4.3}$$

The quantity $g_e(1 - \sigma)$ can be denoted as g and is called the g-factor. The final resonance equation then becomes

$$h\vartheta = g\mu_B H_O(1-\sigma) \tag{4.4}$$

Using this equation the g value corresponding to any ESR experiment can be determined by measuring the field and frequency at which the resonance occurs. The g value of a free electron is approximately equal to 2.002319. If the ratio of the magnetic moment to the angular moment of a system differs from that of a free electron it would imply that the electron in the system has gained or lost angular momentum through the spin orbit coupling as the magnetic moment of an electron is constant, approximately equal to the Bohr magneton. Under any given specific conditions if any system shows a g value different from that of a free electron it implies the difference in the spin-orbit coupling. Hence the change in the g value can also give information on the atomic or molecular orbitals containing the unpaired electrons.

4.1c Resonance peak – to – peak linewidth (ΔH):

The resonance linewidths are measured on the x-axis. It is measured in terms of magnetic induction B or in terms of absorbed applied field. The peak to peak linewidth, ΔH_{PP} (also commonly denoted as ΔH) , can be measured as the full width at half maxima of the resonance spectrum. In the first derivative of the absorption curve, as observed in the ESR, it is measured as the difference between the fields at which the peaks are observed about the centre of the curve which corresponds to zero intensity (figure 4.1). Broadly, the resonance linewidths originate mainly from the relaxation times of the excited electron and also due to the sample imhomogeneities. It is directly connected to the interactions of the spins with their environment and to their motion. Information on the different phase transitions and different competing or coexisting magnetic entities (as in the case of multivalent compounds like manganites) is obtained from ΔH_{PP}.

4.2 Origin of ESR in manganites:

The most common Mn ion observed via ESR is the Mn^{2+} ion (S = 5/2). The Mn^{3+} ($3d^4$ with S = 2) is unlikely to be ESR active as it exhibits a large zero-field splitting and strong spin-lattice relaxation (the ground state of the Mn^{3+} ion is the orbital doublet) [151]. The Mn^{4+} ions ($3d^3$ with S = 3/2) give an ESR signal usually at low temperatures. The manganese ions Mn^{3+} and Mn^{4+}, are commonly seen in doped manganites. Theories suggesting two Mn^{3+} ions transforming into Mn^{2+} and Mn^{4+} ion pairs via thermally excited disproportionation were common [193]. It is generally accepted that manganites do not have, or have a very small ratio of, Mn^{2+} ions and hence do not contribute to the ESR signals exhibited by manganites. ESR signals obtained in La-based manganites have been attributed primarily to Mn^{4+} ions as, in an octahedral anion crystal electric field this has a ground state with a weak spin-lattice relaxation, which makes this ion ESR active even at higher temperatures [171]. Shengelaya *et. al.* [170] attributes the ESR signal to Mn^{4+} in a system of three components: Mn^{4+} ions, Mn^{3+} ions and the lattice, and predicted an FM Curie-Weiss like behaviour for the double integrated line intensity (DI), which is proportional to the static susceptibility, χ_{ESR}, arising from the FM couplings of the Mn^{4+} and Mn^{3+} magnetic subsystems [194]. But the ESR signals cannot be attributed to isolated Mn^{4+} ions. The ESR signal observed in manganites has been assigned to some combination or clusters of Mn^{3+}–Mn^{4+} ions coupled by a strong short-range FM DE interaction [162]. All the Mn ions are assumed to contribute to the ESR signal and the DI is therefore proportional to the number of ESR centres and is also a measure of χ_{ESR}

[175]. If all the Mn ions contribute to the ESR signal then plots of 1/DI vs T should show a linear behaviour in the PM regime. If the spins are ferromagnetically coupled the temperature dependence of the intensity should follow the Curie-Weiss law $(T-\theta)^{-1}$.

4.3 Origin of ΔH in manganites:

Temperature dependence of ESR linewidth, especially in the PM region, has been discussed by many groups proposing different models, to extract the physics from the different behaviours observed for different systems. The region of temperatures just above a phase transition from the PM phase to an ordered phase has always been of interest. In the case of multivalent compounds it has been a challenge to establish the reasons for the magnetic properties exhibited by such compounds and to obtain information about the magnetic entities contributing to it.

Extensive temperature dependent ESR linewidth studies are reported by Castner and Seehra [164], Huber [163], Seehra and Huber [165] and Huber and Seehra [167] in the case of ferromagnets and antiferromagnets. For magnetic systems where the contributing magnetic ions are not isolated but concentrated, various spin–spin interactions are the dominant cause for the observed ESR linewidths. The temperature–dependent ESR linewidths for T > Tc can result from two sources: (1) the phonon modulation of the antisymmetric exchange interaction [164] and (ii) the phonon modulation of the crystalline field being the dominant mechanism for the relaxation of the magnetization as first proposed for the ferromagnet $CrBr_3$ [167] where a linear temperature dependence of the ESR linewidth is observed over an extended temperature range to 500K, well above $T_C \approx 32K$ [168]. This second mechanism is expected to be dominant for non–S–state systems with spin S > 1. For manganates both Mn^{3+} (S = 2) and Mn^{4+} (S = 3/2) are non–S–state ions and, consequently, the situation is similar to that in $CrBr_3$ [167, 168] with S = 3/2 for Cr^{3+} and a linear temperature dependence of the linewidth is expected. As noted in reference 167, a broad band of phonons takes part in the relaxation process, in contrast to the relaxation of an isolated magnetic ion where only narrow bands of phonons with energies comparable to the ionic level splittings are involved in one–phonon processes. This makes the one–phonon relaxation in the concentrated magnetic system far more effective than it is for an isolated magnetic ion. There is no dependence of the EPR linewidth on the microwave frequency for $T >> T_C$ as long as the resonance field << the exchange field. In view of the earlier work on $CrBr_3$ Seehra *et. al.* [169] explained the

linear temperature dependence of ΔH in $La_{0.67}Sr_{0.33}MnO_3$ and $La_{0.62}Bi_{0.05}Cr_{0.33}MnO_3$ for $T > T_C$ in view of spin–phonon coupling.

Shengelaya *et. al.* [170] proposed the ESR signal observed in $La_{(1+x)}Ca_xMnO_{(3+y)}$ to be primarily due to Mn^{4+} ($3d^3$ with S = 3/2) ions. In an octahedral anion crystal electric field this ion has a ground state, corresponding to an orbital singlet A_2. As a consequence the spin–lattice relaxation gets weak, and this makes ESR of Mn^{4+} easy to observe even at high temperatures [171] As the Mn^{3+} ($3d^4$ with S = 2) exhibits a large zero–field splitting and strong spin–lattice relaxation (the ground state of the Mn^{3+} ion is the orbital doublet) an ESR signal is unlikely to be observed [150]. But the observed signal cannot be attributed to isolated Mn^{4+} ions. A model of paramagnetic centers responsible for the ESR signals is constructed considering the fact that doped manganese perovskites are mixed valence compounds with Mn^{4+} and Mn^{3+} ions which are strongly FM DE interacted. The authors attribute the observed characteristic difference in ESR intensity and linewidth in $La_{(1-x)}Ca_xMnO_3$ (x = 0.1, 0.2) ceramic samples to three components: Mn^{4+} ions, Mn^{3+} ions and the lattice. They ascribe the ESR results of variation in intensity and linewidth to the bottleneck model in which a spin relaxation takes place from the Mn^{4+} ion, via the Mn^{3+} J–T ion, to the lattice.

Rettori *et. al.*[172], from their ESR studies on $R_{(1-x)}B_xMnO_{3-\delta}$ (R = La,Pr; B = Ca,Sr) in the PM phase i.e. $1.1T_C \leq T \leq 2T_C$, a linear T increase of the resonance linewidth, ΔH, in powders, ceramic pellets, and single crystals is observed. The temperature dependence of the data till ~ $2T_C$ is attributed to the one–phonon process resembling results in other FM insulators involving spin–lattice relaxation. Above ~ $2T_C$ a slowdown in the T increase of ΔH is associated to the Debye temperature. The large T dependence of the resonance intensity above T_C found from these studies suggests the existence of “spin clusters” in these compounds over a wide range of temperature. In a similar manner Oseroff *et. al.* [162] too observed a linear temperature dependence of ΔH from their studies on $La_{0.67}Ca_{0.33}MnO_{3+\delta}$. In their studies they also confirmed that the ESR signal cannot be attributed to any single Mn ion of any valance state i.e. Mn^{2+}, Mn^{3+} or Mn^{4+}, and conclude that the ESR signal occurs due to contributions of some complex magnetic entity from a collection of Mn^{3+} and Mn^{4+} ions.

Lofland *et. al.* [173] reported the ESR studies on a single crystal of $La_{(1-x)}Sr_xMnO_3$ (x = 0.1, 0.2, 0.3). They consider the ΔH variation well into the PM r egion, i.e. much above the T_C, to avoid the anomalies that occur in ΔH when the T C is approached. The linear increase in ΔH with temperature above T_C is attributed to spin–lattice relaxation

involving a single phonon. The narrowing of the ESR line and the reduction in rate of increase of ΔH with T can be ascribed to the pseudo–cubic system formed with increasing Sr, the increase the Mn^{4+}/Mn^{3+} ratio or an equivalent broadening of the bandwidth and making the J–T interaction more dynamic. They also concluded that all Mn spins contribute to the ESR signal.

Gundakaram *et. al.* [174] reported temperature dependent ESR studies on PM phase ($T > T_C$) of $Pr_{0.7}Sr_{0.3-x}Ca_xMnO_3$. With decreasing temperature the linewidth decreases linearly, reaching a minimum (T_{min}) just above ~T_C. As *x* increases T_{min} shows a monotonic decrease. The linewidth data can be fit to a straight line in the temperature range $1.1T_C < T < 2T_C$. For $T > 2T_C$ the ΔH variation deviates from linearity. The authors suggested the possibility of thermal expansion of the grains at higher temperature which causes a decrease in the dipolar interactions and thus slows down the increase of ΔH with increase in temperature, causing a deviation from linearity. In the FM region, the critical ‘‘slowing down’’ of the spin fluctuations is suggested to increase the linewidth with decreasing temperature. A distribution of the demagnetization factors due to the irregular crystallite shapes in the polycrystalline samples are also found to contribute to the increase in ΔH.

The work by Causa *et. al.* [175] have led to the understanding that all Mn spins contribute to the resonance in perovskite compounds $A_{0.67}M_{0.33}MnO_3$ (A = La, Pr, M = Ca, Sr). They too have considered the temperature dependence of ΔH for $T > T_C$ as from a temperature T_{min} just above T_C anomalies in ΔH are evident which are purely sample and field dependent and could lead to confusing interpretation of results. The authors find their results to agree with the model suggested by Dormann and Jaccarino [176], using Huber’s approach [177] considering the single ion susceptibility and the susceptibility arising from the PM behaviour of a coupled system, in this case the FM coupling of Mn^{3+} and Mn^{4+}. They conclud that the ΔH variation for $T > T_C$ arises due to a single relaxation mechanism, related to spin–spin interactions, with no evidence of spin–phonon contribution.

Ivanshin *et. al.* [178] reported the ESR study in single crystal of $La_{(1-x)}Sr_xMnO_3$ *(*$0 \leq x \leq 0.2$*)*. The deviations of temperature dependent ΔH from a monotonic behaviour is identified with different magnetic and structural phase transitions. The sudden increase of ΔH at T_N is ascribed to the transition from a PM phase to a magnetically ordered phase. An extensive study of the ΔH variation in the PM regime is conducted. A change in the

behaviour of the linewidth in relation to temperature dependent structural transition is observed. They ascribed the linear increase in linewidth for the compositions with 0.075 $\leq x \leq 0.15$ to the spin lattice relaxation and quasilinear behaviour of ΔH for $x > 0.15$ to Heisenberg–like interaction for Mn^{3+}–Mn^{4+} spin pairs.

Hu [179] has given a rigorous derivation of linewidth of DE interaction systems from fundamental mechanisms. Considering the spin correlation caused by DE interaction, SE interaction between manganese ion and anisotropic energy of spins caused by crystal field, the linewidth is found to be approximately proportional to the temperature. At the low temperature end near T_C, there is a minimum below which the linewidth increases sharply. The author claims it to be universal.

Huber and Seehra have applied the theoretical treatment of ESR line broadening and spin – spin relaxation near critical points to the PM state of various ferromagnets and antiferromagnets [166, 167]. Critical exponents describe the behaviour of the physical quantities near continuous phase transitions. They depend on the dimension of the system under consideration, the range of interaction and the spin dimension. Phase transitions occur at a critical temperature, T_C. The phases above and below the critical temperature are characterized by an order parameter, which is a quantity that is zero in one phase (usually above the critical point) and non zero in the other phase. Introducing a reduced temperature given by $\tau = (T - T_C)/T_C$, which is zero at the phase transition, the critical exponent, *k*, can be defined as $f(\tau) \alpha \tau^k$, $\tau \approx 0$, where *f* is a physical quantity in terms of a power law around critical temperature. A direct relationship between spin–spin relaxation time and ESR linewidth has been established.

It has been established that as the temperature approaches T_N from the high temperature region the ESR linewidth for a uniaxial antiferromagnet [180] broadens and narrows for a cubic antiferromagnet [181]. This anomalous behaviour has been explained theoretically by Tomita and Kowasaki [182] and Huber [167]. The anomalies in the temperature dependence of the ESR linewidth result from a coupling between long wave fluctuations in the order parameter and the fluctuations in the total magnetization. The coupling is a result of the presence of anisotropic terms in the Hamiltonian describing the spin system. The temperature induced changes in the ESR linewidth is calculated using this approach and is given by

$$\Delta H(T) = \Delta H_{\infty} + A\left(\frac{T}{T_N} - 1\right)^{\gamma} \qquad (4.5)$$

where ΔH_∞ is a temperature independent contribution, A is a constant describing the magnitude of the critical coupling and γ is the critical exponent. The critical exponent is estimated from the slopes of the log–log plots of$\Delta\ H_T = (\Delta H - \Delta H_\infty)/\Delta H_\infty$ versus $(T - T_N)/T_N$, where $(T - T_N)/T_N = \tau$, which is the reduced temperature. The theory [166] predicts a critical exponent of -5/3 for uniaxial antiferromagnets and -7/2 for ferromagnets.

4.4 Understanding Ordered States in Manganites : Some Prominently Used Models

4.4a Zener Polaron Model :

The first theoretical models to understand manganites were designed focusing on the experimental data of conductivity and magnetic measurements, relating the two studies wherein stating that the polarization of spins lead to increase in conductivity. The concept of DE proposed by Zener [21, 22], was one of the first models used to interpret results in manganites. The model proposed the movement of charges by the generation of a spin polarized state. The DE process has been described in two different ways. One was considering Mn and O ions in a linear Mn^{3+}– O – Mn^{4+} formation. It involves the simultaneous motion of an electron from the oxygen to the Mn^{4+} ion and the motion of the electron from the Mn^{3+} to the oxygen ion. The second, proposed by Anderson and Hasegawa [23], involves a second- order process where the two states mentioned earlier are reached through an intermediate Mn^{3+} – O – Mn^{3+} state. The effective hopping is proportional to the square of the hopping involving the p- and d- orbitals of oxygen and manganese respectively, and also to cos(θ/2) where θ is the angle between the nearest neighbour spins. But DE alone could not explain the AFM ordering observed in manganites. de Gennes [24] used mean field approximations and suggested the transition from an AFM state to an FM state through a canted spin state, where the spins develop a moment in one direction while most spins in the plane perpendicular to the moment are antiparallel. Even in any low doped manganite where this concept is used more commonly, the origin of the canted state needs to be looked into for more clarity.

4.4b Goodenough Model:

Goodenough, along with Loeb [25, 183], proposed a model where the covalent bonding influenced lattice distortions and indirect magnetic exchange interactions

between two magnetic cations separated by an anion to interpret the different results obtained and phenomena exhibited (especially the CO state) in manganites. They termed this magnetic interaction as semicovalent exchange, which was similar to the superexchange mechanism proposed by Kramers and later used by Anderson and Vleck [184]. The one major difference was that in the predictions made in some oxides (e.g. perovskite-type manganites) using the two were entirely contradictory. The model is based on the overlap of the occupied and unoccupied d-orbitals in the 180^{o} Mn – O – Mn bond unit with at least one member of the Mn pair an Mn^{3+} ion. Due to steric hindrances in a close–packed lattice the stable cation orbitals may not overlap with the neighbouring anion orbitals and the empty cation orbitals may not contribute to the state of electrons in the solid and hence they assume the bonding to be ionic. Whereas if the stable empty orbitals overlap with the anion p orbitals the electrons spend some time in the cation orbitals too, the time being dependent on the stability of the orbitals. Now considering the full anion p orbitals (which contain two electrons of opposite spins) overlapping the empty cation orbital, each electron has equal probability to be shared by the cation. But if the cation has a net moment then the electron with the spin parallel to the net cation spin spends more time on the cation, which is in accordance to the Hund's rule. As a single electron plays a decisive role in this bonding, it is called semicovalent. Hence semicovalent bonds are formed below Curie temperature where the cation magnetic moment is oriented with respect to the spin of the net cation spin. Semicovalence occurs when there is a strong overlap of stable, empty cation orbitals and an anion p orbital. The model of Mn – O bonding and the Mn – Mn magnetic exchange is outlined to use this concept to interpret results of studies on manganites. The Mn – O bonds are covalent or semicovalent if an empty manganese orbital points toward the O^{2-} ion, an ionic bond if the empty Mn^{3+} - (dsp^2) orbitals point away from the O^{2-} ion and a metallic- like bond if the O^{2-} ion is between a Mn^{3+} and a Mn^{4+} ion in a lattice of disordered Mn^{3+}, Mn^{4+} ions. The four Mn – O – Mn bonding arrangements are also discussed. If both the Mn – O bonds are covalent, the Mn–Mn separation is the smallest and the cations couple antiferromagnetically below T_C, the transition temperature from the semicovalent bonds to the covalent bonds. If only one Mn – O bond is covalent, below the covalent-admixed transition one bond is ionic and the other is covalent. The Mn – Mn separation is greater than that in the previous case and the O^{2-} ion is displaced toward the Mn ion with which it forms the covalent bond. Below T_C the covalent bond becomes semicovalent and the net magnetic moment is associated with the O^{2-} ion. If neither Mn – O bond is covalent both the bonds are ionic, the Mn- Mn separation is the largest and no indirect magnetic exchange exists. If the anion separates the FM couples Mn^{3+} and Mn^{4+} ions the Mn^{3+} - O -

Mn^{4+} state is degenerate with the Mn^{4+} - O – Mn^{3+} state. Below T_C DE occurs through the metallic-like bond. These predictions are in contrast to those obtained by the SE model as in the SE model the cation s and p orbitals are considered irrelevant. Only one anion electron excites at a time so that two magnetic ions on either sides of the anion couple antiparallel to the net cation spin if the d-shell is half or more filled and parallel if the d-shell is less than half full. According to the SE model a manganite of the formula $A_{(1-x)}B_xMnO_3$ (A = La, Nd etc. B = Ca, Sr etc.) should always be ferromagnetic with lowest resistivity for x = 0.5, which is not the case. Depending on the doping levels, which in turn can alter the Mn^{3+}/Mn^{4+} ratios the magnetic structures can be decided. With increasing Mn^{4+} concentration the system can become more antiferromagnetic and change from a A-type (ferromagnetic sheets coupled antiferromagnetically) to C-type (ferromagnetic rods coupled antiferromagnetically) to G-type (all five Mn – Mn neighbours antiferromagnetically coupled) structure and exhibit other exotic structures like CE-type (antiferromagnetic arrangement of ferromagnetic Mn zig-zag chains) too. These kinds of ordered distribution of the Mn^{3+} and Mn^{4+} ions is used to understand and explain the CO state in manganites in the Goodenough model. It also highlights the importance of the structural distortions on other properties of manganites.

4.4c Bond Valence Model:

According to the Bond valence model [185] (a model that is not commonly quoted while studying the CO state of manganites), an Mn^{3+}/Mn^{4+} CO should result in the setting up of MnO_6 octahedra with very different average Mn-O distances. In the half-doped Mn perovskites, the BVM calculations, which are structure refinements carried out from diffraction data, do not confirm this expectation. Hence, these structure refinements can be interpreted as if there was a partial CO of the type $Mn^{+3.5+\delta}/Mns^{+3.5-\delta}$. In this model the refined structure shows that half of the Mn sites are in elongated oxygen octahedra. These sites are considered as Mn^{3+} ions because they present a J-T-like distortion.

4.5 Charge ordered (CO) state of manganites:

From the Goodenough model, in an ionic picture, the CO state observed in perovskite structured Mn – oxides, is understood as a spatially ordered distribution of Mn^{3+}/Mn^{4+} ions in the lattice which is accompanied by orbital order (OO) which is an ordered occupation of the e_g ($d_{3r^2-z^2}$ or $d_{x^2-y^2}$) orbitals. It is accepted that the driving forces for CO/OO are the minimization of both the Coulomb repulsion (when CO

appears) and the strain energy, due to the strong J–T effect of Mn^{3+} ions (when OO is present). A more realistic scenario for the CO state in manganites has been presented using the concept of the Zener polaron where each e_g electron is trapped in a Mn–O–Mn trio instead of in a single Mn ion. The two Mn ions involved in the trio conserve an intermediate valence state and are FM DE interacted due to the shared e_g electron [186 – 188]. Daoud-Aladine *et. al.* [186, 188], from their analysis of x-ray and neutron diffraction data on $Pr_{0.6}Ca_{0.4}MnO_3$ single crystals have found differences of the Mn^{3+}/Mn^{4+} CO pattern from the Goodenough model. The intermediate valence state for the Mn atoms in this structure is confirmed by the similar Mn – O distance of the two Mn sites, agreeing with the suggestion of an intermediate valence state for Mn at all temperatures in the half doped CO manganites [189].

Exploring the reasons for the charge localization for an intermediate valence state of Mn it is suggested that at low temperatures the elongation of pairs of Mn_1O_6 and Mn_2O_6 octahedra along the same direction (where 1 and 2 denote the long and short Mn – O distances respectively) and the off – centering of Mn_1 and Mn_2 occur, which in turn suggest Mn_1 – Mn_2 dimerization. This is accompanied with the widening of the Mn_1 – O – Mn_2 angle. The widening of this angle can easily delocalize the extra electron per pair of core Mn^{4+}. This fast electron transfer, which leads to the formation of Mn-Mn dimers, was proposed by Zhou and Goodenough [190] and called this dimer a 'Zener polaron' (ZP) because the easy delocalization can be associated to the DE Zener mechanism that ferromagnetically couples both Mn ions in the pair. The LT refined structure of the $Pr_{0.6}Ca_{0.4}MnO_3$ crystal, is viewed as a commensurate Zener polarons ordering (ZPO). The structural distortion favouring a local DE process assures the stability of the ZPO structure.

Daoud-Aladine *et. al.* [186, 188] study the magnetic susceptibility of the crystals and interpret the anomaly observed at T_{CO} while samples are in a PM state. That the magnetic correlations vary from FM to AFM type on lowering the temperature below T_{CO} is well understood in terms of the proposed ZPO model [191, 192]. They attribute the FM correlations at high temperatures as a consequence of a disordered and dynamic DE. According to the Goodenough model the disappearance of these correlations is not due to the diminishing of DE but due to the emergence of AFM correlations because the ZPO changes the nature of the PM units. Below T_{CO} the new units are FM pairs and hence the effective moment is also modified. The emergence of AFM correlations below T_{CO} is confirmed from the decrease in the Curie Weiss temperature, θ, from that above T_{CO}.

The authors deduced the values of the effective magnetic moment from their experiments. Above T_{CO}, there are N sites of PM ions of effective moment $\mu_{eff} = 4.41\mu_B$. ZP formation should lead to N/2 new elemental PM units of effective moment $\mu_p = 7.94\ \mu_B$ (S = 7/2). Hence it is predicted that the Curie constant $C = N/2\ \mu_{eff}^2 k_B$, increases by a factor given by $C_{LT}/C_{HT} = 1.62$, where C_{HT} and C_{LT} are the Curie constant above T_{CO} and between T_{CO} and T_N respectively. They confirmed the validity of these values and hence the ZP model by conducting magnetic measurements on $Y_{0.5}Ca_{0.5}MnO_3$ and found $C_{LT}/C_{HT} = 1.51$ which is very close to the predicted value.

Recently the concept of coexistence of different magnetic phases, also known as phase separation, has been used for understanding the properties of manganites. In the present work coexistence of electronic phases has been detected from ESR data on various compositions of Bi – manganites.

4.6 ESR studies on $Bi_{(1-x)}Ca_xMnO_3$ (BCMO)

Figures 4.2a and 4.2b show the temperature dependent ESR spectra of the BCMO (*x* = 0.4, 0.45, 0.5, 0.6, 0.7, 0.75) system. The intensity of the spectra increases as the temperature is decreased from high temperature. On approaching room temperature the intensity reaches a maxima below which a decrease in intensity begins. With further decrease in the temperature the intensity begins to increase or decrease, depending on the composition. Below a certain temperature the intensity decreases rapidly, signifying a PM – AFM transition.

The g value estimated for various compositions of the samples is ~ 2. In spite of variation in the intensity and peak to peak linewidth, the broad resonance lines can be fitted by a lorentzian line shape in the entire temperature range (figure 4.3) following the equation

$$\frac{dP}{dH} = \frac{d}{dH} A\left[\frac{\Delta H}{4(H-H_O)^2+\Delta H^2} + \frac{\Delta H}{4(H-H_O)^2-\Delta H^2}\right] \qquad (4.6)$$

where ΔH is the full width at half maximum intensity, A is the area under the absorption curve and H_O is the resonance field. The line intensities modified by the size effects of the samples used can be approximately given by the equation

$$I = \eta \chi_{ESR} \omega Q_L (1+b)^{-1/2} \qquad (4.7)$$

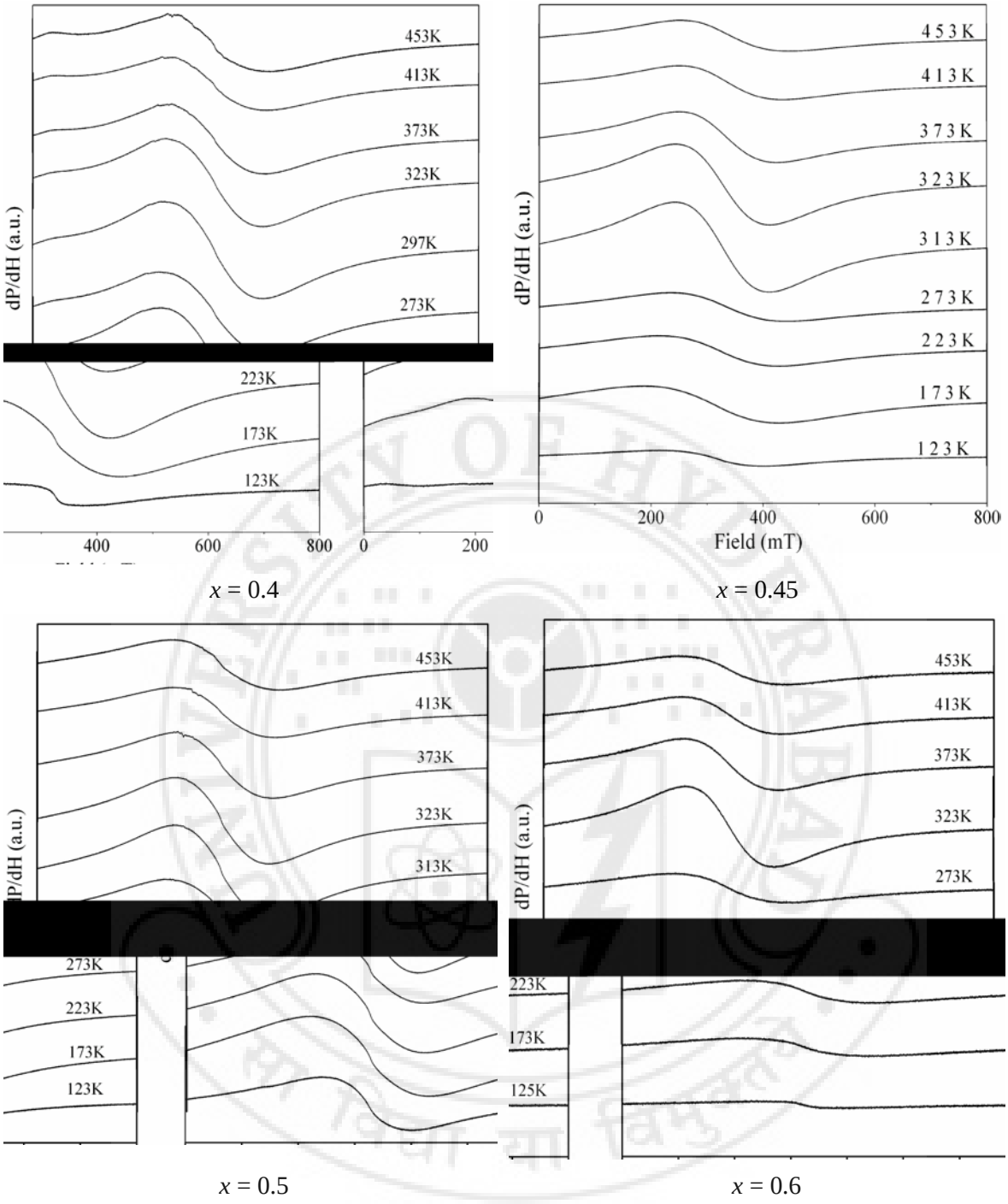

Figure 4.2a Temperature dependent ESR spectra of the $Bi_{(1-x)}Ca_xMnO_3$ system (x = 0.4, 0.45).

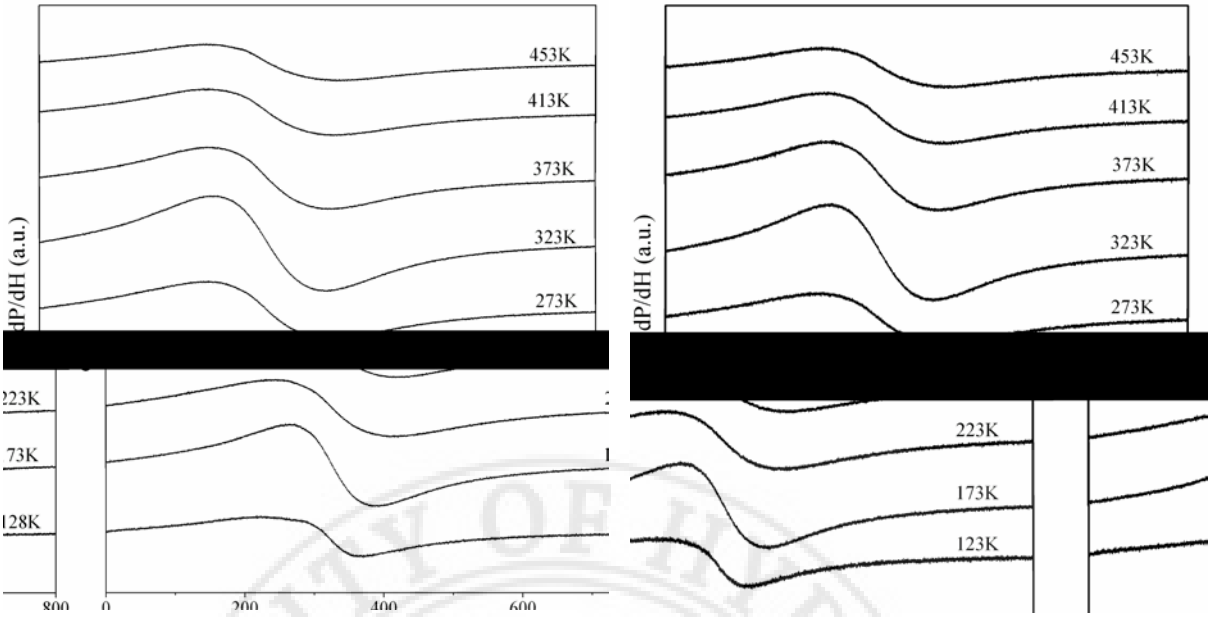

x = 0.7 x = 0.75

Figure 4.2b Temperature dependent ESR spectra of the $Bi_{(1-x)}Ca_xMnO_3$ system (x = 0.5, 0.6, 0.7, 0.75).

with

$$b = \frac{\left(\frac{4\pi}{3}\right)\eta Q_L \chi_{ESR} \omega}{\gamma \Delta H_{pp}} \qquad (4.8)$$

where χ_{ESR} is the static susceptibility corresponding to the resonant species, η is the filling factor, Q_L is the loaded Q of the microwave cavity, ω is the microwave frequency and ΔH_{pp} is the peak to peak linewidth.

The reliability of the spectra is first examined by checking: (1) for overloading of the cavity which could lead to erroneous recording of the resonance spectra and (2) for any skin depth effect of the samples. To ensure that no overloading of the cavity took place the ESR spectrum of a small known quantity of sample was recorded at high amplitude. The absence of clipping of the peak of the resonance lines confirmed that no overloading of the cavity occurred.

The theoretical fit as per equation (4.6) to the data is shown in figure 4.3. This confirms that the size of the samples is smaller than the skin depth of the penetrating microwaves. Hence any change seen in the intensity or peak linewidth is purely an

intrinsic property of the sample and not due to skin depth effects. The skin depth is also estimated using the

$$\delta = \left(\frac{\rho}{\mu_o \omega}\right)^{0.5} \tag{4.9}$$

where ρ is the resistivity at room temperature, μ_o is the permeability of free space given as 4 π x 10^{-7} Vs/Am and ω is the microwave frequency = 2 π x 9 GHz. The calculated values of skin depth for different samples are given in the table 4.1. The skin depth varies between 0.256 and 1.434mm which is larger than the sample size. Hence it is confirmed that any change observed in the ESR spectra is only due to the intrinsic behaviour of the sample.

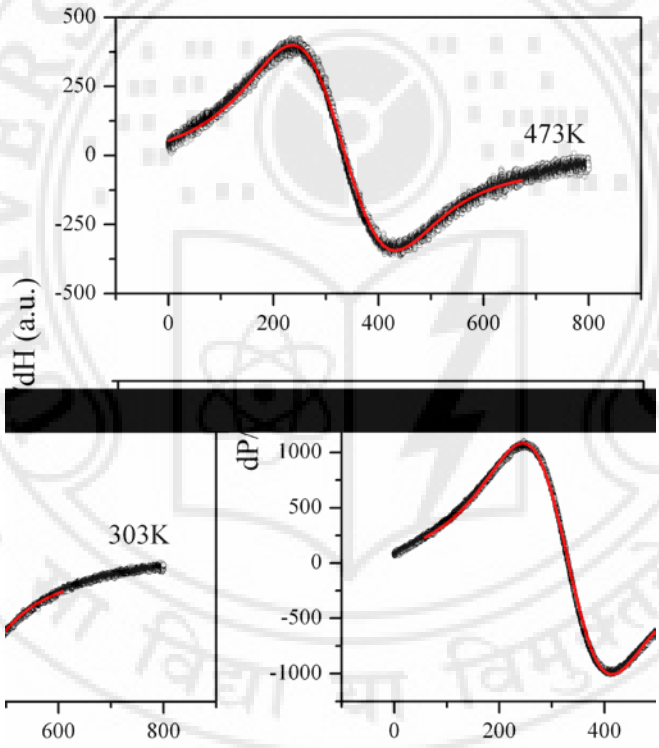

Figure 4.3 Representative figure of Lorentzian fits (solid red line) to the ESR experimental data for $Bi_{(1-x)}Ca_xMnO_3$ at two temperatures.

All the Mn ions are assumed to contribute to the ESR signal and DI, therefore, should be proportional to the number of ESR centres and is a measure of χ_{ESR} [175]. The DI (χ_{ESR}) v temperature plots for the BCMO (x = 0.4, 0.45, 0.5, 0.6, 0.7, 0.75) system are presented in figure 4.4. It can be noticed that on cooling from high temperature, there is an increase in

Sample (x)	T_{CO} (K)	T_N (K)	ΔE (ESR) meV
0.4	301	163	84
0.45	313	153	114
0.5	317	160	163
0.6	316, 290, 250	148	88
0.7	323, 290, 250	150	78
0.75	323, 290, 250	148	74

Table 4.1 The skin depth values for the $Bi_{(1-x)}Ca_xMnO_3$ system

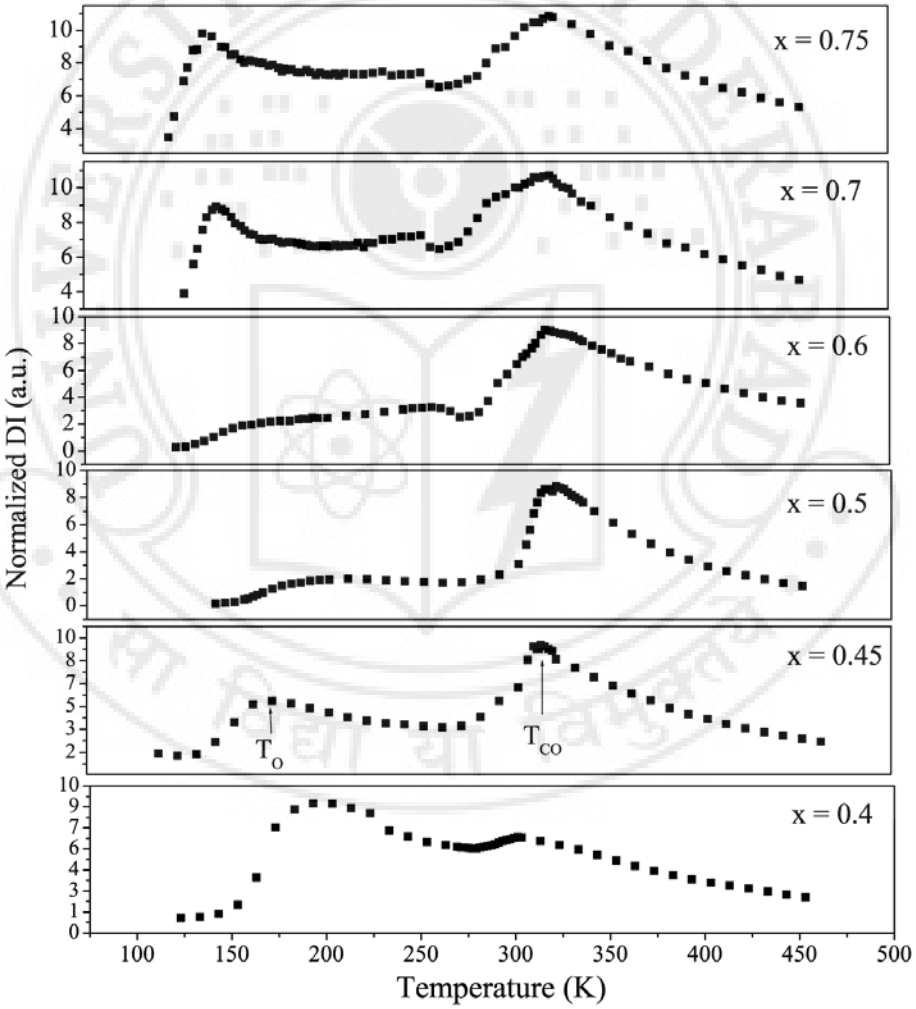

Figure 4.4 DI versus temperature plots for the $Bi_{(1-x)}Ca_xMnO_3$ system.

DI reaching its maximum value. There are two peaks in the plot. The peak at higher temperature is assigned to the charge ordering temperature, T_{CO}, and the peak at lower

temperature indicates the onset of AFM state, T_O. According to these results the charge-ordered (CO) state is paramagnetic (PM). There is a sharp decrease in DI below ~135 – 190K (depending on the composition) until the ESR signal becomes very weak indicating the long-range AFM state. For the samples with $x \geq 0.6$ the main CO peak is accompanied by two minor peaks at 290K and 250K, indicating the formation of two additional minor phases in these samples.

If all the Mn ions contribute to the ESR then the plot of 1/DI versus T show a linear behaviour in the PM regime. If the spins are ferromagnetically coupled, the temperature dependence should follow the Curie – Weiss law, $(T - \theta)^{-1}$, where θ is the Curie 0 Weiss temperature. Figure 4.5 shows the 1/DI v T plots for the BCMO system. There is lack of linearity in Curie – Weiss behaviour of 1/DI above T_{CO} until high temperature is reached. A linear fit is obtained above a temperature where 1/DI departs from high temperature Curie–Weiss law. The positive value of Curie–Weiss temperature θ indicates FM interactions at high temperatures.

According to the cluster model [162, 163], for temperatures above any ordering temperature the DI of the resonance line is given by the Arrhenius equation

$$DI = I_O exp\left(\frac{\Delta E}{k_B T}\right) \quad (4.10)$$

where DI is the double integrated intensity extracted from the resonance line, I_O is a fitting parameter and ΔE is the thermal activation energy for the dissociation of the FM spin clusters. This model suggests that the ESR signals cannot be attributed to an individual Mn ion of any valency i.e. Mn^{2+}, Mn^{3+} or Mn^{4+} or to some complex entity formed by a combination of Mn^{3+} and Mn^{4+} ions in the form of clusters which could be FM DE interacted. The ΔE value can provide the magnetic nature of these clusters. A high positive value can indicate contributions of FM clusters. A decrease in the Δ E would either suggest a decrease in the contributions of FM clusters or the emergence of AFM clusters. This could also suggest the coexistence of competing FM and AFM magnetic phases.

The plots of ln DI versus 1000/T can provide direct information about the different magnetic phases formed in the sample as a function of temperature. The change in the activation energy values will give information about the strength of the magnetic phases that form or emerge [163]. The ln DI versus 1000/T plots for the BCMO system are

shown in figure 4.6. The values of ΔE are given in table 4.1. The activation energy shows a peak at x = 0.5 beyond the substitution of which there are two different phases. With the enhancement of the second phase the activation energy decreases indicating lesser energy for the Mn^{3+} - Mn^{4+} hopping of small polarons. The linear dependence of ln DI in the high temperature range indicates short-range FM correlations. The deviation from linear behaviour at $T > T_{CO}$ indicates the emergence of AFM correlations. The sign of the slope

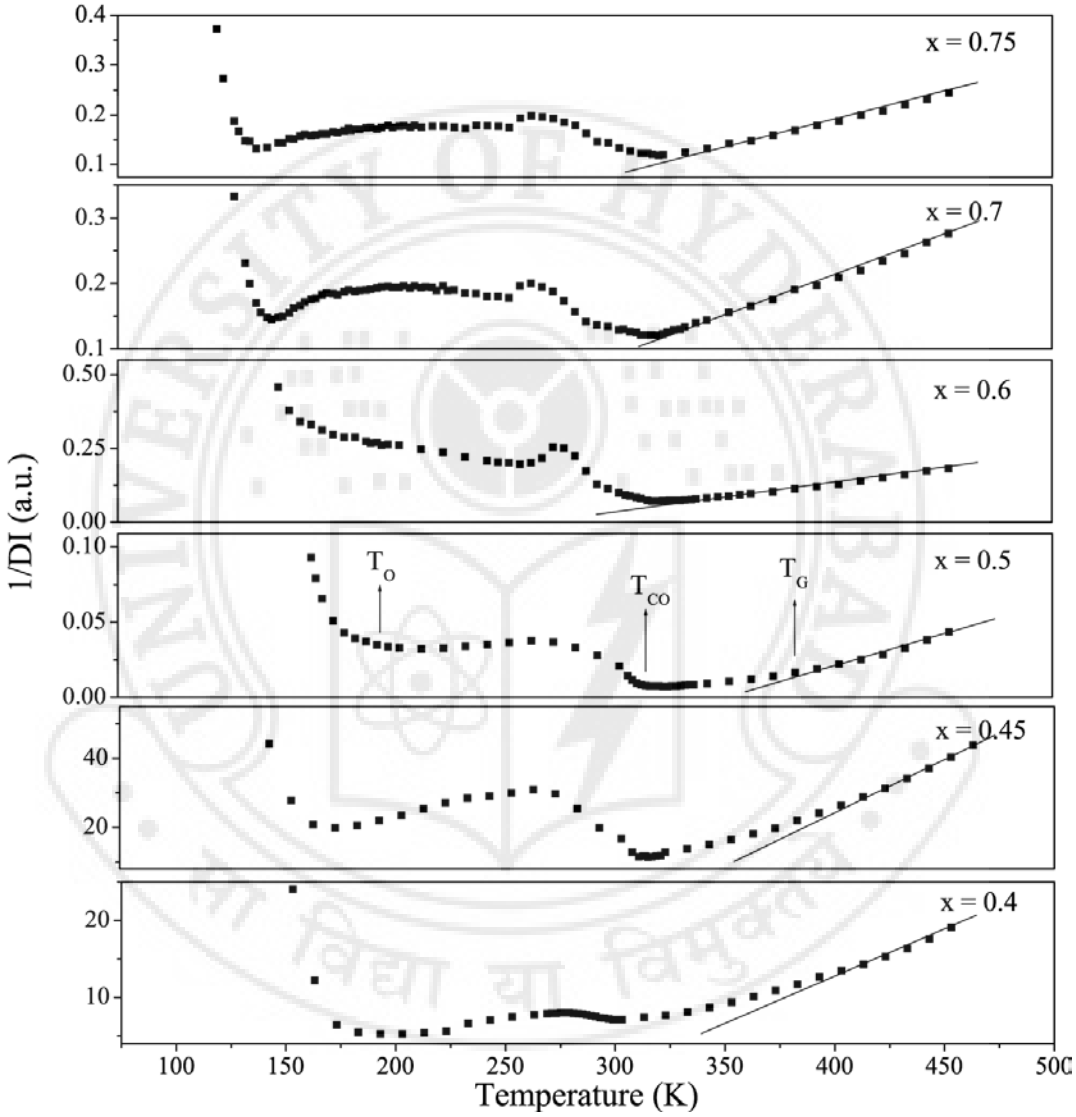

Figure 4.5 1/DI (χ_{ESR}) versus T plots for the BCMO system.

of the plots changes at T_{CO}. In the CO state too a linear behaviour of ln DI is observed. The slope of this linear fit decreases with increasing x value. It becomes negative for the sample with x = 0.6. This indicates the weakening of FM correlations and evolution of AFM clusters on cooling from the high temperature PM state to PM + CO state. The

AFM correlations increase with increasing Ca content. A sharp change in the sign of slope below ~135 – 190 K (depending on the composition), indicating $T_{O,}$ is observed. The samples go into the AFM state below T_O where ln DI becomes temperature independent, presumably due to the existence of FM inhomogeneities embedded in the bulk AFM state. In the PM + CO state, for the samples with x = 0.7 and 0.75, ln DI v T curves exhibit an upward curvature till T_O implying the re-emergence and continuous strengthening of the FM correlations with decrease in temperature. This is due to the presence of minor phases having lower T_{CO} of 290K and 250K. The transition from the PM to PM + CO phase in these samples maybe due to the decrease in the temperature with no change in the strength in the FM interactions.

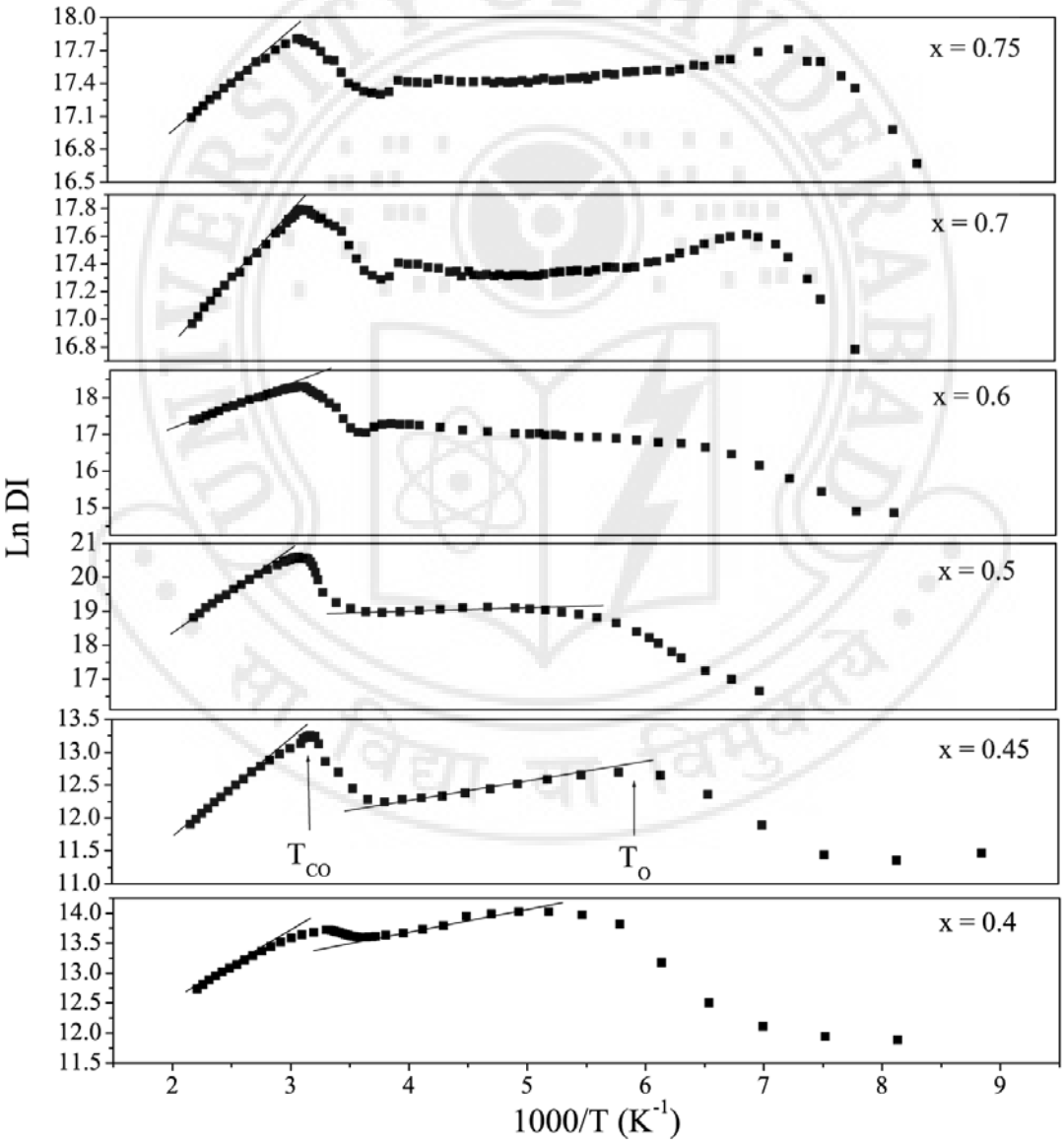

Figure 4.6 ln DI versus 1000/T plots for the BCMO system.

In the temperature range $T > T_{CO}$, the DI follows the Arrhenius equation (4.10) indicating FM correlations which can be attributed to activated $Mn^{3+} – Mn^{4+}$ hopping of a small polaron. In the temperature range $T_{CO} > T > T_N$, charge ordering decreases FM correlations and the AFM correlations strengthen. The domains of FM and AFM spin correlations coexist in this temperature region. The contribution of AFM correlations progressively increase with the increase in Ca content The sharp decrease in ln DI at a lower temperature indicates the onset of long-range AFM order. For $T < T_N$, the temperature independent ln DI indicates the freezing of FM inhomogeneites in the AFM long-range ordered state. The values of T_{CO} and T_N are recorded in table 4.1. The values are very close to the values obtained by other techniques [91, 99].

Figure 4.7 shows the variation of the peak to peak linewidth (ΔH) with temperature. In the temperature range $T > T_C$, ΔH increases linearly with increase in temperature. In the charge ordered state, $T_N < T < T_{CO}$, the ΔH first increases, remains a constant over a temperature range and again increases for samples with $x \leq 0.6$ and decreases for samples with $x \geq 0.7$ with decrease in temperature. The ΔH decreases sharply below T_N for samples with $x \leq 0.6$. The ΔH increases for sample with $x \geq 0.7$ below T_N. The opposite behaviour for these samples is because of the exchange narrowing effect of the dominant FM correlations in this temperature range. The temperature dependence of ΔH in the temperature range $T < T_{CO}$ is completely different from other manganites as summarized in the section 4.5 of this chapter.

The linear temperature dependence of linewidth in the temperature range $T > T_{CO}$ and the sharp upturn at T_{CO} observed in this study can be explained in view of the theoretical treatment given by Hu [179]. The present study does not have data in an extended high temperature range to check the validity of other predictions of the model such as downward bending and $(T/T_C)^{1/2}$ temperature dependence of linewidth in high temperature range. The ΔH temperature dependence for $T < T_{CO}$ in charge ordered state remains unexplained by this theoretical treatment. The ΔH variation of the ESR data for the BCMO system is analyzed for the $T_N < T < T_{CO}$ temperature range for the samples x = 0.4, 0.45, 0.5 and 0.6. The log–log plots of $\Delta H_T = (\Delta H - \Delta H_\infty)/\Delta H_\infty$ versus $(T - T_N)/T_N$, where ΔH_∞ is the constant linewidth, drawn to estimate the critical exponent for the present system, are shown in figure 4.8. The critical exponent varies from −0.73 to −1.12 depending on the composition of the sample in the temperature range $\varepsilon < 0.25$, where $\varepsilon = (T - T_N)/T_N$ [205].

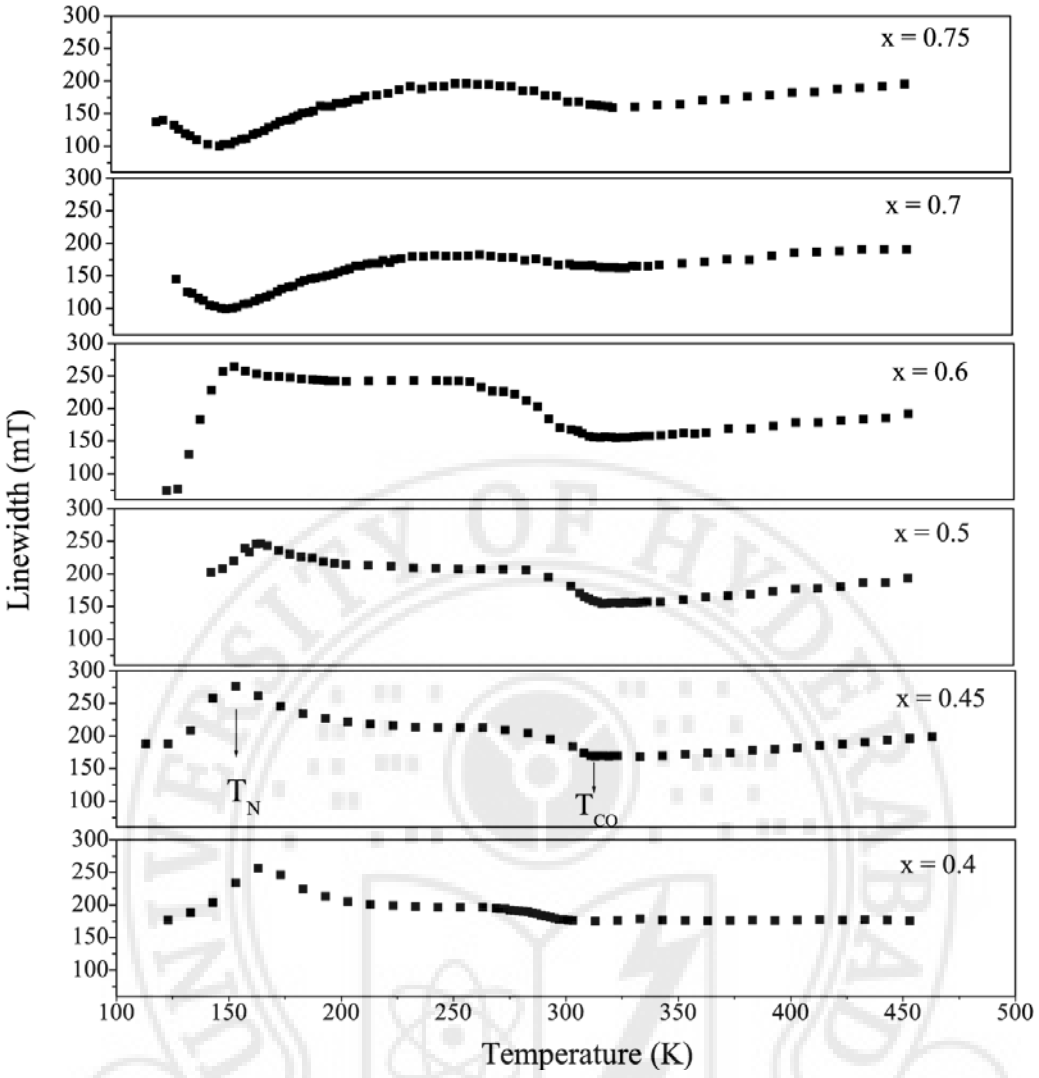

Figure 4.7.Variation of ΔH with respect to temperature for the BCMO system.

The temperature dependence ofΔ H in the range $T_N < T < T_{CO}$ can be due to the phase segregation in view of GP formation. The sharp increase in H occurs whenever there is transition from PM to an ordered magnetic state. Therefore, the sharp increase in ΔH at T_{CO} from the minimum value may be due to the formation of AFM clusters as the temperature is decreased. Since the orbital ordering evolves progressively with decrease in temperature, another sharp increase inΔ H occurs when the AFM clusters form a long-range AFM order at T_N. The sharp decrease inΔ H as temperature decreases below T_N is due to the existence of FM nanoclusters embedded in the AFM matrix of the sample. The gradual increase in ΔH with decrease in temperature and the peaking effect has also been reported in other manganites [206] and one-dimensional antiferromagnets [207]. It is now well known that in manganites there is a strong interplay of spin, charge and orbitals making it difficult to assign the observed variation in ΔH to any one single factor.

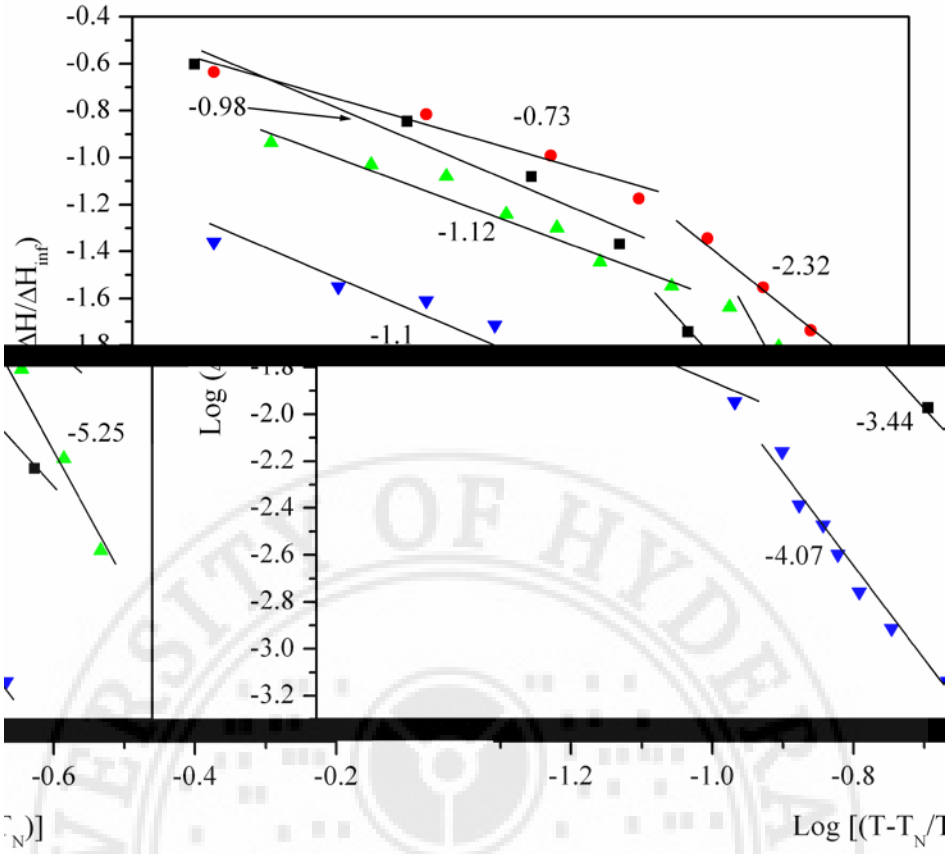

Figure 4.8 Log–log plots to estimate critical exponents for the x = 0.4, 0.45, 0.5 and 0.6

4.7 Magnetization studies on the BCMO system

Figure 4.9 shows the magnetization data of the BCMO system, plotted as magnetic moment per unit mass versus applied field. The data is taken for a maximum field of ±1Tesla at 300K. The slope of these plots provide the susceptibility, χ_{dc}. The value of the Curie constant is estimated using the relation χ_{dc} = C/T, where C is the Curie constant and T is the temperature, which is room temperature in this case. Figure 4.10 represents the variation of the Curie constant with composition. The values of the Curie constant vary between 2.36 and 3.18 emu/mol for the samples, indicating a weak composition dependence. The value of 3.17 emu/mol for the sample with x = 0.5 is close to the value of 2.9 ± 0.1 emu/mol reported by Tzankov *et. al.* [139] and 3 ± 0.1 emu/mol by Bokov *et. al.* [77]. The variation of the magnetic moment or Curie constant can be attributed to the variation in FM correlations. All the samples are in the CO state at room temperature. As the CO state favours AFM correlations, the magnetization data for samples with T_{CO} closer to room temperature can be lowered as the AFM correlations begin to contribute to the magnetic interactions below $T < T_G$. This in turn can be due to the changes in the Mn^{3+}/Mn^{4+} ratio with composition. The effective magnetic moments of the ions are given

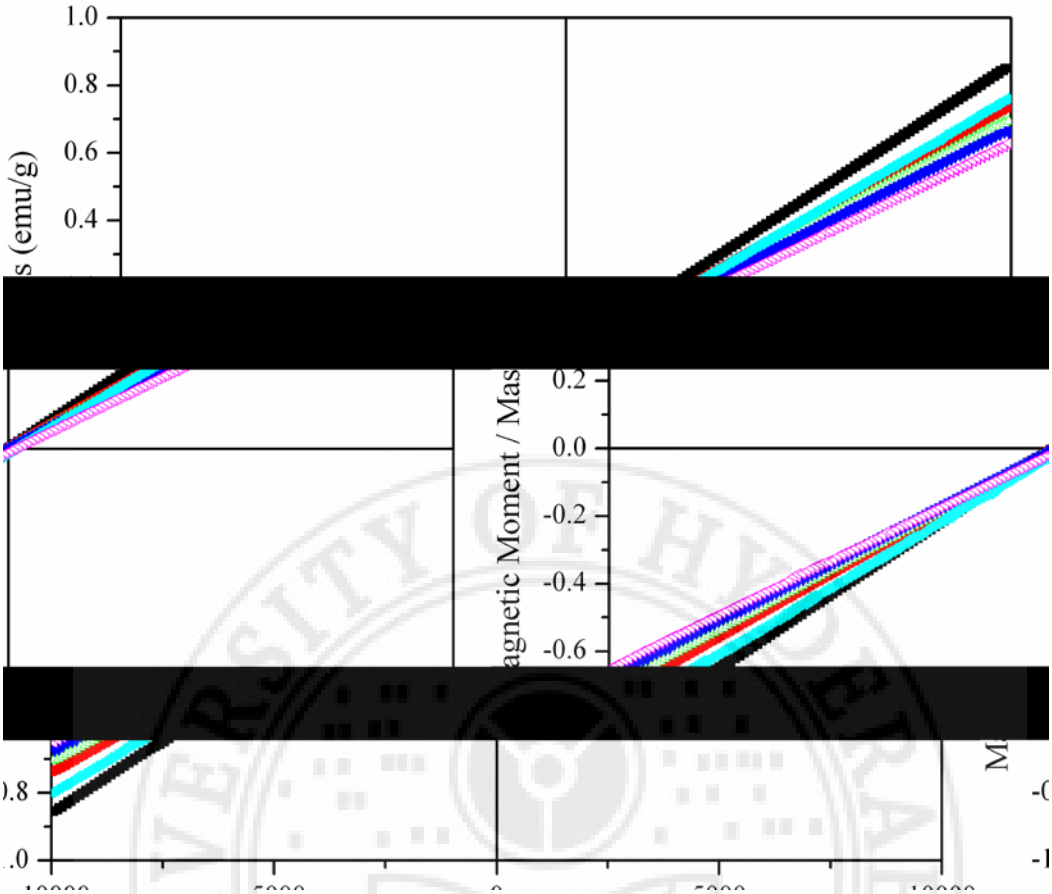

Fig. 4.9 Room temperature magnetization data of the BCMO system.

Figure 4.10 Compositional variation of the Curie Constant of the BCMO system.

as μ_{eff} (Mn^{3+}) = 4.9μ_B and μ_{eff} (Mn^{4+}) = 3.8μ_B [139]. It can hence be expected that with increasing Bi^{3+} the net magnetic moment should increase. The formation of magnetic clusters and the presence of a mixture of Zener pairs (Mn^{3+} – Mn^{4+}) with S = 7/2 and

unpaired Mn^{3+} and Mn^{4+} ions also contribute to the magnetic moment [124, 162, 188] which rules out the possibility of the effective magnetic moments of individual ions alone contributing to the magnetization. The change in structure with composition can also contribute to the non monotonous change in the Curie constant or magnetic moment as the Mn – O bond length and Mn – O – Mn bond angles change, which may favour FM or AFM correlations. This, in turn, may enhance or decrease the magnetic moment accordingly. Hence the non monotonous changes in the Curie constant, which can be considered as small fluctuations about a constant value, cannot be attributed to any single factor or magnetic entity alone. Moreover, the CO anomalies in these compositions are around 300K making it difficult to analyze the composition dependence of C.

4.8 ESR studies on $Bi_{(1-x)}Sr_xMnO_3$ (BSMO)

The temperature dependent ESR spectra of the BSMO system is as shown in figure 4.11. The spectra for the samples are symmetric with respect to the resonance field. On cooling from high temperature the intensity of the spectra increases. With further decrease in the temperature the intensity begins to decrease. This decrease in the intensity of the spectra occurs at the onset of the AFM long range ordering in the samples. A small kink in the spectra is observed at around 300mT. This is characteristic of the existence of the FM clusters in the samples. On increasing Sr content the contribution from these clusters become prevalent in the low temperature spectra. The intensity of this signal is strongly dependent on the material processing. A very weak signal is observed for well processed samples. The g value estimated for all the compositions is ~ 2 and remains almost temperature independent and consistent throughout the temperature range, whatever the nature of the cooperative spin entities in the samples.

Sample (x)	T_N (K)	T_{CO} (K)
0.3	133	600
0.4	153	575
0.45	163	540
0.5	173	525

Table 4.2 The skin depth values for the $Bi_{(1-x)}Sr_xMnO_3$. Values of T_{CO} are taken from references 92, 107 and 112.

In spite of variation in the intensity and peak to peak linewidth, the spectra can be fitted by a lorentzian line shape for the entire temperature range as shown in figure 4.12, following the equation (4.6). The spectra are symmetric with respect to the resonance field. This confirms that the size of the samples is smaller than the skin depth of the penetrating microwaves used. Hence any change seen in the intensity or peak linewidth is purely an intrinsic property of the samples and is not altered due to skin depth effects.

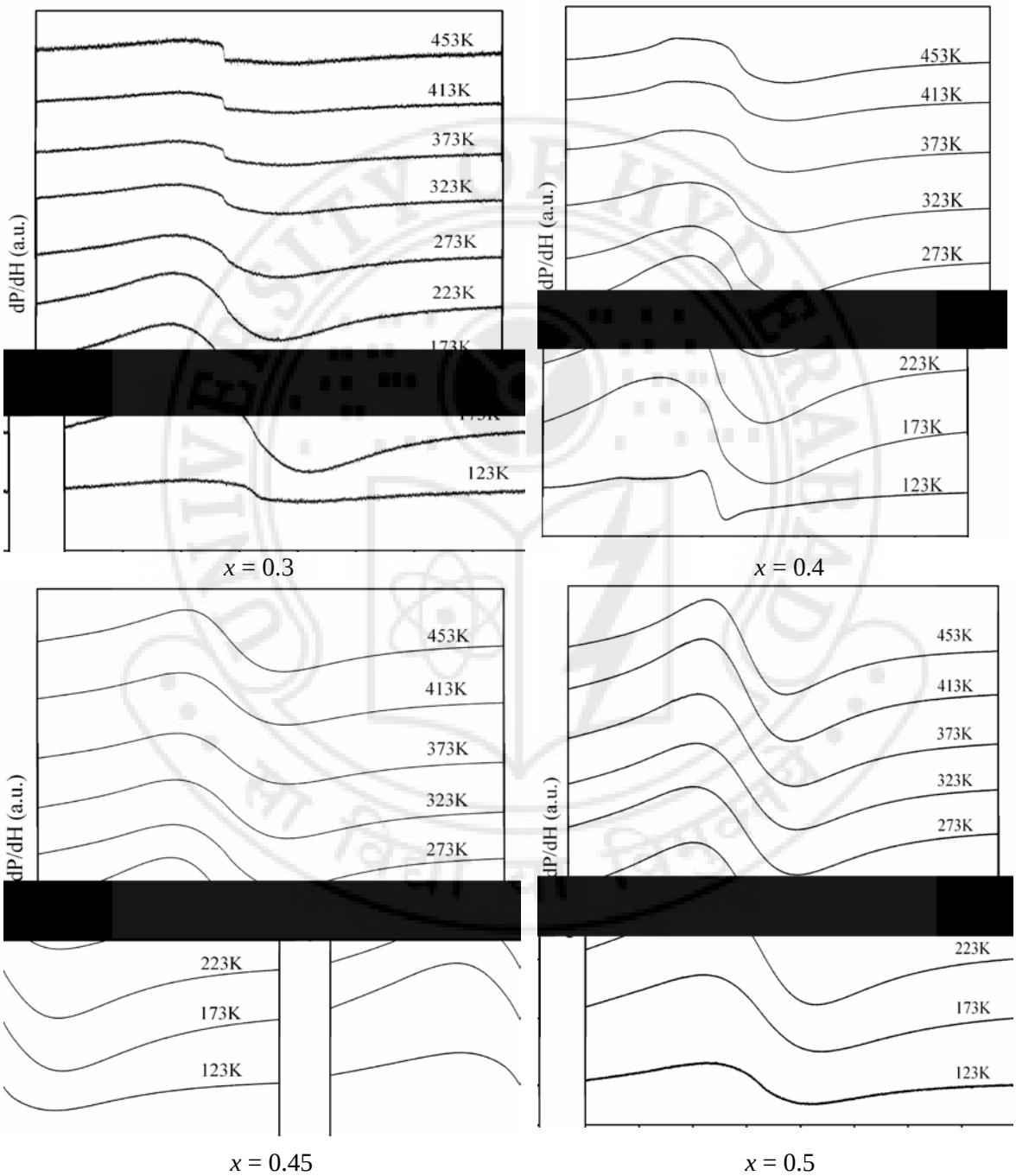

Figure 4.11 Temperature dependent ESR spectra of the BSMO system (x = 0.5, 0.45, 0.4, 0.3).

The skin depth is estimated using equation (4.9). It varies from 0.18mm to 4.19mm which is larger than the sample size. Hence it is confirmed that any change observed in the spectra is only due to the intrinsic behaviour of the samples.

The DI versus temperature plots are shown in figure 4.12. The T_{CO} is not observed for these samples in the temperature range studied confirming that it is above 475K, the maximum temperature achieved in our experimental setup. For the samples $x = 0.3$ the DI value increases monotonously, whereas for the samples with $x \geq 0.3$ DI first increases slowly and then rapidly with decrease in temperature. The temperature at which it increases rapidly decreases with increase in x value. The DI peak is identified as the AFM onset temperature T_O. The values of T_{CO} reported in literature are listed in table 4.2. The data in this figure is for the PM + CO state.

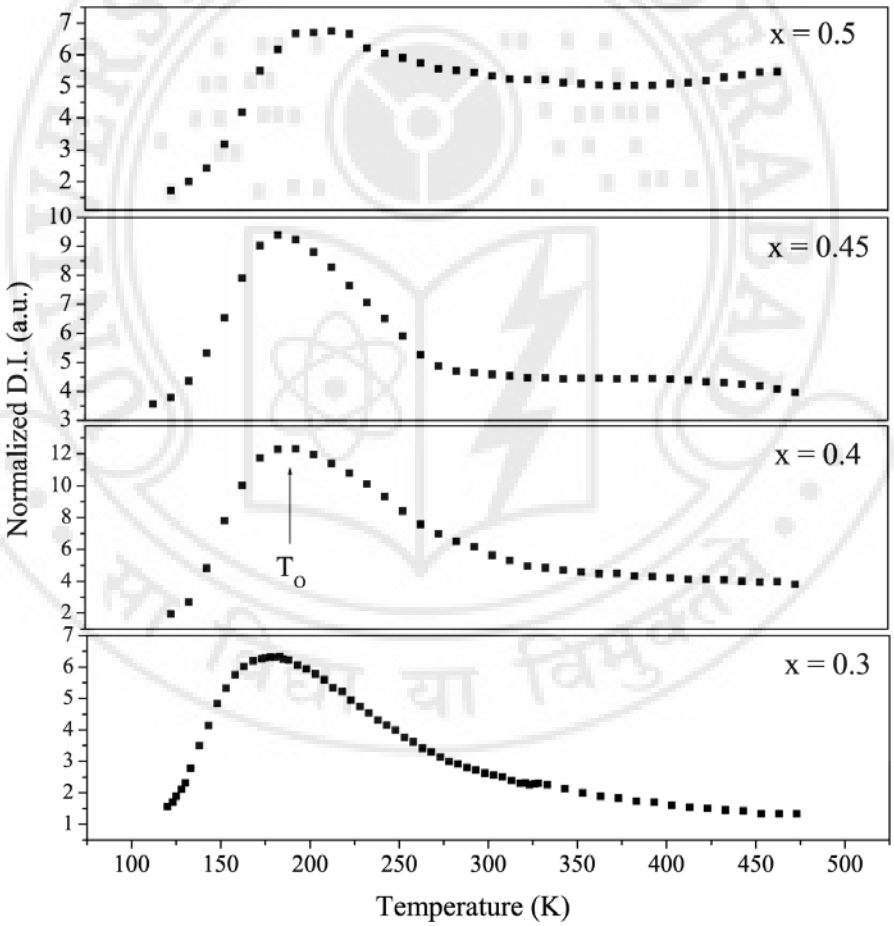

Figure 4.12 DI versus temperature plots for the $Bi_{(1-x)}Sr_xMnO_3$ system.

The validity of Curie – Weiss law at higher temperatures for BSMO has been addressed in earlier studies [92, 107, 109]. As the temperature range in the present study is below the T_{CO} the validity of the Curie – Weiss law is explored in the CO state of the

sample. A linear fit is obtained till very close to T_O for the x = 0.3 sample (figure 4.13). The positive value of the intercept of the linear fit on the temperature axis indicates the presence of FM correlations. On approaching T_O the FM correlations diminish, indicated by the continuously decreasing slope. Sample x = 0.4 shows two straight lines of different slopes that can be fit to the data as temperatures decrease. The change of slope occurs at ~ 320K. The slope of the straight line fit the range 320 – 475K gives a negative intercept on the temperature axis. This is indicative of the enhanced AFM correlations below T_{CO}. Below ~320K, till close to T_O, the straight line fit gives a positive intercept indicative of stronger FM correlations. These FM correlations are present in the high temperatures too, but are downplayed due to the occurrence of the CO state. This is plausible as FM contributions are more likely to be seen with decreasing temperature. A similar situation is also found for the x = 0.45 sample. Two straight lines, one for T > 275K and the other for T < 275K can be fit in the 1/DI v T plots. For the sample with x = 0.5 only one linear fit, with a negative intercept, on the temperature axis is obtained indicating AFM correlations dominating in the CO state of this composition.

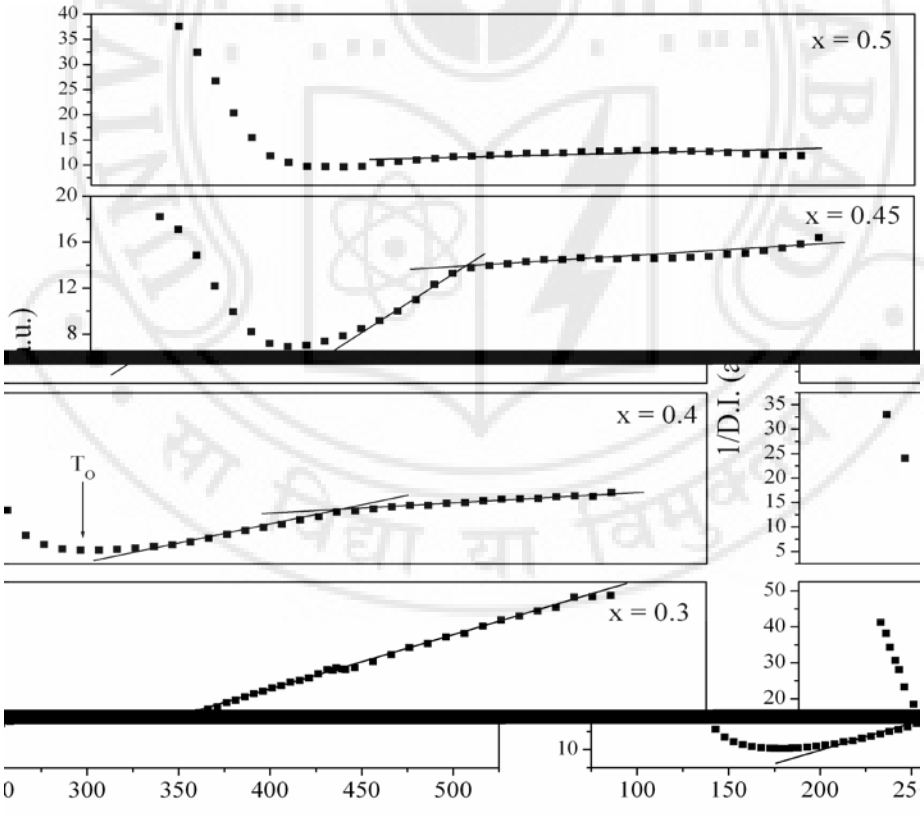

Figure 4.13 1/DI (χ_{ESR}) versus T plots for the $Bi_{(1-x)}Sr_xMnO_3$ system.

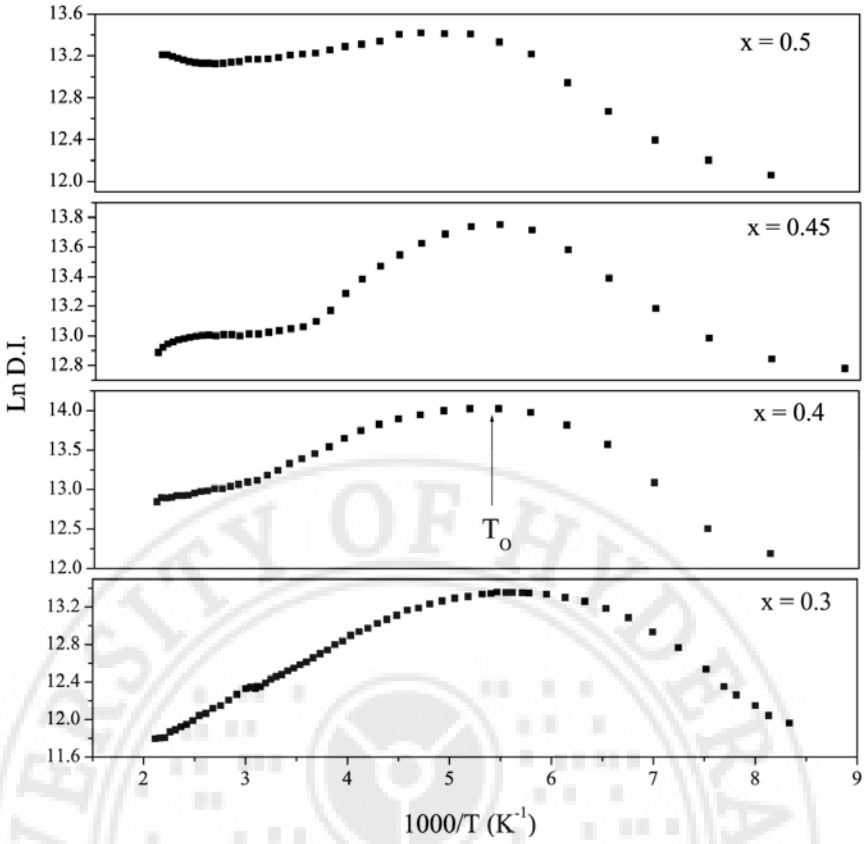

Figure 4.14 ln DI versus 1000/T plots for the BSMO system.

The ln DI versus 1000/T plots for the BSMO system are presented in figure 4.14. The domains of FM and AFM spin correlations coexist in the temperature range $T_{CO} > T > T_N$. The contribution of AFM correlations progressively increase with the increase in Sr content as indicated by decrease in slope of ln DI versus 1000/T plot in the temperature range T < 475K. For the sample with x = 0.5 the FM domain contribution is very small as indicated by the weak temperature dependence of ln DI on T. The sudden decrease in ln DI at low temperatures indicates long range AFM ordering. But the FM correlations exist even below ~ 120K. This is evident as the samples exhibit narrow ESR spectra below T_N.

The temperature dependence of peak to peak linewidth (Δ H) of the ESR resonance line of the BSMO system is shown in figure 4.15. For x = 0.3 and 0.4 samples ΔH remains constant with decrease in temperature till T_O, peaking at T_N and then decreasing with decrease in temperature. For the samples with x = 0.45 and 0.5, at high temperatures there is an initial increase in the ΔH value with decrease in temperature and then it remains constant with decreasing temperature and again increases at the onset of the AFM state, till the T_N is reached. Below T_N, as for the other samples, ΔH decreases rapidly with decreasing temperature. Hence, it can be stated that on nearing 50%

substitution by a divalent ion at the Bi site the FM and AFM contributions in the system can be evidenced both in the temperature dependent DI as well as ΔH.

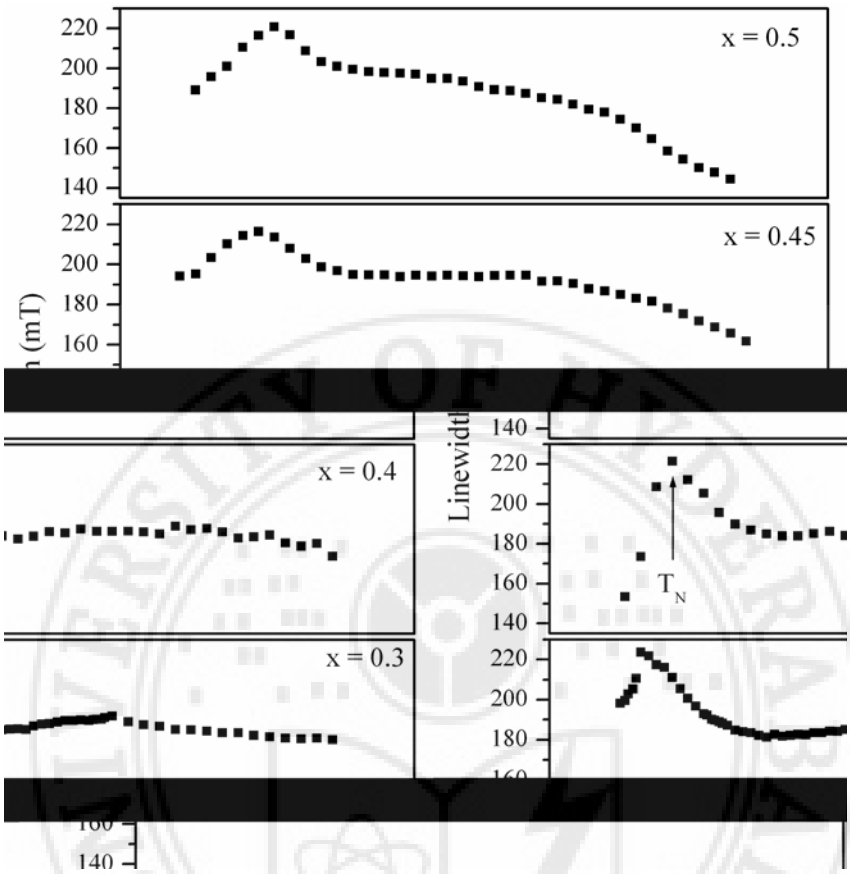

Figure 4.15 Temperature dependent linewidth of the BSMO system.

The minima in ΔH at T_{CO} in the ΔH v T plots (as observed for the previous series) is not observed because of the limited high temperature range. The initial increase in the ΔH values for samples x = 0.45 and 0.5 with decrease in temperature indicates T_{CO} close to 500K as reported in literature [112]. Whereas this feature is not witnessed in the x = 0.3 and 0.4 samples clearly suggesting a higher T_{CO} for these samples. The temperature at which ΔH peaks is the T_N. The values of T_N with increasing x, are recorded in table 4.2. The high value of T_{CO} in this series confirms that samples with lower A-site cationic radius should have higher T_{CO} as compared to the BCMO system.

4.9 Magnetization studies on the BSMO system

The magnetization plots of the BSMO system are shown in figure 4.16 and show the samples to be in the PM phase at room temperature. The susceptibility, χ_{dc}, for the samples is calculated from the slopes of the plots. The value of the Curie constant is

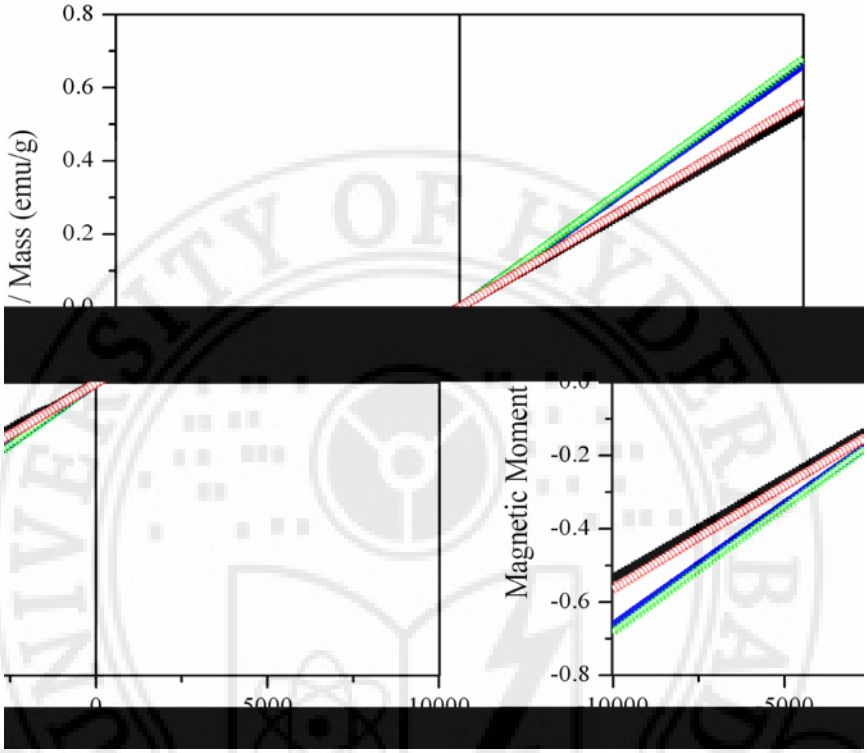

Figure. 4.16 Room temperature magnetization data of the BSMO system.

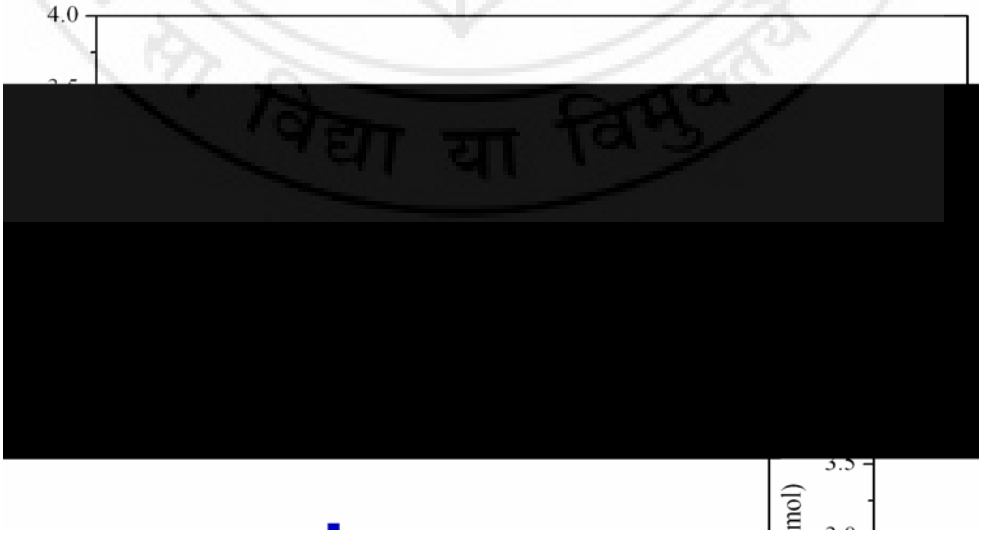

Figure 4.17 Compositional variation of the Curie Constant of the BSMO system.

estimated from the relation χ_{dc} = C/T, where C is the Curie constant and T is the temperature at room temperature in this case. Figure 4.17 represents the variation of the Curie constant with composition. The values of the C vary between 1.98 and 2.51 emu/mol. This small variation in the C value confirms that the Curie constant has only a weak composition dependence. It is to be noted that the C values are for CO state of the present system.

4.10 ESR studies on $Bi_{0.6}Ca_{(1-x)}Sr_xMnO_3$ (BCSMO)

Figures 4.18a and 4.18b represents the temperature dependent ESR spectra of the $Bi_{0.6}Ca_{(1-x)}Sr_xMnO_3$ (0, 0.02, 0.04, 0.06, 0.08, 0.1, 0.16, 0.24, 0.4) system.

The DI v temperature plots of the system $Bi_{0.6}Ca_{(1-x)}Sr_xMnO_3$ are shown in figure 4.19a and 4.19b. For the samples x = 0, 0.02, 0.04 there are two distinct peaks visible. The peak at the higher temperature is assigned to the T_{CO} (table 4.3) while the one at the lower temperature to T_O as represented in the figure. With decreasing temperature DI increases until T_O for all samples. DI decreases below T_O for samples with $0 \leq x \leq 0.04$ and $0.24 \leq x \leq 0.4$. For samples with $0.06 \leq x \leq 0.16$ DI continues to increase with decrease in temperature.

Sample (x)	T_{CO} (K)	T_N (K)
0	313	163
0.02	288	158
0.04	308	163
0.06	313	165
0.08	318	160
0.1	343	147
0.16	393	138
0.24	391	153
0.4	575	153

Table 4.3 The T_{CO} and T_N values for the $Bi_{0.6}Ca_{(1-x)}Sr_xMnO_3$ system.

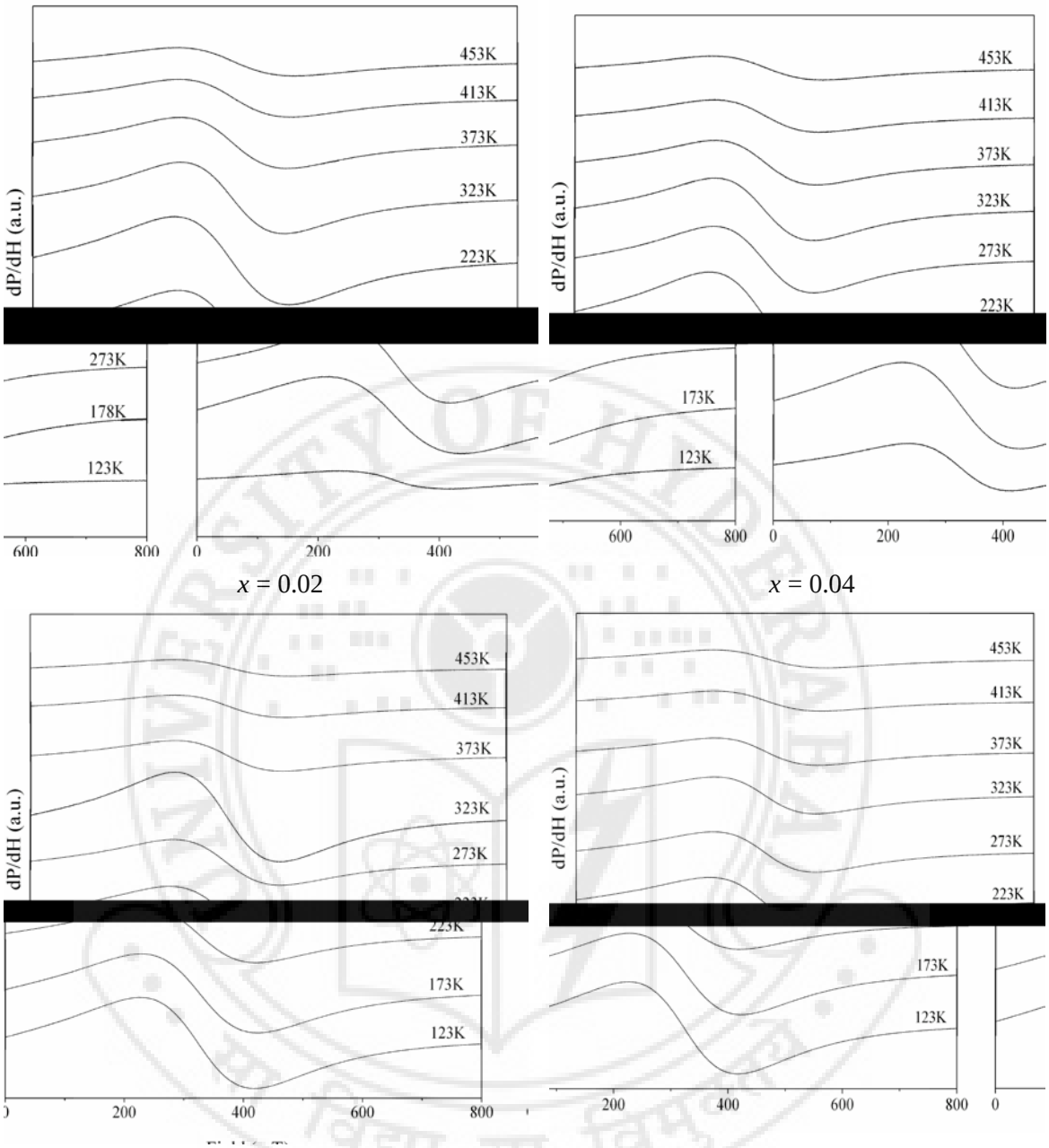

Figure 4.18a Temperature dependent ESR spectra of the $Bi_{0.6}Ca_{(1-x)}Sr_xMnO_3$ system (x = 0.02, 0.04, 0.06, 0.08).

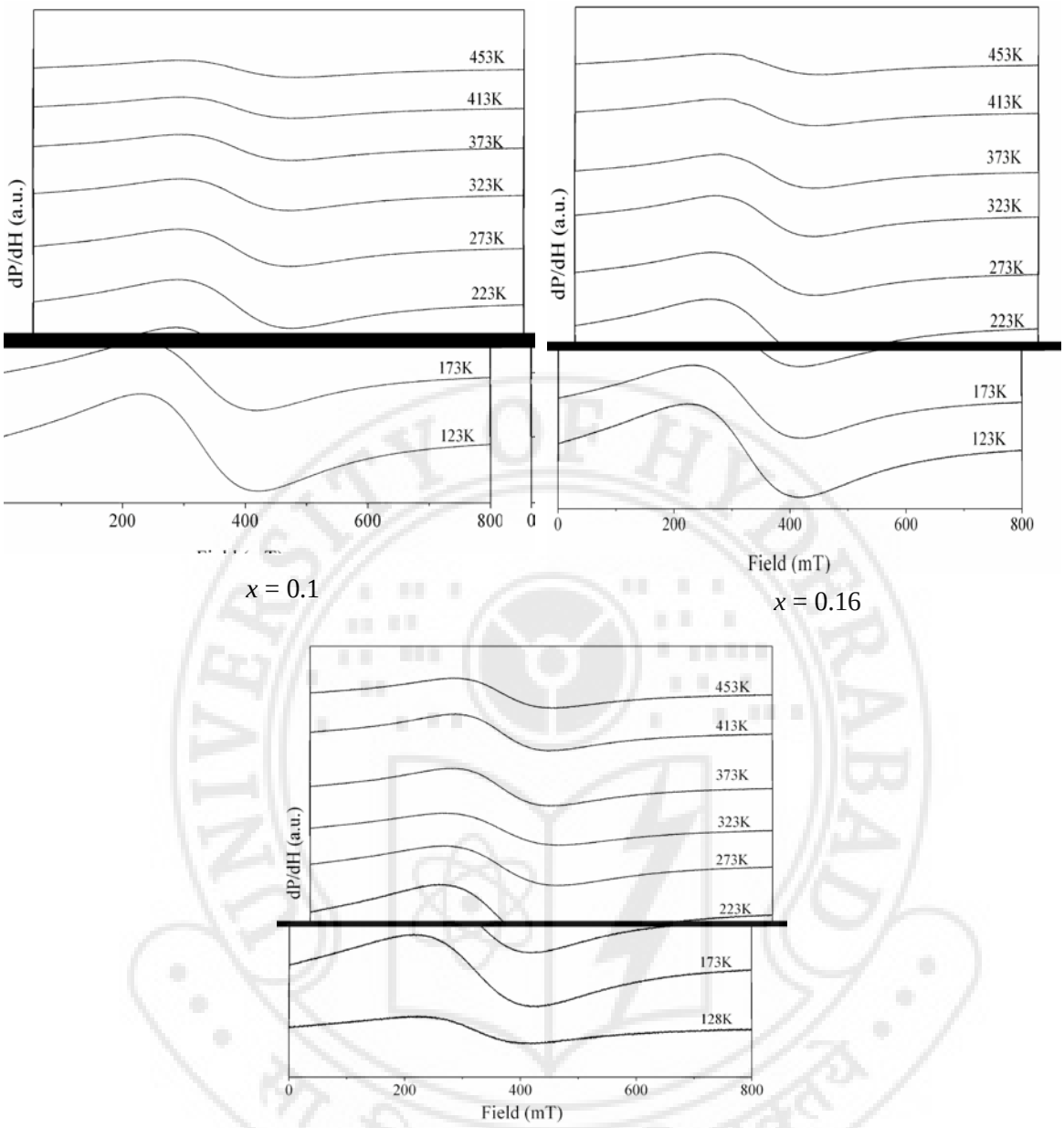

Figure 4.18b Temperature dependent ESR spectra of the $Bi_{0.6}Ca_{(1-x)}Sr_xMnO_3$ system (x = 0.1, 0.16, 0.24).

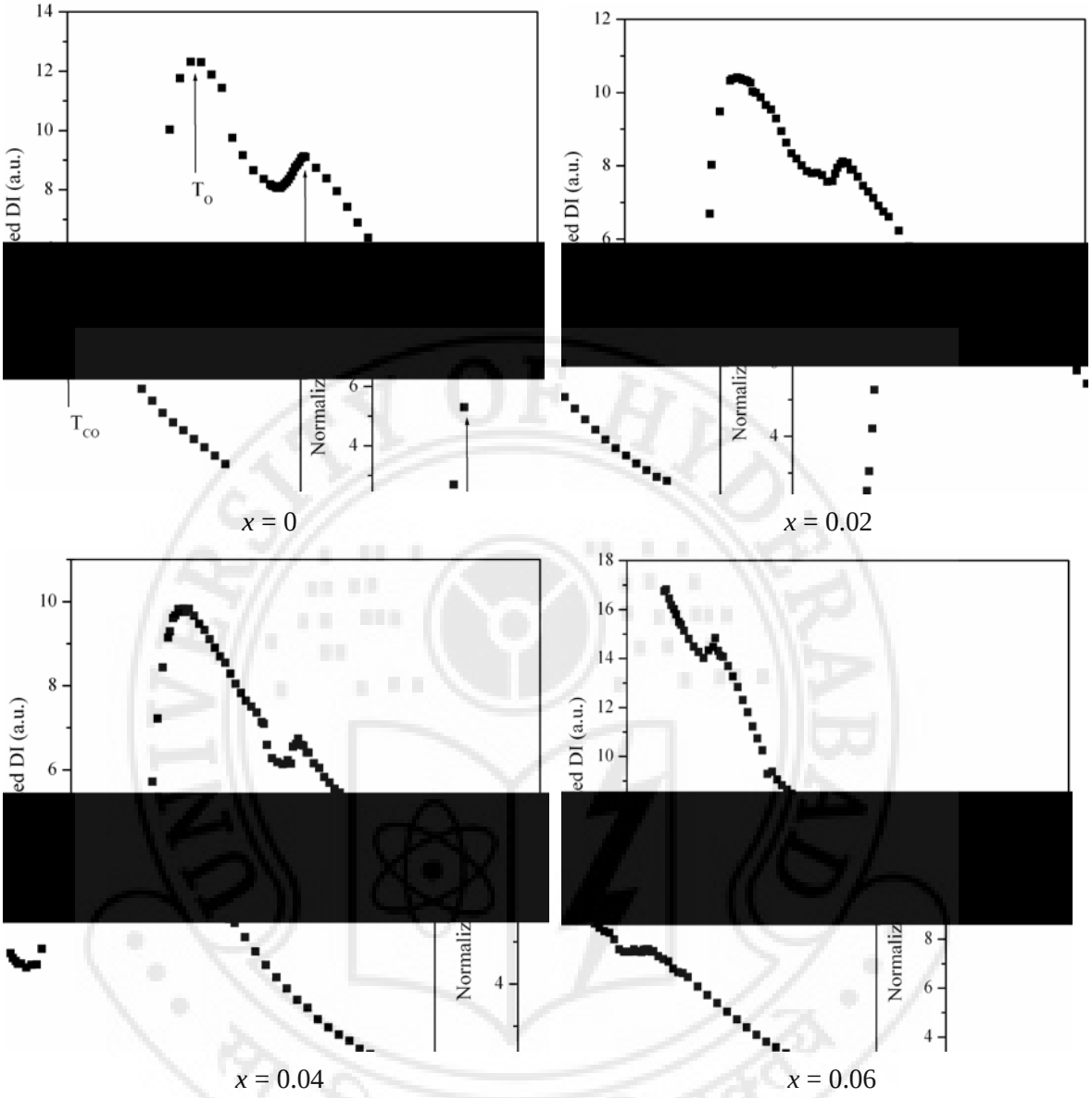

Figure 4.19a DI versus temperature plots for the $Bi_{0.6}Ca_{(1-x)}Sr_xMnO_3$ system.

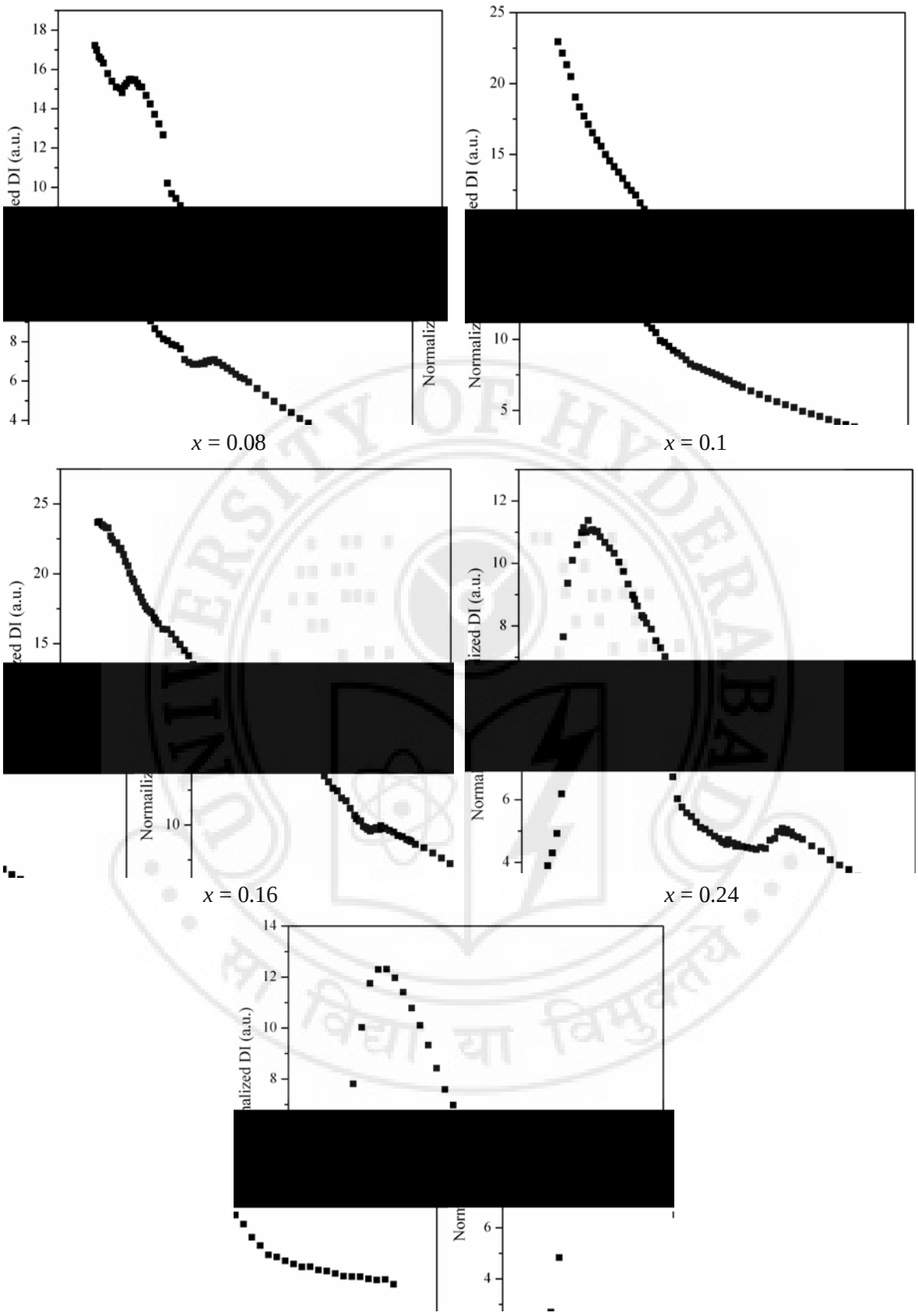

Figure 4.19b DI versus temperature plots for the $Bi_{0.6}Ca_{(1-x)}Sr_xMnO_3$ system.

Figures 4.20a and 4.20b show the 1/DI v temperature plots of the $Bi_{0.6}Ca_{(1-x)}Sr_xMnO_3$ system. The values of T_{CO} and T_O are represented in the plots. Clearly, two straight line fits are obtained in the plots for almost all the samples, one in the range $T > T_{CO}$ and the other in the temperature range $T_O > T > T_{CO}$. For samples x = 0 to 0.24, in the high temperature range, the straight line can be fit for a broad range of temperatures, before it deviates (temperature of deviation marked as T_G) from the linear fit as T_{CO} is approached. The straight line fits indicate the systems to be in the PM regime at high temperatures. The sample with x = 0.4, as mentioned in the earlier sections, is in the PM + CO state as its T_{CO} is above the maximum temperature range of the study.

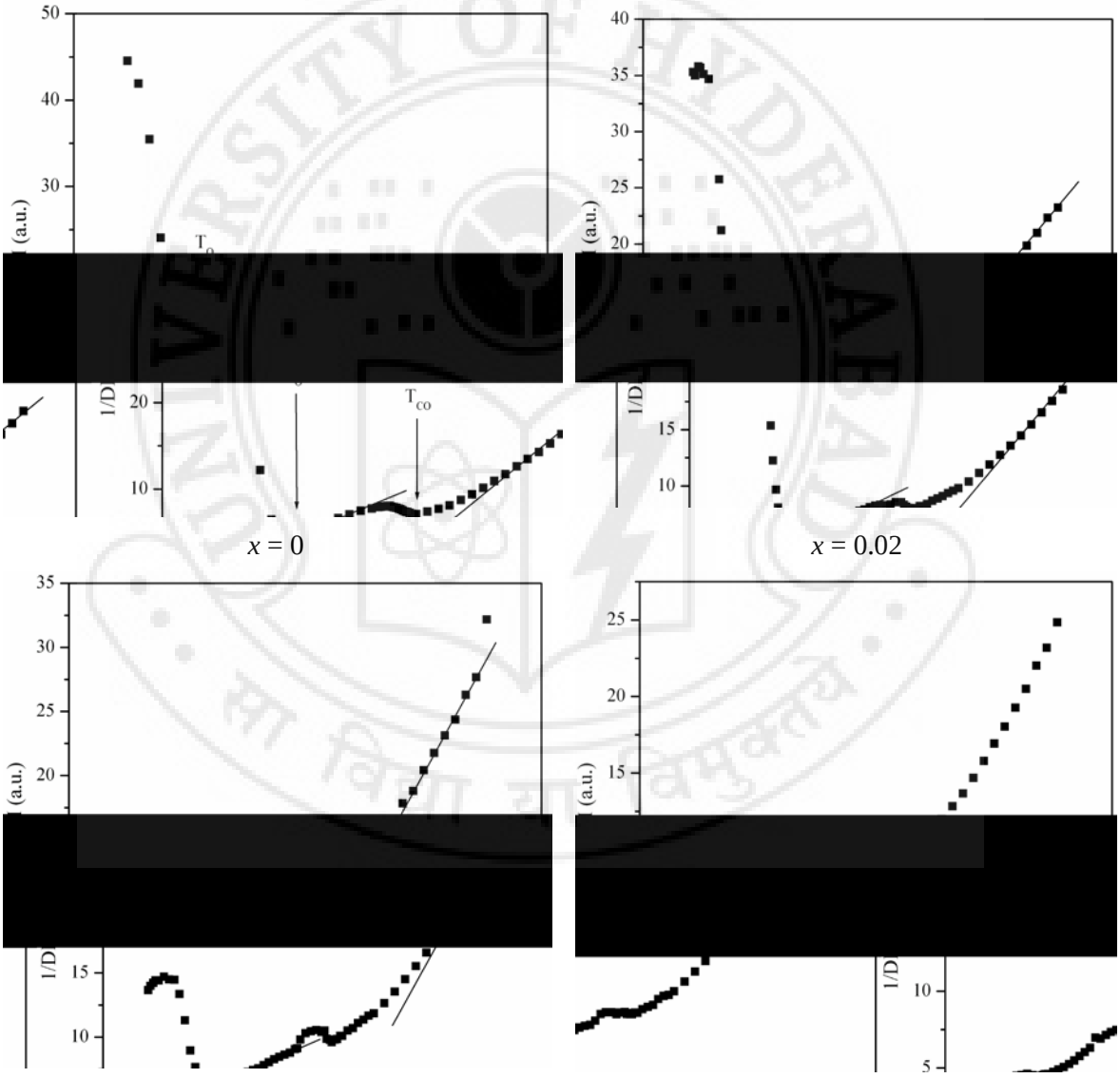

Figure 4.20a 1/DI (χ_{ESR}) versus T plots for the $Bi_{0.6}Ca_{(1-x)}Sr_xMnO_3$ system.

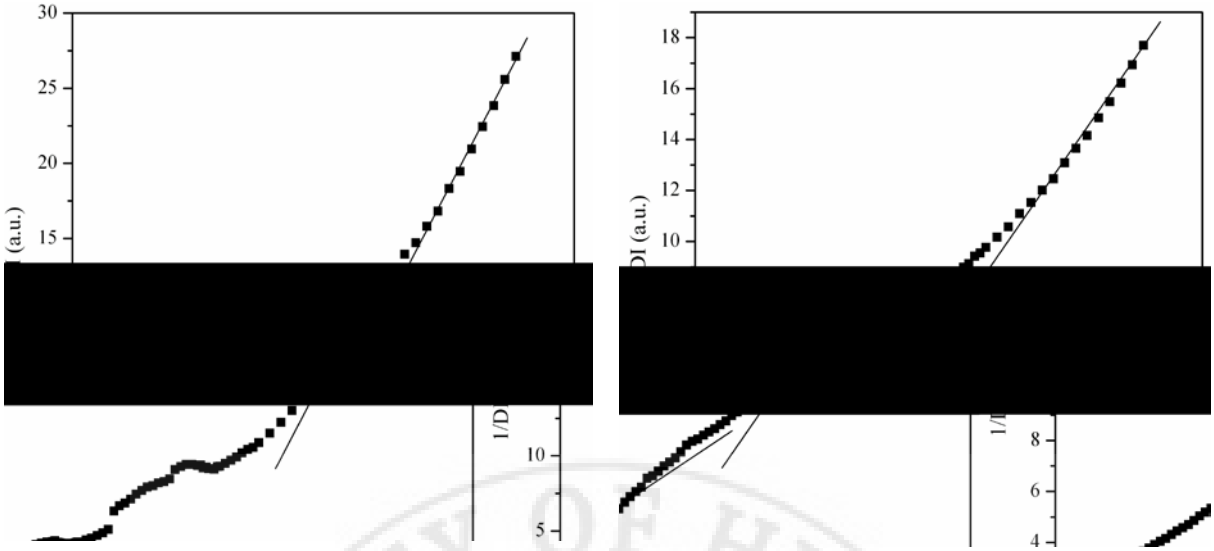

x = 0.08

x = 0.1

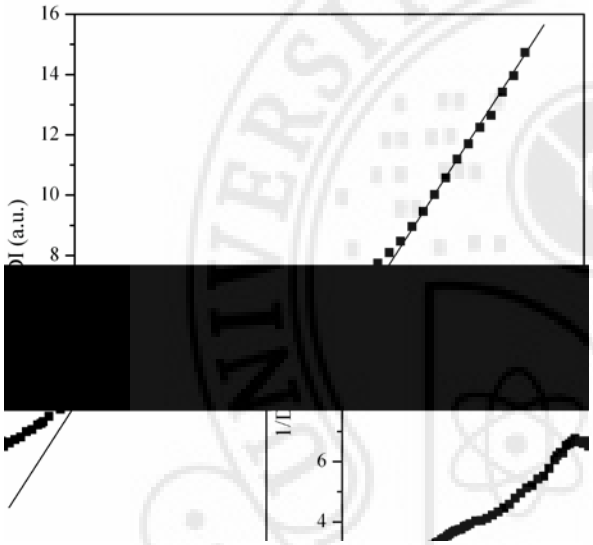

x = 0.16

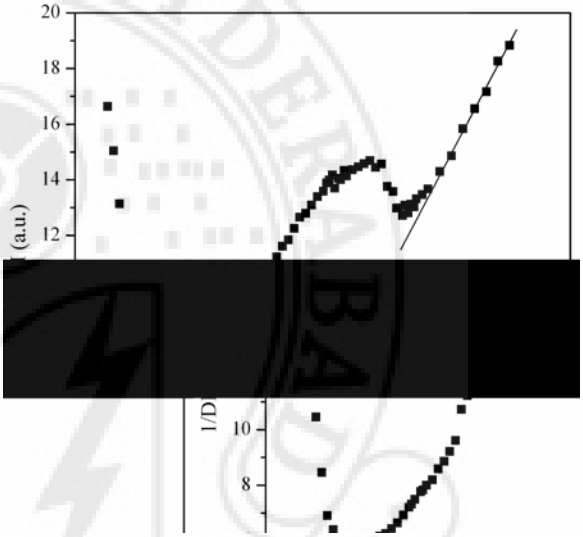

x = 0.24

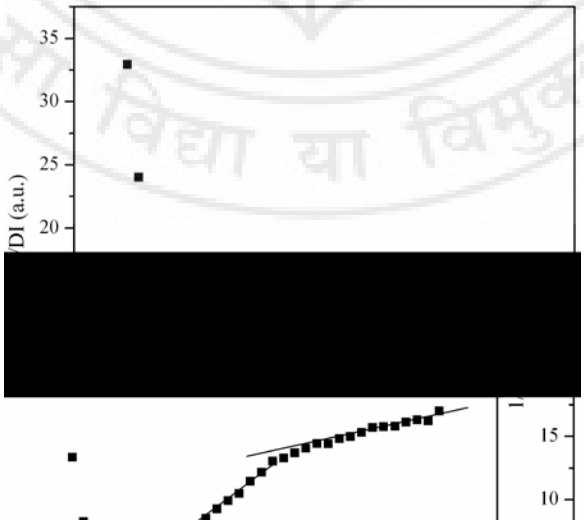

x = 0.4

Figure 4.20a 1/DI (χ_{ESR}) versus T plots for the $Bi_{0.6}Ca_{(1-x)}Sr_xMnO_3$ system.

Figures 4.21a and 4.21b show the ln DI versus 1000/T plots of the $Bi_{0.6}Ca_{(1-x)}Sr_xMnO_3$ system. According to the magnetic cluster model DI is given by the Arrhenius equation shown in equation (4.10). Linear behaviour is observed for all samples in the high temperature range indicating short-range FM correlations. There is a deviation from the linear behaviour at $T > T_{CO}$ indicating formation of AFM clusters for all samples. The sign of the slope of the plot changes at T_{CO}. A straight line fit in the PM + CO state for the samples x = 0, 0.02 and 0.04 with a lesser slope indicates weakening of FM

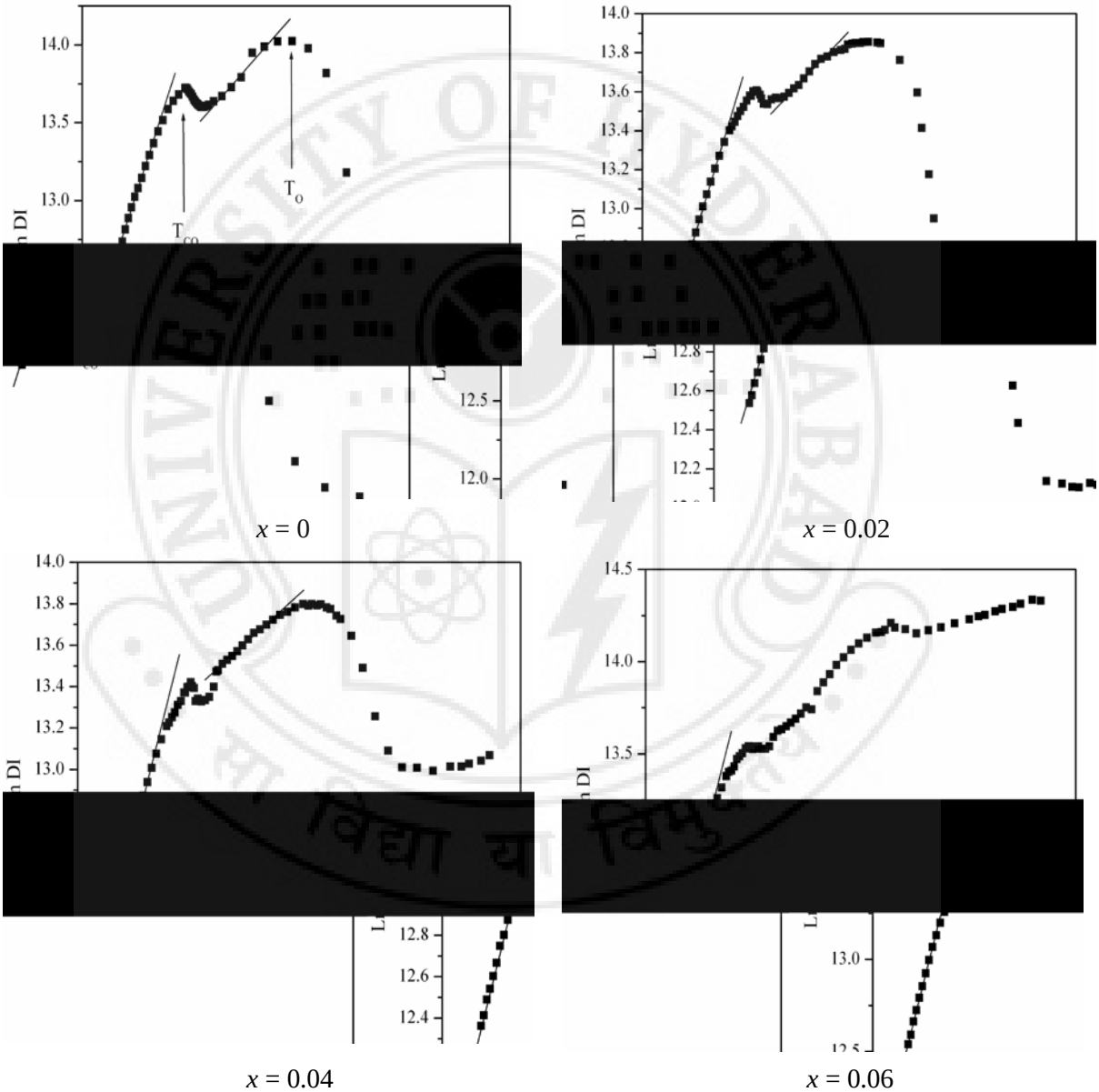

Figure 4.21a Ln DI versus 1000/T plots for the $Bi_{0.6}Ca_{(1-x)}Sr_xMnO_3$ system

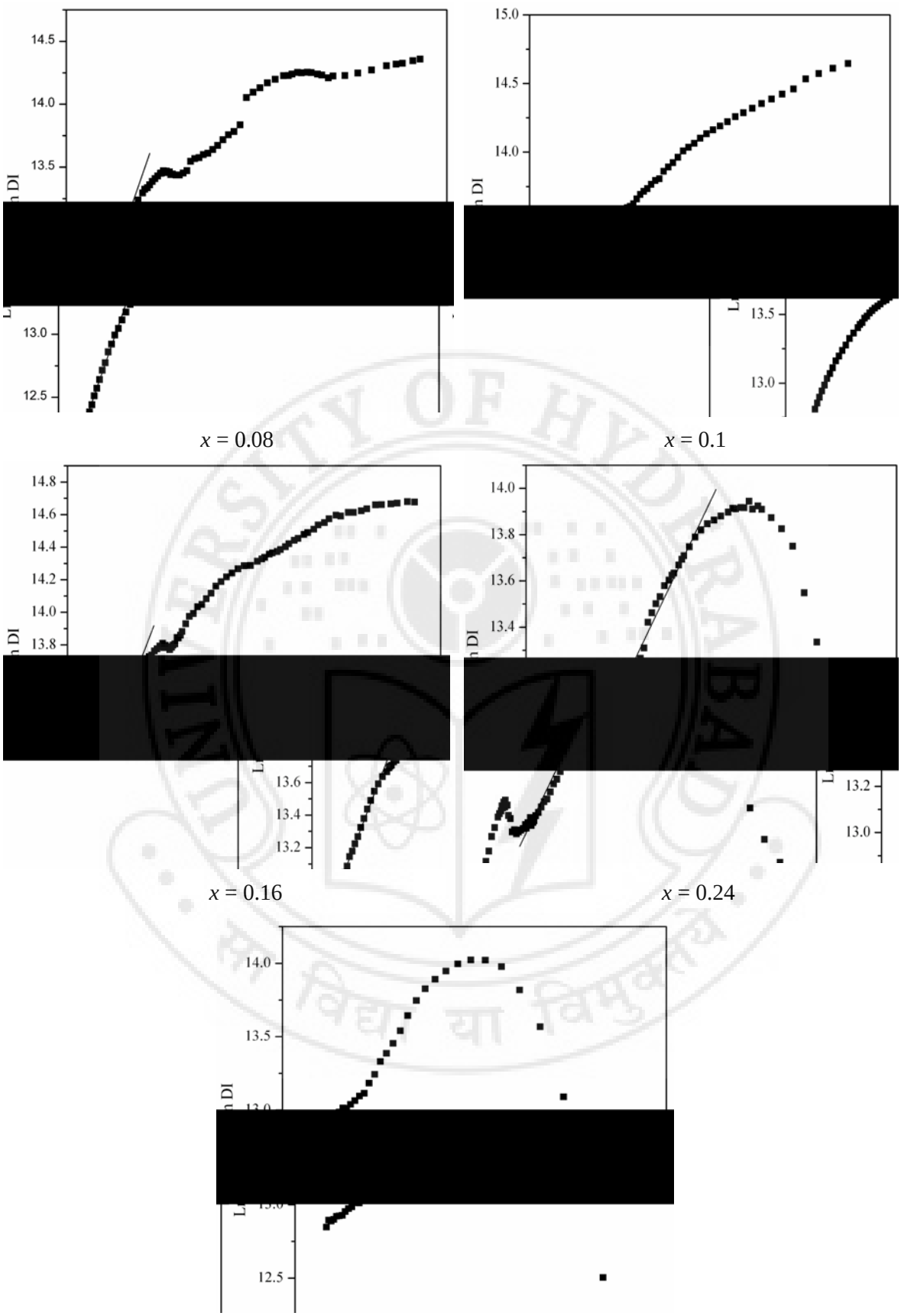

Figure 4.21b Ln DI versus 1000/T plots for the $Bi_{0.6}Ca_{(1-x)}Sr_xMnO_3$ system.

correlations and enhanced contributions of AFM clusters. For the samples with $x \geq 0.06$ the slope in PM + CO state increases with increase in x value, implying increased contributions of FM clusters. This leads to melting of charge ordering and AFM ordering in the sample. These transitions are hardly visible for the sample with $x = 0.1$. With increase in x value to 0.16 the AFM correlations reappear and the CO and AFM transitions are also noticed. When $x = 0.24$ the T_{CO} observed at ~ 390K and T_N at ~ 150K are well defined. This composition is Sr – rich and a phase having a T_{CO} ~ 390K is formed. This may be due to the formation of the $Bi_{0.25}Sr_{0.75}MnO_3$ phase known to have a T_{CO} of ~ 390K [112].

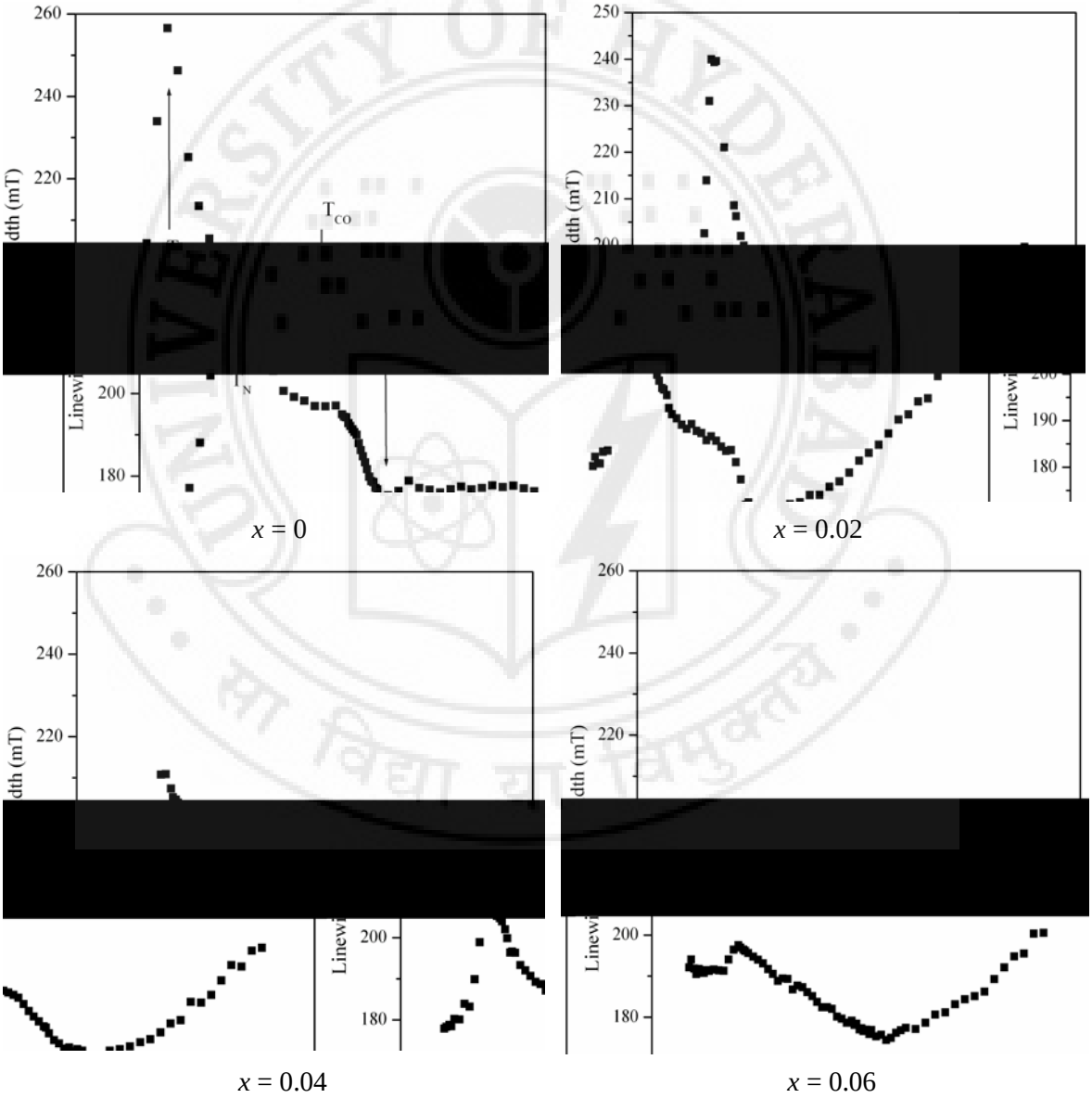

Figure 4.22a Temperature dependent linewidth of the $Bi_{0.6}Ca_{(1-x)}Sr_xMnO_3$ system.

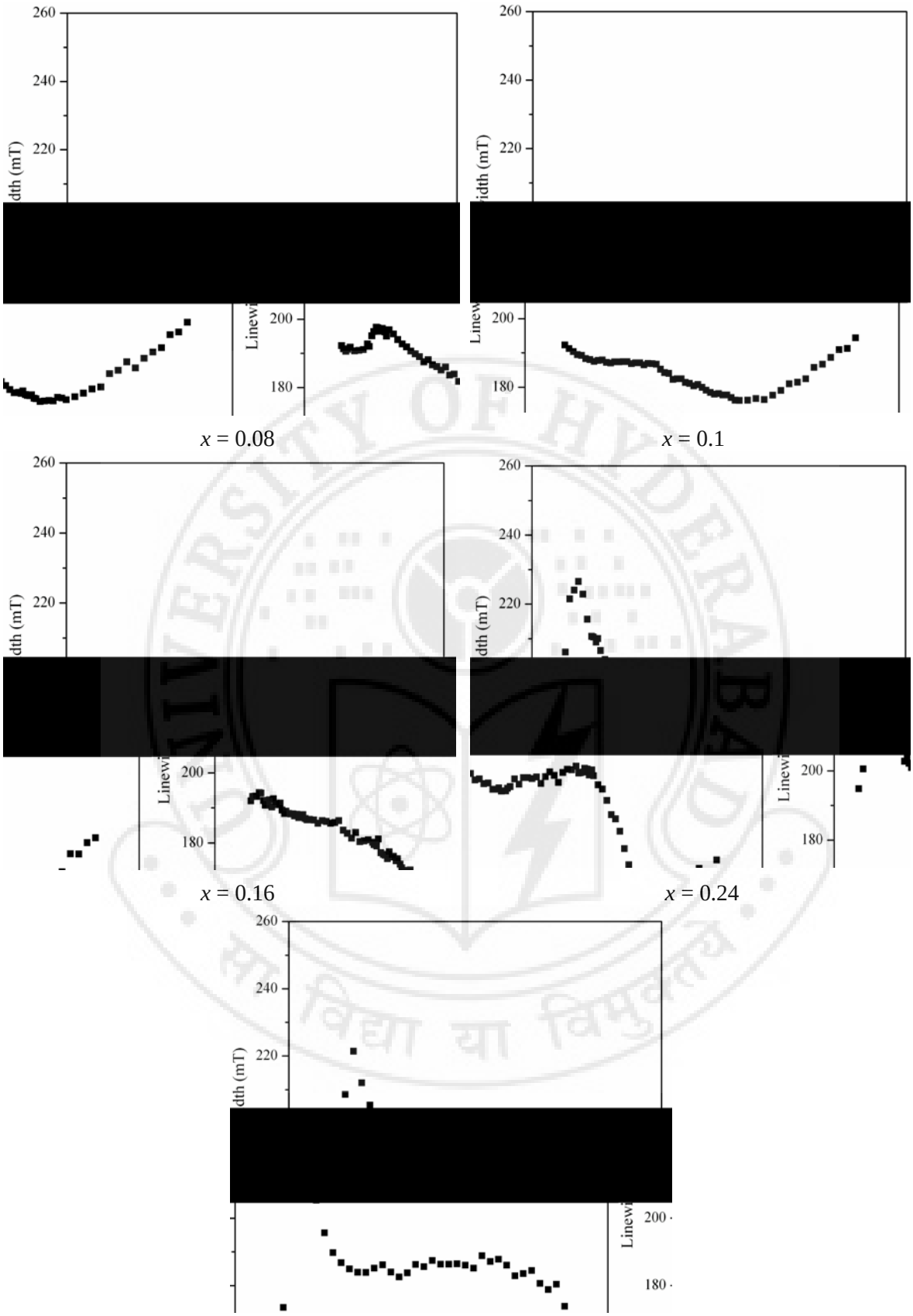

Figure 4.22b Temperature dependent linewidth of the $Bi_{0.6}Ca_{(1-x)}Sr_xMnO_3$ system.

Figures 4.22a and 4.22b depict the ΔH v T plots for the $Bi_{0.6}Ca_{(0.4-x)}Sr_xMnO_3$ system. The values of T_{CO} and T_N are depicted in the plots. All the samples (except sample with x = 0.4) show a decrease in ΔH with decreasing temperature till a minima is reached. This minima is assigned to T_{CO}. Below T_{CO} ΔH increases, remains a constant and then again increases. A peak observed at low temperatures for all samples, except the samples with x = 0.1 and 0.16, is assigned as T_N. With increasing Sr content till x = 0.1 the minima widens and smears out the T_{CO}. For the sample with x = 0.04, a small kink at T ~ 390K is observed. With increasing x the kink becomes more prominent. For x = 0.16, the T_{CO} reappears at ~ 390K, indicative of formation of a phase of composition $Bi_{0.25}Sr_{0.75}MnO_3$ [112]. For x = 0.4, which is the BSMO system, the minima is not observed as the T_{CO} is above the measured highest temperature. The smearing of the T_{CO} is due to the enhancement of the FM clusters with the addition of Sr content. Hence the CO melts with increase in Sr content. The T_N value is ~ 150K for all samples except for x = 0.1 and 0.16. For the sample with x = 0.16 the T_{CO} reappears but the T_N is still not observable. For x = 0.24 the T_{CO} and T_N are observed but with a broader CO phase transition, indicative of strong contributions from Sr – rich phases having higher T_{CO}s. The T_N values for x = 0.1 and 0.16 are estimated from the resistivity data. Below T_N, the ΔH decreases rapidly with decreasing temperature due to the long range AFM ordering at low temperatures. The FM inhomogeneities embedded in the AFM ordered matrix prevent the ESR signal from diminishing completely. For samples with x = 0.1 and 0.16 ΔH continuously increases with decreasing temperature.

The values of T_{CO} and T_N are recorded in table 4.3. The T_{CO} goes through a minimum at x = 0.02 and then continuously rises. The value of T_{CO} for x = 0.4 is taken from literature. The value of T_N on the other hand remains more or less constant for the samples. Hence it can be argued that the T_{CO} is more dependent on the sample composition while the T_N is not as much affected and hence the subtle changes in T_{CO} can be taken to be more reliable to understand the compositional or structural changes of a system.

The ESR studies show that the magnetic phase in $Bi_{0.6}Ca_{(0.4-x)}Sr_xMnO_3$ (x = 0, 0.02, 0.04, 0.06, 0.08, 0.1, 0.16, 0.24) for $T > T_{CO}$ is dominated by FM correlations which can be attributed to activated Mn^{3+} – Mn^{4+} hopping of small polarons. With increasing content of Sr FM correlations increase and the charge ordering and AFM ordering weakens. For x = 0.1 no T_{CO} or T_N is observed from the DI plots, indicating dominant FM correlations and the melting of CO state. When x = 0.16, the Sr – rich phase becomes

dominant, evidenced as a prominent T_{CO} peak at ~ 390K. The changes in the slope of the 1/DI v T plots is attributed to the coexistence of the FM and AFM domains. The sharp change in the slope of ln DI versus 1000/T plot indicates the onset of long-range AFM order. For $T < T_N$, temperature independent ln DI indicates the freezing of FM microdomains/ inhomogeneities in the AFM long-range ordered state.

With the increase in Sr content from $x = 0.04$ to 0.1 the FM correlations increase resulting in the weakening of the CO and AFM transitions. The CO and the AFM transitions are barely noticed in the sample with $x = 0.1$. With further increase in Sr content CO transition reappears but at a higher temperature of ~ 390K, which may be assigned to $Bi_{0.25}Sr_{0.75}MnO_3$ phase [112]. At $x = 0.1$ the FM domains permeate almost the entire volume of the sample with AFM domains interspersed in between. This picture is supported by the observation of very feeble CO and AFM transitions. In summary, addition of Sr first leads to the melting of CO state. At around 25% of Sr the melting of CO state is complete. At around 40% of Sr the CO state reappears due to the formation of $Bi_{0.25}Sr_{0.75}MnO_3$ phase. Further increase in Sr content leads to formation of $Bi_xSr_yMnO_3$ phases having high T_{CO}s. The growth of high T_{CO} phases is a continuous evolution process with increase in Sr content.

4.11 Magnetization studies on the BCSMO system

The magnetization data, plotted as magnetic moment per unit mass versus applied field, for the BCSMO system is shown in figure 4.23. The dc susceptibility of the samples is calculated from the slope of the magnetization plots. The high temperature ESR data show that all the samples (except $x = 0.4$) obey the Curie-Weiss law till the temperature T_G is reached. The variation of the Curie constant with composition is depicted in figure 4.24 The values of the Curie constant vary between 2.51 and 3.18 emu/mol for the samples. This variation of the Curie constant in this narrow range confirms the weak composition dependence of C. The changes in the magnetic moment or Curie constant can be attributed to a number of contributing factors. Almost all the samples are in the CO state at room temperature. As the CO state favours AFM correlations, the magnetization data for samples with T_{CO} closer to room temperature can be lowered as the AFM correlations begin to contribute to the magnetic interactions below $T < T_G$.

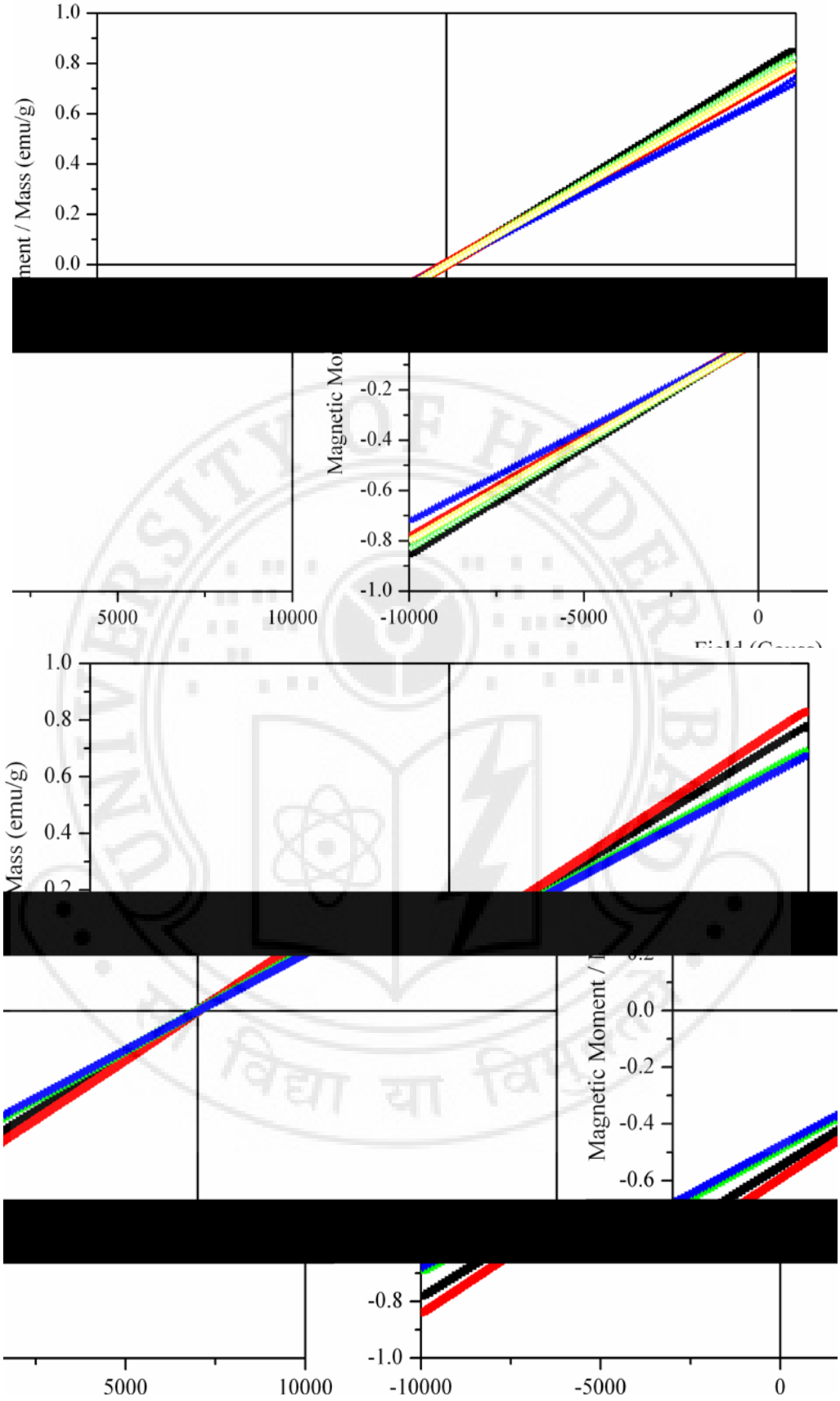

Figure 4.23. Room temperature magnetization data of the $Bi_{0.6}Ca_{(1-x)}Sr_xMnO_3$ system.

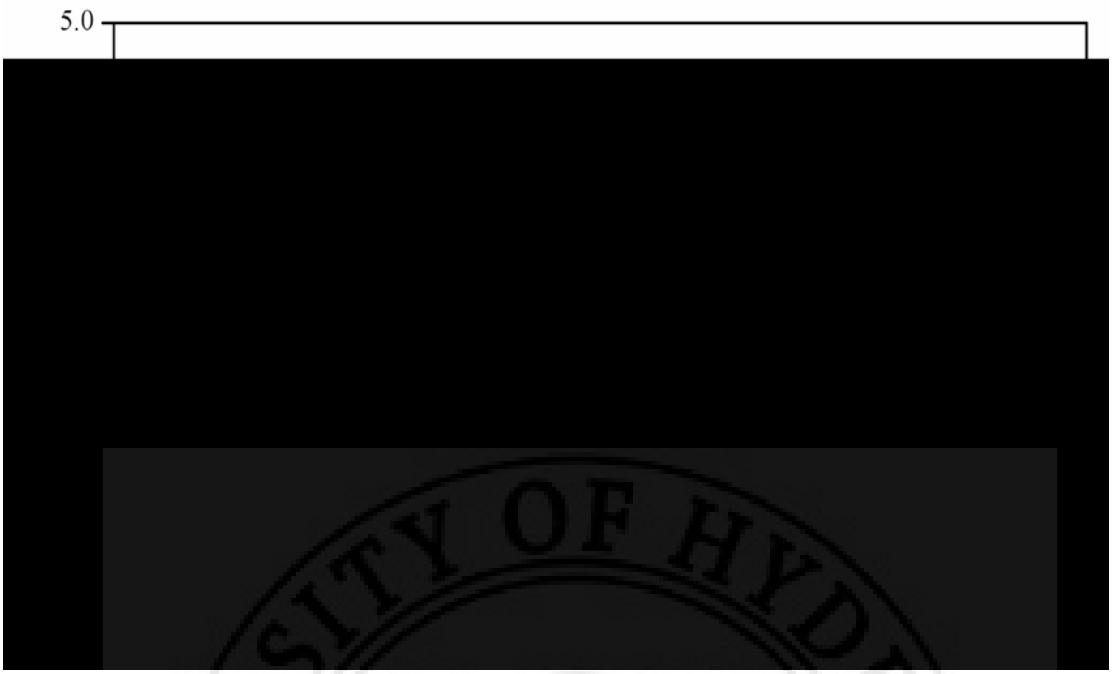

Figure 4.24. Compositional variation of the Curie Constant of the BSMO system.

The magnetization data show that the samples are in the PM state with no macroscopic FM regions. This confirms that the features observed in the ESR studies is due to the correlations of different magnetically ordered entities. The variation in C as a function of composition is strongly affected by the CO anomalies near 300K.

4.12 ESR studies on $Bi_{0.5}Sr_{(0.5-x)}Ce_xMnO_3$ (BSCMO)

The ESR spectra of $Bi_{0.5}Sr_{(1-x)}Ce_xMnO_3$ (x = 0, 0.1, 0.2) is depicted in figure 4.25. The intensity of the spectra increases as the temperature is lowered from high temperature. At low temperatures the intensity of the spectra begins to decrease.

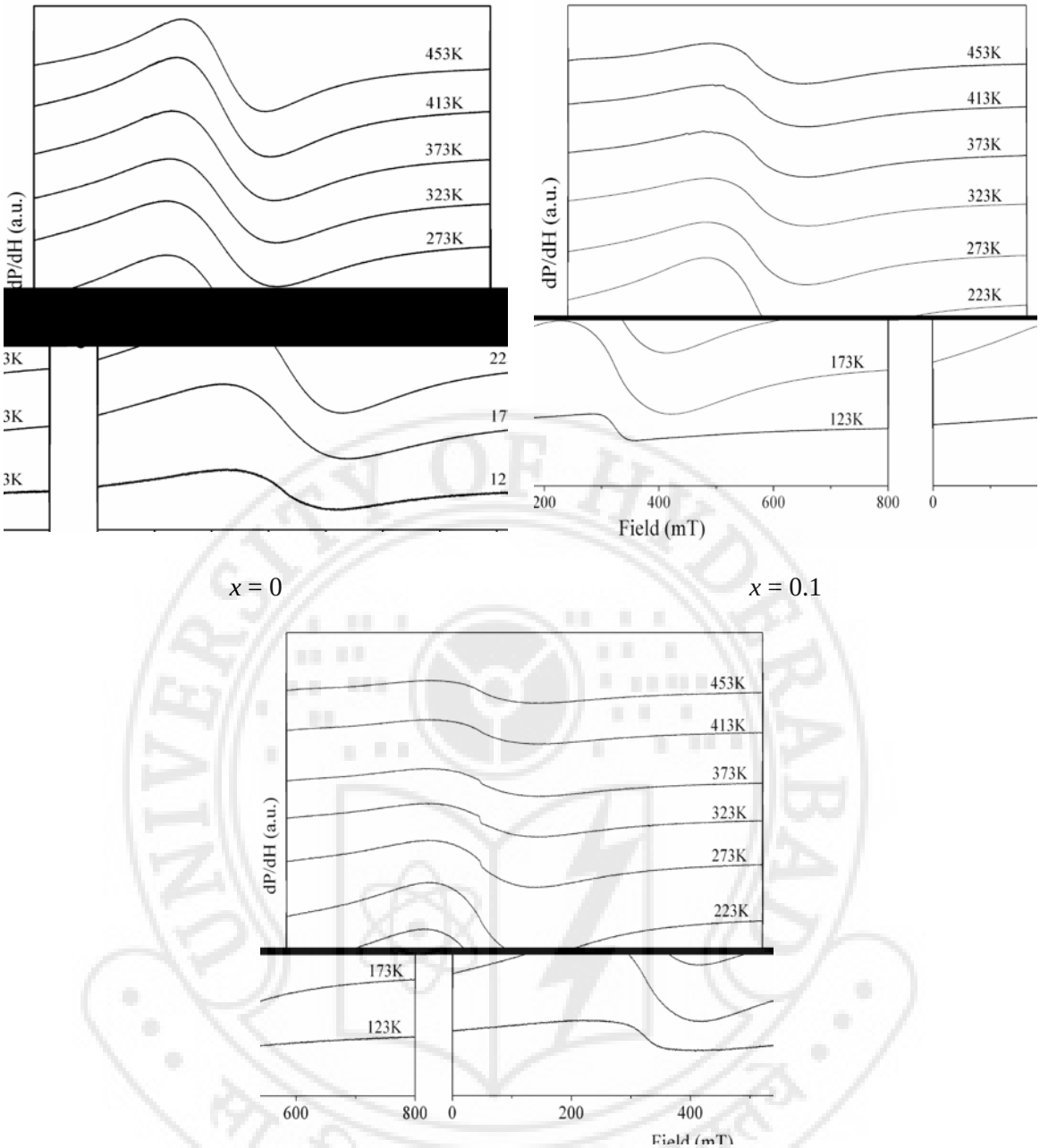

x = 0 x = 0.1

x = 0.2

Fig 4.25 Temperature dependent ESR spectra of the $Bi_{0.5}Sr_{(0.5-x)}Ce_xMnO_3$ system (x = 0, 0.1,0.2).

Figure 4.26 depicts the DI v T plots for the $Bi_{0.5}Sr_{(0.5-x)}Ce_xMnO_3$ system. As in the case of BSMO system, the T_{CO} could not be observed for the present samples in the temperature range 200 – 475K as it is beyond the maximum temperature limit of the experimental set up. The samples are in the charge ordered PM state. With decreasing temperature DI increases. At temperatures ~ 170K to 200K, depending on the sample composition, a drop in DI occurs indicating long range AFM ordering. The T_N values for

the samples are recorded in table 4.4 and are found to decrease with increasing Ce. A narrow ESR signal observed at ~ 330mT is attributed to the existence of FM clusters in the system.

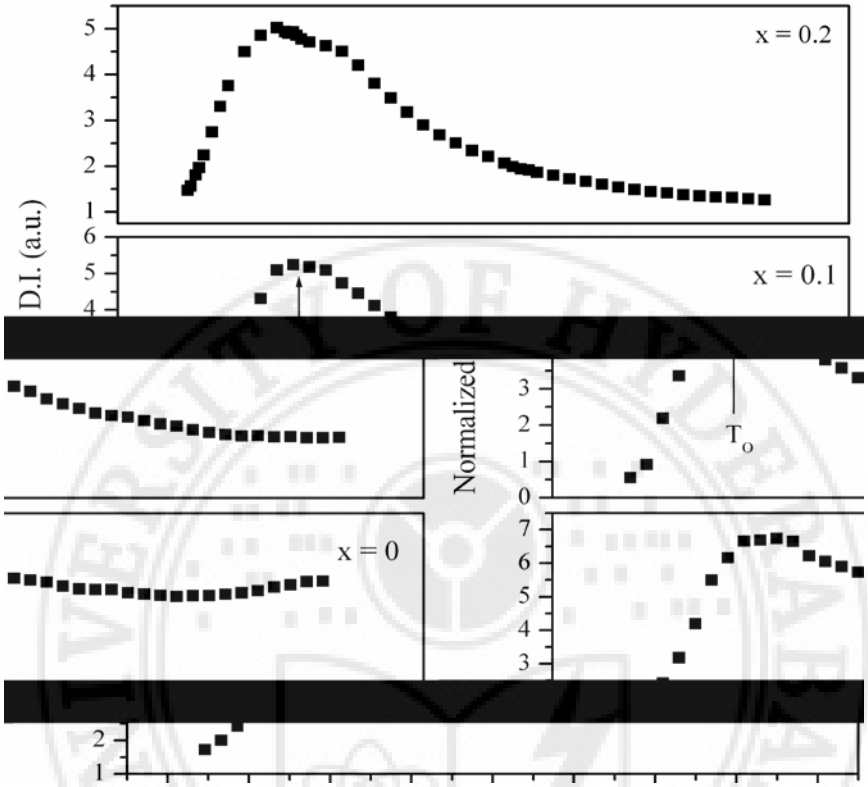

Figure 4.26 DI versus temperature plots for the $Bi_{0.5}Sr_{(0.5-x)}Ce_xMnO_3$ system.

Sample (x)	T_N (K)
0	173
0.1	153
0.2	138

Table 4.4 The skin depth and T_N values for the $Bi_{0.5}Sr_{(0.5-x)}Ce_xMnO_3$ system.

Figure 4.27 depicts the 1/DI v T plots of BSCMO. The possible coexistence of FM as well as AFM clusters in the CO state is examined using these plots. Sample x = 0 shows a straight line fit till close to T_O. The negative intercept of the straight line on the temperature axis suggests that AFM correlations dominate in the PM + CO state. For x = 0.1 two straight line fits are observed in the temperature range above T_O. One in the

temperature range 410 – 475K having a negative intercept.. The straight line fit between T_O and ~ 413K has a positive X-axis intercept indicating stronger FM correlations, overcoming the AFM correlations which begin to set in just above T_{CO}.

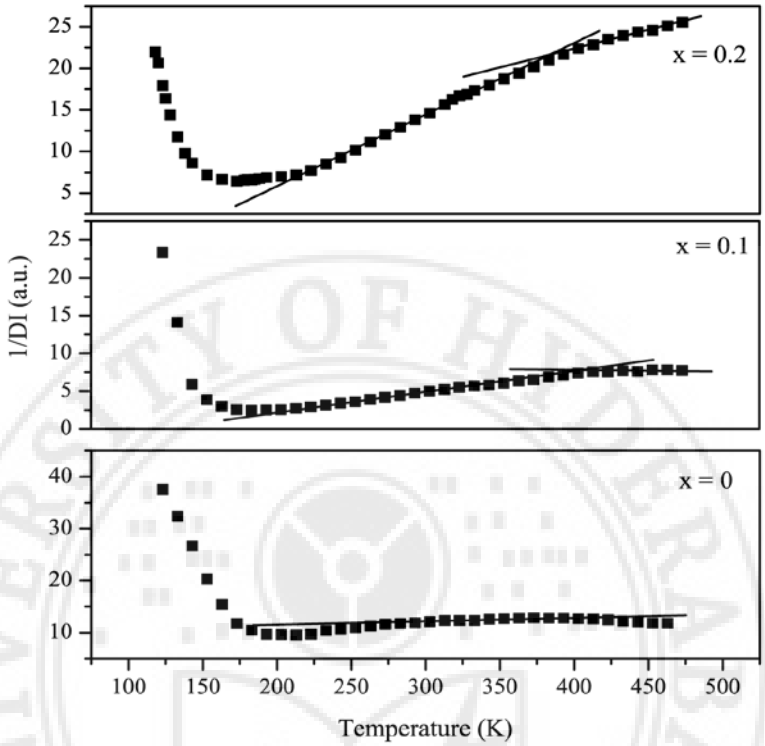

Figure 4.27 1/DI (χ_{ESR}) versus T plots for the $Bi_{0.5}Sr_{(0.5-x)}Ce_xMnO_3$ system.

For x = 0.2 two straight lines with slopes greater than that the for x = 0.1 sample indicates strengthening of FM correlations in this sample. The larger range of temperatures in which the line fits in the higher temperature range indicates the strengthening of FM correlations and weakening of AFM interactions with increasing x. This suggests the increase in T_{CO} values with increasing x. The sharp increase in the 1/DI value below T_O indicate the long range ordered AFM state.

The ln DI v 1000/T plots for the BSCMO system are shown in figure 4.28. The slope of the plots in CO state increases with increasing x is indicative of strengthening of FM correlations. The T_O and T_N values decrease with increase in Ce content. The temperature independent ln DI indicates the freezing of FM inhomogeneities in the long range AFM ordered state.

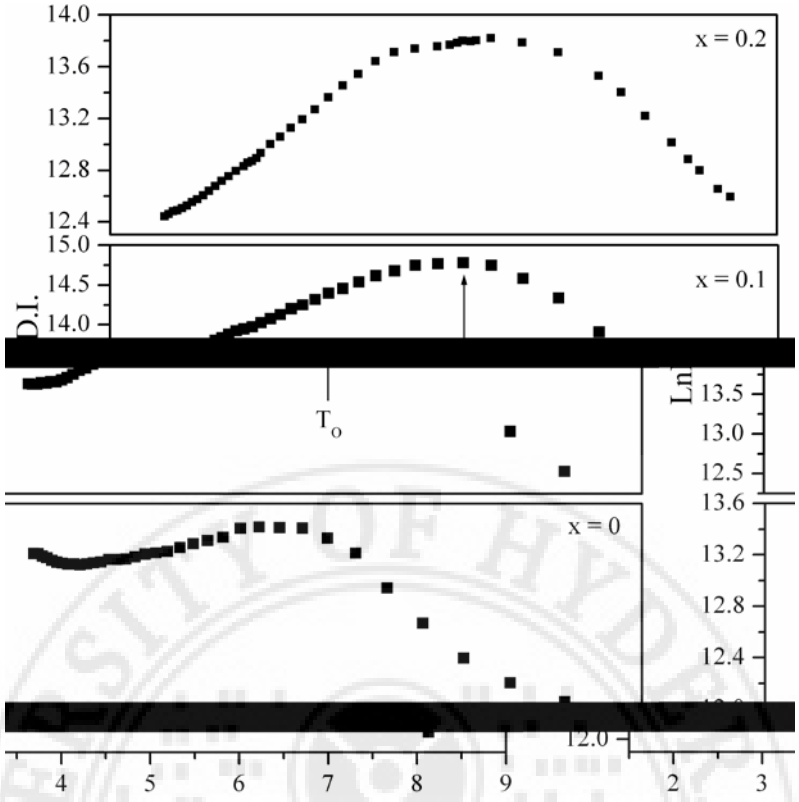

Figure 4.28 ln DI versus 1000/T plots for the $Bi_{0.5}Sr_{(0.5-x)}Ce_xMnO_3$ system.

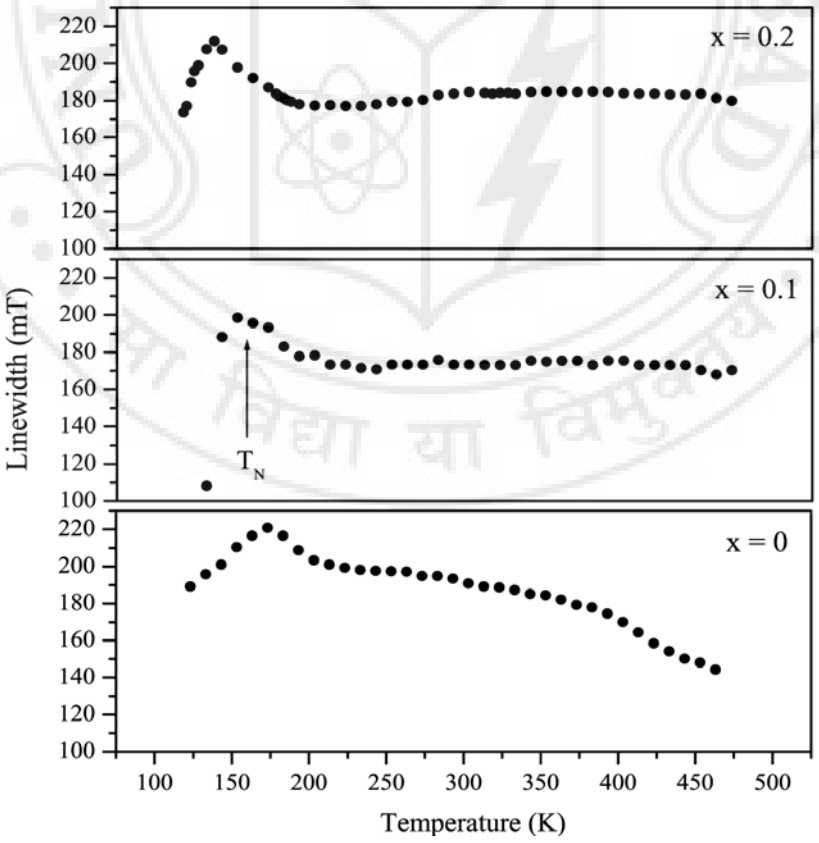

Figure 4.29 Temperature dependent linewidth of the BSCMO system.

Figure 4.29 represents the temperature dependent linewidth of the BSCMO system. The initial upward curve of the ΔH plots for $x = 0$ suggest the formation of AFM domains which emerge above T_{CO}. The slowing down of the upward curvature indicates the competition between the growing AFM and existing FM correlated domains in the PM + CO state. With further decrease in temperature a peak in the linewidth is observed due to the onset of the long range AFM ordering. For $x = 0.1$ ΔH shows a tempera ture independent behaviour throughout the temperature range indicating the coexistence of competing FM and AFM domains. This also reasons out the possible increase in the T_{CO} with increasing Ce content. The $x = 0.2$ sample exhibits an almost temperature independent ΔH. At T_O, ΔH increases rapidly with decreasing temperature due to the dominant AFM correlations, followed by a sharp drop indicating long range AFM ordering.

4.13 Magnetization studies on the BSCMO system

Figure 4.30 shows the magnetization data of the $Bi_{0.5}Sr_{(0.5-x)}Ce_xMnO_3$ system at room temperature. The slope of the plots gives the dc susceptibility of the samples. The value of the Curie constant estimated from χ_{dc} is shown in figure 4.31. It varies between

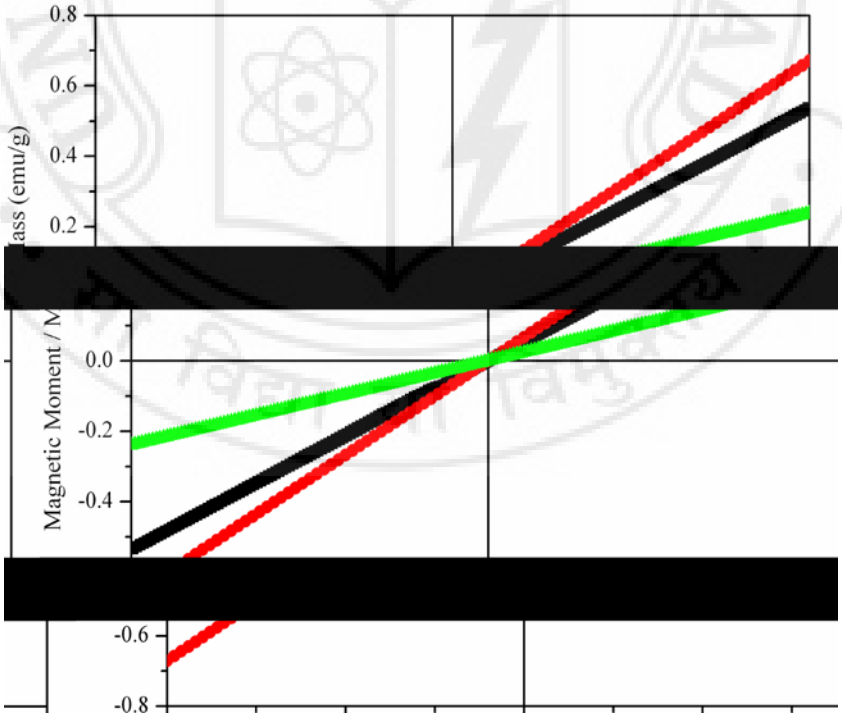

Figure 4.30 Room temperature magnetization data of the $Bi_{0.5}Sr_{(0.5-x)}Ce_xMnO_3$ system.

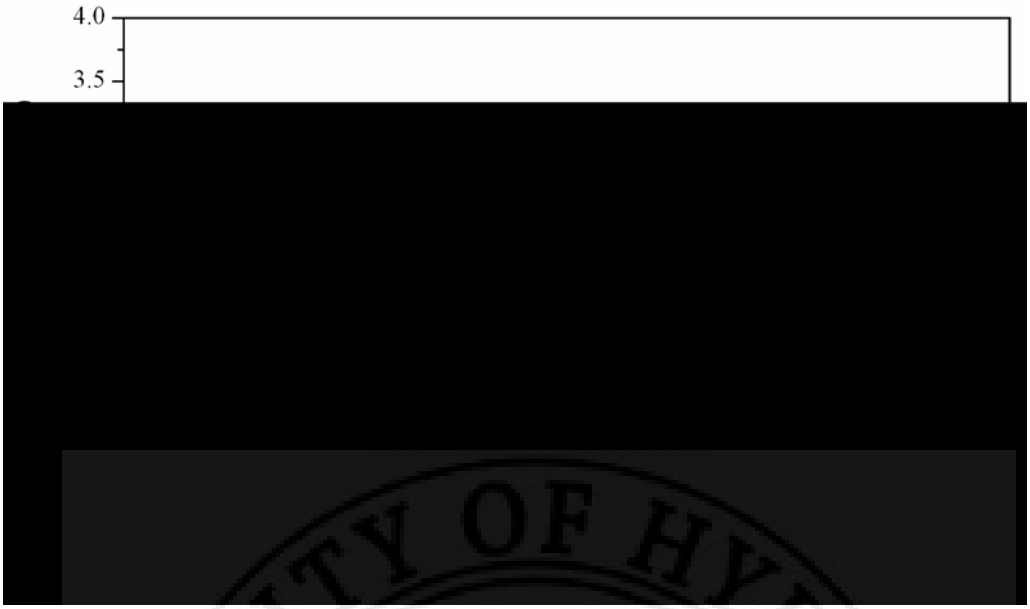

Figure 4.31. Compositional variation of the Curie Constant of the BSCMO system.

0.88 and 2.48 emu/mol for the samples. Cerium is also a magnetic ion. Hence apart from the contributions of the Mn ions to the magnetization Ce too, which is a multi valent ion, adds to the magnetization. The change in the magnetic moment can be attributed to a number of factors. Clusters of magnetic entities formed by the Mn^{3+}, Mn^{4+}, Ce^{3+} and Ce^{4+} ions as well as individual ions contribute to the magnetization of the samples. With changes in the doping levels the structure of the samples change with these changes reflected in the Mn – O bond length as well as the Mn – O – Mn bond angles, which may favour FM or AFM correlations. As Ce is doped in the half doped BSMO system the effect of the lone pair of electrons may play a significant role in deciding the magnetic properties of the system. The observed magnetization data cannot be ascribed to any single factor. The calculated value of C corresponds to the CO state of the present system.

4.14 ESR studies on $Bi_{0.5}Ca_{0.5}Mn_{(1-x)}Cr_xO_3$ (BCMCO)

Manganese is the core of DE in manganite compounds. Studies have been conducted on manganites highlighting the effect of doping at the Mn site. This, to check if DE hetero-ionic coupling is possible between Mn and the dopant ions. Doping with chromium (Cr^{3+}) has been of interest as it is isoelectronic with Mn^{4+}. The one-spin state or the t_{2g} orbitals are filled by Cr^{3+} $\left(t_{2g}^3 e_g^0\right)$ (S = 3/2), analogous to the Mn^{4+} ion and has an ionic radius closer to that of Mn^{3+}. Cr^{3+} ion is more stable and provides weaker binding for the additional e_g electron in spite of the lesser positive charge than Mn^{4+}. But Cr^{3+} is

more affected than Mn^{3+} by electron fluctuations from the adjacent oxygen site, as both the e_g orbitals are empty. The intermediate ionic state, Cr^{2+}, corresponds almost to Mn^{3+}. These peculiar properties of Cr make it an interesting dopant. There are many studies on Cr doped manganites [221 – 229]. Different arguments have been put forth regarding the magnetic coupling between Cr^{3+} and Mn^{3+}: one indicates that the AFM interactions play an important role [221 – 223] and another states that the FM

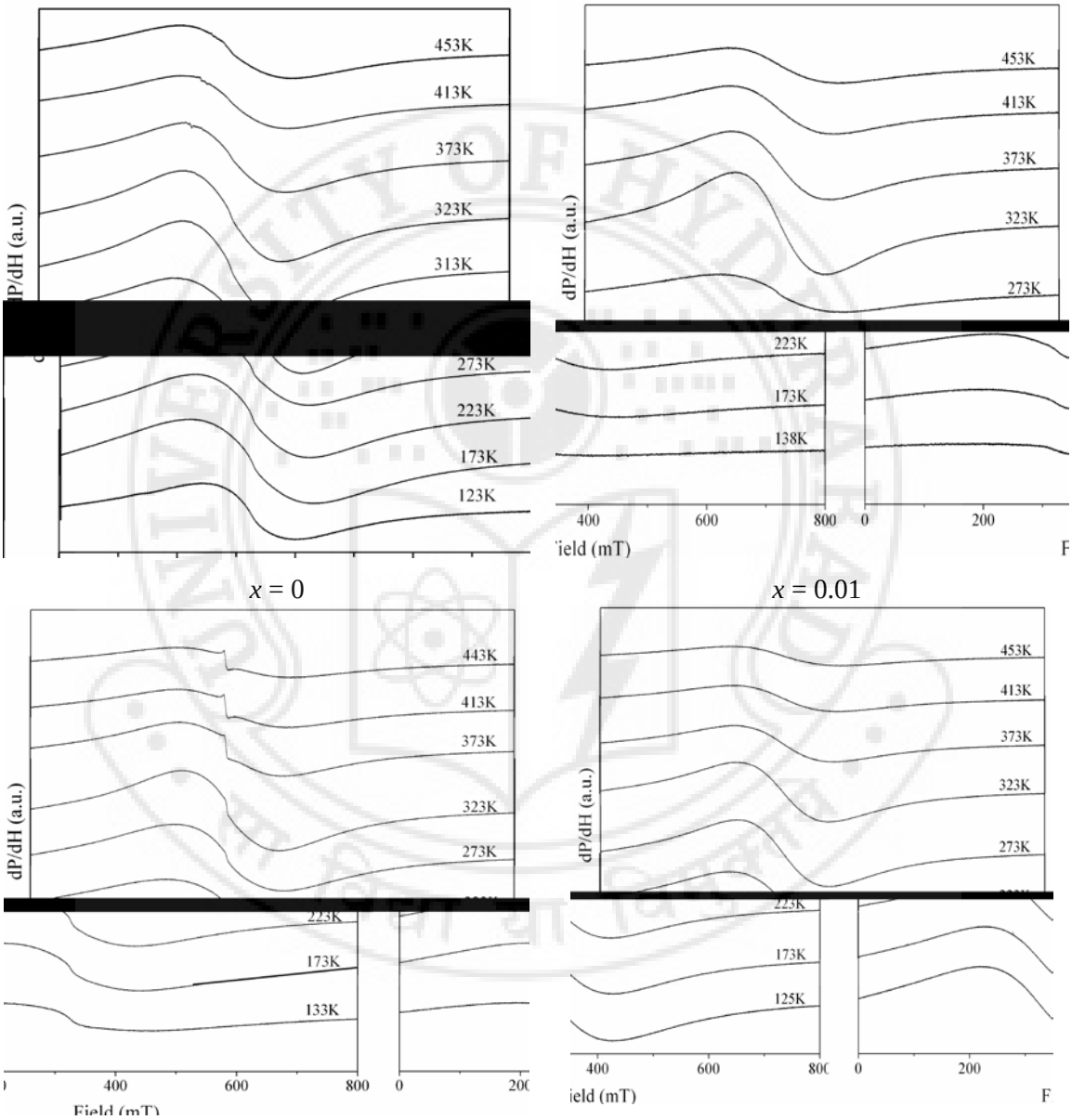

Fig 4.32 Temperature dependent ESR spectra of the $Bi_{0.5}Ca_{0.5}Mn_{(1-x)}Cr_xO_3$ system (x = 0, 0.01,0.03, 0.05).

Sample (x)	T_{CO} (K)	T_N (K)	ΔE (ESR) meV
0	317	163	163
0.01	309	158	78
0.03	295	142	74
0.05	278	133	77

Table 4.5 The skin depth, T_N and T_{CO} values for the $Bi_{0.5}Ca_{0.5}Mn_{(1-x)}Cr_xO_3$ system.

interactions due to superexchange (SE) and/or DE interaction are significant [225 – 229]. Hence the reasons for the different properties of manganites when Cr is doped at the Mn site are not conclusive and leave it to be a more or less open problem to ponder over. In the case of partial replacement of Mn^{3+} by Cr^{3+}, Mn^{3+} - O – Cr^{3+} is SE FM interacted, though this interaction is weaker than the DE FM interaction of Mn^{3+} - O – Mn^{4+}. In addition to this there is also the Cr^{3+} - O - Cr^{3+} antiferromagnetic interaction [230] which is analogous to Mn^{4+} - O - Mn^{4+} [231].

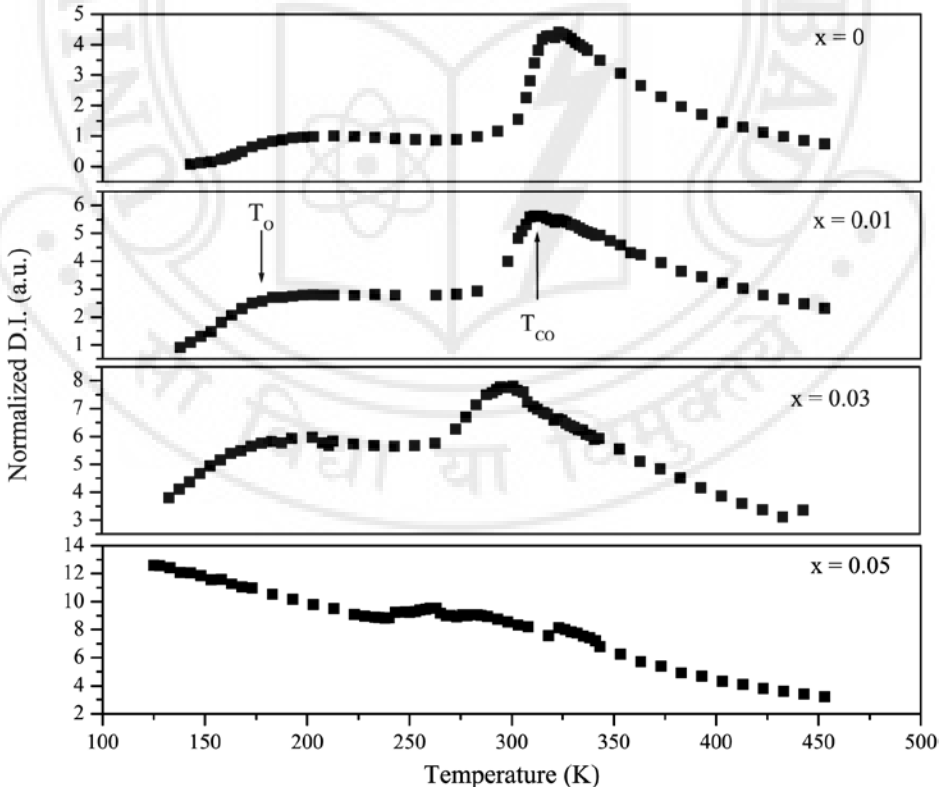

Figure 4.33 DI versus temperature plots for the $Bi_{0.5}Ca_{0.5}Mn_{(1-x)}Cr_xO_3$ system.

Figure 4.32 represents the temperature dependent ESR spectra of $Bi_{0.5}Ca_{0.5}Mn_{(1-x)}Cr_xO_3$ (x = 0, 0.01,0.03, 0.05). The intensity of the spectra increases with decreasing temperature. At temperatures near room temperature the intensity begins to decrease, indicating the setting in of an ordered AFM state. The temperature at which this decrease in the intensity occurs decreases with the increase in Cr content. For the sample with x = 0.05, the intensity of the resonance increases continuously with decreasing temperature indicating the absence of an ordered state in the temperature range of study. The spectra can be fitted by a lorentzian line shape. The skin depth estimated using equation (4.9) varies between 0.47 mm and 0.81 mm and is greater than the sample grain size.

The DI versus T plots of the $Bi_{0.5}Ca_{0.5}Mn_{(1-x)}Cr_xO_3$ system are shown in figure 4.33. Two distinct peaks are visible in the plots of x = 0, 0.01, 0.03. For these samples the peak at the higher temperature is assigned to T_{CO} (recorded in table 4.5) while the peak at the lower temperature to T_O. In the temperature range $T > T_{CO}$. The sample with x = 0.05 does not show any well defined T_{CO} and T_O. A number of minor peaks in the 240 – 340K temperature range indicates the presence of phases with a wide range of T_{CO}.

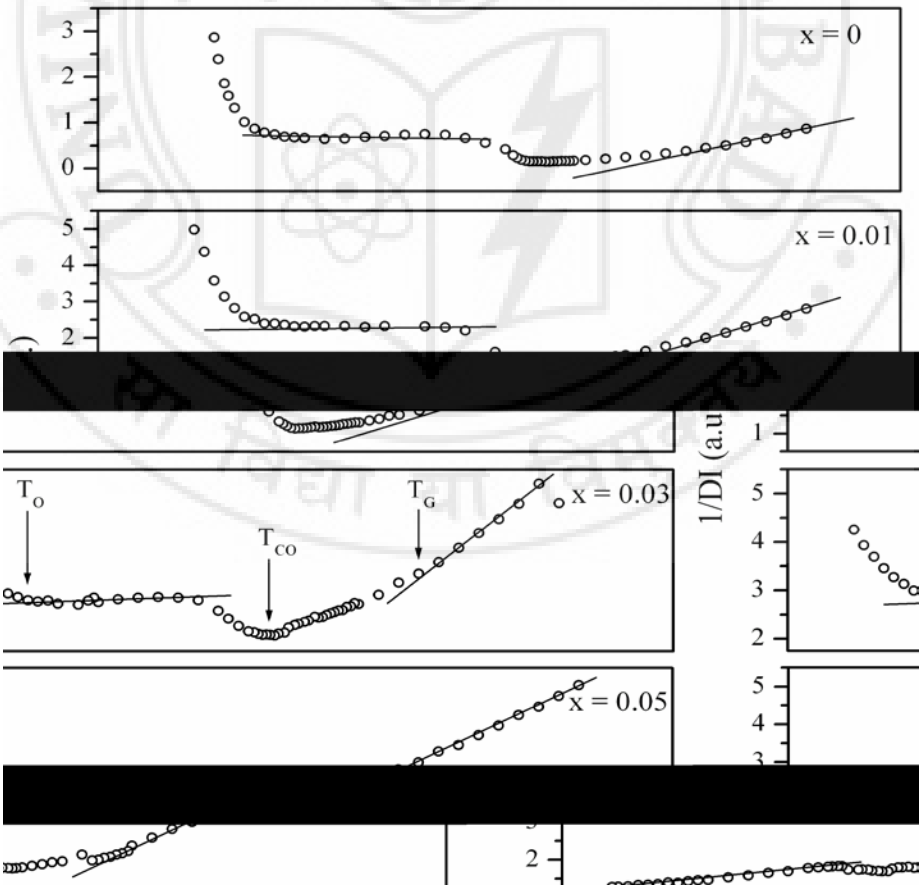

Figure 4.34 1/DI (χ_{ESR}) versus T plots for the $Bi_{0.5}Ca_{0.5}Mn_{(1-x)}Cr_xO_3$ system.

Figure 4.34 depicts the 1/DI v temperature plots of $Bi_{0.5}Ca_{0.5}Mn_{(1-x)}Cr_xO_3$. Samples x = 0, 0.01 and 0.03 obey the Curie-Weiss law in the high temperature region till T_G. As x increases T_G decreases, proving the Curie-Weiss behaviour to extend to a broader

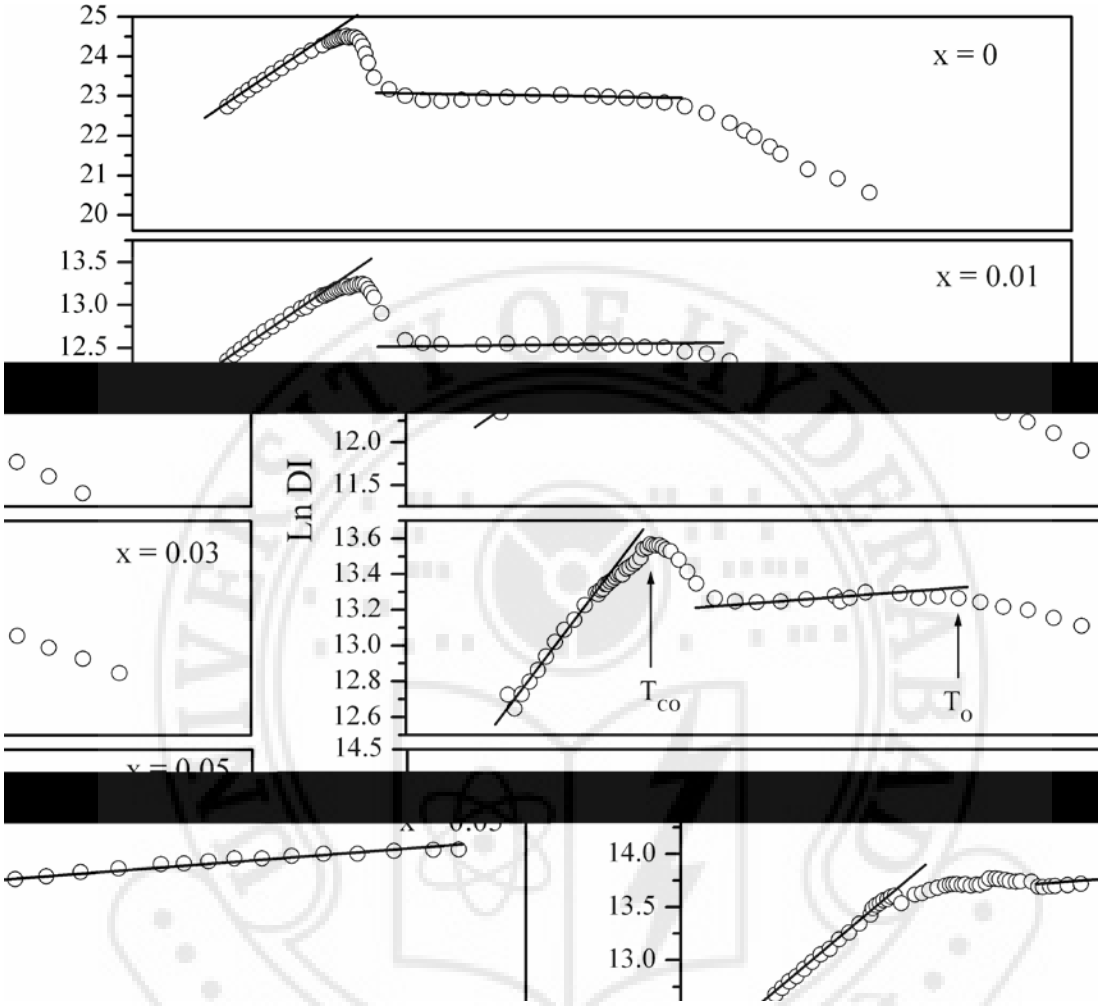

Figure 4.35 ln DI versus 1000/T plots for the $Bi_{0.5}Ca_{0.5}Mn_{(1-x)}Cr_xO_3$ system.

temperature range i.e. FM contributions increase with increasing x. Below T_{CO}, a change in the sign of the slope takes place due to the AFM correlations. The data fits the Curie-Weiss law in the range $T_{CO} > T > T_O$, but with a lower slope indicating stronger AFM correlations in the PM + CO state. The temperature independent region below T_O indicates the existence of FM inhomogenieties embedded in the long range AFM ordered matrix. The x = 0.05 sample shows a continuous decrease in 1/DI with decreasing temperature. Below ~ 340K the slope decreases, indicating emergence of AFM domains.

The ln DI v 1000/T plots of the system are shown in figure 4.35. The high temperature data obeys the cluster model given by the Arrhenius equation (4.10). The

activation energy is recorded in the table 4.5. As mentioned before, AFM clusters begin to form at $T > T_{CO}$. Below T_{CO}, a change in the sign of slope is observed. In the temperature range $T_{CO} > T > T_N$ the slope decreases, indicative of weakening of FM correlations. Below T_O, for the samples x = 0, 0.01 and 0.03, ln DI drops. For the sample x = 0.05, below T_{CO} ln DI continues to increase with decreasing T at a lower rate implying domination of FM correlations over the AFM correlations with no signature of onset of AFM order.

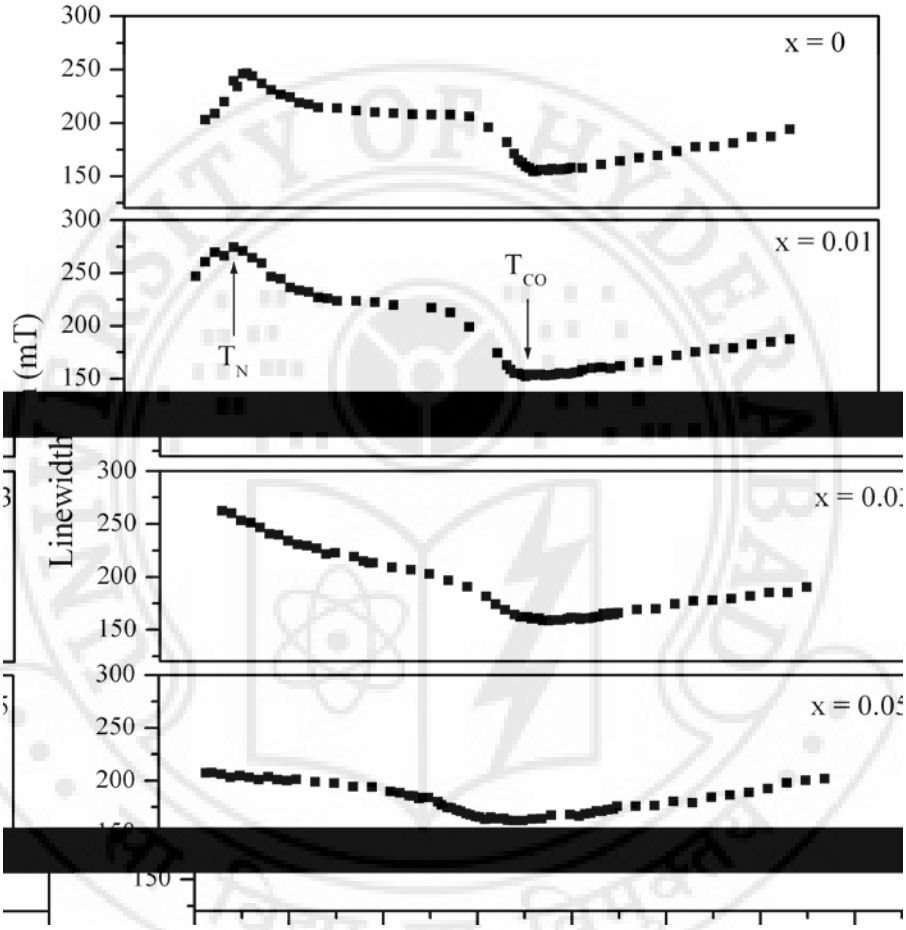

Figure 4.36 Temperature dependent linewidth of the $Bi_{0.5}Ca_{0.5}Mn_{(1-x)}Cr_xO_3$ system.

Figure 4.36 depicts the temperature dependent variation of ΔH of the system. The ΔH decreases continuously on cooling, till a minima is reached. This minima is assigned as T_{CO}. With increasing x T_{CO} decreases, indicating the strengthening of FM correlations at higher temperatures, which hinder the emergence of AFM contributions. The T_{CO} is well defined for samples with lower Cr content. As x increases T_{CO} becomes more diffuse and difficult to pin point. This shows that on nearing T_{CO} the samples with higher content of Cr continue to have stronger FM correlations, suppressing the AFM correlations favoured by the CO state. For samples x = 0 and 0.01, as temperature decreases below

T_{CO}, ΔH increases, remains almost constant and increases again to reach a peak at T_N. Below T_N, ΔH decreases rapidly with decreasing temperature due to the long range AFM ordering at low temperatures. The presence of FM inhomogeneities in the sample give the weak ESR signal even at very low temperatures. In samples with x = 0.03 and 0.05 ΔH show an increasing trend below T_{CO}. In the absence of data below 125K it is not possible to confirm the long range AFM ordering temperature for these samples with x = 0.03 and 0.05. The resistivity data for these samples is used to estimate the T_N and shows that it decreases with increase in Cr content.

4.15 Magnetization studies on the BCMCO system

The magnetization data of the $Bi_{0.5}Ca_{0.5}Mn_{(1-x)}Cr_xO_3$ system is depicted in figure 4.37. The slope of the plots gives the dc susceptibility of each sample. The value of the Curie constant is estimated and found to vary between 2.60 and 3.11 emu/mol as

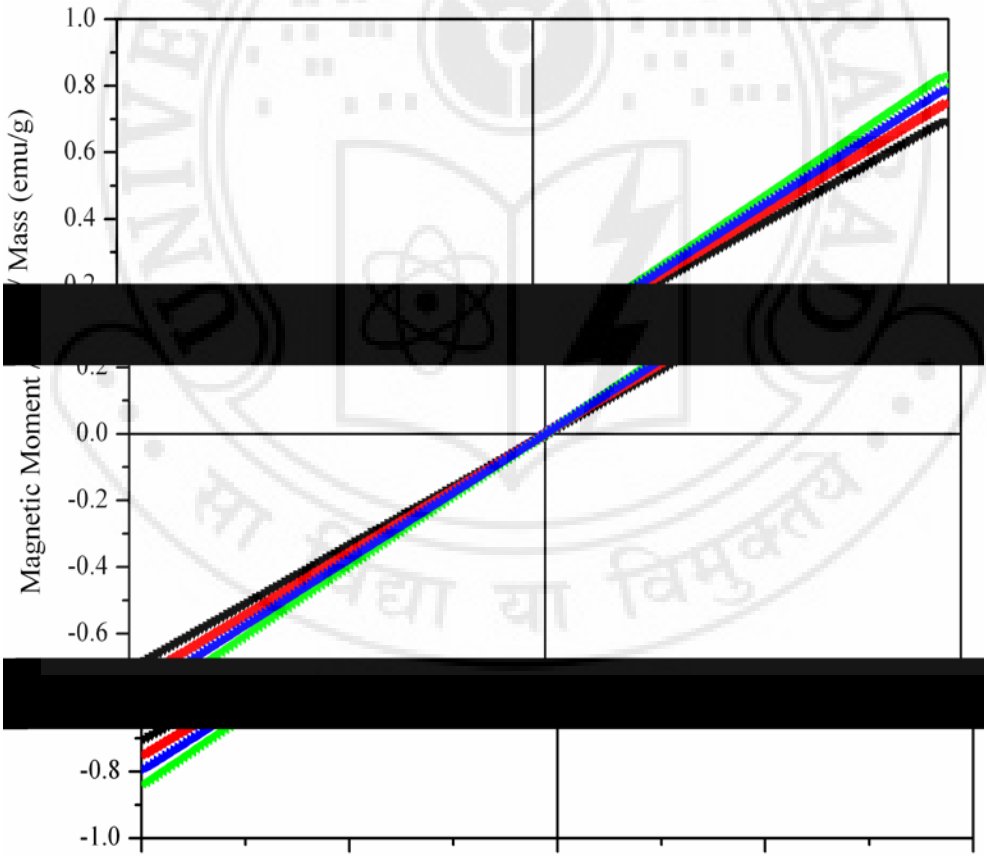

Figure 4.37 Room temperature magnetization data of the $Bi_{0.5}Ca_{0.5}Mn_{(1-x)}Cr_xO_3$ system.

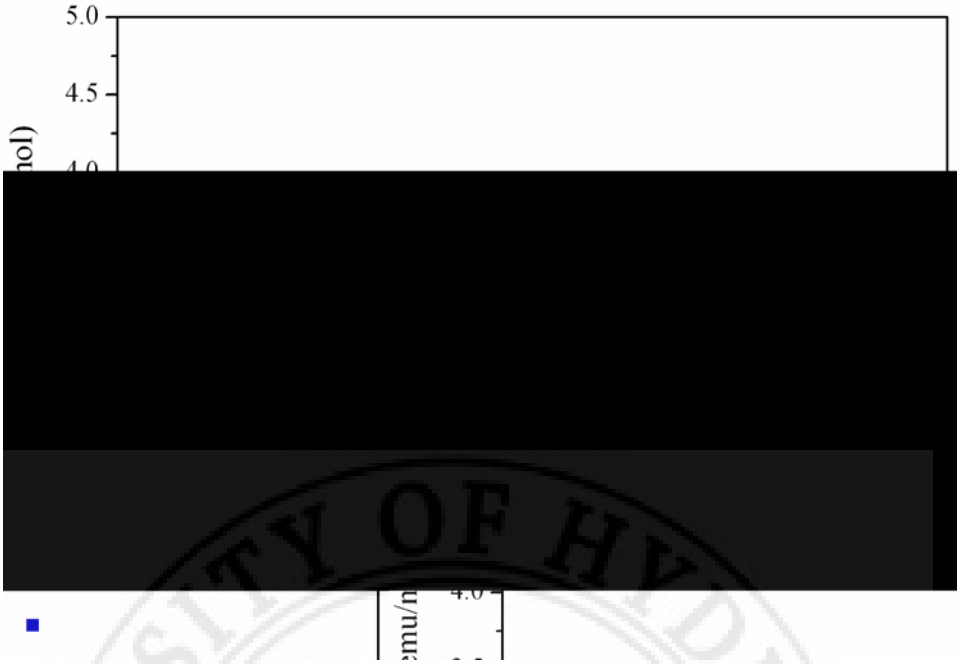

Figure 4.38 Compositional variation of the Curie Constant of the BCMCO system.

shown in figure 4.38. The variation of the magnetic moment or Curie constant can be attributed to the variation in the contributions from FM correlations, the clusters of different magnetic ions like Mn^{3+}, Mn^{4+}, Cr^{2+} and Cr^{3+} and contributions due to the individual ions. The slight variation in the structure with increase in Cr content may also contribute to the variation of magnetic moment.

4.16 ESR studies on $Bi_{0.55}Ca_{0.45}MnO_3$ Nanoparticles

The temperature dependent ESR spectra for the nanoparticle samples are shown in figure 4.39. All the samples show an initial increase in the intensity with decreasing temperature till around room temperature. On further decreasing the temperature the intensity begins to decrease.

Figure 4.40 presents the DI v T plots of the $Bi_{0.55}Ca_{0.45}MnO_3$ bulk and nano-sized samples. On cooling from high temperature, DI (χ_{ESR}) increases, reaching a maxima. This peak is assigned to T_{CO}. It is evident that with decrease in particle size the T_{CO} decreases slightly. Just below T_{CO} the sign of slope changes as seen for similar bulk samples [204, 205]. On further cooling DI increases again to reach a maxima denoted as $T_{O.}$ From these results the CO state is confirmed to be paramagnetic. The DI decreases sharply below ~170K until the ESR signal becomes very weak indicating the long-range AFM state. The T_N for all the samples remain constant at ~ 153K.

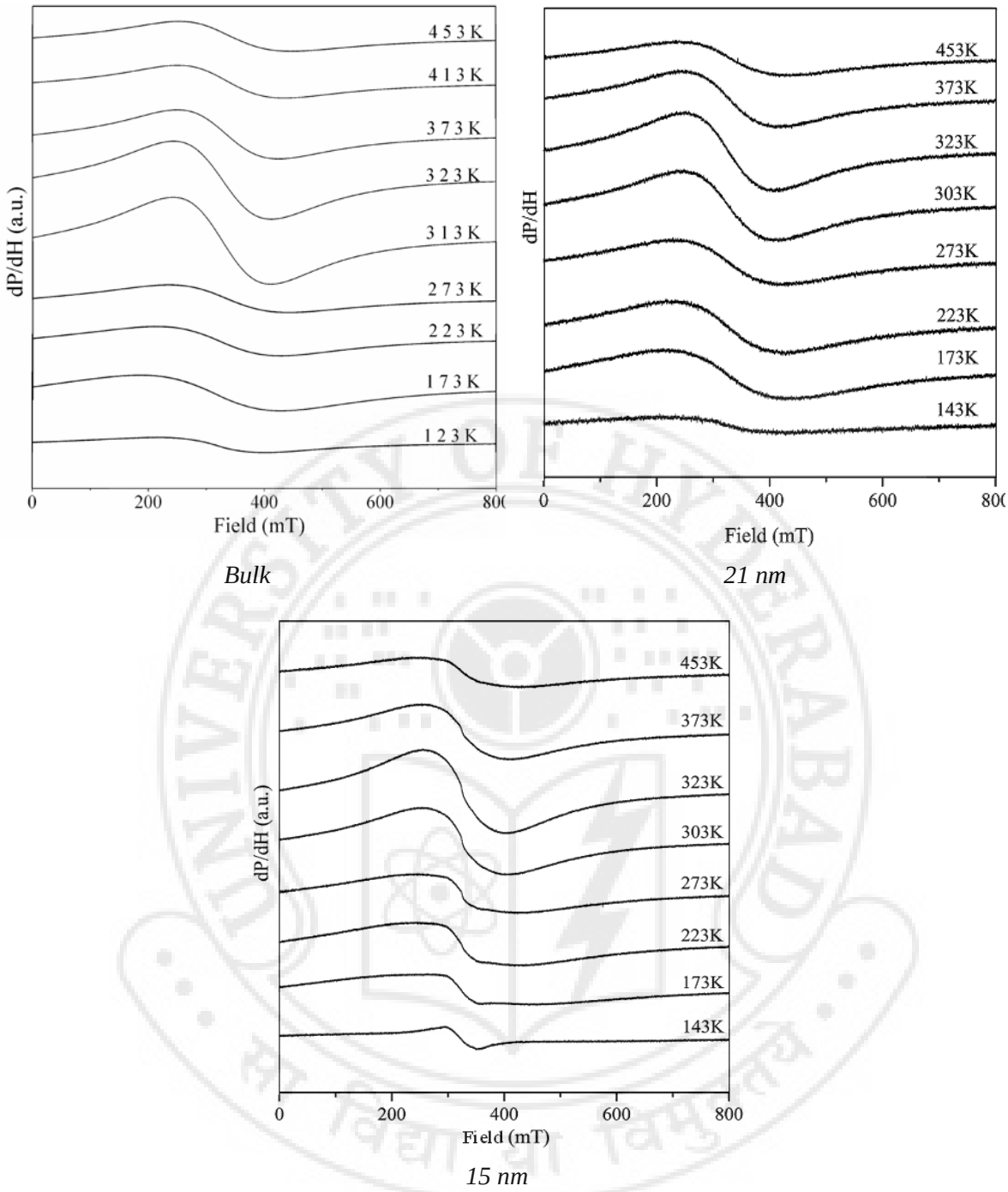

Fig 4.39 Temperature dependent ESR spectra of the $Bi_{0.55}Ca_{0.45}MnO_3$ system.

The non linear decrease of 1/DI with decrease in temperature (figure 4.41) is indicative of FM cluster formation in a PM matrix [204, 205]. The CO state favours AFM order and suppresses the FM-DE interaction giving rise to the peak at T_{CO}. This also explains the deviation from linearity in the 1/DI vs T plots above T_{CO}. In the temperature range $T_{CO} > T > T_N$ orbital-ordering sets in, bringing about long range AFM ordering. In this temperature range the Mn spins do not completely undergo OO and hence there is a

coexistence of FM and AFM phases. At T_{CO} and T_N the FM cluster size reduces as explained above. The features seen in the 1/DI v T plots are ascribed to the competition between the small FM clusters and the AFM matrix. The ESR susceptibility in the temperature range $T_N < T < T_{CO}$ is like PM susceptibility following the Curie – Weiss law with negative intercept on T – axis indicative of AFM correlations (straight line fits in the figure). A plain PM state does not exist in these materials. At temperatures far above T_{CO} FM correlations exist. As temperature decreases AFM correlations develop giving rise to the upward turn in 1/DI vs T plots. It is found that the AFM fluctuation contribution increases with the decrease in particle size. This signals that PM state in the temperature range $T_N < T < T_{CO}$ is dominated by AFM correlations as the particle size decreases.

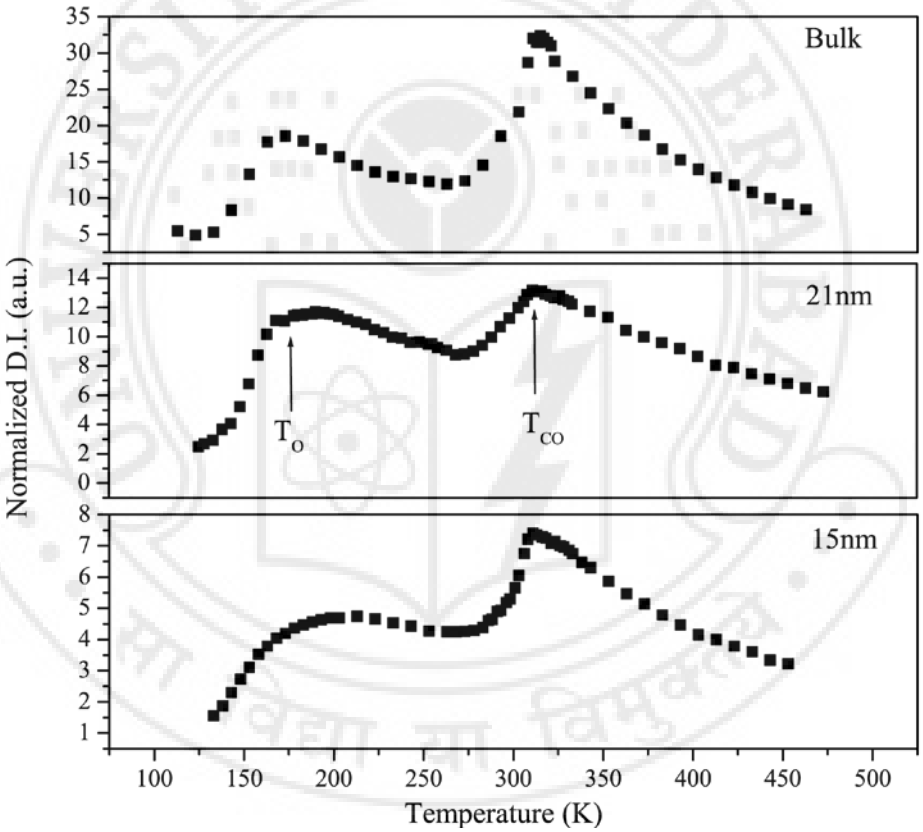

Figure 4.40. DI versus temperature plots for the $Bi_{0.55}Ca_{0.45}MnO_3$ system.

Figure 4.42 depicts the ln DI v T plots of the samples, which give information about magnetic interactions [163, 235]. The linear behaviour observed for the samples on cooling from high temperatures indicates short-range FM correlations. The peak observed between 305K < T < 315K in the plots of the samples is the T_{CO}. There is a deviation from the linear behaviour at a temperature higher than T_{CO} for all samples. The activation

energy calculated according to the magnetic cluster model from equation (4.10) is tabulated in table 4.6. A change in sign of the slope of the plot is observed at T_{CO}. In the CO state too a linear behaviour is observed, but with a decreased slope. The slope in the PM + CO state decreases with decrease in particle size. This indicates the weakening of FM correlations and evolution of AFM clusters as the sample goes from high temperature PM state to PM + CO state, with decreasing particle size. There is a sharp change in the

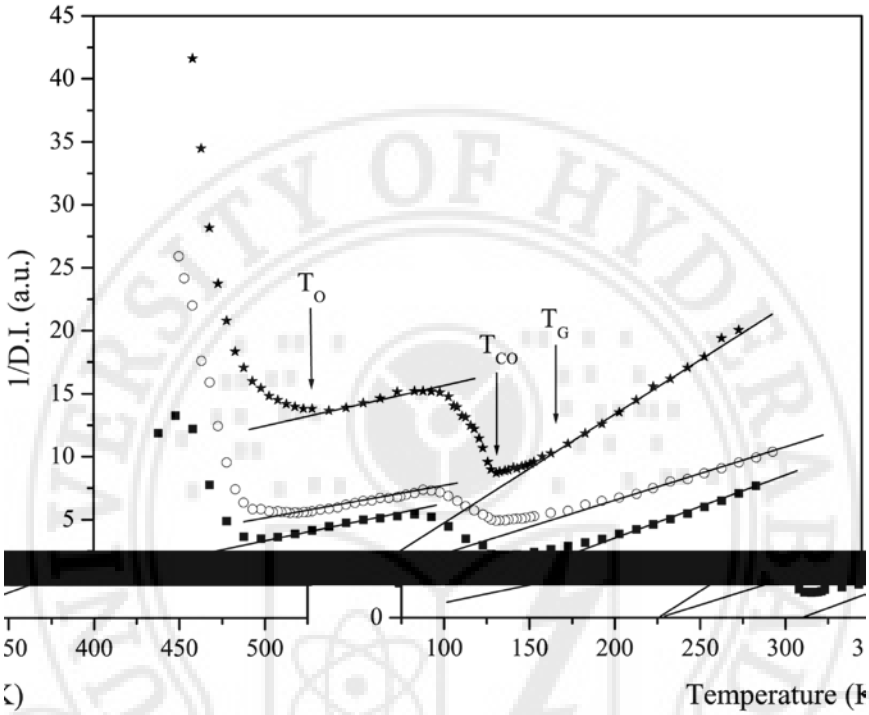

Figure 4.41. 1/DI vs T plots for the samples Bulk sample (filled squares), 21nm nanoparticles (open circles), 15nm nanoparticles (filled stars).

Sample	T_{CO} (K)	ΔE (meV)
Bulk	313	114
21nm	311	71
15nm	306	79

Table 4.6. Different parameters from the ESR studies of the $Bi_{0.55}Ca_{0.45}MnO_3$ system.

slope below ~ 170K. These results indicate that the onset of long-range AFM ordering takes place around this temperature. The sample goes into the AFM state at a lower

temperature where ln DI becomes temperature independent, presumably due to the existence of FM inhomogeneities embedded in the bulk AFM state.

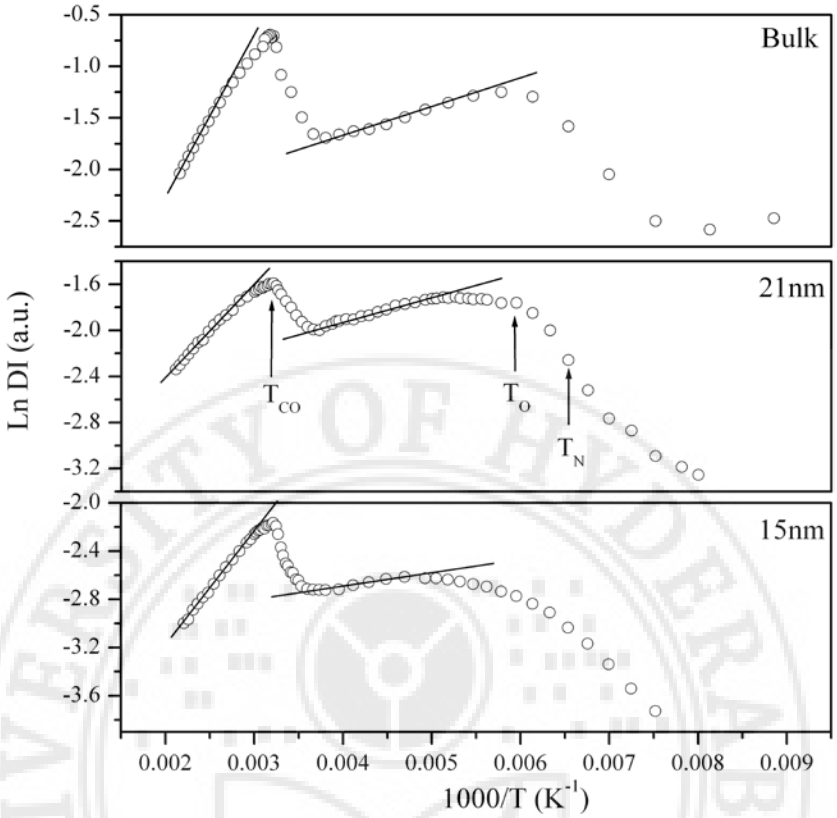

Figure 4.42. LnDI versus temperature plots for the $Bi_{0.55}Ca_{0.45}MnO_3$ system

Figure 4.43 shows the variation of peak to peak linewidth (ΔH) with temperature till T_N. In the temperature range $T > T_{CO}$, ΔH increases linearly with increasing temperature. In the CO state, $T_N < T < T_{CO}$, the ΔH first increases, remains constant over a temperature range and then increases again with decrease in temperature. ΔH is lowest for 15 nanometer-size sample among all samples and it increases sharply at T_{CO} and at T_N. This is depicted in a comparative plot of the ESR spectra at room temperature for all the samples is shown in figure 4.50. This implies that this sample has lowest concentration of magnetic inhomogeneities. The PM state in temperature range $T_N < T < T_{CO}$ is dominated by AFM correlations as the particle size decreases.

Hu's [179] rigorous derivation of linewidth of double-exchange (DE) interaction systems from fundamental mechanisms (as explained before) has been taken into consideration to explain the temperature dependent ΔH variation. Considering the spin correlation caused by DE interaction and superexchange (SE) interactions between manganese ions and anisotropic energy of spins caused by crystal field, the linewidth is

found to be approximately proportional to the temperature. The linear temperature dependence of linewidth in the temperature range $T > T_{CO}$ and the sharp upturn at T_{CO}

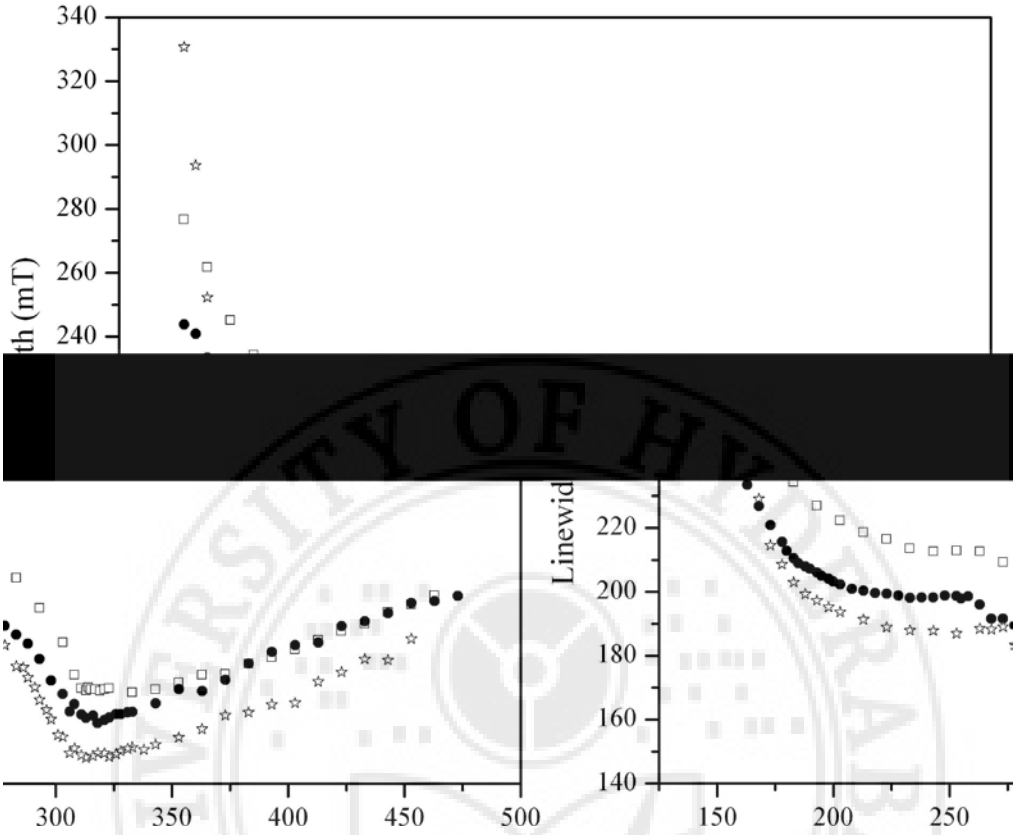

Figure 4.43. Linewidth vs T plots of the samples; Bulk sample (open squares), 21nm nanoparticles (filled circles), 15nm nanoparticles (open stars).

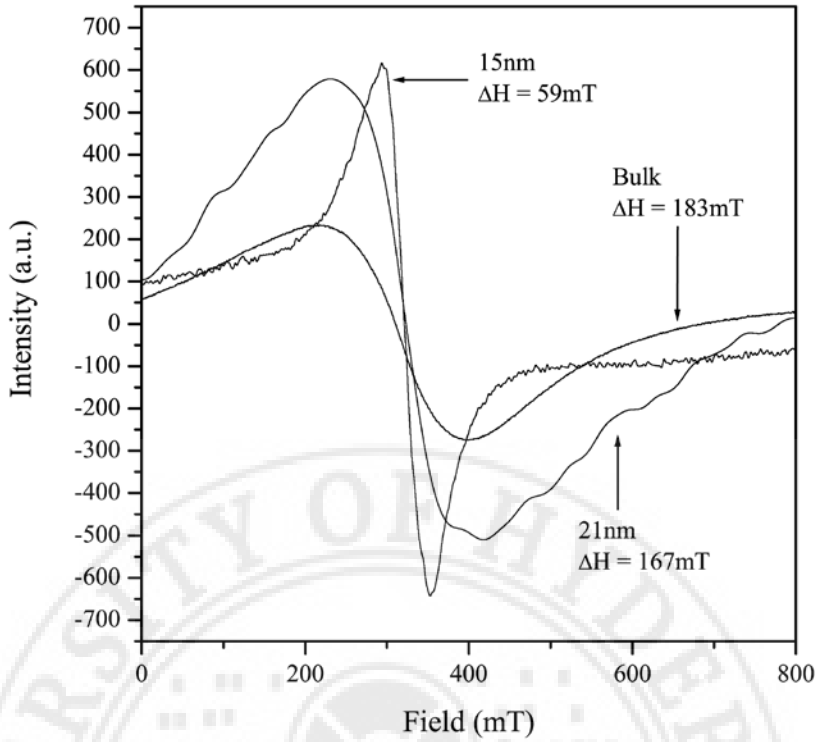

Figure 4.44. Variation of ESR spectra of the samples at 143K.

observed in the present study can be explained in view of this theoretical treatment. However, the ΔH temperature dependence for $T < T_{CO}$ in the CO state remains unexplained by this theoretical treatment.

Figure 4.44 depicts the variation of the resonance linewidth of the ESR signal from the FM inhomogeneities in the AFM long range ordered state at $T < T_N$ for different grain sizes. It shows that smaller the grain size the narrower is the linewidth. This is indicative of the decrease in average size of FM inhomogeneities with decrease in sample size. This also confirms that the increase in the sharpness of transitions at T_{CO} and T_N with decrease in the grain size is due to the decreased volume fraction of the FM inhomogeneities introduced in the samples as the grain size decreases.

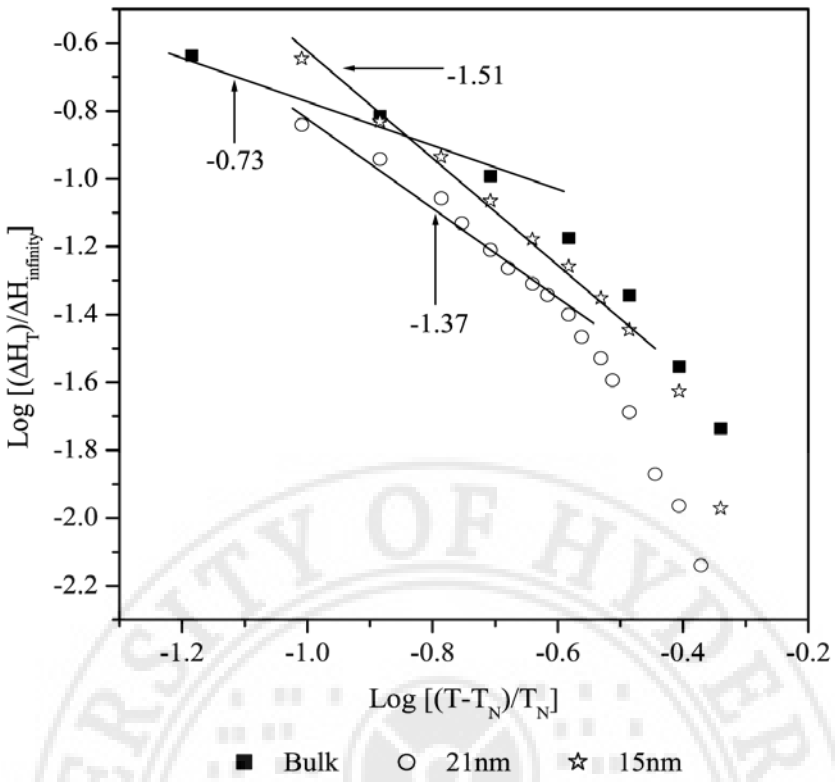

Figure 4.45. Residual linewidth vs temperature for the samples; Bulk sample (filled squares), 21nm nanoparticles (filled circles), 15nm nanoparticles (open stars).

The model developed by Huber and Seehra [166, 167], applied to the PM state of various ferromagnets and antiferromagnets, for plain PM - AFM transition, is examined for the linewidth variation for all the samples to the present (PM + CO) - (AFM + CO) transition state within the temperature range $T_N < T < T_{CO}$. The CO background is common in the PM as well as AFM state. Figure 4.45 shows the log – log plots of $\Delta H_T = (\Delta H - \Delta H_\infty)/\Delta H_\infty$ vs $(T-T_N)/T_N$, where ΔH_∞ is the constant linewidth, drawn to estimate the critical exponent for two samples with the slope values. The critical exponent increases with decrease in grain size. The critical exponent of -1.51 for 15 nanometer-size sample in the temperature range $\varepsilon < 0.3$, where $\varepsilon = (T-T_N)/T_N$ is close to theoretical value of -5/3 predicted by the model for plain PM to AFM transition. In this temperature range the AFM fluctuations dominate in these samples as explained earlier. It is possible that this model may be applicable in the case of a charge-ordered material with a PM state dominated by AFM correlations.

Summary of the ESR studies.

Temperature dependent ESR studies were carried out on various Bi – based manganites. The plots of double integrated intensity (DI) v temperature (T), ln DI v T and ΔH v T are used to get information on the magnetic interactions in different Bi – manganites. The room temperature magnetic moment measurements were carried out on all the samples to ensure the magnetic state of the materials.

The values of charge-ordering temperature T_{CO} and Neel temperature T_N estimated from ESR data for the BCMO system vary in the range 301 – 320K and 148 – 160K respectively and are comparable to values obtained by other techniques reported in the literature. It is found that the magnetic phase for $T > T_{CO}$ is dominated by FM

correlations which can be attributed to activated Mn^{3+}–Mn^{4+} hopping of a small polaron. In the temperature range $T_{CO} > T > T_N$, the domains of FM and AFM spin correlations coexist. The contribution of AFM correlations progressively increase with the increase in Ca content for samples with $0.4 \leq x \leq 0.6$ while for samples with $x = 0.7$ and 0.75 at lower temperatures the re emergence of FM correlations is evidenced. The sharp change in the slope of ln DI versus 1000/T plot at ~170–190K indicates the onset of long–range AFM order. For $T < T_N$, temperature independent ln DI indicates the freezing of FM microdomains/ inhomogeneities in the AFM long-range ordered state.

The ESR studies were conducted on the BSMO system with the samples in the CO state. The T_{CO} is not observed for these samples in the temperature range of study confirming that it is above 475K, the maximum temperature achieved in the experimental setup. The T_N values increase from 133K to 173K with increase in Sr content and are comparable with values reported in literature estimated by other techniques. In the temperature range $T_{CO} > T > T_N$, the domains of FM and AFM spin correlations coexist. The contribution of AFM correlations progressively decreases with the increase in Sr content. The temperature range of the PM + CO phase is narrowed with increase in Sr content. Similar to the BCMO system, the sharp change in the slope of ln DI versus 1000/T plot indicates the onset of long – range AFM order. For $T < T_N$, temperature independent ln DI indicates the freezing of FM microdomains/ inhomogeneities in the AFM long-range ordered state.

The ESR studies on the BCSMO system explore the effect of mixed (Ca,Sr) doping on the electronic phase separation of the material. With increasing Sr content, till $x = 0.1$, FM correlations increase, melting the charge ordering and weakening the long range AFM ordering. The T_{CO} values estimated for $0 \leq x \leq 0.1$ vary between 288 and 320K. For the sample with $x = 0.1$ the T_{CO} is hardly visible. On further increase of Sr content the T_{CO} reappears at a higher temperature of ~ 390K. This is assigned to the formation of an Sr – rich $Bi_{0.25}Sr_{0.75}MnO_3$. The T_N is ~ 150K for all samples except the samples with $x = 0.1$ and 0.16, which show no AFM ordering. With the increase in Sr content from $x = 0.04$ to 0.1 the FM correlations increase resulting in the weakening of the CO and AFM transitions. The CO and the AFM transitions are barely noticed in the sample with $x = 0.1$. With further increase in Sr content CO transition reappears but at a higher temperature of ~ 390K, which may be assigned to $Bi_{0.25}Sr_{0.75}MnO_3$ phase [112]. At $x = 0.1$ the FM domains permeate almost the entire volume of the sample with AFM domains interspersed in between. This picture is supported by the observation of very feeble CO

and AFM transitions. In summary, addition of Sr first leads to the melting of CO state. At around 25% of Sr the melting of CO state is complete. At around 40% of Sr the CO state reappears due to the formation of $Bi_{0.25}Sr_{0.75}MnO_3$ phase. Further increase in Sr content leads to formation of $Bi_xSr_yMnO_3$ phases having high T_{CO}s. The growth of high T_{CO} phases is a continuous evolution process with increase in Sr content.

The temperature dependent ESR studies on BSCMO system in the PM + CO phase confirm the coexistence of FM and AFM correlations in this phase. The T_N values decrease from ~ 173K to ~ 138K with increase in Ce content. The variation of the slope in the 1/DI v T plots indicate that with increase in Ce the AFM correlations strengthen. The CO state widens with increasing Ce content. For $T < T_N$, temperature independent ln DI indicates the freezing of FM microdomains/ inhomogeneities in the AFM long-range ordered state.

The effect of Cr doping on the magnetic phase separation in $Bi_{0.5}Ca_{0.5}Mn_{(1-x)}Cr_xO_3$ (x = 0 - 0.05) was explored by temperature dependent ESR studies. The volume fraction of FM domains increase at the expense AFM domains. The Charge Ordering is suppressed with the increase in Cr content. With increase in Cr content the CO transition is smeared and it almost disappears at $x = 0.05$. The T_{CO} decreases from 317K to 278K as x increases from 0 to 0.05. The value of T_N, is ~160K for the $x = 0$ and 0.01 samples and it decreases to ~ 120K for sample with $x = 0.05$. A strong competition between the FM and AFM correlations is observed as a function of composition and temperature in the temperature range $T_N < T < T_{CO}$.

Temperature dependent ESR studies were carried out on two samples of $Bi_{0.55}Ca_{0.45}MnO_3$ (grain size 21 and 15 nm) synthesized by sol-gel process and compared with the studies on corresponding bulk sample. The T_{CO} value decreases from 313K for bulk to 306K for 15 nm size sample. The T_N values remain around 153K for all the samples. The magnetic phase for $T > T_{CO}$ is dominated by FM correlations which is attributed to activated Mn^{3+}–Mn^{4+} hopping of a small polaron. In the temperature range $T_{CO} \leq T \leq T_N$, the domains of FM and AFM spin correlations coexist. The FM phase volume decreases and the PM – PM + CO and PM + CO − AFM + CO transitions become sharp with decrease in grain size.

In the temperature range $T > T_{CO}$, ΔH increases linearly with increase in temperature. In the charge-ordered state, $T_N < T < T_{CO}$, the ΔH first increases, remains constant over a temperature range and then again increases with decrease in temperature.

The ΔH decreases sharply below T_N. The temperature dependence of ΔH in the temperature range $T < T_{CO}$ is completely different from other manganites. The linear temperature dependence of linewidth in the temperature range $T > T_{CO}$ and the sharp upturn at T_{CO} observed can be explained in view of the theoretical model given by Hu [179]. The validity of other predictions of the model such as downward bending and $(T/T_C)^{1/2}$ temperature dependence of linewidth in high temperature range cannot be check as no data is available in an extended high temperature range. The ΔH temperature dependence for $T < T_{CO}$ in charge ordered state remains unexplained by this theoretical treatment.

The ΔH variation in the samples for the temperature range $T_{CO} > T > T_N$ is analyzed in view of the theoretical treatment of ESR line broadening and spin–spin relaxation near critical points given by Huber and Seehra [166, 167] which has been applied to the PM state of various ferromagnets and antiferromagnets. The CO background is common in the PM as well as AFM state. The critical exponents estimated for the BCMO system from the log – log plots varies from − 0.73 to − 1.12 depending on the composition of the sample in the temperature range $\varepsilon < 0.25$, where $\varepsilon = (T - T_N)/T_N$. For the BCMO nanoparticle system the critical exponent increases with decrease in grain size. The critical exponent of -1.51 for 15 nm size sample in the temperature range $\varepsilon < 0.3$ is close to theoretical value of -5/3 predicted by the model. It is possible that this model may be applicable in the case of charge ordered material having PM state dominated by AFM correlations.

The ESR data on these Bi -manganites strongly suggest the existence of two-phase behaviour in the temperature range between T_{CO} and T_N. The phase separation between hole rich FM domains and AFM domains near the CO regime has been predicted to be universal for manganites [58]. The optical conductivity studies [119] and neutron scattering studies [118] on single crystals of $Bi_{(1-x)}Ca_xMnO_3$ (x = 0.74 and 0.82) have provided evidence of coexistence of AFM and FM clusters in $T_{CO} > T > T_N$ temperature range. These studies have shown that the magnetic intensity from AFM clusters develops at the expense of magnetic intensity from FM clusters in $T_{CO} > T > T_N$ temperature range. In recent years, coexistence of FM and AFM domains in different types of manganites has been treated in terms of the Griffiths phase (GP) concept. A number of experimental studies have revealed the existence of GP in the PM state of manganites, namely, ESR studies by Deisenhofer *et. al.* in $La_{1-x}Sr_xMnO_3$ [195] Zhou *et. al.* in

La_2NiMnO_6 [196], magnetization studies by Qian *et. al.* [197] in $La_{0.15-x}Y_xCa_{0.85}MnO_3$, Raman scattering by Kim *et. al.* [198] in $La_xPr_yCa_{1-x-y}MnO_3$.

According to the Griffiths theory [67], there is always a finite probability of finding FM clusters for a system with randomly distributed spins in the temperature range of $T_{C(p)} < T < T_G$ between the random transition temperature $T_{C(p)}$ and the pure transition temperature T_G. Bray [199] extended the argument to any bond distribution that reduces transition temperature, terming the phase between $T_{C(p)}$ and T_G as GP. GP is thus characterized by the formation of FM clusters below T_G. These clusters are formed thermodynamically during cooling and nucleated by the intrinsic randomness of a doped material, and amplified by the tendency for polaron formation and charge segregation [200, 201]. The existence of the GP is therefore intrinsic to perovskite manganites and in general to all magnetic systems [13].

The GP physics model can be used to explain the present ESR measurements. When lowering the temperature from high temperatures, the susceptibility first increases due to the formation of short-range FM clusters which are segregated within the PM matrix. The FM clusters have larger spins (and hence larger susceptibilities) compared with individual magnetic ions and as a consequence a higher value of Curie–Weiss temperature θ is obtained. But this tendency to FM order is destroyed by charge ordering that favours AFM giving rise to quenching of DE interaction and a peak in the DI versus T plots at T_{CO}. This explains the deviation of 1/DI versus T plots from Curie–Weiss form in the PM state for $T > T_{CO}$. In the temperature range $T_{CO} > T > T_N$ orbital ordering sets in progressively leading to long-range AFM order at around 150K. In this temperature range the Mn ions remain charge ordered without complete orbital ordering. In this picture, the FM and AFM domain coexist at all temperatures below the first formation of charge ordered state. These conclusions are supported by the SANS measurements by Qin *et. al.* [105] on $Bi_{0.125}Ca_{0.875}MnO_3$. These studies have revealed the formation of FM spin clusters (average size 1–10 nm) in the AFM background when temperature is decreased. Above T_C large magnetic clusters exist. When the temperature is further decreased smaller clusters (size 1–3 nm) will emerge, causing a decrease in average cluster size but increased overall magnetization. In the present system the larger FM clusters formed in the PM state may undergo a reduction in size at T_{CO} and T_N. The small FM clusters (size 1–3 nm) may persist in the long-range AFM state as indicated by temperature independent DI below ~150K for the samples. The complicated DI versus T behaviour as a function of composition in the temperature range $T_{CO} > T > T_N$ arises due to strong

competition between AFM and FM clusters whose size (volume fraction) will be decided by the composition of the sample and the average size of the FM clusters in the PM state.

The temperature dependence of ΔH in the range $T_N < T < T_{CO}$ can be due to the phase segregation in view of GP formation as discussed above. The sharp increase in ΔH occurs whenever there is transition from PM to an ordered magnetic state. Therefore, the sharp increase in ΔH at T_{CO} from the minimum value may be due to the formation of AFM clusters as the temperature is decreased. Since the orbital ordering evolves progressively with decrease in temperature, another sharp increase in ΔH occurs when the AFM clusters form a long-range AFM order at T_N. The sharp decrease in ΔH as temperature decreases below T_N is due to the existence of FM nanoclusters embedded in the AFM matrix of the sample. The gradual increase in ΔH with decrease in temperature and the peaking effect has also been reported in other manganites [206] and one-dimensional antiferromagnets [207]. It is now well known that in manganites there is a strong interplay of spin, charge and orbitals making it difficult to assign the observed variation in ΔH to any one single factor.

This chapter deals with the electrical resistivity studies on various synthesized compositions of Bi – manganites

5.1 Introduction of dc conduction in manganites:

The electrical resistivity of CMR materials were initially attributed solely to the DE mechanism. A theoretical consideration [238] of $La_{(1-x)}Sr_xMnO_3$ predicted band broadening at the FM transition, reducing the gap and leading to increased or metallic conductivity in the FM state and activated conductivity above T_C. But magnetic interactions alone cannot explain CMR [31]. Jaime *et. al.* [239] reported the low temperature and high temperature resistivity of partially annealed $La_{2/3}Ca_{1/3}MnO_3$ films, suggesting transport via small polarons and magnetic polarons respectively.

Mott and Davies discussed the formation and transport properties of small lattice polarons in strong electron-phonon (*e*-ph) coupled systems, in which charge carriers are susceptible to self-localization in energetically favorable lattice distortions, in disordered materials [240] and later extended to crystals [49, 241, 242] Kasuya and Yanase [243] described the transport mechanism as being the thermal polaron hopping between sites, considering the behaviour of purely magnetic polarons, defined as a carrier localized at impurity centers by a polarization cloud. They concluded that the hopping activation energy disappears if the moments are aligned by an external magnetic field and that the material transforms from a semiconductor to a 'dirty' metal, exhibiting a large negative magnetoresistance. Mott [49] argued that the mobility of purely magnetic polarons is diffusive in nature, i.e., it obeys a power law rather than exhibiting a thermally activated temperature dependence. Emin [241] considered the nature of lattice polarons in magnetic semiconductors where, magnetic polarons are carriers self-localized by lattice distortions but also surrounded in a magnetic cloud.

In semiconducting or insulating manganites the temperature dependent transport properties are usually explained by the small polaron hopping conduction or the variable range hopping conduction mechanism.

A brief theoretical review of these models is given below:

5.1a Thermally activated polaron hopping model:

The conductivity of a material interpreted in terms of the polaron hopping conduction theory by Mott is based on the strong electron – phonon coupling approximation. If the carrier together with its associated crystalline distortion is comparable in size to the cell parameter, the object is called a small, or *Holstein,* polaron. A band of local states can form as a number of sites in the crystal lattice which will be energetically equivalent. These energy bands are extremely narrow and the carrier mobility associated with them is predominant only at low temperatures. These are not extended states even at the highest temperatures. Electrical conduction then occurs via either quantum tunneling or thermal hopping of the small (Holstein) polaron among sites. Three different temperature regimes can be distinguished. At very low temperatures, where $k_BT \leq 10^{-4}$ eV, the only possible mechanism is quantum tunneling between neighbouring distortions. For the temperature range $T \leq \theta_D/2$ (where θ_D is the Debye temperature), phonon assisted hopping dominates, producing a conductivity whose general formula is given as $\sigma \propto exp(T^{-1/4})$, which is not associated with variable range hopping. At the highest temperatures the dominant mechanism is thermally activated hopping of carriers. The expression for small polaron hopping conduction is given by [49, 244 – 248]

$$\sigma_{dc} = \sigma_O exp(-2\alpha R)\left[\exp\left(-\frac{W_H}{k_B T}\right)\right] \tag{5.1}$$

where ,

$$\sigma_O = \frac{ne^2R^2\vartheta C}{k_B(1-C)} \tag{5.2}$$

Here n is the density of the polaron, υ is the optical phonon frequency, W_H is the activation energy which could be connected to the binding energy of the polaron or also called the polaron hopping energy, α is a factor inversely proportional to the localization length of the hydrogenic wavefunction describing the localized state, the term exp(-αR) represents the electron overlap integral between sites and R is the hopping distance of a polaron which is taken as the average intersite spacing obtained from the unit volume and C is the polaron concentration. For this type of conduction there are two specific cases to be considered: the adiabatic and non adiabatic cases. It represents the ease with which the small polaron adjusts with modifications in the ionic position. If it readily adjusts then the hopping is adiabatic or else non adiabatic. In the adiabatic case, the polaron has a high probability of jumping into the next site, and it is assumed that the polaron makes several

jumps back and forth before the phonon wave recedes [244, 249]. The hopping of the small polarons occur between the nearest – neighbour Mn ions which leads to mobility in the thermally activated form. The equation for the conductivity in the adiabatic case is given as :

$$\sigma_{dc}T = \frac{ne^2R^2\vartheta}{k_B}\left[\exp\left(-\frac{W_H}{k_BT}\right)\right] \tag{5.3}$$

In the non adiabatic approximation, the polaron is assumed to have a small probability of making a jump during each attempt period, and the equation for this case is given as :

$$\sigma_{dc}T^{3/2} = \frac{ne^2R^2}{k_B}\frac{\pi J^2}{h}\left(\frac{\pi}{W_H k_B}\right)^{1/2} exp\left(-\frac{W_H}{k_BT}\right) \tag{5.4}$$

where J is the polaron bandwidth.

From the model proposed by Mott and Davis [49] J can be calculated independently and is given as

$$J \sim e^3\left[\frac{N(E_F)}{\varepsilon_p^3}\right]^{1/2} \tag{5.5}$$

where

$$\varepsilon_p = \left(\frac{1}{\varepsilon_S} - \frac{1}{\varepsilon_\infty}\right) \tag{5.6}$$

where ε_∞ and ε_S are the high frequency and static dielectric constants of the samples under study respectively.

If the density of states, $N(E_F)$, of a system is known the nature of the hopping conduction can be identified from the Holstein's condition [240]. According to this condition the polaron bandwidth J should satisfy the inequality $J > \varphi$ for the adiabatic hopping conduction and $J < \varphi$ for the non adiabatic hopping conduction where

$$\varphi = \left(\frac{2k_BTW_H}{\pi}\right)^{1/4}\left(\frac{h\vartheta_{ph}}{\pi}\right)^{1/2} \tag{5.7}$$

Here υ_{ph} is the phonon frequency. The calculated values from equation (5.5) are compared with that of equation (5.7) and by the Holstein's condition the type of hopping conduction the samples under study follow is determined.

The *J* value can also be estimated from the equation

$$J \propto exp(-\alpha R) \tag{5.8}$$

or

$$J = J_0 exp(-\alpha R) \tag{5.9}$$

The ion–ion separation influences the conduction mechanism [43]. When the overlap integral $J_0 exp(-\alpha R)$ approaches J_0, i.e. $exp(-\alpha R)$ approaches 1, the hopping is adiabatic ($\alpha \sim 0$) and the semiconducting behaviour is then controlled mainly by the activation energy. Hence the dc conductivity can be given by a general formula

$$\sigma_{dc} \sim \sigma_O exp\left(-\frac{W}{k_B T}\right) \tag{5.10}$$

otherwise the hopping conduction mechanism is non-adiabatic ($\alpha \neq 0$). The equation (5.9) can generally explain the semiconducting behaviour for all samples at high temperatures i.e. for $T > \theta_D/2$. The activation energy also plays an important role in the conduction mechanism at high temperatures. For the activation energy of hopping conduction for $T > \theta_D/2$ can be written as [246]

$$W = W_H + \frac{W_D}{2} \tag{5.11}$$

where W_D is the disorder energy.

The polaron radius r_P can be calculated if the number of transition metal ions (Mn) per unit volume, N, is known by the relation

$$r_p = \frac{1}{2}\left[\frac{\pi}{6N}\right]^{1/3} \tag{5.12}$$

In the polaron model W_H decreases with the decrease in temperature. For $T < \theta_D/4$ the activation energy of hopping conduction is equal to the disorder energy as the polaron hopping energy $W_H \approx 0$, and hence it can be stated that $W \approx W_D$.

The activation energy for the hopping conduction is energy for the Emin and Holstein [245] gave a generalized polaron hopping model based on a molecular crystal model in which the disorder energy $W_D = 0$. According to this model the polaron bandwidth *J* should satisfy the condition $J < W_H/3$ for the formation of a small polaron.

5.1b Mott's variable range hopping model (VRH):

With decreasing temperature the concentration of electrons decreases exponentially and their contribution to conduction diminishes [250]. Tunneling transitions of electrons between localized states dominate the charge transport in disordered semiconductors. This transport is called hopping as this kind of an incoherent chain of tunneling transitions of electrons . From the study on disordered insulators Mott [49] derived a formula for the dc conductivity due to the variable range hopping of carriers. Mott considered electron transport via a system of randomly distributed localized states at low temperatures. At low temperatures the electron transitions between states with energies closer to that of the Fermi level will be more efficient. This is because the filled and empty states having energies similar to each other are found within the range of energies closer to that of the Fermi level.

The simplest form of hopping conduction is when an electron hops through a system of isoenergetic sites randomly distributed in space. If the electrons are strongly localized they prefer to hop between spatially nearest sites and the transport in this regime is called the nearest neighbour hopping (NNH). This type of hopping occurs when the temperatures correspond to the energies where the thermal energy k_BT is larger than the energy scale of the DOS.

For temperatures which are not very high and the thermal energy k_BT is smaller than the energy scale of the DOS the conduction is dependent not only on spatial factors but also on energy dependent factors, which becomes more important the lower the temperature is. The spatial nearest neighbours may have different energies where it will be favourable for the electron to hop to a distant site with a closer energy than to a closer site with a higher energy as shown in figure 5.1. Hence the lengths of these electron transitions increase with decreasing temperature and this transport regime is called the variable range hopping.

Mott's temperature dependent conductivity in the variable range hopping regime (also known as the VRH model in three dimensions) is obtained as

$$\sigma = \sigma_0 exp\left[-\left(\frac{T_0}{T}\right)^{1/4}\right] \tag{5.13}$$

where T_0, the characteristic temperature, is given by the equation

$$T_0 = \frac{\beta}{k_B N(E_F)\alpha^3} \tag{5.14}$$

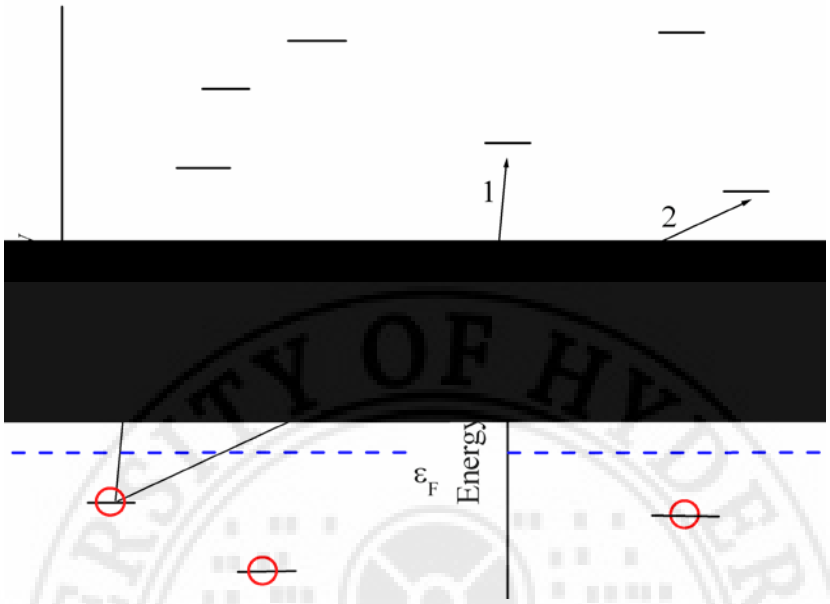

Figure 5.1 Transition 1 and 2 correspond to nearest neighbour and variable range hopping regimes. The dashed line is the Fermi energy level.

5.1c ES – VRH Model :

According to Mott's law the DOS near the Fermi level is energy independent. But for long range electron-electron interactions in a system of localized electrons, a gap (Coulomb gap) emerges. Considering the Coulomb gap too, Efros and Shklovskii [251, 252] obtained the energy distribution described by the density of states (DOS) function, given as

$$N(E) = \frac{\eta\kappa^3}{e^6}(E - E_F)^2 \tag{5.15}$$

where κ is the dielectric constant, e is the elementary charge and η is a numerical coefficient. The Coulomb gap vanishes as the temperature rises [252]. The hopping conductivity in the VRH regime in the low temperature is modified due to the Coulomb gap and the conductivity is given by the equation

$$\sigma = \sigma_0 exp\left[-\left(\frac{T_0}{T}\right)^{1/2}\right] \tag{5.16}$$

with

$$T_0 = \frac{\beta e^2}{\kappa \alpha k_B} \qquad (5.17)$$

where β is a numerical coefficient.

Equation 5.16 is known as the Efros – Shklovskii variable range hopping model or the ES-VRH model. This also gives the hopping conduction in one dimension.

5.2 Percolation Model of Electrical Conduction:

According to the percolation theory introduced by Broadbent and Hammersley [254] a square grid is considered with each site on the grid occupied with probability *p* or vacant with probability (1-*p*), independent of all the other sites on the grid. A collection of the sites occupied by the nearest neighbours is called a `percolation cluster', which have been used to model different phenomena [255, 256] . The number of occupied sites

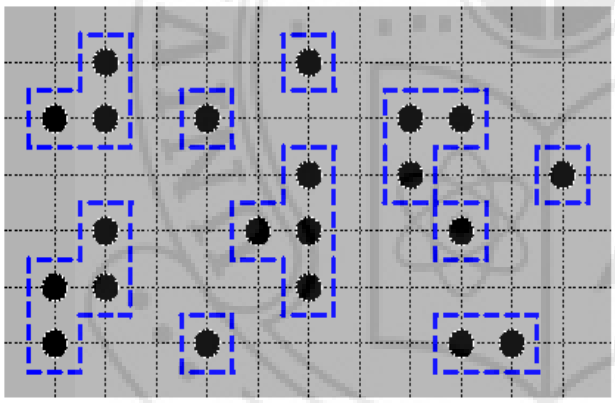

Figure 5.2 Percolation clusters: five clusters of mass 1, one of mass 2, two of mass 3 and two of mass 4.

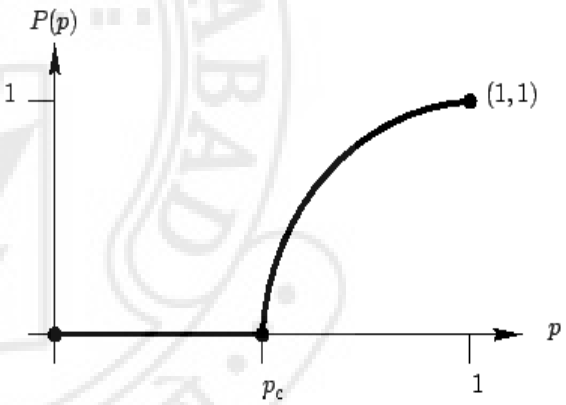

Figure 5.3 The expected behaviour of the percolation probability, *P(p)*.

within a cluster is called its `mass' (figure 5.2). Apart from occupying the sites on the lattice, occupation of the bonds or a combination of both sites as well as bonds can be considered giving rise to site-percolation, bond-percolation and site-bond-percolation. As the occupation probability, *p*, is increased from zero, the average clusters become larger, in terms of the number of sites as well as geometric size. Defining the percolation probability, *P(p)*, as the probability that the origin is part of an infinite cluster, then below a certain value $p = p_c$, called the critical probability, *P(p)*, is always zero. As *p* is increased above p_c, the percolation probability becomes non-zero (figure 5.3). This

change in behaviour is an example of a phase transition. This forms the basis of the percolation model of electrical conduction.

The basic concept of percolation model can be used qualitatively to understand the temperature dependent conductivity of manganites. This is explained based on percolation in a system which exhibits phase separation between metallic and insulating domains. The phase separation can be electronic with nanometer-sized clusters or structural where disorder can induce up to micrometer-sized clusters [257]. Experimentally it has been used to interpret resistivity of manganites qualitatively [63, 258, 259]. The model explains the temperature dependent resistivity using a random resistor network.

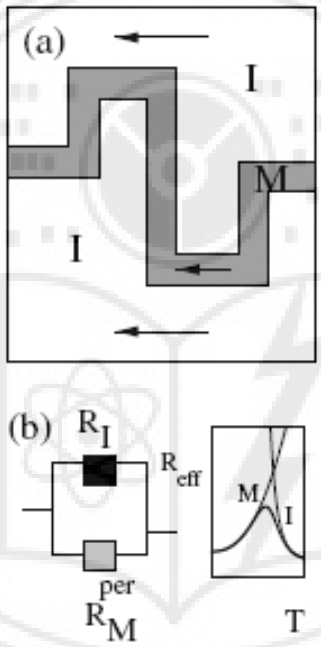

Figure 5.4 Pictorial representation of understanding percolation using a random resistor network. Figure taken from reference 259.

Consider a manganite material which has got insulating and metallic regions with the conduction taking place via the metallic regions by percolation. The insulating and metallic regions are assumed to have resistances R_I (T) and R_M^{per}(T) respectively. This is pictorially represented as two parallel-connected resistors of the above mentioned values as shown on the left had side of figure 5.4 (b). At high temperature $R_I < R_M^{per}$ and hence conduction takes place via R_I i.e. through the insulator. As temperatures decrease $R_I > R_M^{per}$ making R_M^{per} a lesser resistive path and easier to conduct through. The plot on the right hand side of figure 5.4 (b) gives the effective resistance as a result of the parallel

connection of R_I and R_M^{per}. The conduction follows the path 'I' at high temperatures. On cooling the effective resistance begins to taper as R_M^{per} decreases. The peak at intermediate T is due to the transition of conduction via the insulating region to that via the metallic region. Figure 5.4 (a) shows the mixed phase state of a material near percolation. The arrows indicate the conduction through the insulating and metallic regions depending on the temperature.

5.3 Resistivity Studies on $Bi_{(1-x)}Ca_xMnO_3$ (BCMO):

The temperature dependent resistivity of the BCMO system is shown in figure 5.5. The room temperature resistivity (figure 5.6) of the samples vary from the order of ~ 1 – 10^2 Ωcm as *x* increases from 0.4 to 0.75. The lowest temperature at which the resistivity

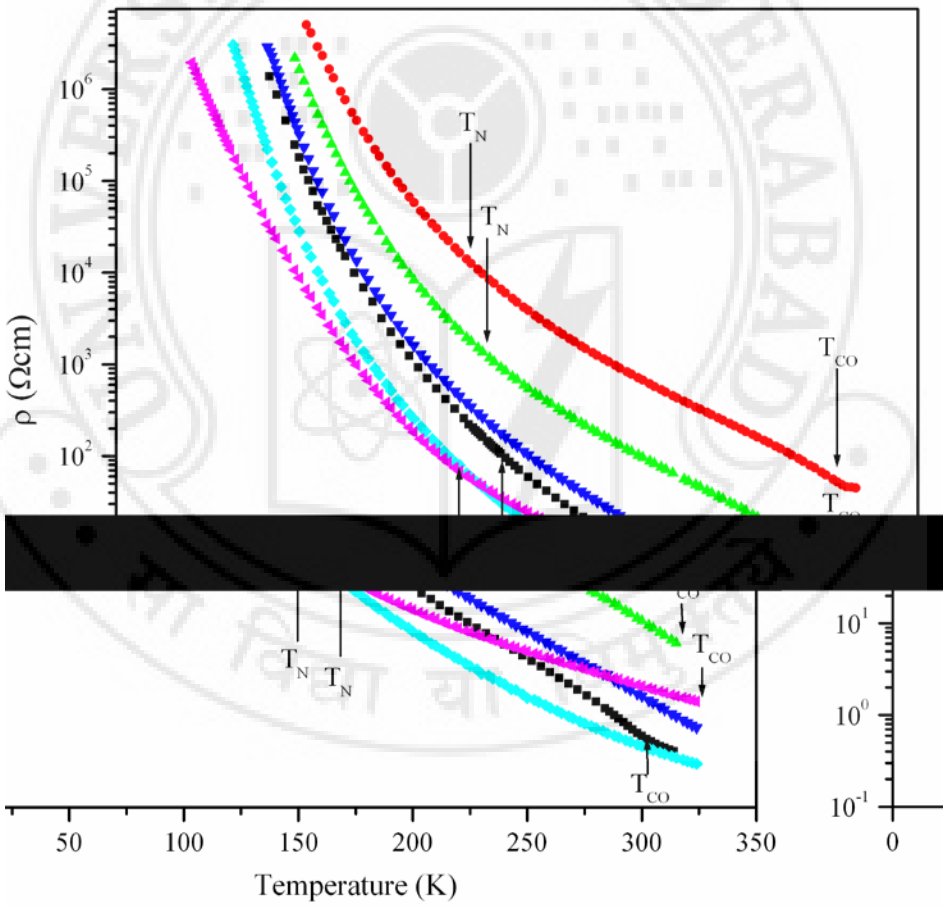

Figure 5.5 Resistivity vs temperature plots for $Bi_{(1-x)}Ca_xMnO_3$.

was measured is ~ 34K (for x = 0.75) as the resistance of other samples was very high (beyond the measurable range of the equipment) at low temperatures. Manganites which exhibit CO and OO [107] are known to have high values of resistivity as both these

promote the localization of the itinerant electrons. The T_N and T_{CO} values obtained from the ESR studies are marked on the ρ vs T plots. A sharp increase in ρ below T_N is observed. A step like increase in ρ is observed at T_{CO}.

The resistivity data in the semiconducting region of La-based manganites has been analyzed by some groups [239, 260] using the thermally activated polaron hopping model. A general form of the equation for resistivity can be written using equations 5.3, 5.4 and 5.10 as

$$\rho = \rho_0 T^n exp\left(\frac{W}{k_B T}\right) \qquad (5.18)$$

where n = 1 and 1.5 for adiabatic and non-adiabatic conduction mechanisms respectively. Jaime *et al.* [261] propose the interesting feature of the coexistence of localized and itinerant carriers at low temperatures.

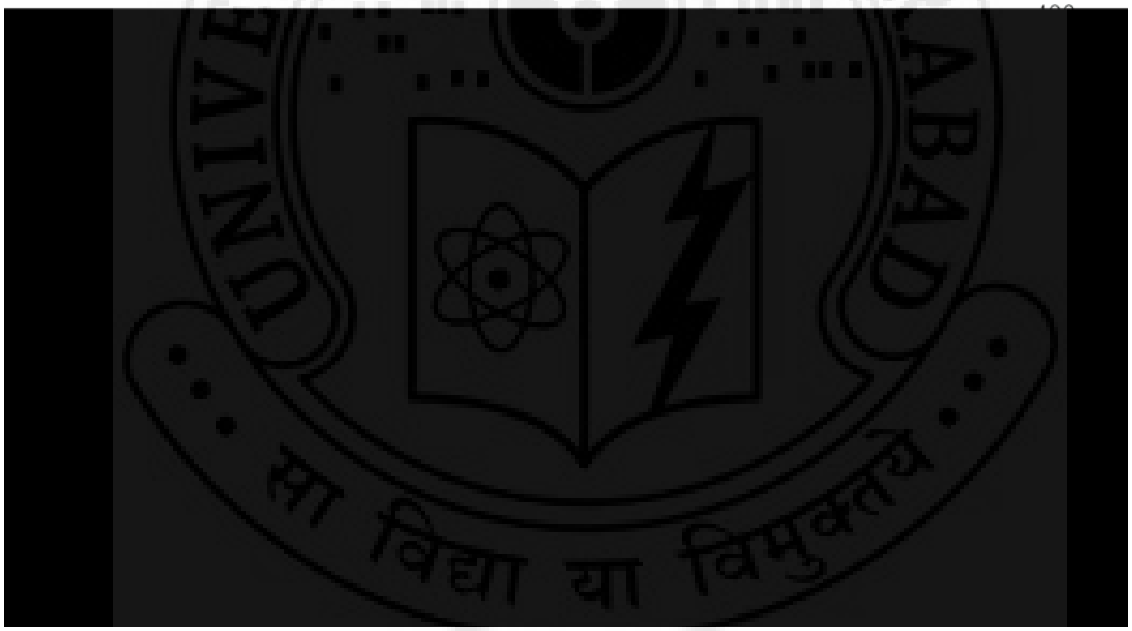

Figure 5.6 Variation of resistivity at 300K and the T_{CO} of the BCMO system with respect to composition

The resistivity data of the present system is analyzed in view of the polaron model. Figure 5.7 shows the ln(ρ/T) versus 1000/T plot for equation (5.18) with the value of n = 1. The continuous curvature in these plots indicate that the thermally activated polaron model is not applicable for this system in the range of temperatures recorded. Similar plots are observed with n = 1.5 in equation (5.18). There have been reports which show

that the temperature dependence of the electrical resistivity in the paramagnetic phase of La-based [261 – 266], Pr-based [267, 268] and Nd-based [269] manganites is well described by the Motts variable-range hopping (VRH) model given by the simplified equation [49, 247]

$$\rho = \rho_o exp\left\{2.06\left[\frac{\alpha^3}{N(E_F)kT}\right]^n\right\} \tag{5.19}$$

with

$$kT_o = \frac{18\,\alpha^3}{N(E_F)} \tag{5.20}$$

where $N(E_F)$ is the density of states at the Fermi level and n can take values of $^1/_2$, $^1/_3$ or $^1/_4$ which denotes dimensionalities of 1, 2 or 3 respectively. The density of states near the Fermi level is assumed to be constant in the derivation of the above equation. The average hopping distance in this model is given by

$$R^4 = \frac{9}{8\pi\alpha k_B T N(E_F)} \tag{5.21}$$

and the hopping energy is given by

$$W = \frac{3}{4\pi R^3 N(E_F)} \tag{5.22}$$

The resistivity data for the present system was analyzed in view of the Motts VRH model. Figure 5.8 shows the lnρ versus $T^{-1/4}$ plots for various compositions of the BCMO system, below T_{CO}. The T_{CO} is estimated from the deviation of the straight line fit in the high temperature region. The resistivity does not show any anomaly other than an increase in slope of the plots at T_N. The T_0 values are estimated from the slope of the curves and are listed in table 5.1. The T_0 parameter in this model is related to the spatial extension/localization length (~1/α) of the localized states and to the density of states $N(E_F)$ as per equation (5.20). The increase in the T_0 parameter in the AFM state can be due to the decrease in $N(E_F)$ and/or localization length ξ. In the absence of any

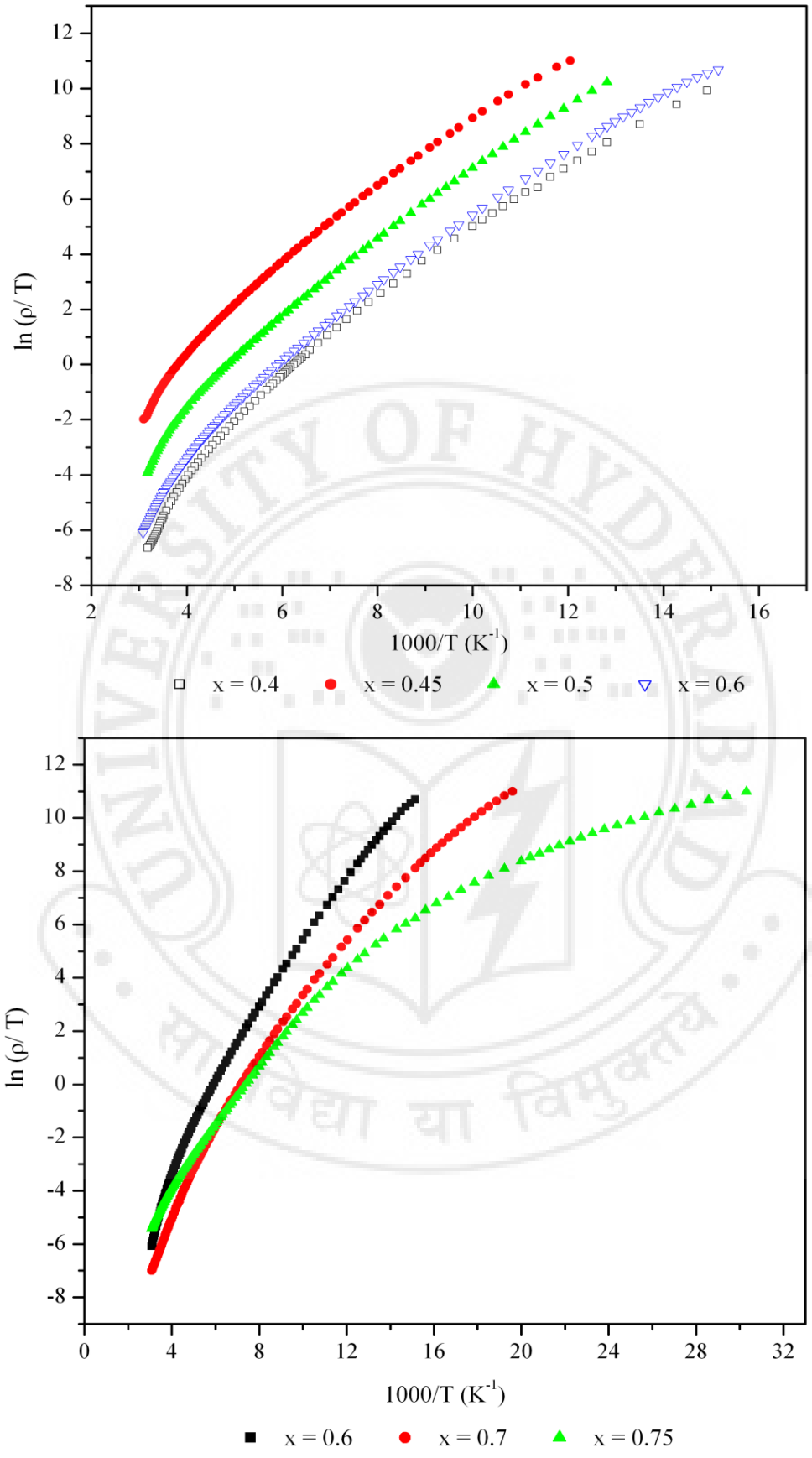

Figure 5.7 ln(ρ/T) versus (1000/T) plots of $Bi_{(1-x)}Ca_xMnO_3$

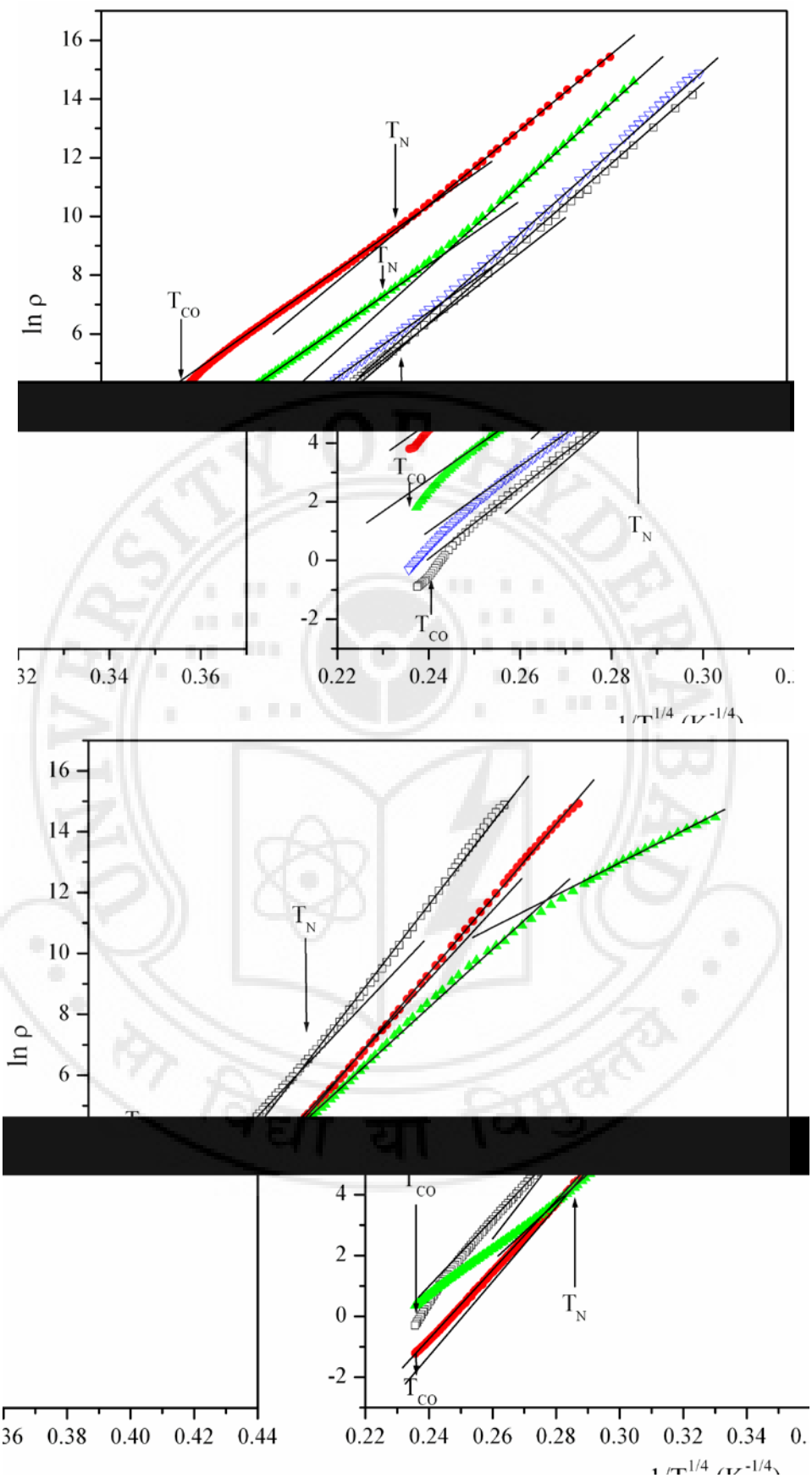

Figure 5.8 ln ρ versus 1/T $^{(1/4)}$ plots of the $Bi_{(1-x)}Ca_xMnO_3$.

experimental estimation of $N(E_F)$ for bismuth manganites we have assumed a reasonable value of $N(E_F) \sim 10^{21}$ cm^{-3} eV^{-1} to estimate the localization length $\xi \sim 1/\alpha$. The localization length is$\approx$1A ^{o}. At room temperature the average hopping distance is in the range 1.07– 1.16 nm. The localization length must be greater than the Mn–Mn distance, which is ~5 nm, and the hopping distance should be several times that of the Mn–Mn distance. Hence this is a physically unacceptable value for hopping distance.

A similar situation is reported in La-based manganites by Viret *et. al.* [265]. They suggested that either the density of states changes drastically with temperature or the localization mechanism is different. It is proposed that a random potential of mainly magnetic origin is responsible for carrier localization above T_C. In the present system the ESR studies indicate that the FM interactions dominate at high temperatures and weaken in the CO state. The AFM interactions start appearing below T_{CO}. These interactions lead to localization and reduce the density of states drastically. Keeping this in mind the localization length, hopping distance and hopping energy is estimated, taking $N(E_F) \sim 10^{18}$ cm^{-3} eV^{-1}. The estimated values are listed in table 5.2. The hopping distance is several times the Mn–Mn distance and localization length is greater than the Mn–Mn distance. This is a physically acceptable situation.

The rapid increase in resistivity with the onset of long range AFM order when temperature decreases from T_N gives rise to higher value of T_O. This indicates that the charge transfer in the AFM phase may be more difficult than in the PM phase, leading to the increase in T_O below T_N. This may be because of antiparallel alignment of the magnetic moment of Mn ion in the AFM phase, which makes charge transfer more difficult. The decrease in ξ and R and the increase in W values below $T < T_N$ supports this conclusion.

Efros and Shklovskii developed a VRH theory which takes into account the electron–electron Coulomb interaction, which reduces the density of states near the Fermi level [269]. It was suggested that the Coulomb interaction may have an important effect on the hopping conduction of electrons in manganese oxides [270, 271]. Hence, the theory of weak localization and VRH in the presence of a Coulomb gap, as developed by Efros and Shklovskii (ES), could account for the temperature dependence of conductivity in manganites. Specifically, for half-doped manganites, the Coulomb interaction is believed to be not only the source of CO [272] but also the convincing candidate for the anisotropy in the orbital ordered states [273]. Therefore, half-doped manganites can be

model systems for clarifying whether the ES-VRH conduction mechanism dominates the electrical transport in their PM state. The ES-VRH theory predicts the temperature dependence of resistivity as

$$\rho = \rho_o \left(\frac{T_o}{T}\right)^{1/2} \qquad (5.23)$$

Sample x	T_0 (10^8K)		ρ_0 10^{-13}(Ωcm)	
	$T_{CO} > T > T_N$	$T < T_N$	$T_{CO} > T > T_N$	$T < T_N$
0.4	2.28	3.06	1.5	0.1
0.45	1.5	2.6	3000	27.7
0.5	1.75	3.64	33.2	0.04
0.6	1.88	3.68	13.3	0.02
0.7	1.67	2.38	6.3	0.3

Table 5.1. T_0 and ρ_0 values obtained from ln ρ versus $T^{-1/4}$ plots in different temperature ranges for the $Bi_{(1-x)}Ca_xMnO_3$ system.

Sample x	ξ (A^o)		R (nm)		W (meV)	
	$T_{CO} > T > T_N$	$T < T_N$	$T_{CO} > T > T_N$	$T < T_N$	$T_{CO} > T > T_N$	$T < T_N$
0.4	6.7	6.1	7.5	7.3	191	206
0.45	7.8	6.5	7.7	7.4	172	198
0.5	7.4	5.8	7.6	7.2	179	215
0.6	7.2	5.7	7.6	7.2	182	215
0.7	6.6	5.8	7.4	7.2	193	215

Table 5.2 Various VRH model parameters estimated for $Bi_{(1-x)}Ca_xMnO_3$ using $N(E_F) \approx 3\times10^{18}$ cm^{-3} eV^{-1} in different temperature ranges

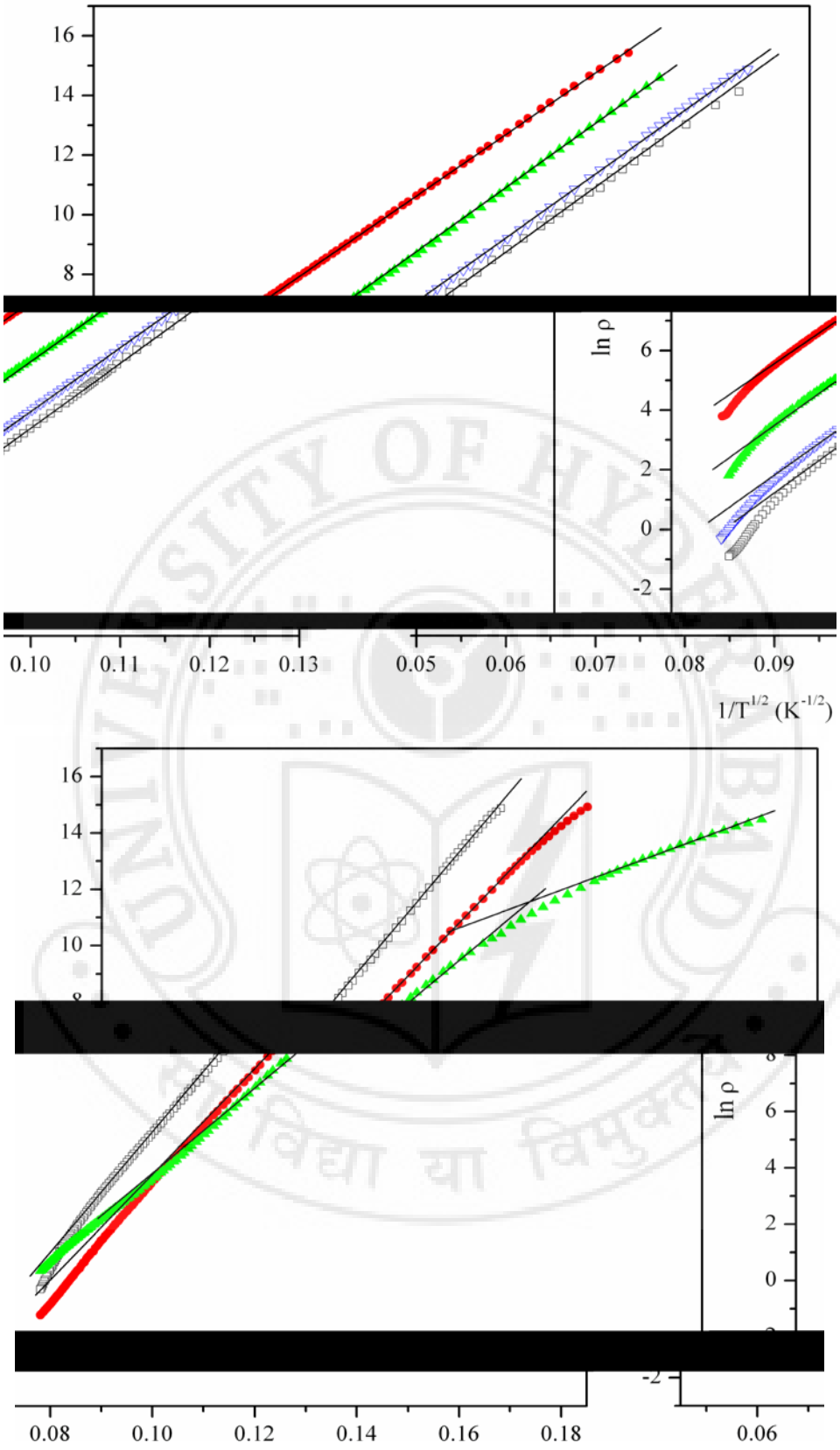

Figure 5.9 ln ρ versus $1/T^{(1/2)}$ plots of the $Bi_{(1-x)}Ca_xMnO_3$ system.

Figure 5.9 shows ln ρ versus $T^{-1/2}$ plots for various compositions. A linear fit in the entire temperature range below T_{CO} is obtained. The average localization length is estimated using

$$k_B T_O \approx \frac{e^2}{\kappa \xi} \tag{5.24}$$

where ξ is the average localization length and κ is the dielectric constant. In the absence of any measurement of κ, we take it to be 500. The values of κ in the range 500–1000 are reported for La-manganites. It is found that ξ ≈ 0.01 Å, which is not of the order of unit cell dimension and is unreasonable. The ρ_0 values are much lower than the expected theoretical values predicted by Mott [49] for these materials. The energy scale of fitting regions (T ≤ 300 K) is very high in comparison with the ordinary size of the Coulomb gap (10 –100 K) [252].

In view of this it is unlikely that the observed ES-type behaviour is due to the emergence of the Coulomb gap. A similar situation of ES-VRH type behaviour is reported in the case of the insulating Ca_2RuO_2 system and has been ascribed to the existence of disorder-modified Mott gap in the system [274]. In the case of the present Bi-manganites, the fact that AFM ordering takes place in the insulating phase and that resistivity does not show any anomaly at T_N confirm the Mott insulating ground state in these materials. The phase separation in Bi-manganites can create coexisting clusters of competing ordered states.

The ESR studies indicate competing magnetic interactions in the CO state as a function of composition and temperature. The phase separation or inhomogeneities may lead to the formation of strongly localized states around the closing of the Mott– Hubbard gap, which in turn may be responsible for resistivity behaviour similar to that predicted by Efros and Shklovskii [251, 252].

The resistivity data can be qualitatively analyzed in view of the percolation model for mixed phase manganites [259]. A jump in resistivity at T_{CO} occurs due to the formation of AFM insulating clusters. With decrease in temperature the AFM (insulating) clusters grow progressively at the expense of FM (metallic) clusters giving rise to increase in resistivity. The FM cluster size decreases as the long range AFM order sets in. The volume fraction occupied by FM clusters is very small compared with the volume of the AFM phase. A sharp increase in resistivity observed below T_N, therefore, may be due

to quite low connectivity between FM clusters. The slow increase of ρ with decrease in temperature in the case of sample with x = 0.75 can be due to the connectivity between FM clusters. The ESR studies on this samples show the formation of FM clusters.

5.4 Resistivity Studies on $Bi_{(1-x)}Sr_xMnO_3$ (BSMO):

The temperature dependence of resistivity of $Bi_{(1-x)}Sr_xMnO_3$ is plotted in figure 5.10. The resistivity shows a strong semiconducting behaviour with values reaching to ≈ 10^7 Ωcm at low temperatures ~ 80K. The resistance becomes too high to measure below this temperature by the available equipment. The variation of resistivity at 300K of the BSMO system with respect to composition is shown in figure 5.11.

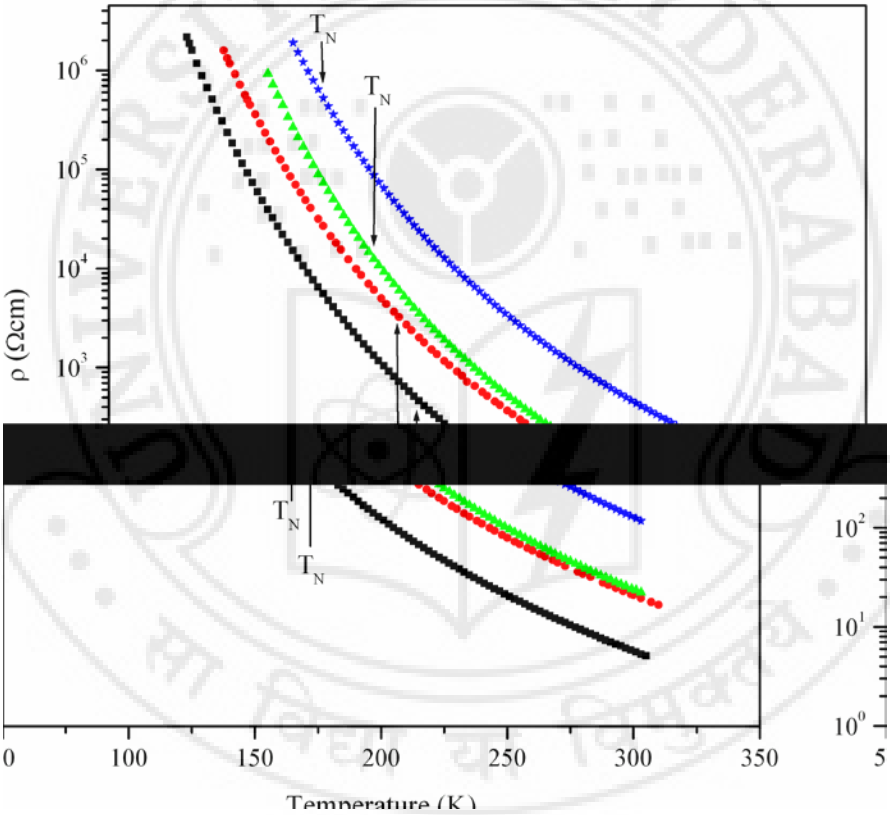

Figure 5.10 The resistivity vs temperature plots of the $Bi_{(1-x)}Sr_xMnO_3$.

The T_{CO} is not observed from the resistivity data indicating it is beyond the highest measured temperature. The resistivity increases sharply below T_N, as the temperature is decreased. The resistivity data is analyzed using the two different approaches. The first is the charge localization due to the small polaron formation and the second, variable range hopping.

Figure 5.12 shows the ln(ρ/T) versus 1000/T plot corresponding to equation (5.18) with the value of n = 1 (adiabatic hopping). Ln(ρ/T) varies linearly with 1000/T as per equation (5.18) in the high temperature range. The deviation from linearity starts at a temperature which can be taken as $\theta_D/2$ as per the polaron model. Similar plots are obtained for n = 1.5. The activation energy for both cases is calculated at tabulated in table 5.3. For a temperature $T < \theta_D/4$, $W \approx W_D$, the disorder energy. As the resistivity of the samples at low temperatures is very high, the measurement in the temperature range below $\theta_D/4$ was possible only for sample with $x = 0.5$. The estimated W_D value of 0.01eV for this sample is close to the predicted value as per the polaron model.

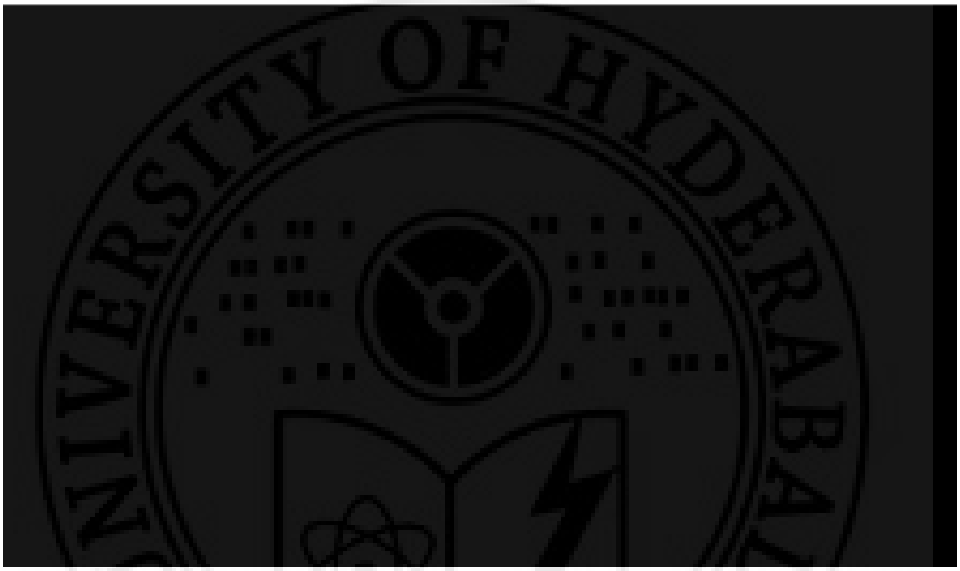

Figure 5.11 Variation of resistivity 300K and T_{CO} of the BSMO system with respect to composition

Unlike the BCMO system the polaron model can be used to explain the conduction mechanism of the BSMO system in the high temperature regime. This is because of the strong insulating behaviour, coupled with high room temperature resistivity of this system. This is indicative of strong localization of the itinerant electron i.e. strong Anderson localizations [275, 276] in this system.

It is not possible to ascertain whether the hopping is adiabatic (n = 1) or non adiabatic (n = 1.5) from the ln (ρ/T) vs 1/T plots. It is pointed out that a plot of $\log_{10}$ ρ vs W can resolve this [277]. If the T value estimated from the slope of the plot is close to the temperature at which the $\log_{10}$ ρ value is taken, then the polaron hopping is in the adiabatic regime. If it is very much different, then it is in the non adiabatic regime. Figure 5.13 depicts the $\log_{10}$ ρ versus W plots for the BSMO system, at 300K [W values

obtained from equation (5.18) for n = 1]. The slope of the plot is $1/k_BT$, which gives T≈ 354K. This value being very close to 300K (temperature at which the value of resistivity is taken), confirms that the polaron hopping conduction in the high temperature range is in the adiabatic regime. This means that the resistivity is dependent on the activation energy alone and the pre-exponential factor in equation (5.18) does not play any significant role.

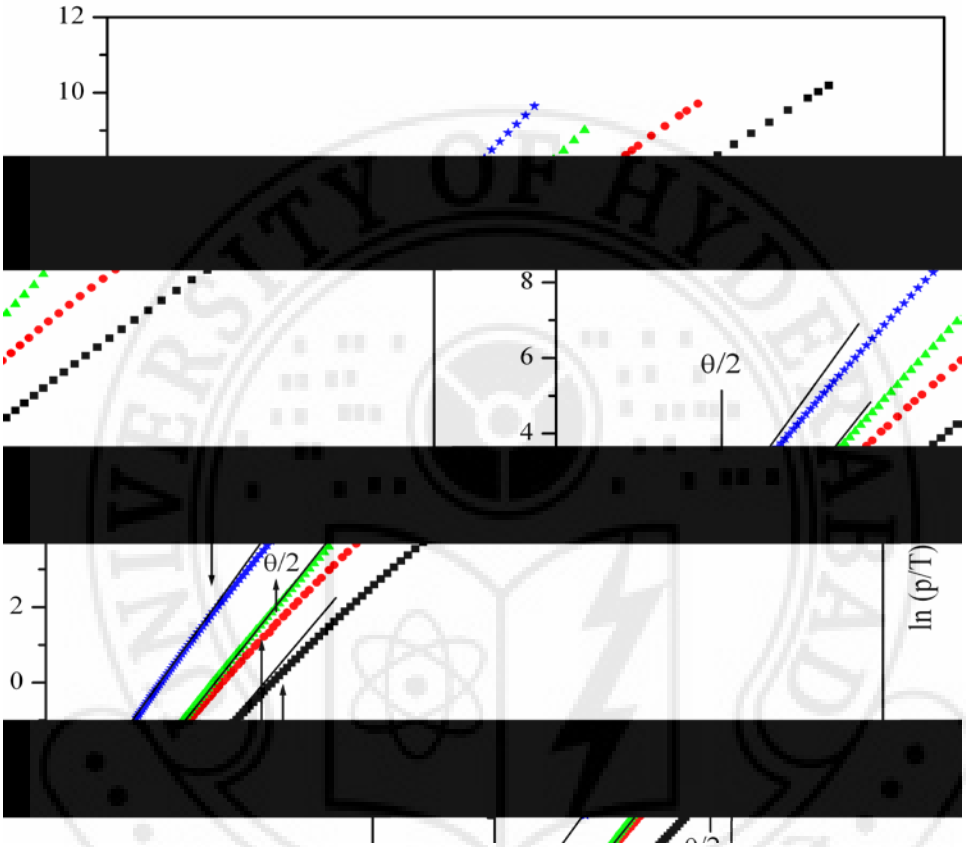

Figure 5.12. ln(ρ/T) versus (1000/T) plots of the $Bi_{(1-x)}Sr_xMnO_3$.

Sample *x*	ρ Ωcm	θ K	W for n = 1 meV	W for n = 1.5 meV
0.3	125	430	226	226
0.4	23.5	394	211	211
0.45	21	390	198	198
0.5	5.6	375	178	189

Table 5.3. Debye temperature and activation energies from the thermally activated polaron hopping model for n = 1 and 1.5 for the $Bi_{(1-x)}Sr_xMnO_3$ system.

Figure 5.13 Log ρ versus activation energy for the $Bi_{(1-x)}Sr_xMnO_3$ system

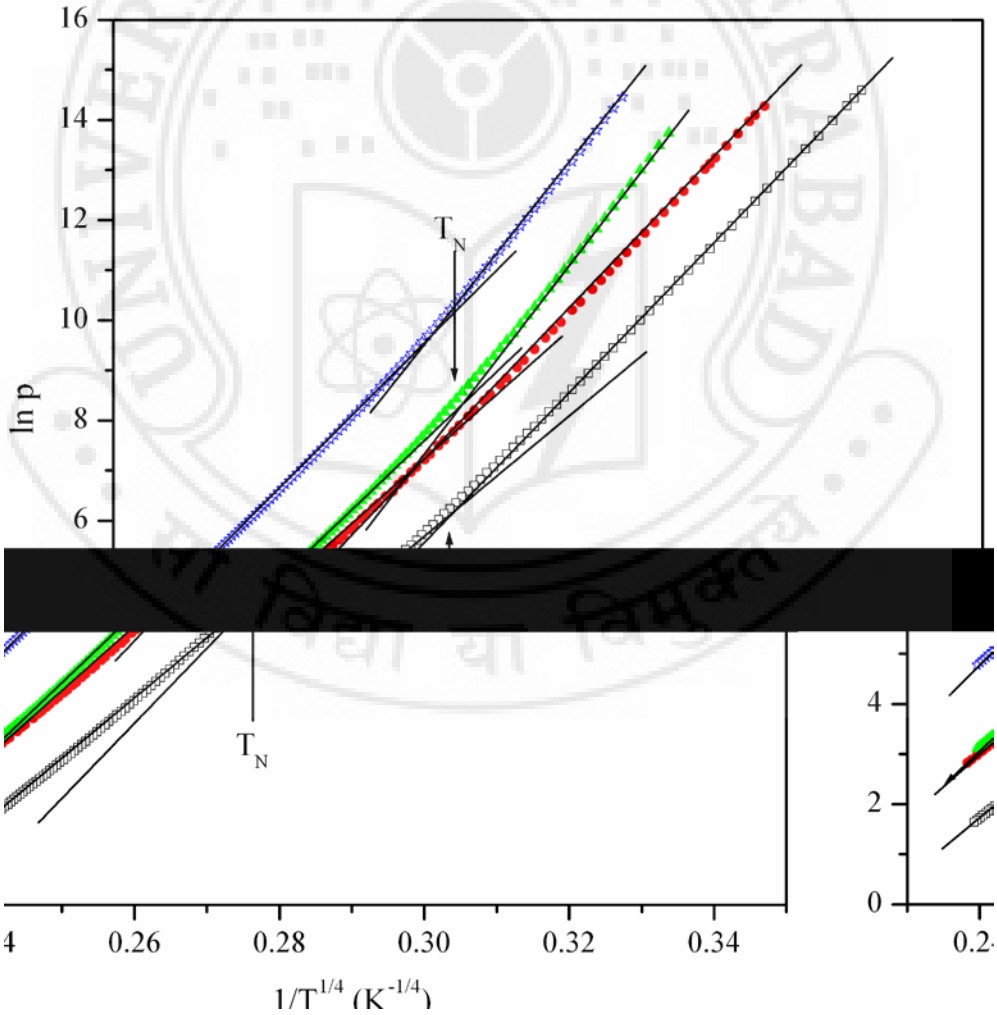

Figure 5.14 ln ρ versus $1/T^{(1/4)}$ plots of the $Bi_{(1-x)}Sr_xMnO_3$.

The data is analyzed in view of the Motts VRH model also. Figure 5.12 shows plots of ln ρ versus $T^{-1/4}$ for various compositions. There is an increase in slope at T_N similar to that seen in the BCMO system. The model parameter T_0 for both the regions are listed in table 5.4. The T_0 parameter is related to spatial extension/localization length, ξ, of the localized states and to the density of states $N(E_F)$ as per equation (5.20) and its increase in T_0 parameter with the onset of AFM state can be due to decrease in $N(E_F)$ and/or localization length ξ .

Adopting a reasonable value of $N(E_F) \sim 10^{21}$ cm^{-3} eV^{-1} the localization length $\xi \sim 1/\alpha$ is estimated. The localization length must be greater than the Mn–Mn distance, which is ~5 nm, and the hopping distance should be several times that of the Mn–Mn distance. The localization length and the average hopping distance are found to be of unreasonable values, similar to that seen in the BCMO system. The ESR studies of this system indicate that the FM interactions which are dominant at high temperature weaken with the onset of the CO state because of the appearance of AFM interactions just above T_{CO}. The AFM interactions lead to localization and reduce the density of states drastically. Keeping this in mind the localization length, hopping distance and hopping energy are estimated, using $N(E_F) \sim 10^{18}$ cm^{-3} eV^{-1} (table 5.5). The hopping distance is several times the Mn–Mn distance and localization length is greater than the Mn–Mn distance. This is a physically acceptable situation.

Sample *x*	T_0 (10^8K)		ρ_0 (Ωcm)	
	$T_{CO} > T > T_N$	$T < T_N$	$T_{CO} > T > T_N$ (x 10^{-13})	$T < T_N$ (x 10^{-19})
0.3	3.9	10.6	2.9	57.5
0.4	3.0	12.3	4.5	1
0.45	2.2	5.5	41.4	9320
0.5	2.0	4.9	20.9	6840

Table 5.4. T_0 and ρ_0 values obtained from ln ρ versus $T^{-1/4}$ plots in different temperature ranges for the $Bi_{(1-x)}Sr_xMnO_3$ system.

Sample x	ξ (A^o)		R (nm)		W (meV)	
	$T_{CO} > T > T_N$	$T < T_N$	$T_{CO} > T > T_N$	$T < T_N$	$T_{CO} > T > T_N$	$T < T_N$
0.3	8.2	5.8	10.3	9.5	218	280
0.4	8.9	5.5	10.5	9.4	205	291
0.45	6.8	5.0	7.5	6.9	189	238
0.5	7.0	5.2	7.6	7.0	185	231

Table 5.5 Various VRH model parameters estimated for $Bi_{(1-x)}Sr_xMnO_3$ using $N(E_F) \approx 3\times10^{18}$ cm^{-3} eV^{-1} in different temperature ranges

Figure 5.15 shows ln ρ versus $T^{-1/2}$ plots for the different compositions. A linear fit in the entire temperature range below T_{CO} is obtained only for the x = 0.5 sample. For samples with higher resistivity there is a change in the slope at T_N. From the estimated values of T_0 and ρ_0 the average localization lengths were estimated using equation (5.24), but were found to be unreasonable. In view of this it is unlikely that the observed ES-type behaviour is due to the emergence of the Coulomb gap. The Mott insulating ground state in the BSMO system is confirmed from the fact that the AFM ordering takes place in the insulating phase and resistivity does not show any anomaly at T_N. The coexistence of clusters of competing phases is a result of phase separation in the BSMO system. The PS or inhomogeneities may be responsible for resistivity behaviour similar to that predicted by Efros along with Shklovskii [251, 252].

The resistivity data for this system can be qualitatively analyzed in view of the percolation model for mixed phase manganites [259]. From the ESR studies it is observed that FM interactions dominate in the CO state of the sample with x = 0.3 implying that this sample should have the lowest resistivity. This is found to be correct experimentally. With increase in x the AFM interactions (clusters) grow at the expense of the FM clusters giving rise to increase in resistivity at R.T. With decrease in temperature the AFM (insulating) clusters grow progressively at the expense of FM (metallic) clusters giving rise to increase in resistivity. The FM cluster size decreases as the long AFM order sets in. The volume fraction occupied by FM clusters is very small compared with the volume of the AFM phase. A sharp increase in resistivity observed below T_N, therefore, may be due to quite low connectivity between FM clusters.

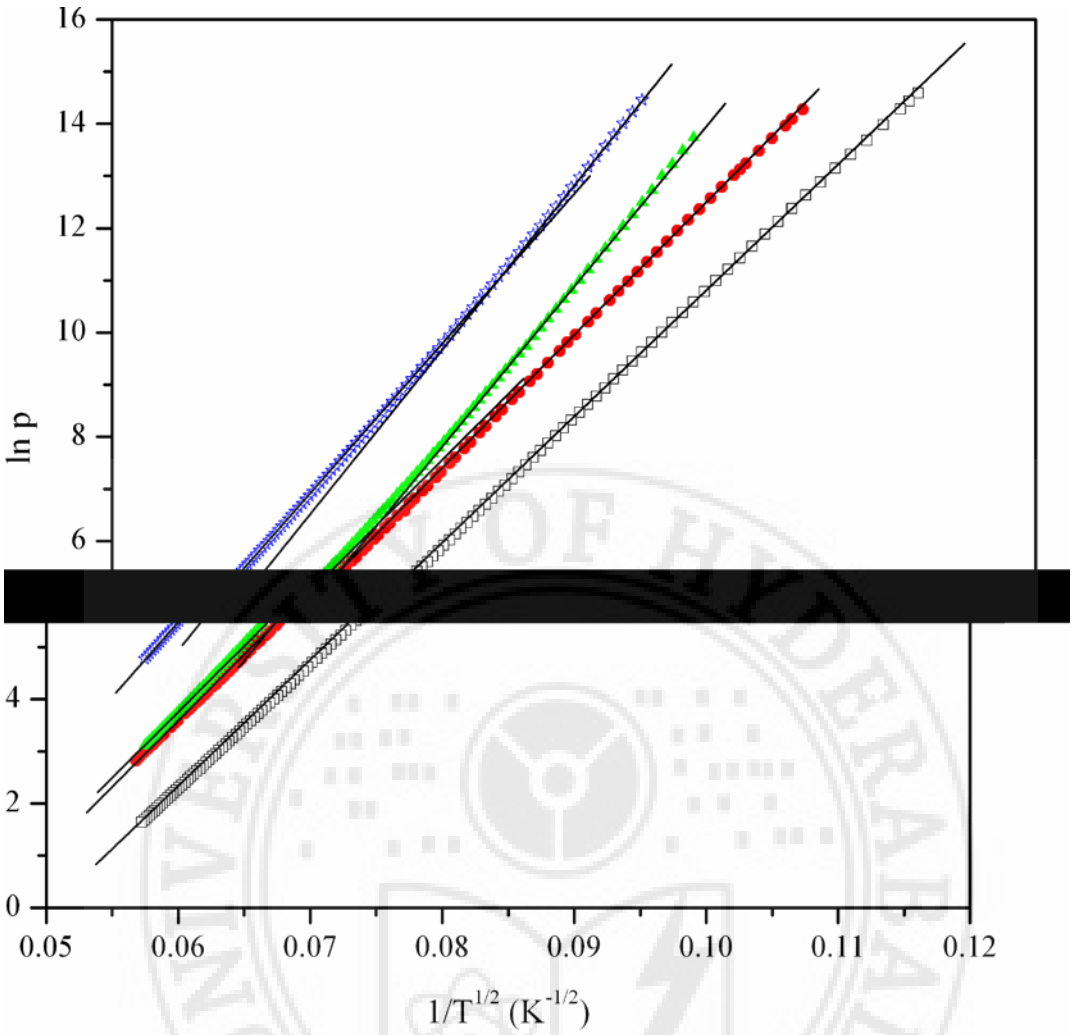

Figure 5.15 ln ρ versus 1/T $^{(1/2)}$ plots.

5.5 Resistivity Studies on $Bi_{0.6}Ca_{(0.4-x)}Sr_xMnO_3$ (BCSMO)

The temperature dependent resistivity data of the system $Bi_{0.6}Ca_{(0.4-x)}Sr_xMnO_3$ (x = 0, 0.02, 0.04, 0.06, 0.08, 0.1, 0.16, 0.24, 0.4) is shown in figure 5.16 (a), 5.16 (b) and 5.16 (c).

Figure 5.17 shows resistivity variation with x. As x increases, the resistivity increases, showing a maxima at x = 0.06 followed by a decrease with increase in x. Only for x = 0 sample, the resistivity data shows an anomaly which indicates the T_{CO}. With small addition of Sr the CO transition is smeared. It is hardly noticed for sample with x = 0.02. The T_{CO}, however, can be noticed from the ln ρ vs $1/T^{¼}$ plots upto x = 0.08. Below T_N the resistivity increases rapidly with decrease in temperature.

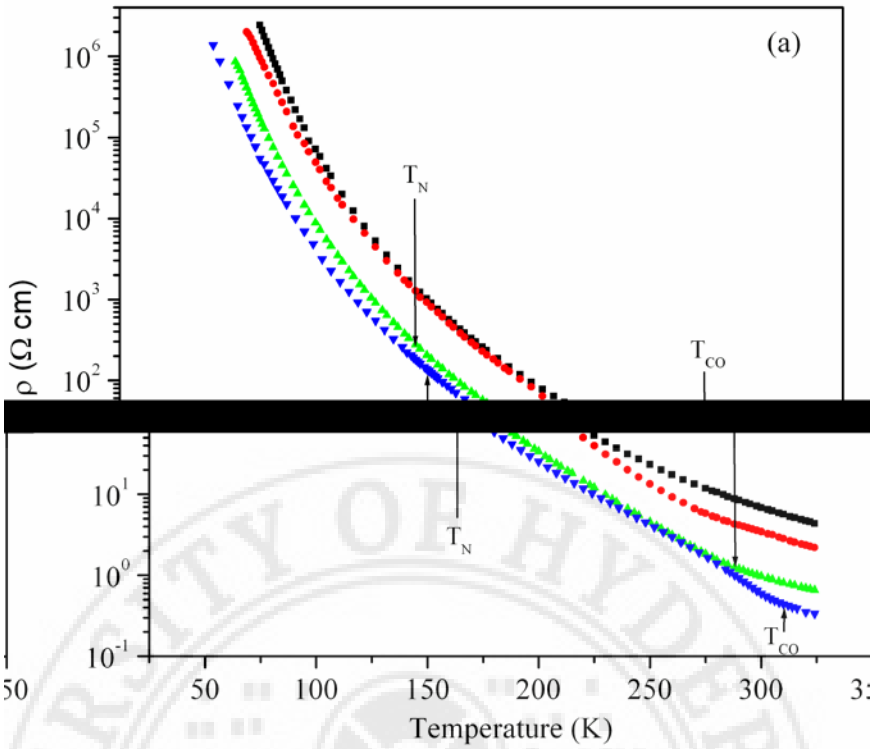

Figure 5.16a. Resistivity vs temperature plots of BCSMO system for x = 0, 0.02, 0.04 and 0.06.

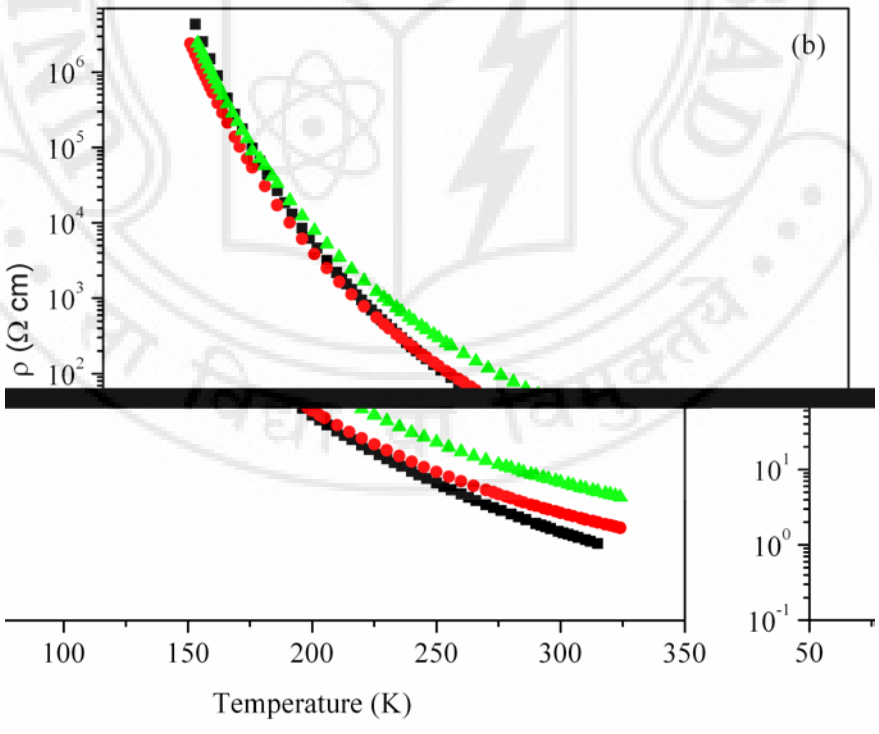

Figure 5.16b. Resistivity vs temperature plots of BCSMO system for x = 0.06, 0.08 and 0.1.

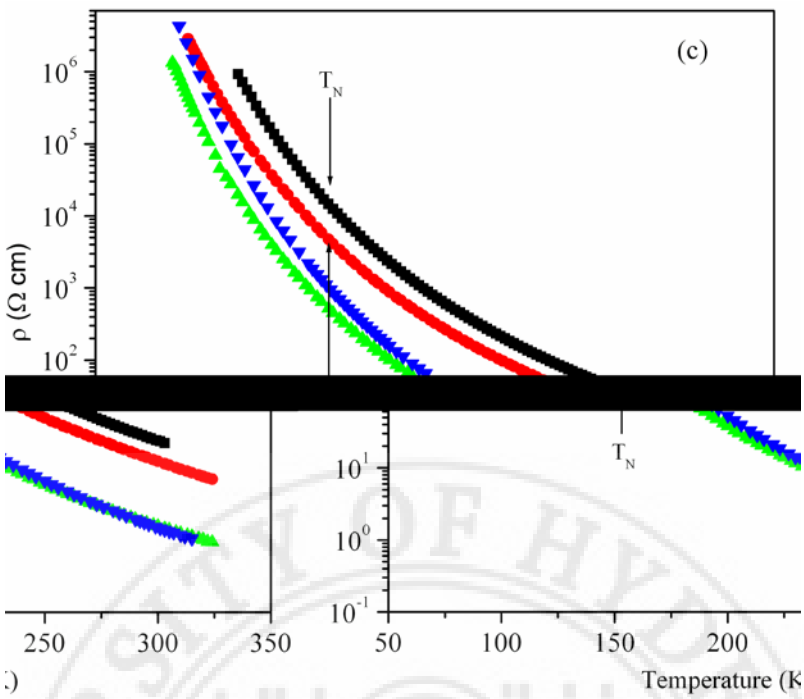

Figure 5.16c. Resistivity vs temperature plots of BCSMO system for x = 0.1, 0.16, 0.24, 0.4.

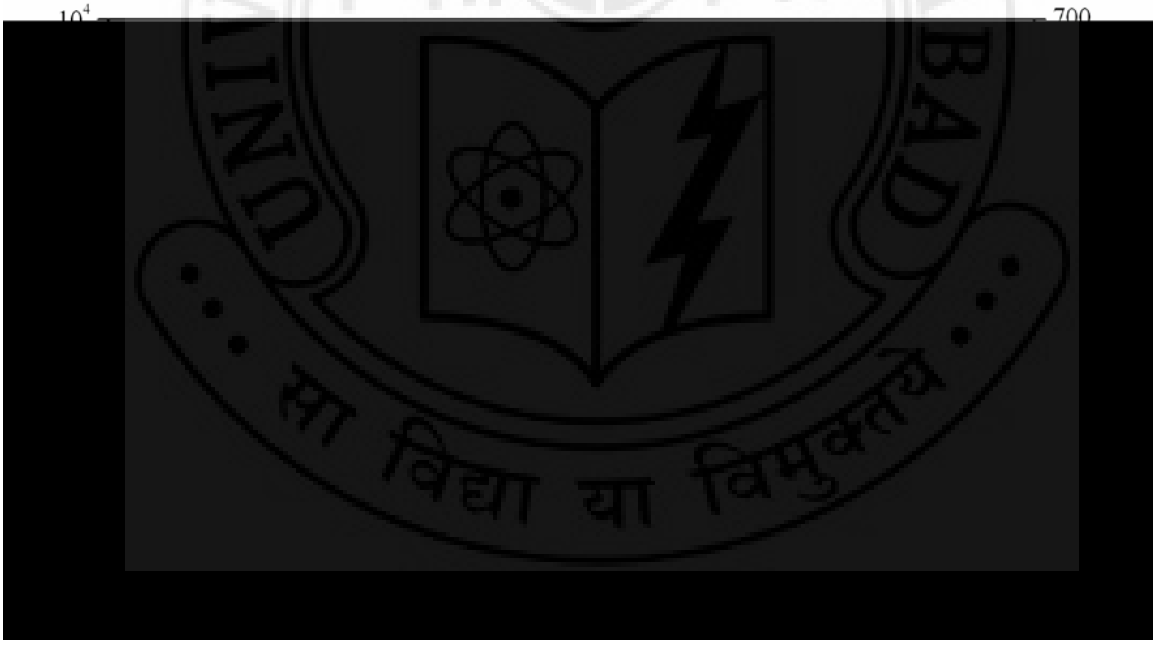

Figure 5.17 Variation of resistivity at 300K and T_{CO} of the BCSMO system with respect to composition

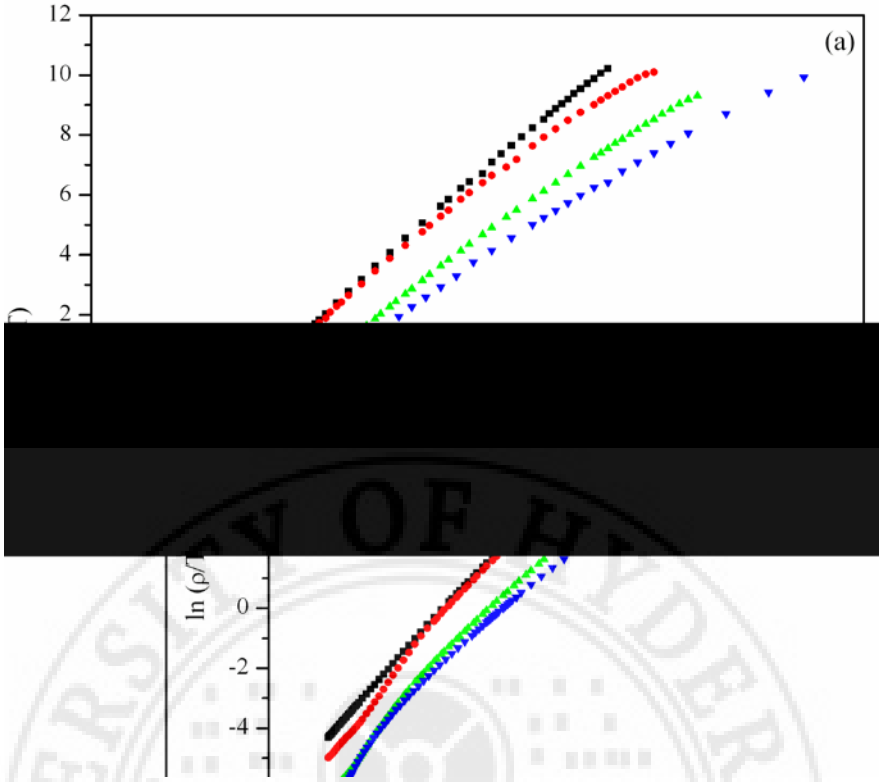

Figure 5.18a ln(ρ/T) versus (1000/T) plots of BCSMO for x = 0, 0.02, 0.04 and 0.06.

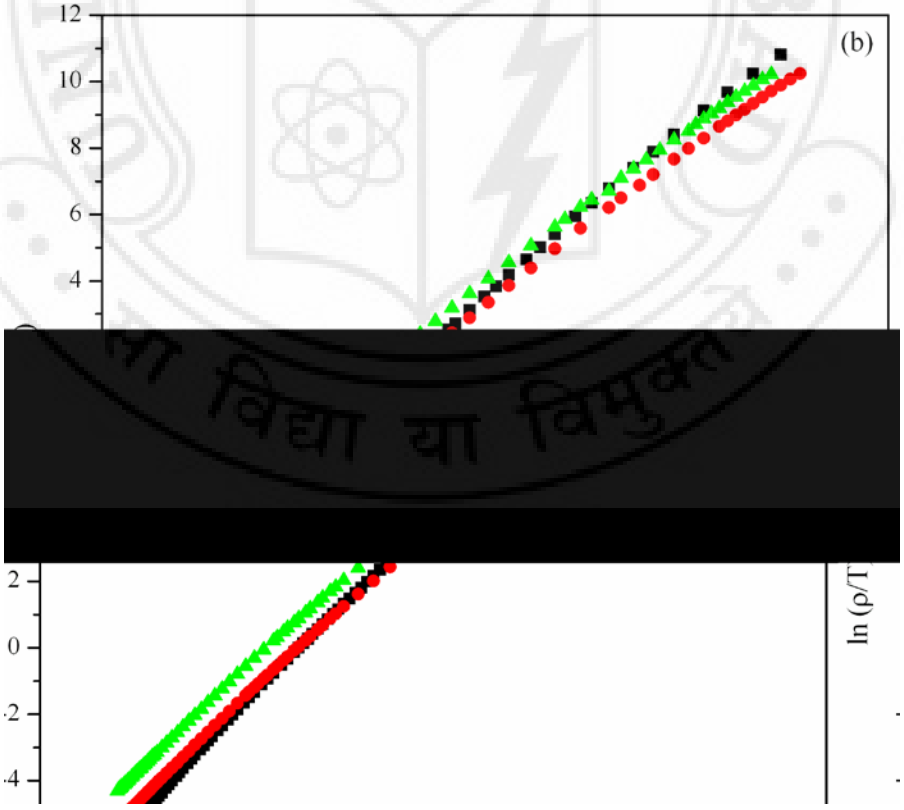

Figure 5.18b ln(ρ/T) versus (1000/T) plots of $Bi_{0.6}Ca_{(0.4-x)}Sr_xMnO_3$ for x = 0.06, 0.08 and 0.1.

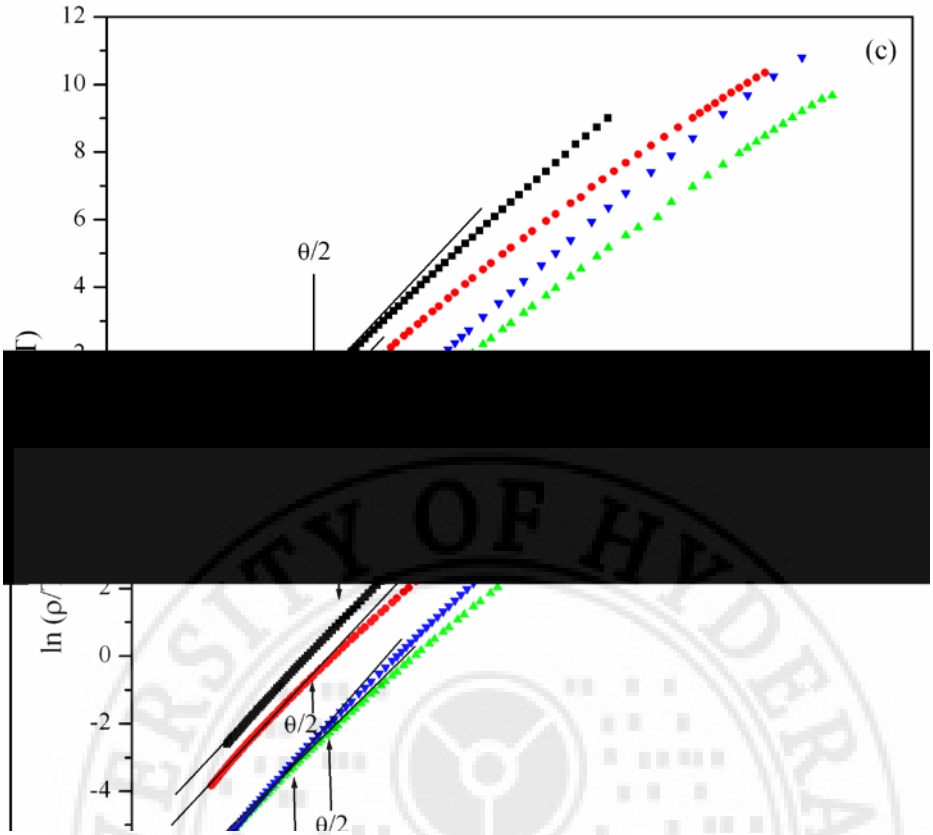

Figure 5.18c ln(ρ/T) versus (1000/T) plots of BCSMO for *x* = 0.1, 0.16, 0.24 and 0.4.

Sample *x*	ρ Ωcm	θ K	W for n = 1 meV	W for n = 1.5 meV	W_D (at T < θ/4) meV
0.1	1.46	344	201	211	
0.16	1.58	356	185	195	113
0.24	12.47	386	193	204	111
0.4	23.53	394	211	211	

Table 5.6. Debye temperature and activation energies from the thermally activated hopping model for n = 1 and 1.5 for the $Bi_{0.6}Ca_{(0.4-x)}Sr_xMnO_3$ system.

The ln (ρ/T) v 1000/T plots as per equation (5.18) for the BCSMO system are depicted in figure 5.18a, 5.18b and 5.18c. In the temperature range below T_{CO} the slope of the plots for Ca – rich samples continuously decrease, implying a continuous decrease in the activation energy. Whereas in the case of Sr-rich samples, where the T_{CO} is above

room temperature, the thermally activated hopping model fits the high temperature data as shown in figure 5.18a. The Debye temperature and the activation energy are estimated from the plots for both n = 1 and n = 1.5 in equation (5.18) and are tabulated in table 5.6. Experimental data in the low temperature region, $T < \theta_D/4$, is obtained only for samples with x = 0.16 and 0.24. The activation energy for hopping conduction, $W \approx \theta_D$ is estimated and tabulated in table 5.6. Similar plots are obtained for n = 1.5 The conduction mechanism in the high temperature regime of the samples of the $Bi_{0.6}Ca_{(0.4-x)}Sr_xMnO_3$ with $x > 0.1$ can be explained by the polaron model.

To ascertain whether the hopping is in the adiabatic or non adiabatic regime the plot of $\log_{10} \rho$ vs W were drawn. Figure 5.19 depicts the log ρ versus activation energy plots for the BCSMO system with $x \geq 0.16$. The value of ρ is taken at 300K and the W used is estimated from equation (5.18) for n = 1. The slope of the plot gives T = 289K. This is very close to 300K (temperature at which the value of resistivity is taken) implying that the polaron hopping conduction in the high temperature regime is adiabatic in the BCSMO system with $x \geq 0.16$.

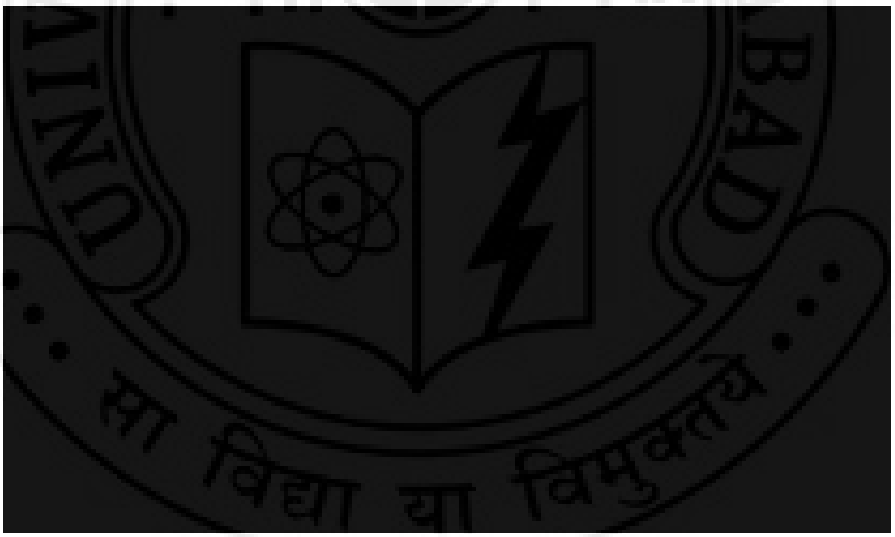

Figure 5.19 Log ρ versus activation energy for the $Bi_{0.6}Ca_{(0.4-x)}Sr_xMnO_3$ system

The ln ρ vs $1/T^{(1/4)}$ plots of the BCSMO system are shown in figure 5.20a, 5.20b and 5.20c. Though the T_{CO} is not visible in the mixed phase samples the deviation from the straight line fits in the higher temperature regions can be associated to the T_{CO}. At around T_N an increase in slope is observed. From T_0 values using the density of states $N(E_F) \sim 3\times10^{18}$ cm^{-3} eV^{-1} the localization length, hopping distance and average hopping energy has been calculated using equations 5.20, 5.21 and 5.22 respectively. The values of the parameters are listed in tables 5.7 and 5.8.

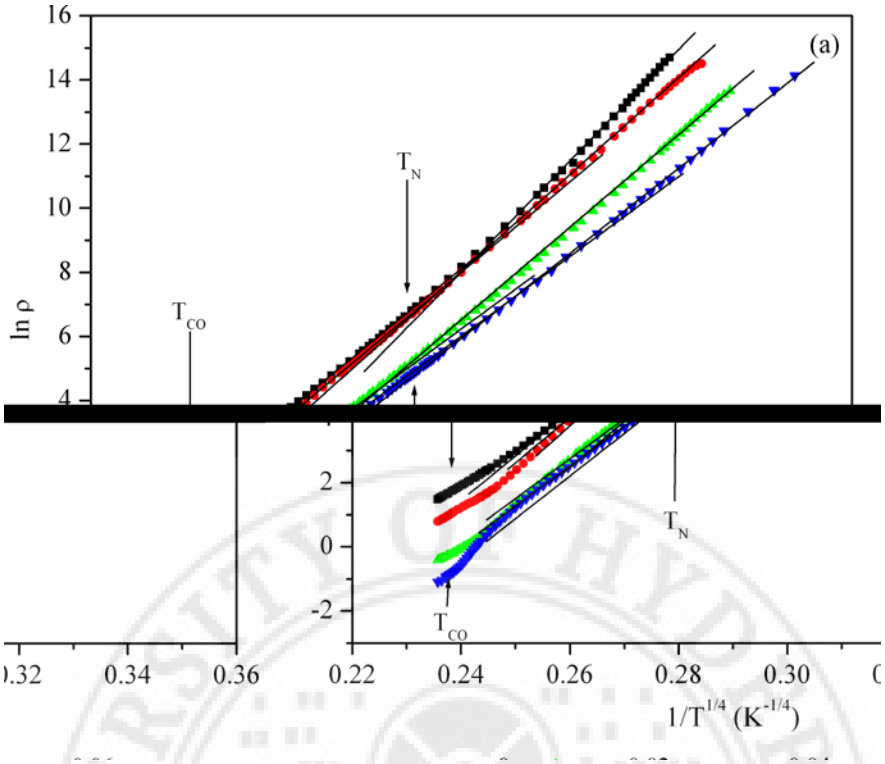

Figure 5.20a ln ρ versus 1/T $^{(1/4)}$ plots of BCSMO for x = 0, 0.02, 0.04 and 0.06.

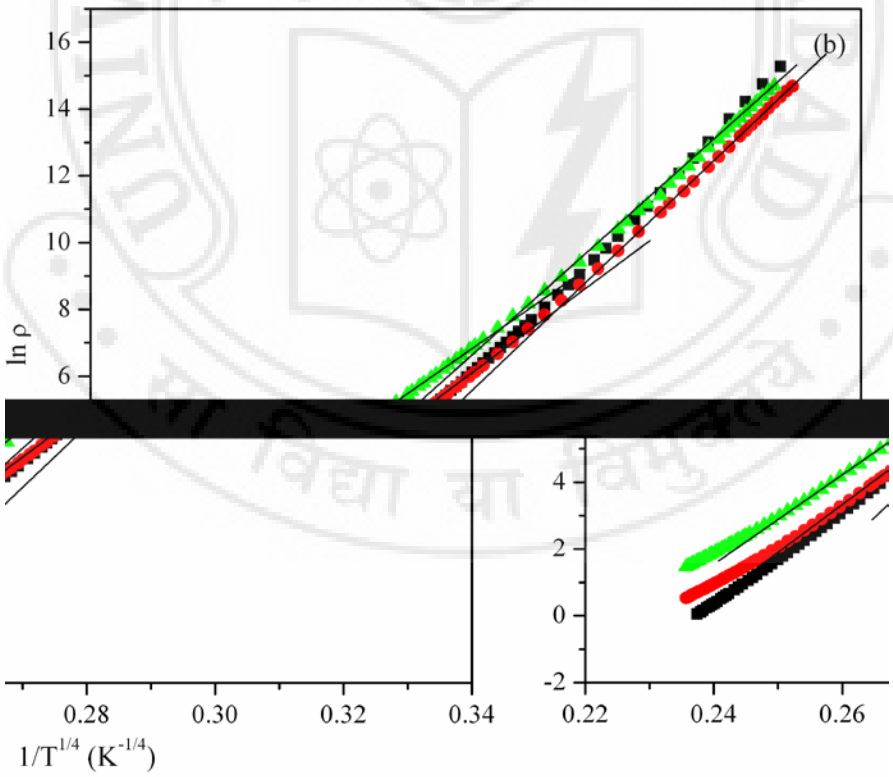

Figure 5.20b ln ρ versus 1/T $^{(1/4)}$ plots of BCSMO for x = 0.06, 0.08 and 0.1.

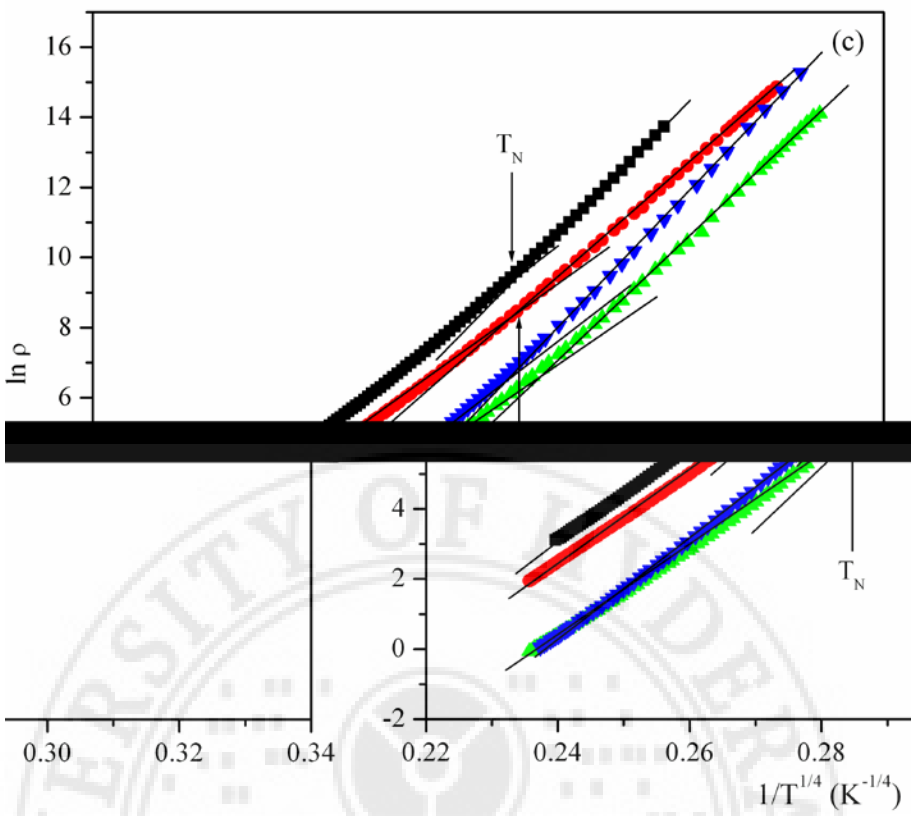

Figure 5.20c ln ρ versus $1/T^{(1/4)}$ plots BCSMO for x = 0.1, 0.16, 0.24 and 0.4.

Sample x	T_0 (10^8K)		ρ_0 (Ωcm)	
	$T_{CO} > T > T_N$	$T < T_N$	$T_{CO} > T > T_N$ ($\times 10^{-15}$)	$T < T_N$ ($\times 10^{-17}$)
0	2.28	3.063	160	1100
0.02	3.227	4.95	10.8	12
0.04	3.876	5.027	8.0	55.4
0.06	1.244	9.606	6590	0.026
0.08	1.462	10.85	907	0.003
0.1	3.328	15.49	12	0.0003
0.16	2.236	10.23	27.1	0.003
0.24	2.584	3.599	724	3.6
0.4	2.987	12.33	446	0.01

Table 5.7 T_0 and ρ_0 values obtained from ln ρ versus $T^{-1/4}$ plots in different temperature ranges for the $Bi_{0.6}Ca_{(0.4-x)}Sr_xMnO_3$.

Sample x	ξ (A^o)		R (nm)		W (meV)	
	$T_{CO} > T > T_N$	$T < T_N$	$T_{CO} > T > T_N$	$T < T_N$	$T_{CO} > T > T_N$	$T < T_N$
0	6.7	6.1	7.5	7.3	191	206
0.02	6.0	5.2	7.3	7.0	209	233
0.04	5.6	5.2	7.1	7.0	218	233
0.06	8.2	4.2	7.9	6.6	164	274
0.08	7.8	4.02	7.8	6.6	171	282
0.1	5.9	3.6	7.2	6.4	210	309
0.16	6.8	4.1	7.5	6.6	190	282
0.24	6.5	4.6	7.4	6.8	197	253
0.4	8.9	5.5	10.5	9.4	205	291

Table 5.8 Various VRH model parameters estimated for $Bi_{0.6}Ca_{(0.4-x)}Sr_xMnO_3$ using $N(E_F) \approx 3\times10^{18}$ cm^{-3} eV^{-1} in different temperature ranges

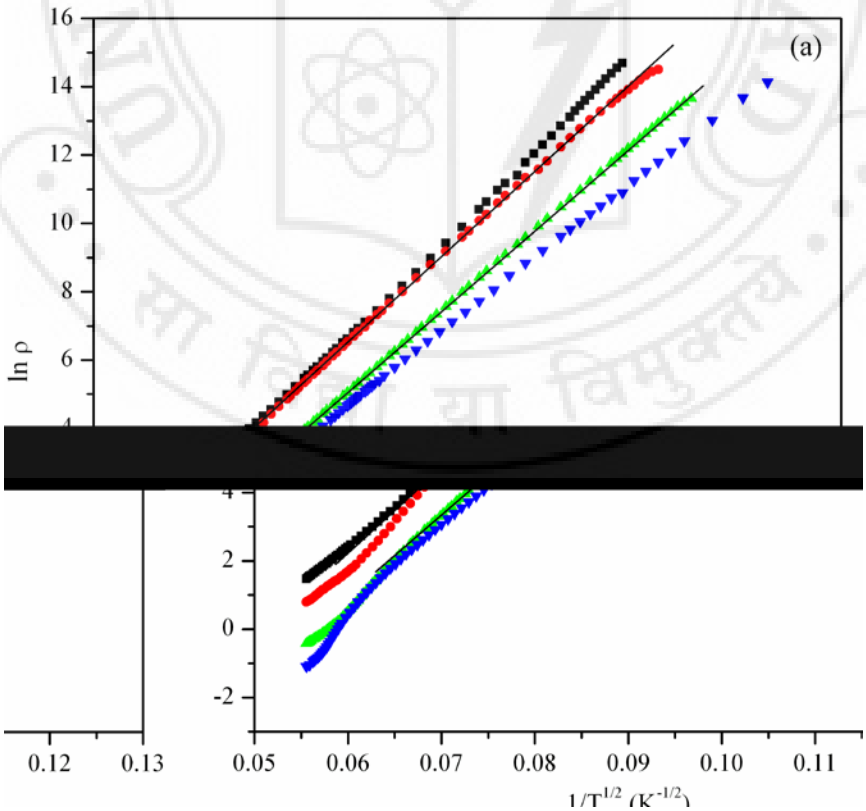

Figure 5.21a ln ρ versus $1/T^{(1/2)}$ plots of BCSMO for x = 0, 0.02, 0.04 and 0.08.

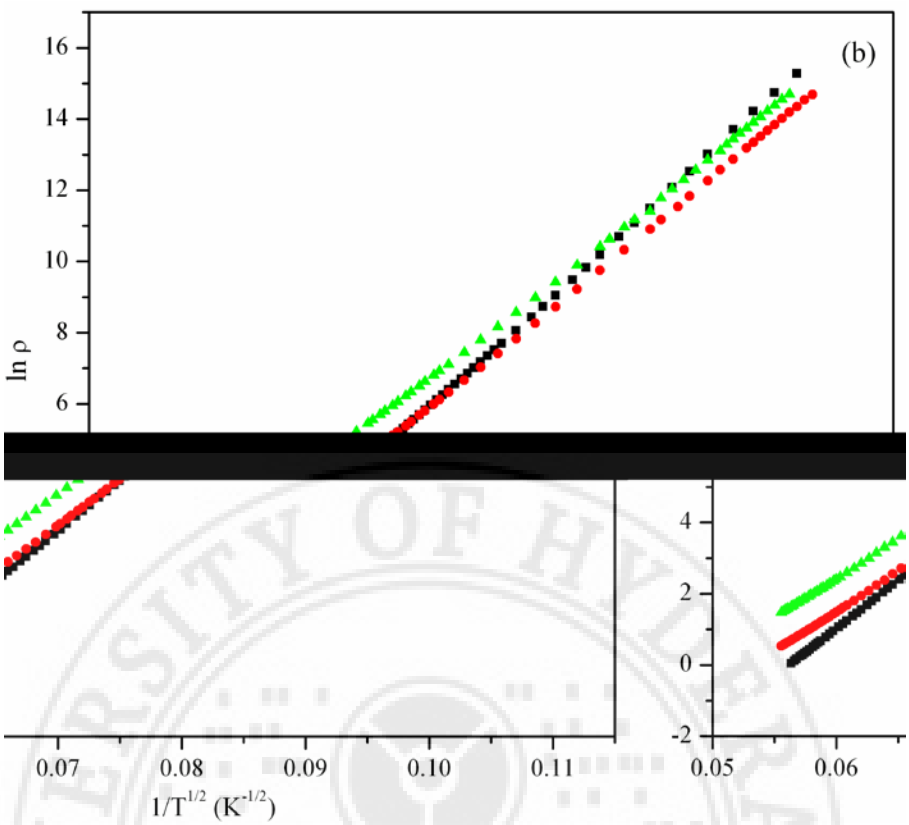

Figure 5.21b ln ρ versus 1/T $^{(1/2)}$ plots of BCSMO for *x* = 0.06, 0.08 and 0.1.

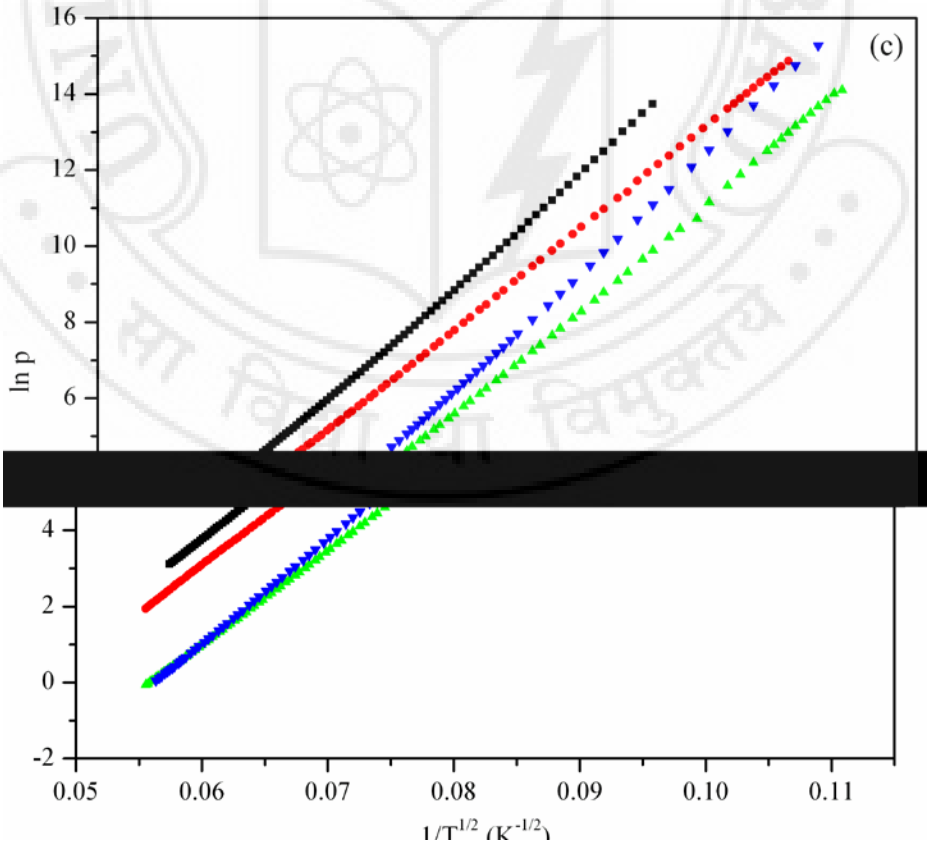

Figure 5.21c ln ρ versus 1/T $^{(1/2)}$ plots of BCSMO for *x* = 0.1, 0.16, 0.24 and 0.4.

The ln ρ vs $T^{-1/2}$ plots are shown in figure 5.21a, 5.21b and 5.21c. These plots are linear in the entire temperature range for compositions with $x \leq 0.06$. For compositions with $x \geq 0.08$, there is an increase in the slope of the linear fits at T_N. This feature may be ascribed to the existence of disorder-induced localized electronic states populating the Mott–Hubbard gap. Hence the Mott's VRH model can be relied upon to analyze the temperature dependent resistivity data of the BCSMO system for $x \leq 0.06$.

As observed for the other samples, the resistivity data for these samples can be explained qualitatively by the percolation model. The ESR studies indicate the increase in the contributions of the FM correlations with the increase in Sr content. Inclusion of disconnected FM clusters in the AFM matrix leads to increase in resistivity upto $x = 0.06$. With further increase in Sr content the concentration of FM clusters increase leading to formation of some percolative conduction paths leading to decrease in resistivity. When Sr content is further increased, Sr – rich CO (AFM) phase appears and the resistivity increases. The AFM clusters grow with decreasing temperature, at the expense of FM clusters and the sharp increase of resistivity below T_N is being attributed to the long range AFM ordering leading to low connectivity of the FM clusters. The increase in resistivity with the decrease in temperature is sharp for the samples ($x = 0.1$ and 0.16) having low resistivity at 300K. The high Curie constant also supports the existence of FM clusters in these compositions. Similar interpretation is given by Qin *et. al.* [105] to explain the formation of FM clusters in the $Bi_{0.125}Ca_{0.875}MnO_3$ sample.

5.6 Resistivity Studies on $Bi_{0.5}Sr_{(0.5-x)}Ce_xMnO_3$ (BSCMO)

The temperature dependent resistivity variation for the BSCMO system is plotted in figure 5.22. All samples show a semiconducting behaviour throughout the temperature range. The resistivity at 300K increases from ~ 0.1 to ~ 3Ωcm. No anomaly is observed around this temperature in these plots.

To analyze the resistivity data the three models, namely, the small polaron model, Mott's VRH model and ES-VRH model, are used by plotting the ln (ρ/T) v 1000/T, ln ρ v $(1/T)^{(1/4)}$ and ln ρ v $(1/T)^{(1/2)}$ graphs respectively.

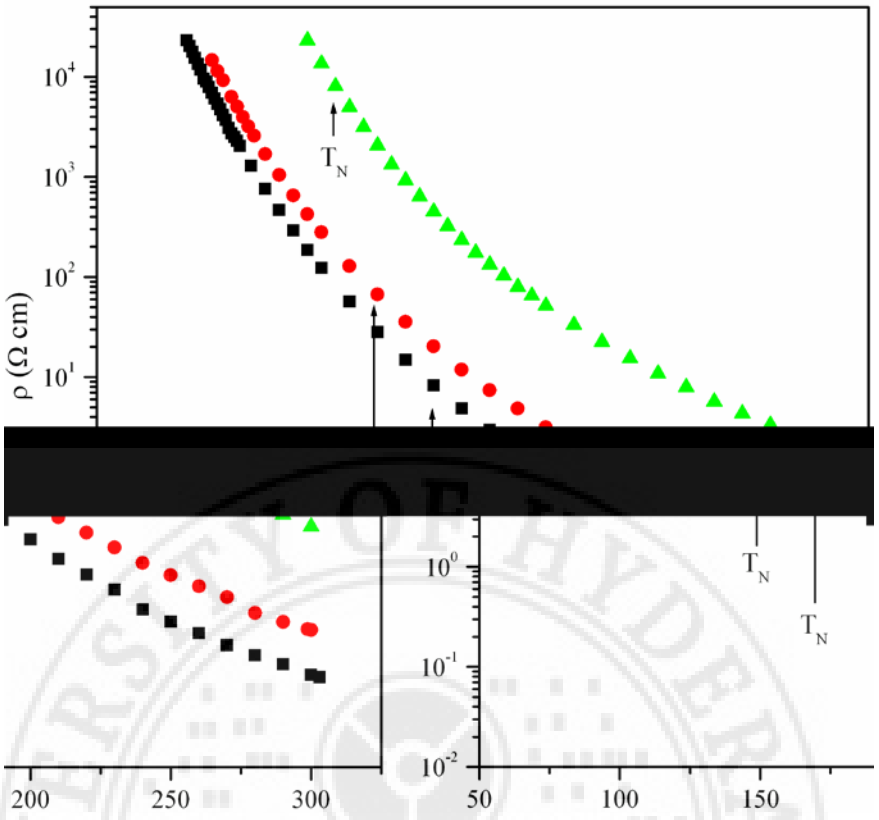

Figure 5.22. Resistivity vs temperature plots for $Bi_{0.5}Sr_{(0.5-x)}Ce_xMnO_3$.

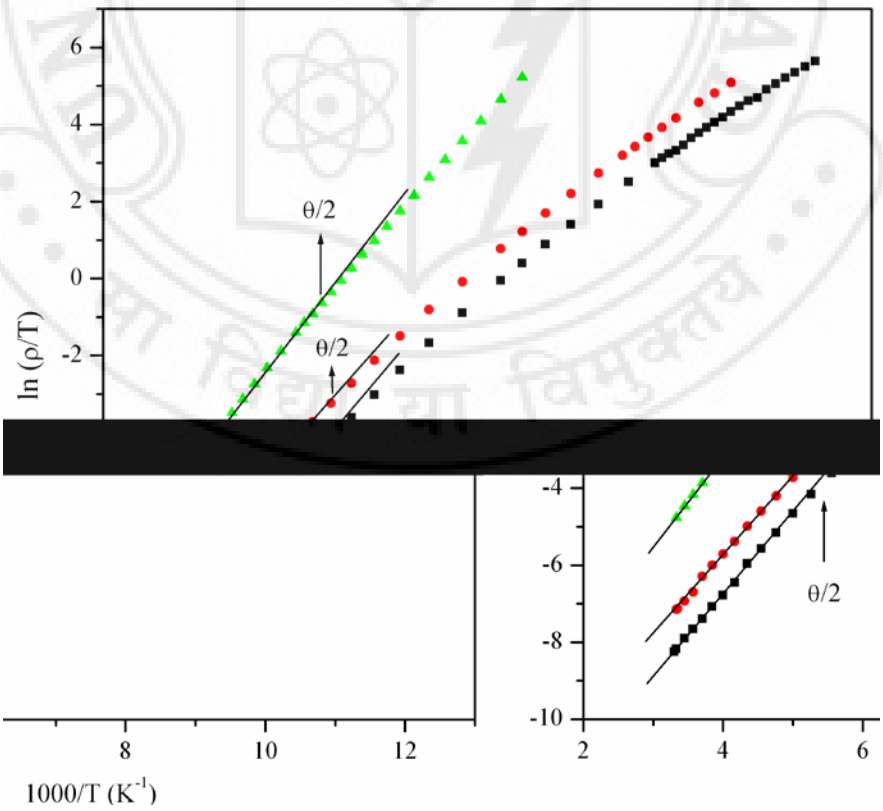

Figure 5.23 ln(ρ/T) versus (1000/T) plots of $Bi_{0.5}Sr_{(0.5-x)}Ce_xMnO_3$.

The ln(ρ/T) versus (1000/T) graphs for the BSCMO system are plotted in figure 5.23. The high temperature data fits for a small range of temperatures for both the adiabatic (n=1) as well as non adiabatic (n = 1.5) hopping conduction, according to equation (5.18), making it indistinguishable for a better fit of the two. A continuous curvature below $\theta_D/2$ implies the continuous decrease in W as per the polaron model. From the linear fits to the high temperature data the θ_D as well as W for hopping are calculated for the samples (table 5.9). In the low temperature region, i.e. $T < \theta_D/4$, $W \approx W_D$, values for samples x = 0 and 0.1 are listed in table 5.9.

Sample x	θ K	E_P for n = 1 meV	E_P for n = 1.5 meV	W_D (for $T < \theta/4$) meV
0	374	178	189	100
0.1	380	176	187	99
0.2	400	198	210	

Table 5.9. Debye temperature and activation energies from the thermally activated hopping model for n = 1 and 1.5 for the $Bi_{0.5}$ $Sr_{(0.5-x)}Ce_xMnO_3$ system.

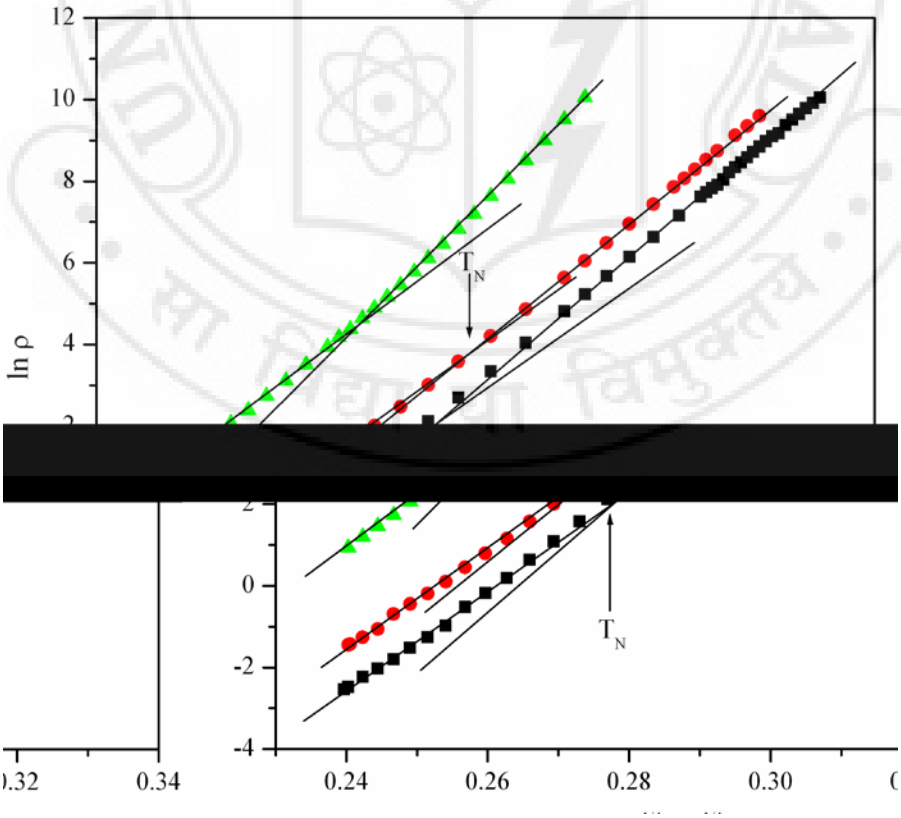

Figure 5.24 ln ρ versus $1/T^{(1/4)}$ plots of the $Bi_{0.5}Sr_{(0.5-x)}Ce_xMnO_3$

The ln ρ vs $1/T^{(1/4)}$ plots of the BSCMO system are shown in figure 5.24. The T_{CO} for these samples is observed in the temperature range of measurement. The slope increases at ~T_N like that for other series of samples. The estimated model parameters are listed in table 5.11.

Sample *x*	T_0 (10^8K)		ρ_0 10^{-13} (Ωcm)	
	$T_{CO} > T > T_N$	$T < T_N$	$T_{CO} > T > T_N$ (x 10^{-13})	$T < T_N$ (x 10^{-18})
0	2.013	4.851	20.9	684
0.1	2.058	4.09	0.71	146
0.2	3.531	9.428	0.12	0.38

Table 5.10. T_0 and ρ_0 values obtained from ln ρ versus $T^{-1/4}$ plots in different temperature ranges for $Bi_{0.5}Sr_{(0.5-x)}Ce_xMnO_3$.

Sample *x*	ξ (A°)		R (nm)		W (meV)	
	$T_{CO} > T > T_N$	$T < T_N$	$T_{CO} > T > T_N$	$T < T_N$	$T_{CO} > T > T_N$	$T < T_N$
0	7.0	5.2	7.6	7.0	185	231
0.1	7.0	5.2	7.6	7.0	185	231
0.2	5.8	4.2	7.2	6.6	213	273

Table 5.11. Various VRH model parameters estimated for $Bi_{0.5}Sr_{(1-x)}Ce_xMnO_3$ using $N(E_F) \approx 3\times10^{18}$ cm^{-3} eV^{-1} in different temperature ranges

The cogency of the ES-VRH model is checked as these samples. As observed for the previously studied Bi manganite systems from equation (5.24) the value of the calculated localization length ξ and is not found to be of the order of the unit cell dimension and the values of ρ_0 are also different from those predicted by Mott [49]. This is regardless of the fact that almost all of the ln ρ with $T^{-1/2}$ (figure 5.25) plot for the samples have a linear variation in the entire temperature range for the samples x = 0 and 0.1. The disorder-induced localized electronic states populating the Mott–Hubbard gap can be the cause of this observation. The Mott's VRH model can be relied upon to analyze the temperature dependent resistivity data of the BSCMO system. The resistivity data for the BSCMO

system can also be qualitatively analyzed in view of the percolation model. The increase of resistivity with Ce is ascribed to the formation of isolated FM correlated domains in the AFM matrix as supported by the ESR studies. The AFM clusters grow as temperature decreases and the FM contribution decreases with the sharp increase of resistivity below T_N being attributed to the long range AFM ordering leading to low connectivity of the FM clusters.

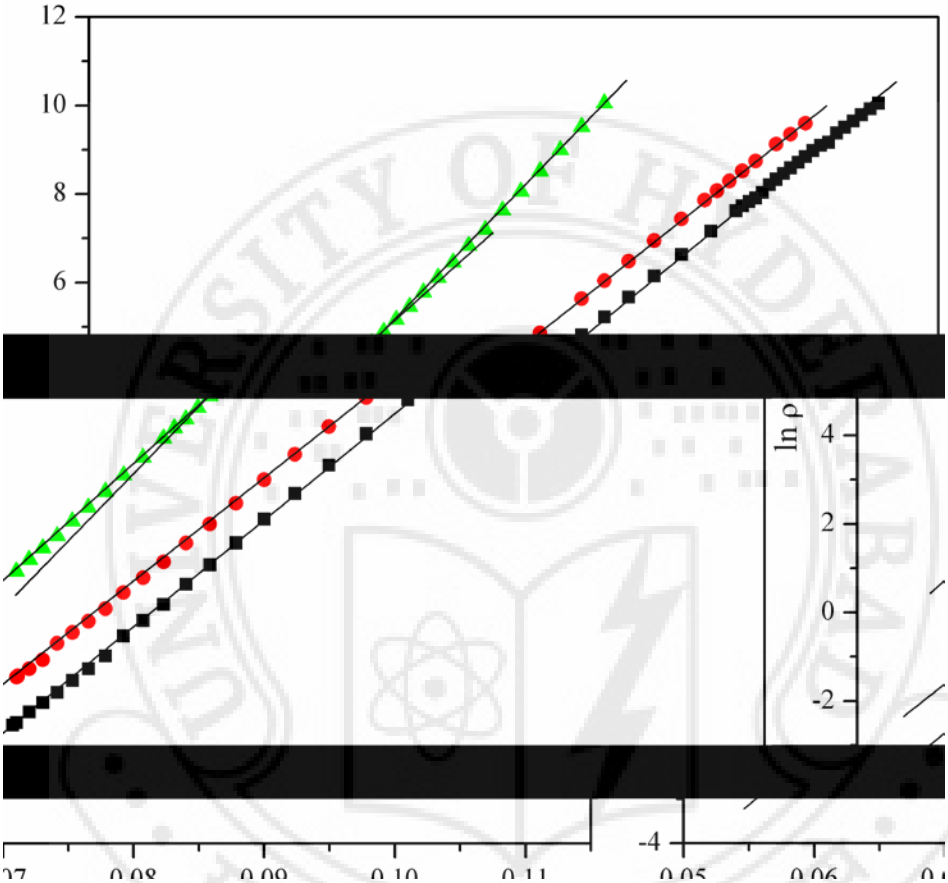

Figure 5.25 ln ρ versus $1/T^{(1/2)}$ plots of the $Bi_{0.5}Sr_{(0.5-x)}Ce_xMnO_3$

The high temperature conduction mechanism of manganites exhibiting strong insulating behaviour (especially at low temperatures) is explained by the polaron model. In the BSCMO system the Bi $6s^2$ lone pair of electrons favour charge localization resulting in the high resistivity of the material and hence play a significant role in deciding the electrical conductivity of these samples [99, 114]. The Ce^{4+} ions, which are non magnetic but which stabilize easily, too can be a major contributor to the higher resistance. This is also indicative of stronger Andersons localizations. As a result, the high temperature resistivity can be understood in view of the polaron model.

With increasing Ce content the resistivity increases. In the BSMO system, as the content of Sr increases the resistivity decreases as the Mn^{3+}/Mn^{4+} ratio decreases because Sr being in the +2 valence state favours the formation of Mn^{4+} ions. When cerium, with a valence state of +4, is substituted for Sr in the BSMO system the formation of Mn^{2+} ions is required for charge neutralization. But there is also a possibility of Ce to exist in the Ce^{3+} state, which would introduce Mn^{3+} ions in the sample. For an excess of oxygen content Mn can also take also take +4 state along with the +2 and +3 state. The double exchange (Mn^{3+}- O – Mn^{4+}) and superexchange (Mn^{2+}- O – Mn^{3+} and Mn^{3+}- O – Mn^{3+}) mechanisms play a role in determining the resistivity of the samples. The competition between the two can hamper the mobility of the carriers [25, 26]. The electron hopping between Mn^{2+} and Mn^{3+} will occur at a lower rate than that of hole hopping between Mn^{4+} and Mn^{3+} [155, 275, 276]. Hence Mn^{2+} sites can be considered to act as blocking sites for polaron hopping.

The Mn ions existing in different valence states have different ionic radius, it being the largest for Mn^{2+} and the smallest for the Mn^{4+} ion. The ionic radius of Ce^{3+} is bigger than that of the Ce^{4+} ion. The difference in the ionic radii of all the ions which can possibly be present in the samples can bring about a distortion in the structure of the samples. This distortion is reflected in the XRD studies as a change from the tetragonal to orthorhombic structure. This in turn changes the bond length and angle which hinders the mobility of the carrier. As seen from the SEM studies the Ce-rich particles/grains which lie at the grain boundaries and in between the regions of the other grains can also contribute to the increase in the resistivity [154].

5.7 Resistivity Studies on $Bi_{0.5}Ca_{0.5}Mn_{(1-x)}Cr_xMnO_3$ (BCMCO)

The temperature dependent resistivity of the BCMCO system is depicted in figure 5.26. The lowest temperature at which the resistivity was measured was limited to ~ 68K as the resistance of the samples was very high below this temperature. A step like change in ρ with decreasing temperature is observed at high temperatures, indicating the T_{CO}. The resistivity has a continuous curvature with a steep increase at T_N. With increasing *x* the T_{CO} decreases. This is similar to other reports on Cr-doped Bi-manganites [137, 138]. Room temperature (300K) resistivity and T_{CO} variation with composition are shown in figure 5.27.

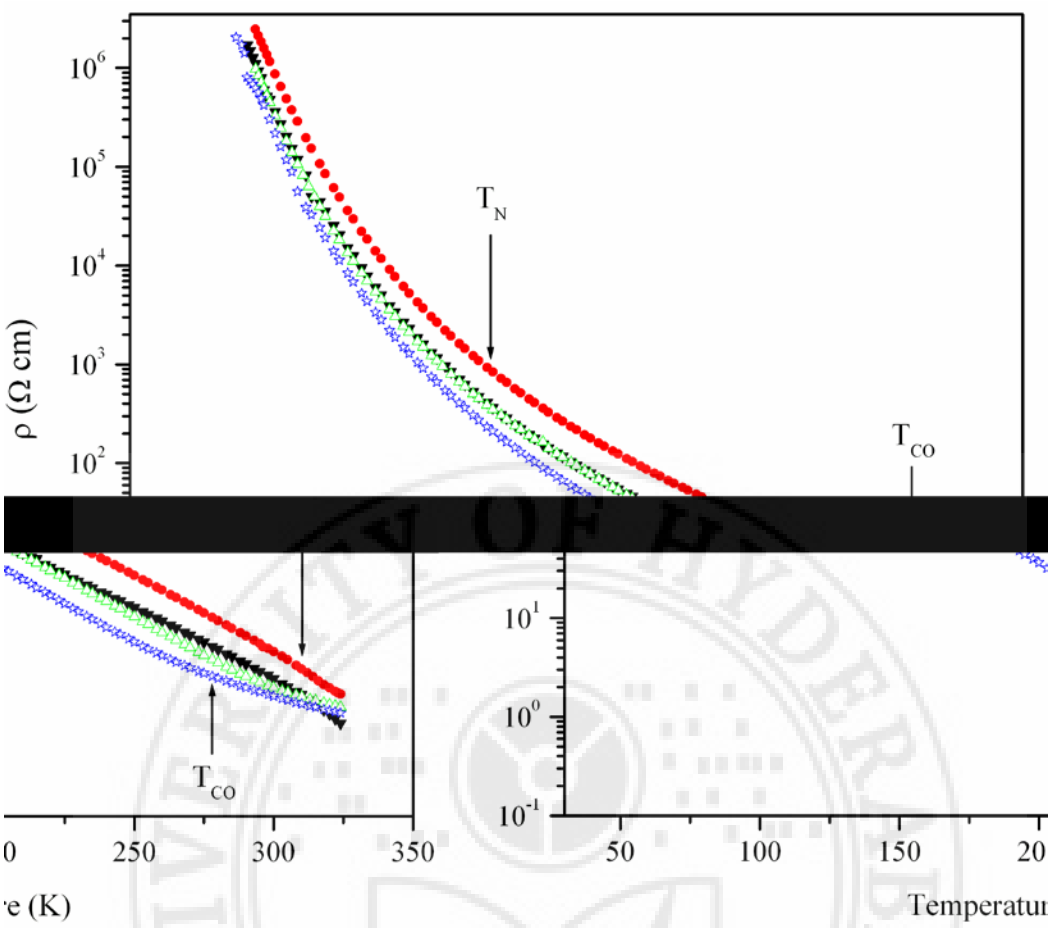

Figure 5.26. Resistivity vs temperature plots for $Bi_{0.5}Ca_{0.5}Mn_{(1-x)}Cr_xO_3$.

Figure 5.27 Variation of resistivity 300K and T_{CO} of the BCMCO system with respect to composition

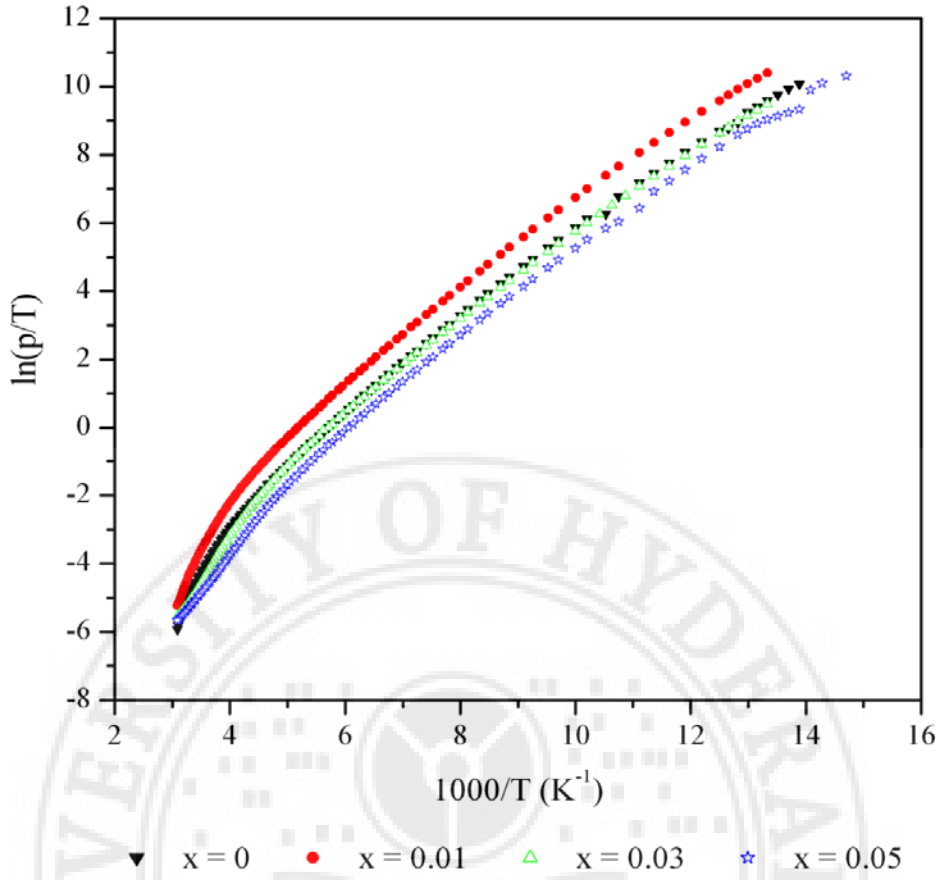

Figure 5.28 ln(ρ/T) versus (1000/T) plots of $Bi_{0.5}Ca_{0.5}Mn_{(1-x)}Cr_xO_3$.

The resistivity data is analyzed in view of the polaron model by plotting the ln (ρ/T) versus 1000/T according to equation (5.18) with the value of n = 1 (figure (5.28). A continuous curvature is observed in the ln (ρ/T) versus 1000/T plots for all the samples of this system. A similar variation of ln (ρ/T) is observed for n = 1.5. The temperature dependent resistivity studies on Cr doped La based manganites have yielded results confirming the validity of the small polaron model in the high temperature range [277 – 280].

The validity of the VRH model for dimensionality of 2 and 3 (with the value of n = 1/3 and 1/4 respectively) in the high temperature range [283, 284] and in some cases up to very low temperatures too [221 – 223, 278 – 282], have been reported for Cr doped manganites. The data analysis in view of the Motts VRH model is done for the present samples by plotting ln ρ versus $1/T^{(1/4)}$ (figure 5.29). The straight line fits, with increase in slope at T_N, are obtained. The T_0 values are estimated from the slope of these curves and listed in table 5.12. The values of localization length, hopping distance and hopping energy are estimated from the equations 5.20, 5.21 and 5.22 (table 5.13). The T_{CO} is

estimated from the deviation of the straight line fit in the high temperature region. These values match with the values obtained from the ESR data.

Figure 5.30 depicts the ln ρ versus $1/T^{(1/2)}$ plots, as per the ES-VRH model. The curvature observed at high temperatures of the plots indicates the T_{CO}. Below T_{CO} the plots are linear till the lowest temperature. The values of T_0 and ρ_0 are calculated from equation (5.23). The localization length, ξ, is estimated from equation (5.24). It is found that the value of ξ is not of the order of unit cell dimension and is thus unreasonable. The

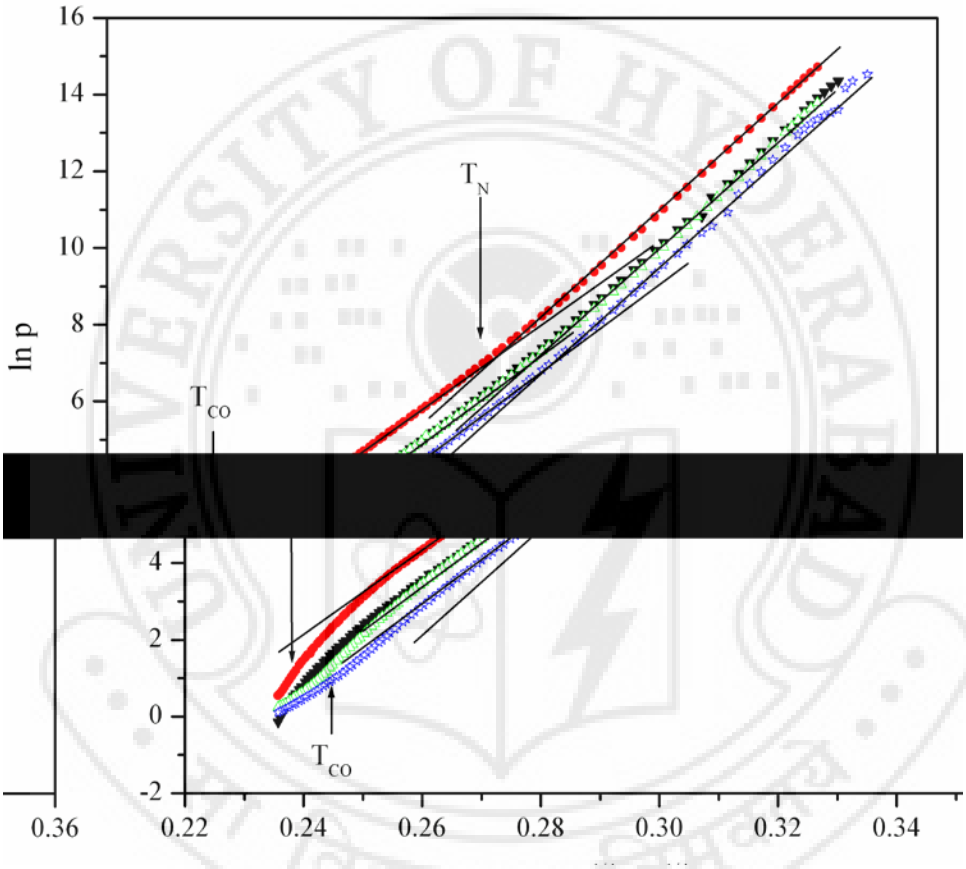

Figure 5.29 ln ρ versus $1/T^{(1/4)}$ plots of the $Bi_{0.5}Ca_{0.5}Mn_{(1-x)}Cr_xO_3$

ρ_0 values are much lower than the expected theoretical values predicted by Mott [49] for these materials. The ordinary size of the Coulomb gap is in the range 10–100 K [251, 252]. The energy scale of fitting regions in the BCMCO system is $T \leq 300$ K, which is very high. Taking this into account it is unlikely that the observed ES-type behaviour is due to the emergence of the Coulomb gap as pointed out in the case of other series of samples analyzed earlier.

As seen from the ESR studies, with the addition of Cr the FM contributions increase. When Mn^{3+} is partially replaced with Cr^{3+}, Mn^{3+} - O – Cr^{3+} is SE FM interacted, though it is weaker than the DE FM interaction of Mn^{3+}- O –Mn^{4+}. In addition to this there is also the Cr^{3+} - O - Cr^{3+} AFM interaction which enhances the proportion of Mn^{4+} - O - Mn^{4+} interactions [230, 231].

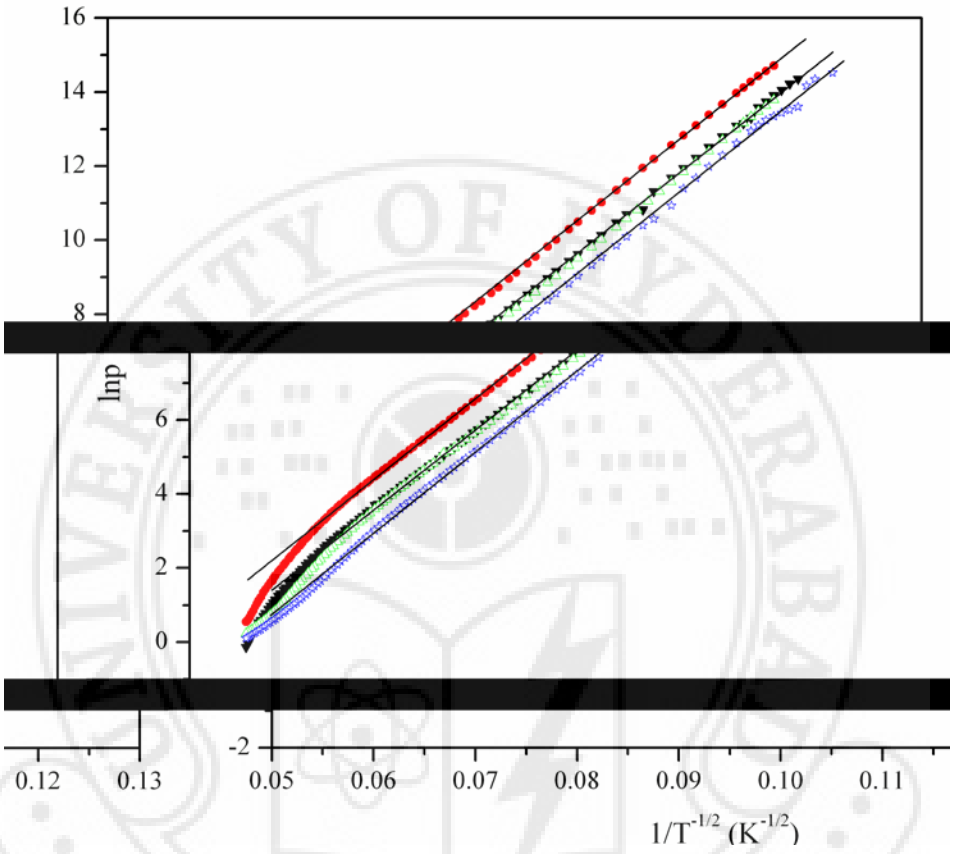

Figure 5.30 ln ρ versus $1/T^{(1/4)}$ plots of the $Bi_{0.5}Ca_{0.5}Mn_{(1-x)}Cr_xO_3$

Sample *x*	T_0 (10^8K)		ρ_0 (Ωcm)	
	$T_{CO} > T > T_N$	$T < T_N$	$T_{CO} > T > T_N$ (x 10^{-13})	$T < T_N$ (x10^{-16})
0	1.752	3.641	33.4	40
0.01	1.728	3.974	85.0	36
0.03	1.811	4.262	24.7	6.0
0.05	1.903	4.289	9.7	4.0

Table 5.12. T_0 and ρ_0 values obtained from ln ρ versus $T^{-1/4}$ plots in different temperature ranges for $Bi_{0.5}Ca_{0.5}Mn_{(1-x)}Cr_xO_3$.

Sample x	ξ (A^o)		R (nm)		W (meV)	
	$T_{CO} > T > T_N$	$T < T_N$	$T_{CO} > T > T_N$	$T < T_N$	$T_{CO} > T > T_N$	$T < T_N$
0	7.4	5.8	7.6	7.2	179	215
0.01	7.4	5.6	7.6	7.1	178	220
0.03	7.3	5.5	7.6	7.1	180	224
0.05	7.2	5.5	7.6	7.1	183	224

Table 5.13 Various VRH model parameters estimated for $Bi_{0.5}Ca_{0.5}Mn_{(1-x)}Cr_xO_3$ using $N(E_F) \approx 3\times10^{18}$ cm^{-3} eV^{-1} in different temperature ranges.

The resistivity data of the BCMCO system can be qualitatively analyzed in view of the percolation model, mentioned before. Introduction of 1% (x = 0.01) of Cr enhances the Mn^{3+} ionic content, which is SE correlated. This hinders the hopping of the carriers, increasing the resistivity of the sample. For $x \geq 0.03$ the resistivity is lower than that of the undoped and 1% doped samples. The addition of Cr beyond 1% introduces FM correlations domains. The connectivity of these domains provides the percolation path for conduction and thus reduces the resistivity. At T_{CO}, due to the formation of AFM clusters a jump in the resistivity is observed. With decreasing temperature the AFM clusters grow at the expense of the FM clusters. This increases the resistivity as the AFM clusters promote an insulating phase. With the long range AFM order setting in the size of the FM clusters decrease. At $T < T_N$ a sharp increase in resistivity occurs due to the low connectivity of the FM clusters.

Summary of the resistivity studies.

Temperature dependent resistivity studies were carried out on different Bi- based manganites to understand the conduction mechanism in these systems. All the samples show a semiconducting behaviour throughout the temperature range of 70 – 300K. The resistivity data could not be acquired at lower temperatures as the resistance of the samples was very high (beyond the measurable range of the equipment) at low temperatures. The temperature dependent resistivity data is analyzed in view of the polaron model, the Motts variable range hopping model and the ES-VRH model.

The polaron model is valid for Sr – based BSMO and BSCMO systems and the Sr – rich BCSMO system which have high resistivity (1 – 10^2 Ωcm) at 300K. The values of activation energy W, the disorder energy W_D and the Debye temperature θ_D were found to be in the range (178 – 226meV), (99 – 113meV) and (344 – 430K) respectively depending on the composition of these samples. The polaron hopping conduction is found to be in the adiabatic regime. The polaron model is found to be inapplicable for the Ca – based BCMO and BCMCO systems and the Ca – rich BCSMO system which have room temperature resistivity in the range (0.1 – 10 Ωcm) at 300K.

The resistivity data analyzed in view of Mott's VRH model show that ln ρ varies linearly with $1/T^{1/4}$ with a change in slope at T_N for all the samples. The model parameters characteristic temperature T_0, localization length ξ, hopping distance R and hopping energy W are found to be ~ 10^8K, 4.2 – 8.9 A^o, 6.6 – 10.5 nm and 185 – 290 meV for the Sr – based and Sr – rich samples and ~ 10^8K, 5.5 – 7.8A^o, 7.1 – 7.7nm and 172 – 206 meV for the Ca – based and Ca – rich samples respectively, which were estimated using the density of states $N(E_F) \approx 10^{18} cm^{-1} eV^{-1}$. The values are found to be physically acceptable validating the Motts VRH model for the Bi – manganites. In the absence of any reported value $N(E_F)$ is assumed to be ~10^{18} cm^{-1} eV^{-1}, with the dielectric constant ε ~ 10^3. For $N(E_F)$ ~10^{20} cm^{-1} eV^{-1} the dielectric constant will be ε ~ 10^6 to obtain physically acceptable value to validate the Motts VRH model. It is found that the T_0 values are higher in the AFM state than in the PM + CO state for all the samples studied. This is due to the different magnetic structure of AFM and PM state. In the AFM state the moments are aligned antiparallel to the neighbouring magnetic moments making the carrier hopping difficult compared to the PM state where magnetic moment are randomly oriented.

The resistivity data is analyzed in view of the ES VRH model too. It is found that ln ρ varies linearly with $T^{-1/2}$ in the entire temperature range below T_{CO} for the Ca – based BCMO and BCMCO systems and the Ca – rich ($x < 0.06$) BCSMO system. The fitting parameters estimated from these plots do not present physically acceptable values. This $T^{-1/2}$ dependence of ρ can be ascribed to the existence of disorder-induced localized electronic states populating the Mott–Hubbard gap. The Sr doped (or Sr – rich) samples follow the polaron hopping conduction mechanism in the high temperature range they do not exhibit a straight line fit throughout the temperature range as per the ES VRH model.

The plots of resistivity at 300K (ρ_{300}) and T_{CO} with composition for the Sr doped (or Sr – rich) systems show that resistivity values scale with T_{CO} for almost all the compositions. Whereas, this is not the case for the Ca doped (or Ca – rich) samples. The lower resistivity and T_{CO} values are found in Ca – based and Ca – rich compositions in comparison to the Sr – based and Sr – rich compositions. These differences are reported in literature for the Ca and Sr based systems. These differences have been explained in view of the highly polarizable Bi^{3+} $6s^2$ lone pair of electrons. The effective ionic radius of Bi^{3+} depends on the character of the $6s^2$ lone pair. When the lone pair character is dominant Bi^{3+} takes an ionic radius of $1.24A^o$, while for a constrained lone pair character Bi^{3+} takes an ionic radius of $1.16A^o$. The different values of T_{CO} in the BSMO and BCMO system can be attributed to the orientation of the lone pair towards a surrounding anion (O^{2-}), which produces a local distortion or a hybridization between the 6s-Bi-orbitals and 2p-O-orbitals. Hybridization hinders the movement of the itinerant e_g electrons through the Mn – O – Mn bonds. This localizes the electrons and favours charge ordering. In the BCMO system the lone pair is strongly screened with a preferred orientation far from the Bi-O bonds. Conversely, the lone pair character is dominant in BSMO, weakly screening the $6s^2$ lone pair and the electron density of the lone pair may be high along some Bi-O bonds. This electronic density could be involved in strong covalent interactions with Bi-O bonds. producing an effective bigger Bi^{3+} ionic size [114, 192].

The resistivity data of the samples can be explained qualitatively by the percolation conduction model for mixed phase manganites. In the PM state of the samples on lowering the temperature the existence of FM correlations give rise to a slow increase of resistivity. On approaching the T_{CO} AFM correlations emerge. At T_{CO}, a step like increase in the resistivity is observed due to the contributions of AFM clusters favoured by the CO state. With change in composition the AFM interactions (clusters) enhance or

diminish at the expense of the FM clusters giving rise to increase or decrease in resistivity at R.T respectively. This is supported by the variation in Curie constant as a function of composition. With decrease in temperature the AFM (insulating) clusters grow progressively at the expense of FM (metallic) clusters giving rise to increase in resistivity. The FM cluster size decreases as the long AFM order sets in. The volume fraction occupied by FM clusters is very small compared with the volume of the AFM phase. A sharp increase in resistivity observed below T_N, therefore, may be due to quite low connectivity between FM clusters. The emergence and growth of different magnetic clusters with change in temperature is confirmed from the ESR studies and also understood in view of the phase separation concept.

SUMMARY

Perovskite structured manganites of the general formula $ABMnO_3$ are mixed valence materials with the A site constituting trivalent ions (e.g. La, Bi, Pr, Nd, etc) and the B site, divalent ones (e.g. Sr, Ca, Pb, etc) and which exhibit properties like CMR, magnetic field induced phase transition, the phenomenon of charge and orbital ordering and electric, magnetic phase transitions with electron or hole doping etc. The slightest change in the composition can bring drastic changes in the electrical and magnetic behaviour of the materials. The knowledge of competing magnetic, structural and charge interactions is essential to understand different properties in perovskite manganites. In the recent years the phenomena of electronic phase separation (PS), i.e. the coexistence of different magnetic phases, has been intensely studied in various manganites in terms of Griffiths Phase (GP) concept.

Electron spin resonance (ESR) is known to be a powerful technique for understanding the spin structure and its dynamics. The changes in short – range magnetic interactions and micro – magnetic phases can be easily detected because of its high sensitivity. There are very few ESR studies on Bi- manganites.

In this thesis, the detailed temperature dependent ESR studies on different compositions of Bi – manganites are reported. The temperature dependence of resistivity for all the compositions was also carried out with the objective of understanding the conduction mechanisms in these materials and possible correlation with the ESR data.

The different series of Bi-manganite samples studied are:

1. $Bi_{(1-x)}Ca_xMnO_3$ ($0.4 \leq x \leq 0.75$) (BCMO)
2. $Bi_{(1-x)}Sr_xMnO_3$ ($0.3 \leq x \leq 0.5$) (BSMO)
3. $Bi_{0.6}Ca_{(0.4-x)}Sr_xMnO_3$ ($0 \leq x \leq 0.4$) (BCSMO)
4. $Bi_{0.5}Sr_{(0.5-x)}Ce_xMnO_3$ ($0 \leq x \leq 0.2$) (BSCMO)
5. $Bi_{0.5}Ca_{0.5}Mn_{(1-x)}Cr_xO_3$ ($0 \leq x \leq 0.05$) (BCMCO)
6. $Bi_{0.55}Ca_{0.45}MnO_3$ nanoparticles.

The phase formation, structural change with different dopants, grain homogeneity and the compositional analysis of the samples were ascertained and studied from the XRD, SEM and EDAX studies. Temperature dependent ESR studies were undertaken in

view of understanding the different micromagnetic phases that are formed in the samples with varying dopant contents at different sites in the Bi – manganites. The ESR spectra parameters like linewidth (ΔH) and double integrated intensity of the resonance line (DI) (which is proportional to ESR susceptibility, χ_{ESR}) were calculated for all the samples. DI vs temperature (T), 1/DI vs T (following the Curie Weiss law), ln DI vs 1/T (following the Arrhenius equation) and ΔH vs T were plotted to provide information about T_{CO}, T_N and existence of and competition between various magnetic phases/domains as a function of composition and temperature. Room temperature magnetization data gives information on the variation of the magnetic moment and Curie constant of the samples as a function of composition. The detailed temperature dependence of resistivity for the samples was carried out with the objective of understanding the conduction mechanisms in these materials. A possible correlation between the ESR and resistivity data is explored.

The single phase formation of all the samples is verified from the XRD plots. The BCMO system shows a change from triclinic (~ monoclinic) to orthorhombic (~ tetragonal) structure with increasing Ca content. The XRD plots of the BSMO system show a change from a ~ monoclinic structure for $x = 0.3$ to a ~ tetragonal structure at $x = 0.5$. With increasing Sr content in the BCSMO system the structure of the samples gradually change from triclinic (for $x = 0$) to tetragonal (~ orthorhombic) (for $x = 0.4$). The Ce doped BSCMO system is analyzed for a tetragonal (~ orthorhombic) structure while the addition of Cr at the Mn site in the half doped BCMO system changes the structure from orthorhombic to a ~ tetragonal type. XRD studies on the sol-gel synthesized BCMO nanoparticles show single phase formation and the average particles size estimated using Scherrer formula are found to be 21nm and 15nm for samples prepared under different conditions.

The SEM data show the grain size ranging from a few hundred nanometers to a few microns for all the samples. Samples with higher content of Bi show formation of large grain agglomerates. EDAX analysis of select samples confirmed the composition.

The transition temperatures, T_{CO} and T_N, were obtained for various Bi – manganites from the temperature dependent ESR studies. The values of T_{CO} and T_N estimated for the BCMO system vary in the range 301 – 320K and 148 – 160K respectively. In the BSMO system the T_{CO} is not observed as it is above ~ 475K, the maximum temperature achieved in the experimental setup. The T_N values increase from 133K to 173K with increase in Sr content. With increasing Sr content in the BCSMO system the T_{CO} values estimated for 0

$\leq x \leq 0.1$ vary between 288 and 320K while for $0.1 \leq x \leq 0.4$ the T_{CO} increases from ~ 343K to 575K with increase in Sr content. The T_N values for all samples vary between ~138 to 163K.

In the BSCMO system the T_{CO} is not observed as it is above the maximum temperature achieved in the experimental setup. The T_N values decrease from ~ 173K to ~ 138K with increase in Ce content. The T_{CO} decreases from 317K to 278K as *x* increases from 0 to 0.05. The value of T_N is ~160K for the $x = 0$ and 0.01 samples and it decreases to ~ 120K for sample with $x = 0.05$. The values estimated for the samples are comparable with values reported in literature estimated by other techniques

The magnetic phase for the samples in the temperature range $T > T_{CO}$ is dominated by FM correlations which can be attributed to activated Mn^{3+}–Mn^{4+} hopping of a small polaron. In the temperature range $T_{CO} > T > T_N$, the domains of FM and AFM spin correlations coexist. For $T < T_N$, temperature independent ln DI indicates the freezing of FM microdomains/ inhomogeneities in the AFM long-range ordered state. The ESR measurements of the different Bi – manganite systems are explained in view of the GP physics model.

In the temperature range $T > T_{CO}$, the linear increase of ΔH with increase in temperature and the sharp upturn at T_{CO} observed can be explained in view of the theoretical model given by Hu. In the charge-ordered state, $T_N < T < T_{CO}$, the ΔH first increases, remains constant over a temperature range and then again increases with decrease in temperature. The ΔH decreases sharply below T_N. The critical exponents estimated for the BCMO system in the temperature range $T_{CO} > T > T_N$ vary from − 0.73 to − 1.12 depending on the composition of the sample in the temperature range $\varepsilon < 0.25$, where $\varepsilon = (T - T_N)/T_N$. In the BCMO nanoparticle system the critical exponent increases with decrease in grain size from -0.73 for the bulk to -1.51 for 15 nanometer-size sample in the temperature range $\varepsilon < 0.3$, which is close to theoretical value of -5/3 predicted by theoretical model for plain PM to AFM transition.

Temperature dependent resistivity studies carried out on different Bi–manganites show all the samples exhibiting a semiconducting behaviour throughout the temperature range of 70 – 300K. The temperature dependent resistivity data is analyzed in view of the polaron model, the Motts variable range hopping model and the ES-VRH model.

The polaron model is valid for Sr – based BSMO and BSCMO systems and the Sr – rich BCSMO system which have high resistivity (1 – 10^2 Ωcm) at 300K. The values of activation energy W, the disorder energy W_D and the Debye temperature θ_D were found to be in the range (178 – 226meV), (99 – 113meV) and (344 – 430K) respectively depending on the composition of these samples. The polaron hopping conduction is found to be in the adiabatic regime. The polaron model is found to be inapplicable for the Ca – based BCMO and BCMCO systems and the Ca – rich BCSMO system which have room temperature resistivity in the range (0.1 – 10 Ωcm) at 300K.

The resistivity data analyzed in view of Mott's VRH model show that ln ρ varies linearly with $1/T^{1/4}$ with a change in slope at T_N for all the samples. The model parameters characteristic temperature, T_0, localization length, ξ, hopping distance, R, and hopping energy, W, are found to be ~ 10^8K, 4.2 – 8.9 A^o, 6.6 – 10.5 nm and 185 – 290 meV for the Sr – based and Sr – rich samples and ~ 10^8K, 5.5 – 7.8A^o, 7.1 – 7.7nm and 172 – 206 meV for the Ca – based and Ca – rich samples respectively, which were estimated using the density of states $N(E_F) \approx 10^{18}$cm^{-1}eV^{-1}. The values are found to be physically acceptable validating the Motts VRH model for the Bi – manganites. It is found that the T_0 values are higher in the AFM state than in the PM + CO state for all the samples studied as the AFM state the moments are aligned antiparallel to the neighbouring magnetic moments making the carrier hopping difficult compared to the PM state where magnetic moment are randomly oriented.

The resistivity data is analyzed in view of the ES VRH model too. It is found that ln ρ varies linearly with $T^{-1/2}$ in the entire temperature range below T_{CO} for the Ca – based BCMO and BCMCO systems and the Ca – rich ($x < 0.06$) BCSMO system. The fitting parameters estimated from these plots do not present physically acceptable values. This $T^{-1/2}$ dependence of ρ can be ascribed to the existence of disorder-induced localized electronic states populating the Mott–Hubbard gap. The Sr doped (or Sr – rich) samples follow the polaron hopping conduction mechanism in the high temperature range they do not exhibit a straight line fit throughout the temperature range as per the ES VRH model.

The resistivity for the Sr doped (or Sr – rich) systems at 300K show that resistivity values scale with T_{CO} for almost all the compositions. Whereas, this is not the case for the Ca doped (or Ca – rich) samples. The lower resistivity and T_{CO} values are found in Ca – based and Ca – rich compositions in comparison to the Sr – based and Sr – rich

compositions. These differences are reported in the literature for the Ca and Sr based systems. These differences have been explained in view of the Bi^{3+} $6s^2$ lone pair effect.

The resistivity data of the samples can be explained qualitatively by the percolation conduction model for mixed phase manganites. The emergence and growth of different magnetic clusters with change in temperature is confirmed from the ESR studies and also understood in view of the phase separation concept.

PUBLICATIONS

Journals:

1. Electron spin resonance study of $Bi_{(1-x)}Ca_xMnO_3$,
   Joji Kurian and R.Singh, J. Appl. Phys. **103**, 07F707 (2008).
2. Electron Spin Resonance and Resistivity Studies of Charge Ordered $Bi_{1-x}Ca_xMnO_3$,
   Joji Kurian and R.Singh, J. Phys. D: Appl. Phys. **41** 215006 (2008).
3. Electron spin resonance study of $Bi_{0.55}Ca_{0.45}MnO_3$ nanoparticles,
   Joji Kurian and R.Singh, J. Appl. Phys **105** 07D718 (2009).
4. Effect of Cr doping on magnetic phase separation in $Bi_{0.5}Ca_{0.5}MnO_3$,
   Joji Kurian and R.Singh (communicated).
5. ESR and Resistivity Studies on Sr substituted $Bi_{0.6}Ca_{(0.4-x)}Sr_xMnO_3$,
   Joji Kurian and R.Singh (communicated).
6. Electron Spin Resonance and Resistivity Studies of $Bi_{1-x}Sr_xMnO_3$,
   Joji Kurian and R.Singh (to be communicated).

Conference papers:

1. Electrical and Magnetic Properties of $Bi_{0.5}Sr_{(0.5-x)}Ce_xMnO_3$,
   Joji Kurian and R.Singh, Solid State Physics, India **50** (2005) 693.
2. ESR Study of Charge-Ordered $Bi_{0.5}Sr_{0.5}MnO_3$,
   Joji Kurian and R.Singh, Solid State Physics, India **51** (2006) 947.
3. FMR of insulating state of $La_{0.7}Ca_{0.3}MnO_3$ nanoparticles,
   Joji Kurian and R.Singh, Solid State Physics, India **52** (2007) 1005.

REFERENCE

1. G. H. Jonker and J. H. Van Santen *Physica* **16**, 337 (1950).
2. J. H. Van Santen and G. H. Jonker *Physica* **16**, 599 (1950).
3. J. Volger *Physica* **20**, 49 (1954).
4. S. Jin, T. H. Tiefel, M. McCormack, R. A. Fastnatch, R. Ramesh and L. H. Chen *Science* **264**, 413 (1994).
5. R. Von Helmolt, J. Wecker, B. Holzapfel, L. Schultz and K. Samwer *Phys. Rev. Lett.* **71**, 2331 (1993).
6. http://www.freepatentsonline.com/y2004/0005483.html
7. A. Gupta, G. Q. Gong, Gang Xiao, P. R. Duncombe, P. Lecoeur, P. Trouilloud, Y. Y. Wang, V. P. Dravid and J. Z. Sun, *Phys Rev. B* **52**, R15629 (1996).
8. N. D. Mathur, G. Burnall, S. P. Issac, T. J. Jackson, B. S. Teo, J. L. Macmanus-Dricoll, L. F. Cohen, J. E. Evetts and M. G. Blamire *Nature* **387**, 266 (1997).
9. M. Dominguez, S. M. Bhagats. S. E. Lofland, J. S. Ramachandran, G. C. Xiong, H. L. Ju, T. Venkatesan, R. L. Greene *Europhys. Lett.* **32**, 349 (1995).
10. A. Goyal, M. Rajeswari, R. Shreekala, S. E. Lofland, S. M. Bhagat, T. Boettcher, C. Kwon, R. Ramesh and T. Venkatesan *Appl. Phys. Lett.* **71**, 2535 (1997).
11. A. K. Pradhan, R. Bah, R. B. Konda, R. Mundle, H. Mustafa, O. Bamiduro, and R. R. Rakhimov *J. Appl. Phys.* **103**, 07F704 (2008).
12. Hongwei Qin, Jifan Hua, Bo Li, Yanming Hao, Juan Chen and Minhua Jiang *J. Magn. Magn. Mater.* **320**, 2770 (2008)
    N. Zurauskiene *Thin Solid Films* **515**, 576 (2006).
13. Elbio Dagotto *New J. of Phys*.**7**, 67 (2005).
14. E. O. Wollan and W. C. Koehler *Phys. Rev.* **100**, 545 (1955).
15. C. W. Searle and S. T. Wang *Can. J. Phys.* **48**, 2023 (1970).
16. Z. Jirak, S. Vratislav and J. Zajicek *Phys. Stat. Sol. (a)* **52**, K39 (1979)
    Z. Jirak, S. Krupicka, Z. Simsa, M. Dlouha and S. Vratislav *J. Magn. Magn. Mater.* **53**, 153 (1985).
17. E. Pollert, S. Krupicka and E. Kuzmicova *J. Phys. Chem. Solids* **43**, 1137 (1982).
18. R. M. Kusters, J. Singleton, D. A. Keen, R. McGreevy and W. Hayes *Physica B* **155**, 362 (1989).
19. Ken-ichi Chahara, Toshiyuki Ohno, Masahiro Kasai and Yuzoo Kozono *Appl. Phys. Lett.* **63**, 1990 (1993).
20. H. L. Ju, C. Kwon, Qi Li, R. L. Greene, and T. Venkatesan *Appl. Phys. Lett.* **65**, 2108 (1994).

21. C. Zener *Phys. Rev.* **81**, 440 (1950).
22. C. Zener *Phys. Rev.* **82**, 403 (1951).
C. Zener *Phys. Rev.* **83**, 229 (1951).
23. P. W. Anderson and H. Hasegawa *Phys. Rev.* **100**, 675 (1955).
24. P.-G. de Gennes *Phys. Rev.* **118**, 141 (1960).
25. J. B. Goodenough *Phys. Rev.* **100**, 564 (1955).
J. B. Goodenough *Phys. Rev. B* **55**, 3015 (1955).
26. J. Kanamori, *J. Phys. Chem. Solids* **10**, 87 (1959).
27. S. Sugano, Y. Tanabe and H. Kamimura *Multiplets of Transition-Metal Ions* (Academic Press, 1970).
28. H. A. Jahn and E. Teller *Proceedings of the Royal Society of London series* A **161**, 220 (1937).
29. L. M. Rodríguez-Martínez and J. P. Attfield *Phys. Rev. B* **63**, 024424 (2000).
30. B. Raveau, A. Maignan, C. Martin and M. Hervieu *Colossal Magnetoresistance, Charge Ordering and Related Properties of Manganese Oxides* edited by C N R Rao and B Raveau (Singapore: World Scientific, 1998) 43
M. R. Ibarra and J. M de Teresa *Colossal Magnetoresistance, Charge Ordering and Related Properties of Manganese Oxides* (1998) 83.
31. A. J. Millis, P. B. Littlewood and B. I. Shraiman *Phys. Rev. Lett.* **74**, 5144 (1996).
32. H. Roder, J. Zang and A. R. Bishop *Phys. Rev. Lett.* **76**, 1356 (1996).
33. A.S. Moskvin and I. L. Avvakumov *Physica B* **322**, 371 (2002).
34. J. W. Verwey *Nature* **144**, 327 (1939).
35. H. Kuwahara, Y. Tomioka, A. Asamitsu, Y. Moritomo, and Y. Tokura *Science* **270**, 961 (1995).
36. Y. Moritomo, H. Kuwahara, Y. Tomioka, and Y. Tokura *Phys. Rev. B* **55**, 7549 (1997).
37. V. Kiryukhin, D. Casa, J. P. Hill, B. Keimer, A. Vigliante, Y. Tomioka, and Y. Tokura *Nature* **386**, 813 (1997).
38. C. H. Chen and S. W. Cheong *Phys. Rev. Lett.* **76**, 4042 (1996).
39. H. Kawano, R. Kajimoto, H. Yoshizawa, Y. Tomioka, H. Kuwahara and Y. Tokura *Phys. Rev. Lett.* **78**, 4253 (1997).
40. K. Knizek, Z. Jirak, E. Pollert and F. Zounova *J. Solid State Chem.* **100**, 292 (1992).
41. J. F. Mitchell, D. N. Argyriou and J. D. Jorgensen *Colossal Magnetoresistive Oxides* edited by Yoshinori Tokura, (Gordon and Breach Science Publishers 2000) 189.
42. P. G. Radaelli, D. E. Cox, M. Marezio and S. W. Cheong *Phys. Rev. B* **55**, 3015 (1997).

43. J. B. Goodenough, *Magnetism and the Chemical Bond*, edited by F. A. Cotton, (John Wiley & Sons, New York, 1963).
44. J. F. Mitchell, D. N. Argyriou, C.D.Potter, D.G.Hinks J.D.Jorgensen and S.D.Bader, *Phys. Rev. B* **54**, 6172 (1996).
45. D.N.Argyriou, J.F.Mitchell, C.D.Potter, D.G.Hinks, J.D.Jorgensen and S.D.Bader, *Phys. Rev. Lett* **76**, 3826 (1996).
46. E. L. Nagaev *Colossal Magnetoresistance and Phase Separation in Magnetic Semiconductors* (Imperial College Press, London, 2002).
47. E. L. Nagaev *JETP Lett.* **6**, 18 (1967)
    E. L. Nagaev *JETP Lett.* **16**, 394 (1972)
    E. L. Nagaev, *Phys. Stat. Sol. (b)* **186**, 9 (1994).
48. T. Kasuya *Solid State Commun.* **8**, 1635 (1970).
49. N. F. Mott and E. A. Davis *Electronic Processes in Non-Crystalline Materials* (Oxford: Clarendon, 1971).
50. N. Furukawa *J. Phys. Soc. Japan* **66**, 2523 (1997).
51. L. P. Gor'kov and V. Z. Kresin *JETP Lett.* **67**, 985 (1998).
52. E. Dagotto, T. Hotta and A. Moreo *Phys. Rep.* **344**, 1 (2001).
53. D. Arovas and F. Guinea *Phys. Rev. B* **58**, 9150 (1998).
54. A. Moreo, S. Yunoki and E. Dagotto *Science* **283**, 2034 (1999).
55. J. Burgy, A. Moreo and E. Dagotto *Phys. Rev. Lett.* **92**, 097202 (2004).
56. N. D. Mathur and P. B. Littlewood *Solid State Commun.* **119**, 271(2001).
57. K. H. Ahn, T. Lookman and A. R. Bishop *Nature* **428**, 401 (2004).
58. S. Yunoki, J. Hu, A. L. Malvezzi, A. Moreo, N. Furukawa, and E. Dagotto, *Phys. Rev. Lett.* **80**, 845 (1998).
59. Y. Murakami, H. Kawada, H. Kawatz, M. Tanaka, T. Arima, Y. Moritomo and Y.Tokura *Phys. Rev. Lett.* **80**, 1932 (1998).
60. S. Yunoki, A. Moreo, and E. Dagotto *Phys. Rev. Lett.* **81**, 5612 (1998).
61. T. G. Perring, G. Aeppli, Y. Moritomo, and Y. Tokura *Phys. Rev. Lett.* **78**, 3197 (1997).
62. P. Levy, F. Parisi, G. Polla, D. Vega, G. Leyva, H. Lanza, R.S. Freitas and L. Ghivelder *Phys. Rev. B* **62**, 6437 (2000).
63. M. Uehara, S. Mori, C. H. Chen and S.-W. Cheong *Nature* **399**, 560 (1999).
64. J. C. Loudon, N. D. Mathur and P. A. Midgley *Nature* **420**, 797 (2002).
65. P. Levy, F. Parisi, L. Granja, E. Indelicato and G. Polla, *Phys. Rev. Lett.* **89**, 137001 (2002).

66. L. Granja, E. Indelicato, P. Levy, G. Polla, D. Vega and F. Parisi, *Physica B* **320**, 94 (2002).
67. R. B. Griffith *Phys. Rev. Lett.* **23**, 17 (1969).
68. A. J. Millis, *Nature* **392**, 147 (1998).
69. Elbio Dagotto, *Nanoscale Phase Separation and Colossal Magnetoresistance* (Berlin: Springer) (www.springer.de) (2002).
70. D. D. Sarma, Dinesh Topwal, U. Manju, S. R. Krishnakumar, M. Bertolo, S. La Rosa, G. Cautero, T.Y. Koo, P. A. Sharma, S.-W. Cheong and A. Fujimori *Phys. Rev. Lett.* **93**, 097202 (2004).
71. D. N. Argyriou, U. Ruett, C.P. Adams, J. W. Lynn and J. F. Mitchell, *New J. of Phys.* **6**, 195 (2004).
72. R. Mathieu, D. Akahoshi, A. Asamitsu, Y. Tomioka and Y. Tokura (arXiv:cond-at/0406550).
73. V. Kiryukhin, A. Borissov, J. S. Ahn, Q. Huang, J. W. Lynn, and S-W. Cheong, (arXiv:cond-mat/0411081).
74. F. Sugawara, S. Iida, Y. Syono and S. Akimoto *J. Phys. Soc. Jpn.* **20**, 1529 (1965).
75. A. Morira dos Santos, S. Parashar, A. R. Raju, Y. S. Zhao, A. K. Cheetham and C. N. R. Rao *Solid State Commun.* **122**, 49 (2002).
76. F. Sugawara, S. Iida, Y. Syono, and S. Akimoto *J. Phys. Soc. Jpn.* **25**, 1553 (1968).
77. V. A. Bokov, I. E. Myl'nikova, S. A. Kizhaev, M. F. Bryzhina, and N. A. Grigoryan *Sov. Phys. Solid. State* **7**, 2993 (1966).
78. Yu. Ya. Tomashpol'skii, E. V. Zubova, K. P. Burdina, and Yu. N. Venevtsev *Izv. Akad. Nauk SSSR, Inorg. Mater.* **3**, 2132 (1967).
79. I. O. Troyanchuk, N. V. Kasper, O. S. Mantytskaya, and S. N. Pastushonok *Sov. Phys. JETP* **78**, 212 (1994).
80. T. Atou, H. Chiba, K. Ohoyama, Y. Yamaguchi and Y. Syono *J. Solid State Chem.* **145**, 639 (1999).
81. H. Faqir, H. Chiba, M. Kikuchi and Y. Syono *J. Solid State Chem.* **142**, 113 (1999).
82 Nicola A. Hill, Karin M. Rabe *Phys. Rev. B* **59**, 8759 (1999).
83. Ram Seshadri and Nicola A. Hill *Chem. Mater.* **13**, 2892 (2001)
84. Pio Baettig, Ram Seshadri and Nicola A. Spaldin *J. Am. Chem. Soc.* **129**, 9854 (2007).
85. A. Moreira dos Santos, A. K. Cheetham, T. Atou, Y. Syono, Y. Yamaguchi, K. Ohoyama, H. Chiba and C. N. R. Rao *Phys. Rev. B* **66**, 064425 (2002).
86. T. Kimura, S. Kawamoto, I. Yamada, M. Azuma, M. Takano and Y. Tokura *Phys. Rev. B* **67**, 180401 (R) (2003).

87. H. Yang, Z. H. Chi, F. Y. Li, C. Q. Jin and R. C. Yu *Phys. Rev. B* **73**, 024114 (2006).
88. Erica Montanari, Lara Righi, Gianluca Calestani, Andrea Migliori, Edmondo Gilioli, and Fulvio Bolzoni *Chem. Mater.* **17**, 1765 (2005)
Erica Montanari, Gianluca Calestani, Andrea Migliori, Monica Dapiaggi, Fulvio Bolzoni, Riccardo Cabassi and Edmondo Gilioli *Chem. Mater.* **17**, 6457 (2005).
E. Montanari, G. Calestani, L. Righi, E. Gilioli, F. Bolzoni, K. S. Knight, and P. G. Radaelli *Phys. Rev. B* **75**, 220101 (R) (2007).
89. T. Shishidou, N. Mikamo, Y. Uratani, F. Ishii and T. Oguchi *J. Phys.: Condens. Matter* **16**, S5677 (2004).
90. Alexei A. Belik, Satoshi Iikubo, Tadahiro Yokosawa, Katsuaki Kodama, Naoki Igawa, Shinichi Shamoto, Masaki Azuma, Mikio Takano, Koji Kimoto, Yoshio Matsui and Eiji Takayama-Muromachi, *J. Am. Chem. Soc.* **129**, 971 (2007)
Tadahiro Yokosawa, Alexei A. Belik, Toru Asaka, Koji Kimoto, Eiji Takayama-Muromachi and Yoshio Matsui *Phys. Rev. B* **77**, 024111 (2008)
91. V. A. Bokov, N. A. Grigoryan and M. F. Bryzhina *Phys. Stat. Sol.* **20**, 745 (1967).
92. H. Chiba, M. Kikuchi, K. Kusaba and Y. Syono *Solid State Commun.* **99**, 499 (1996).
H. Chiba, T. Atou, H. Faqir, M. Kikuchi, Y. Syono, Y. Murakami and D. Shindo *Solid State Ionics* **108**, 193 (1998).
93. Sudipta Pal, Aritra Banerjee, P. Chatterjee and B. K. Chaudhuri *Phys. Stat. Sol. (b)* **237**, 513 (2003).
94. P. N. Santhosh, J. Goldberger, P. M. Woodward, T. Vogt, W. P. Lee and A. J. Epstein *Phys. Rev. B* **62**, 14928 (2000).
95. S. Yoon, M. Rubhausen, S. L. Cooper, K. H. Kim and S.-W. Cheong *Phys. Rev. Lett.* **85**, 3297 (2000).
96. Ch. Renner, G. Aeppli, B.-G. Kim, Yeong-Ah Soh & S.-W. Cheong *Nature* **416**, 518 (2002).
M. Varela, A. R. Lupini, K. van Benthem, A. Y. Borisevich, M. F. Chisholm, N. Shibata, E. Abe and S. J. Pennycook *Annu. Rev. Mater. Res.* **35**, 539 (2005).
Maria Varela, Timothy J. Pennycook, Wei Tian, David Mandrus, Stephen J. Pennycook, Vanessa Pena, Zouhair Sefrioui and Jacobo Santamaria *J. Mater. Sci.* **41**, 4389 (2006).
97. H. Woo, T. A. Tyson, M. Croft, S-W. Cheong and J. C. Woicik *Phys. Rev. B* **63**, 134412 (2001).
Hyungje Woo, Trevor A. Tyson, Mark Croft and Sang-Wook Cheong *J. of Phys.: Condens. Matter* **16**, 2689 (2004).

98. J. L. Garcia-Munoz, M. A. G. Aranda, A. Llobet, C. Frontera, M. J. Martınez-Lopez, C. Ritter, M. Respaud, J. M. Broto *J. Alloys. Comp.* **323–324,** 408 (2001).
99. C. Frontera, J. L. Garcia-Munoz, A. Llobet, M. A. G. Aranda, C. Ritter, M. Respaud and J. Vanacken *J. of Phys.: Condens. Matter* **13**, 1071 (2001).
Carlos Frontera, Jose Luis Garcia-Munoz, Miguel Angel G. Aranda, Clemens Ritter, Anna Llobet, Marc Respaud and Johad Vanacken *Phys. Rev. B* **64**, 054401 (2001).
100. I. O. Troyanchuk, O. S. Mantytskaya and A. N. Chobot *Phys. Solid State* **44**, 2266 (2002).
101. S. B. Wilkins, P. D. Spencer, P. D. Hatton, D. Mannix, S. D. Brown, T. d'Almeida and S-W. Cheong *Physica B* **318**, 295 (2002).
102. W. J. Lu, Y. P. Sun, B. C. Zhao, X. B. Zhu and W. H. Song *Phys. Rev. B* **73**, 214409 (2006).
103. S. Grenier, K. J. Thomas, J. P. Hill, U. Staub, Y. Bodenthin, M. Garcia-Fernandez, V. Scagnoli, V. Kiryukhin, S-W. Cheong, B. G. Kim and J. M. Tonnerre *Phys. Rev. Lett.* **99**, 206403 (2007).
104. S. Grenier, V. Kiryukhin, S-W. Cheong, B. G. Kim, J. P. Hill, K. J. Thomas, J. M. Tonnerre, Y. Joly, U. Staub, V. Scagnoli *Phys. Rev. B* **75**, 085101 (2007).
105. Yuhai Qin, Trevor A. Tyson, Klaus Pranzas and Helmut Eckerlebe *J. Phys: Condens Matter*. **20**, 195209 (2008).
106. Kenji Shimizu, Y. Qin and T. A. Tyson *Phys. Rev. B* **73**, 174420 (2006).
107. H. Chiba, T. Atou and Y. Syono *J. of Solid State Chem.* **132**, 139 (1997).
108. J. L. Garcia Munoz, C. Frontera, M. A. G. Aranda, C. Ritter, A. Llobet, M. Respaud, M. Goiran, H. Rakoto, O. Masson, J. Vanacken and J. M. Broto *J. of Solid State Chem.* **171**, 84 (2003).
Jose Luis Garcia-Munoz, Carlos Frontera, Marc Respaud, Maud Giot, Clemens Ritter and Xavier G. Capdevila *Phys. Rev. B* **72**, 054432 (2005).
109. D. Sedmidubsky, O. Bene, P. Beran, J. Hejtmanek and M. Marysko *J. Magn Magn Mater.* **272-276**, E285 (2004).
110. B. H. Kim, J. S. Kim, M. S. Kim, C. J. Zhamg, K. H. Kim, B. G. Kim, H. C. Kim and Y. W. Park *Phys. Lett. A* **351**, 368 (2006).
111. Byung Hoon Kim, Jun Sung Kim, Tae Hoi Park, Seung Joo Park, Kyung Hyun Kim, Bog G. Kim and Yung Woo Park *J. Phys: Condens Matter* **19**, 476203 (2007).
112. O. S. Mantytskaya, I. O. Troyanchuk, A. N. Chobot and H. Szymczak *Low Temp. Phys.* **30**, 218 (2004).
113. A. Rebello and R. Mahendiran *Appl. Phys. Lett.* **94**, 112107 (2009).

114. J. L. Garcia-Munoz, C. Frontera, M. A. G. Aranda, A. Llobet and C. Ritter *Phys. Rev. B* **63**, 064415 (2001).
J. L. Garcia-Munoz, C. Frontera, P. Beran, N. Bellido, J. S. Lord, C. Ritter and I. Margiolaki *J. of Phys.: Condens. Matter* **19**, 406212 (2007).
115. A. Kriste, M. Goiran, M. Respaud, J. Vanaken, J. M. Broto, H. Rakoto, M. von Ortenberg, C. Frontera and J. L. Garcia-Munoz *Phys. Rev. B* **67**, 134413 (2003).
116. Premysl Beran, Sylvie Malo, Christine Martin, Antoine Maignan, Milos Nevriva, Maryvonne Hervieu and Bernard Raveau *Solid State Sci.* **4**, 917 (2002).
117. W. J. Lu, Y. P Sun, X. B. Zhu, W. H. Song and J. J. Du *Solid State Commun.* **138**, 200 (2006).
J. C. Loudon, L. Fitting Kourkoutis, J. S. Ahn, C. L. Zhang, S.-W. Cheong and D. A. Muller *Phys. Rev. Lett.* **99**, 237205 (2007).
118. Wei Bao, J. D. Axe, C. H. Chen and S-W. Cheong *Phys. Rev. Lett.* **78**, 543 (1997).
119. H. L. Liu, S. L. Cooper and S-W. Cheong *Phys. Rev. Lett.* **81**, 4684 (1998).
120. M. Rubhausen, S. Yoon, S. L. Cooper, K. H. Kim and S.-W. Cheong *Phys. Rev. B.* **65**, R4782 (2000).
121. M. Giot, P. Beran, O. Peraz, S. Malo, M. Hervieu, B. Raveau, M. Nevriva, K. Knizek and P. Roussel *Chem. Mater.* **18**, 3225 (2006)
M. Giot, A. Pautrat, O. Perez, C. Simon, M. Nevriva, M. Hervieu *Solid State Sci.* **8**, 1414 (2006)
122. Y. Su, C-H. Du, P. D. Hatton, S. P. Collins and S-W. Cheong *Phys. Rev. B* **59**, 11687 (1999).
123. I. I. Smolyaninov, V. N. Smolyaninova, C. C. Davis, B. G. Kim, S.-W. Cheong and R. L. Greene *Phys. Rev. Lett.* **87**, 127204 (2001).
124. J. Hejtmanek, K. Knizek, Z. Jirak, M. Hervieu, C. Martin, M. Nevriva and P. Beran *J. Appl. Phys.* **93**, 7370 (2003).
125. S. Yamada, E. Sugano, S. Nishiyama, Y. Watanabe and T. Arima *J Magn Magn Mater.* **310**, 771 (2007);
Shigeki Yamada, Takuya Matsunaga, Eri Sugano, Hajime Sagayama, Shota Konno, Shinji Nishiyama, Yosuke Watanabe and Taka-hisa Arima *Phys. Rev. B* **75**, 214431 (2007).
126. G. Subias, M. C. Sanchez, J. Garcia, J. Blasco, J. Herrero-Martin, C. Mazzoli, P. Beran, M. Nevriva and J. L. Garcia-Munoz *J. Phys.: Condens. Matter* **20**, 235211 (2008).
127. Y. Z. Chen, J. R. Sun, D. J. Wang, S. Liang, J. Z. Wang, Y. N. Han, B. S. Han and B. G. Shen *J. Phys: Condens Matter* **19**, 442001 (2007).

Y. Z. Chen, J. R. Sun, S. Liang, W. M. Lv, B. G. Shen and W. B. Wu *J. Appl. Phys.* **103**, 096105 (2008).

128. J. Z. Wang, J. R. Sun, W. Zhang, R. C. Yu, Y. Z. Chen, B. G. Shen and W. B. Wu *Europhys. Lett.* **82**, 16002 (2008).
129. M. Gajek, M. Bibes, A. Barthelemy, K. Bouzehouane, S. Fusil, M. Varela, J. Fontcuberta and A. Fert *Phys. Rev. B.* **72**, 020406 (R) (2005).
130. S. Chaudhuri and R. C. Budhani *Phys. Rev B* **74**, 054420 (2006).
131. Chan-Ho Yang, Sung-Ho Lee, Tae Yeong Koo and Yoon Hee Jeong *Phys. Rev B* **75**, 140104(R) (2007).
132. Eriko Ohshima, Yuko Saya, Masashi Nantoh and Maki Kawai *Solid State Commun.* **116**, 73 (2000)
133. Alok Sharan, James Lettieri, Yunfa Jia, Wei Tian, Xiaoqing Pan, Darrell G. Schlom and Venkatraman Gopalan *Phys. Rev. B* **69**, 214109 (2004)
134. E. Langenberg, M. Varela, M. V. Garcia-Cuenca, C. Ferrater, F. Sanchez and J. Fontcuberta *Mater. Sci. Eng. B* **144**, 138 (2007).
135. Hiroshi Naganuma, Andras Kovacs, Tetsuro Harima, Hiromi Shima, Soichiro Okamura and Yoshihiko Hirotsu *J. Appl. Phys.* **105**, 07D915 (2009).
136. C. M. Xiong, J. R. Sun, R. W. Li, S. Y. Zhang, T. Y. Zhao and B. G. Shen *J Appl. Phys.* **95**, 1336 (2004).
137. Lan Luan, Zhe Qu, Shun Tan, Xi Lin and Yuheng Zhang *J Magn. Magn. Mater.* **312**, 107 (2006).
138. Shigeki Yamada, Eri Sugano and Taka-hisa Arima *J. Solid State Chem.* **179**, 3121 (2006).
139. D. Tzankov, D. Kovacheva, K. Krezhov, R. Puzniak, A. Wisniewski, E. Svab and M. Mikhov *J. Phys.: Condens Matter* **17**, 4319 (2005).
140. O. Toulemonde, I. Skovsen, F. Mesguich and E. Gaudin *Solid State Sci.* **10**, 476 (2008).
141. R. R. Zhang, G. L. Kuang, X. Luo and Y. P. Sun *J. Alloys. Comp.* (In press).
142. S. S. Rao and S. V. Bhat *J. Nanoscience and Nanotechnolgy*, **7,** 2025 (2007).
143. Jun Fang, Qiang Wang, Youming Zou, Xiaman Yu, Renwan Li and Yuheng Zhang *J. Appl. Phys.* **104**, 123905 (2008).
144. Carlos Vazquez-Vazquez, M. Carmen Blanco, M. Arturo Lopez-Quintela, Rodolfo D. Sanchez, Jose Rivas and Saul B. Oseroff *J. of Mater.Chem* **8**, 991 (1998).
145. J. Mahia, C. Vazquez-Vazquez, M. I. Basadre-Pampın, J. Mira, J. Rivas, M. A. Lopez-Quintela and S. B. Oseroff *J. Am. Ceram. Soc.*, **79**, 407 (1996).
146. W. H. R. Shaw and J. J. Bordeaux *J. Am. Chem. Soc.*, **77**, 4729 (1955).

147. The chemical reaction in which water molecules split into hydrogen and hydroxide ions is called hydrolysis. These ions may participate in further reactions. The change in the pH can change the rate of the hydrolysis process.
148. F. W. Miller Jr. and H. R. Dittmar *J. Am. Chem. Soc.* **56**, 848 (1934).
149. B. D. Culity *Elements of X-ray Diffraction* (Addison-Wesley Publishing Company Inc. 1978).
150. A. Abragam and B. Bleaney *Electron Paramagnetic Resonance of Transition Ions*, (Clarendon Press, Oxford 1970).
151. Colin N. Banwell and Elaine M. McCash *Fundamentals of Molecular Spectroscopy* (Tata McGraw-Hill Publishing Company Limited 1997)
152. M. Hervieu, S. Malo, O. Perez, P. Beran, C. Martin, G. Baldinozzi, and B. Raveau *Chem. Mater.* **15**, 523 (2003).
M. Hervieu, A. Maignan, C. Martin, N. Nguyen, and B. Raveau *Chem. Mater.* **13**, 1356 (2001).
153. A. Barnabe, M. Hervieu, C. Martin, A. Maignan and B. Raveau *J. Phys. Chem. Solids* **62**, 1365 (2001).
154. K. Padmavathi, G. Venkataiah and P. Venugopal Reddy *J. Magn. Magn. Mater.***309**, 237 (2007).
155. J. Philip and T. R. Kutty *J. Phys.: Condens. Matter* **11**, 8537 (1999).
156. P. Mandal and S. Das *Phys. Rev. B* **56**, 15073 (1997).
157. R. Ganguly, I. K. Gopalakrishnan, and J. V. Yakhmi *J. Phys.: Condens. Matter* **12**, L719 (2000).
158. G. Alejandro and D. G. Lamas *Phys. Rev. B* **67**, 064424 (2003).
159. R. Suryanarayanana, V. Gasumyants *Solid State Commun.* **123**, 353 (2002).
160. A. Sundaresan, J. L. Tholence, A. Maignan, C. Martin, M. Hervieu, B. Raveau and E. Suard *Eur. Phys. J. B* **14**, 431 (2000).
161. J. Dukic, S. Boskovic and B. Matovic *Ceramics International* (In Press) (2008).
162. S. B. Oseroff, M. Torikachvili, J. Singley, S. Ali, S-W. Cheong and S. Schultz *Phys. Rev. B* **53**, 6521 (1996).
163. A. I. Shames, E. Rozenberg, G. Gorodetsky, J. Pelleg and B. K. Chaudhuri *Solid State Commun.* **107**, 91 (1998).
A. I. Shames, E. Rozenberg, W. H. McCarroll, M. Greenblatt and G. Gorodetsky *Phys. Rev. B* **64**, 172401 (2001).
A. I. Shames, E. Rozenberg, G. Gorodetsky and Ya. M. Mukovskii *Phys. Rev. B* **68**, 174402 (2003).
164. T. G. Castner and M. S. Seehra *Phys. Rev. B* **4**, 38 (1971).

165. D. L. Huber *J. Phys. Chem. Solids* **32**, 2145 (1971)
D. L. Huber *Phys. Rev. B* **3**, 836 (1971).
166. M. S. Seehra and D. L. Huber *AIP Conf. Proc.* **24**, 261 (1975).
167. D. L. Huber and M. S. Seehra *J. Phys. Chem. Solids* **36**, 723 (1975).
168. M. S. Seehra and R. P. Gupta *Phys. Rev. B* **9**, 197 (1974).
169. M. S. Seehra, M. Ibrahim, V. S. Babu and G. Srinivasan *J. Phys.: Condens. Matter* **8**, 11283 (1996).
170. A. Shengelaya, G. M. Zhao, H. Keller and K. A. Muller *Phys. Rev. Lett.* **77**, 5296 (1996).
171. K. A. Müller *Phys. Rev. Lett.* **2**, 341 (1959).
172. C. Rettori, D. Rao, J. Singley, D. Kidwell, and S. B. Oseroff, M. T. Causa, J. J. Neumeier and K. J. McClellan, S-W. Cheong, S. Schultz *Phys. Rev. B* **55**, 3083 (1997).
173. S. E. Lofland, P. Kim, P. Dahiroc, S.M. Bhagat, S.D. Tyagi, S. G. Karabashev, D. A. Shulyatev, A. A. Arsenov, Y. Mukovskii *Phys. Lett. A* **233**, 476 (1997).
174. R. Gundakaram, J. G. Lin and C.Y. Huang *Phys. Rev.* B **58**, 12247 (1998).
175. M. T. Causa, M. Tovar, A. Caneiro, F. Prado, G. Ibanez, C. A. Ramos, A. Butera, B. Alascio, X. Obradors, S. Pinol, F. Rivadulla, C. Vazquez- Vazquez, M. A. Lopez Quintela, J. Rivas, Y. Tokura and S. B. Oseroff *Phys. Rev. B* **58**, 3233 (1998).
176. E. Dormann and V. Jaccarino *Phys. Lett. A* **48**, 81 (1974).
177. D. L. Huber *J. Phys. Chem. Solids* **32**, 2145 (1971).
178. V. A. Ivanshin, J. Deisenhofer, H. A. Krug von Nidda, A. Loidl, A. A. Mukhin, A. M. Balbashov and M. V. Eremin *Phys. Rev.* B **61**, 6213 (2000).
179. C. D. Hu *J. Phys.: Condens. Matter* **16**, 6293 (2004).
180. Mohinder S. Seehra *J. Appl. Phys.* **42**, 1290 (1971).
181. D. L. Huber *Phys. Rev. B* **6**, 3180 (1972).
182. K. Tomita and T. Kawasaki *Progr. Theor. Phys.* **44**, 1173 (1970).
183. J. B. Goodenough and A. L. Loeb *Phys. Rev.* **98**, 391 (1955).
184. H. A. Kramers *Physica* **1**, 182 (1934)
P.W. Anderson *Phys. Rev.* **79**, 350 (1950)
J. H. Van Vleck *J. Phys. Radium* **12**, 262 (1951).
185. I. Brown *Acta Crystallogr. Sect. B* **48**, 553 (1992).
186. A. Daoud-Aladine, J. Rodrıguez-Carvajal, L. Pinsard-Gaudart, M. T. Fernandez-Dıaz and A. Revcolevschi *Phys. Rev. Lett.* **89**, 097205 (2002).
187. J. Rodriguez-Carvajal, A. Daoud-Aladine, L. Pinsard-Gaudart, M. T. Fernandez-Dıaz, and A. Revcolevschi, *Physica B* **320**, 1 (2002).

188. A. Daoud-Aladine, J. Rodrıguez-Carvajal, L. Pinsard-Gaudart, M. T. Fernandez-Dıaz, and A. Revcolevschi, *Appl. Phys. A: Mater. Sci. Process.* **74**, S1758 (2002).
189. Joaquín García, M. Concepción Sánchez, Gloria Subías and Javier Blasco, *J. Phys.: Condens. Matter* **13**, 3229 (2001).
190. J.-S. Zhou and J. B. Goodenough *Phys. Rev. B* **62**, 3834 (2000).
191. F. Millange, S. de Brion and G. Chouteau *Phys. Rev. B* **62**, 5619 (2000).
192. Carlos Frontera , Jose Luis Garcia-Munoz, Clemens Ritter, Lluis Manosa, Xavier G. Capdevila, Albert Calleja *Solid State Commun.* **125**, 277, (2003).
193. J. W. Stevenson, M. M. Nasrallah, H. U. Anderson, D. M. Sparlin, *J. Solid State Chem.* **102**, 175 (1993).
K. A. Müller, *Phys. Rev. Lett.* **2**, 341 (1959).
K. A. Muller, W. Berlinger, K. W. Blazey, J. Albers, *Solid State Commun.* **61**, 21 (1987).
194. J. E. Gulley and V. Jacarrino *Phys. Rev. B.* **6**, 58 (1972).
195. J. Deisenhofer, D. Braak, H. A. Krug von Nidda, J. Hemberger, R. M. Eremina, V. A. Ivanshin, A. M. Balbashov, G. Jug, A. Loidl, T. Kimura, and Y. Tokura *Phys. Rev. Lett.* **95**, 257202 (2005).
196. S. Zhou, L. Shi, H. Yang and J. Zhao *Appl. Phys. Lett.* **91**, 172505 (2007).
197. T. Qian, P. Tong, B. Kim, S. L. Lee, N. Shin, S. Park and B. G. Kim *Phys. Rev.* B **77**, 094423 (2008).
198. M. Kim, H. Barath, S. L. Cooper, P. Abbamonte, E. Fradkin, M. Rubhausen, C. L. Zhang and S.W. Cheong *Phys. Rev.*B **77**, 134411 (2008).
199. A. J. Bray and M. A. Moore *J. Phys. C: Solid State Phys.* **15**, L765 (1982).
A.J. Bray *Phys. Rev. Lett.* **59**, 586 (1987).
200. D. P. Arovas, G. Gomez-Santos and F. Guinea *Phys. Rev.* B **59**, 13569 (1999).
201. J. Burgy, M. Mayr, V. Martin-Mayor, A. Moreo and E. Dagotto *Phys. Rev Lett.* **87**, 277202 (2001).
202. Maud Giot, Alain Pautrat, Gilles Andre, Damien Saurel, Maryvonne Herviru and Juan Rodriguez Carvajal *Phys. Rev. B* **77**, 134445 (2008).
203. R. J. Goff, J.P. Attfield *J. Solid State Chem.* **179**, 1369 (2006).
204. Joji Kurian and R. Singh *J. Phys. D: Appl. Phys.* **41**, 215006 (2008).
205. Joji Kurian and R.Singh *J. Appl. Phys.* **103**, 07F707 (2008).
Joji Kurian and R.Singh *J. Appl. Phys.* **105**, 07D718 (2009).
206. J. P. Joshi, R. Gupta, A. K. Sood and S.V. Bhat *Phys. Rev.* B **65**, 024410 (2001).
207. T. T. P. Cheung and Z. G. Soos *Phys. Rev.* B **17**, 1266 (1978).

208. P. M. Woodward, D. E. Cox, T. Vogt, C. N. R. Rao and A. K. Cheetham, *Chem. Mater.* **11**, 3652 (1999).
209. J. Blasco, J. Garcıa, J. M. de Teresa, M. R. Ibarra, J. Perez, P. A. Algarabel, C. Marquina, and C. Ritter *J. Phys.: Condens. Matter* **9**, 10321 (1997).
210. O. Richard, W. Schuddinck, G. Van Tendeloo, F. Millange, M. Hervieu, V. Caignaert, and B. Raveau *Acta Crystallogr. Sect. A: Found. Crystallogr.* **55**, 704 (1999).
211. J. Garcia, M.C. Sanchez, J. Blasco, G. Subıas, and M.G. Proietti, *J. Phys.: Condens. Matter* **13**, 3243 (2001).
212. D. Cox, P. Radaelli, M. Marezio and S.-W. Cheong *Phys. Rev. B* **57**, 3305 (1998).
213. R.D. Shannon, *Acta Crystallogr. Sect. A.: Cryst. Phys., Diffe., Theor. Gen. Crystallogr.* **32**, 751 (1976).
214. N. D. Mathur, P. B. Littlewood *Phys. Today* **56**, 23 (2003).
215. Adriana Moreo, Seiji Yunoki and Elbio Dagotto *Science* **283**, 2034 (1999).
216. V. Podzorov, B. G. Kim, V. Kiryukhin, M.E. Gershenson and S.-W. Cheong, *Phys. Rev. B* **64**, 140406 (2001).
H. J. Lee, K. H. Kim, M. W. Kim, T. W. Noh, B. G. Kim, T. Y. Koo, S.-W. Cheong, Y. J. Wang and X. Wei *Phys. Rev. B* **65**, 115118 (2002).
V. Podzorov, C. H. Chen, M. E. Gershenson and S.-W. Cheong *Europhys. Lett.* **55**, 411 (2001).
V. Kiryukhin, B. G. Kim, V. Podzorov, S.-W. Cheong, T. Y. Koo, J. P. Hill, I. Moon, J. H. Jeong, *Phys. Rev. B* **63**, 024420 (2001).
217. F. Rivadulla, L. E. Hueso, D. R. Miguens, P. Sande, A. Fondado, J. Rivas, and M. A. Lopez-Quintela *J. Appl. Phys.* **91**, 7412 (2002).
Z. Q. Li, H. Liu, Y. H. Cheng, W. B. Mi, A. Yu, H. L. Bai, E. Y. Jiang, *Physica B* **353**, 324 (2004).
Wei Ning, Fen Wang, Xiang-Qun Zhang, Zhao-Hua Cheng and Young Sun *J. Magn. Magn. Mater.* **321**, 88 (2008).
218. C. N. R. Rao, A. Arulraj, P. N. Santhosh, A. K. Cheetham *Chem. Mater.* **10**, 2714 (1998).
219. P. Raychaudhuri, S. Mukherjee, A. K. Nigam, J. John, U. D. Vaisnav, R. Pinto, P. Mandal *J. Appl. Phys.* **86**, 5718 (1999).
220. H. Y. Hwang, S.W. Cheong, P. G. Radaelli, M. Marezio and B. Batlogg, *Phys. Rev. Lett.* **75**, 914 (1995).
221. O. Cabeza, M. Long, C. Severac, M. A. Bari, C. M. Muirhead, M. G. Francesconi and C. Greaves *J. Phys. Condens. Matter* **11**, 2569 (1999).

222. I. O. Troyanchuk and M. V. Bushinsky *Low Temp. Phys.* **28**, 45 (2002).
223. T. Kimura, R. Kumai, Y. Okimoto and Y. Tomioka, *Phys. Rev. B* **62**, 15021 (2000).
224. L. Capogna, A. Martinelli, M. G. Francesconi, P. G. Radaelli, J. Rodriguez Carvajal, O. Cabeza, M. Ferretti, C. Castellano, T. Corridoni, and N. Pompeo *Phys. Rev. B* **77**, 104438 (2008).
225. A. Maignan, C. Martin, F. Damay, M. Hervieu, B. Raveau *J. Magn. Magn. Mater.* **188**, 185 (1998).
F. Damay, C. Martin, A. Maignan, M. Hervieu, B. Raveau, F. Boure and G. Andre *Appl. Phys. Lett.* **73**, 3772 (1998).
226. K. Ghosh, S. B. Ogale, R. Ramesh, R. L. Greene, T. Venkatesan, K. M. Gapchup, Ravi Bathe, and S. I. Patil *Phys. Rev. B* **59**, 533 (1999).
227. S. Roy, I.S. Dubenko, A.Y. Ignatov and N. Ali *J. Phys.: Condens. Matter* **12**, 9465 (2000).
228. Y. Sun, X. Xu and Y. Zhang *Phys. Rev. B* **63**, 054404 (2001).
Y. Sun, W. Tong, X. Xu and Y. Zhang *Appl. Phys. Lett.* **78**, 643 (2001).
229. Z. Qu, L. Pi, S. Tan, S. Chen, Z. Deng and Y. Zhang *Phys. Rev. B* **73**, 184407 (2006).
230. Z.M. Wang, G. Ni, H. Sang and Y. W. Du *J. Magn. Magn. Mater.* **234**, 213 (2001).
Z. M. Wang, G. Ni, Q. Y. Xu, H. Sang and Y. W. Du *J. Magn. Magn. Mater.* **234**, 371 (2001).
231. H. P. Gao, B. M. Wu and B. Li *Physica B* **389**, 252 (2007).
232. T. Kimura, Y. Tomioka, R. Kumai, Y. Okimoto, and Y. Tokura *Phys. Rev. Lett.* **83**, 3940 (1999).
233. B. Raveau, A. Maignan, and C. Martin *J. Solid State Chem.* **130**, 162 (1997).
234. Y. Moritomo, A. Machida, S. Mori, N. Yamamoto and A. Nakamura *Phys. Rev. B.* **60**, 9220 (1999).
235. A. I. Shames, A. Yakubovsky, V. Amelichev, O. Gorbenko and A. Kaul *Solid State Commun.* **121**, 103 (2002).
236. S. Savitha Pillai, Rajasekhar Madugundo, Santhosh. P. Nagappan Nair *J. Rare Earths*, **26**, 237 (2008).
237. Larson, A. C. Von Dreele, GSAS R B. General Structural Analysis System, LANSCE, Los Alamos National Laboratory: Los Alamos, NM, 1994.
238. J. Mazaferro, C. A. Balseiro, and B. Alascio, *J. Phys. Chem. Solids* **46**, 1339 (1985).
239 M. Jaime, M. B. Salamon, K. Pettit, M. Rubinstein, R. E. Treece, J. S. Horwitz, and D. B. Chrisey *Appl. Phys. Lett.* **68**, 1576 **(**1996).

M. Jaime, M. B. Salamon, M. Rubinstein, R. E. Treece, J. S. Horwitz, and D. B. Chrisey *Phys. Rev. B* **54**, 11914 (1996).
240. T. Holstein *Ann. Phys.* (N.Y.) **8**, 343 (1959).
241. D. Emin, in *Electronic Structure Properties of Amorphous Semiconductors*, edited by P. G. Le Comber and N. F. Mott (Academic Press, New York, 1973).
M. S. Hillery, D. Emin, and Nai-li H. Liu *Phys. Rev. B* **38**, 9771 (1988).
242. A. Moliton and B. Lucas *Ann. Phys.* (France) **19**, 299 (1994).
243. T. Kasuya and A. Yanase *Rev. Mod. Phys.* **40**, 684 (1968).
244. T. Holstein *Ann. Phys.* **21**, 193 (1968).
245. D. Emin and T. Holstein *Ann. Phys.* **53**, 439 (1969).
246. I. G. Austin and N. F. Mott *Adv. Phys.* **18**, 41 (1969).
247. H. Boettger and V. Bryksin *Hopping Conduction in Solids* (Berlin: Akademic 1985).
248. N. F. Mott *Conduction in Non-crystalline Materials* (New York: Oxford University Press 1993).
249. D. C. Worledge, G. Jeffrey Snyder, M. R. Beasley, T. H. Geballe, Ron Hiskes and Steve DiCarolis *J. Appl. Phys.* **80**, 5158 (1996).
250. Springer Handbook of Electronic and Photonic Materials edited by Kasap and Capper
251. B. I. Shklovskii and A. L. Efros Electronic Properties of Doped Semiconductors (Springer, Berlin, Heidelberg 1984).
252. A.L. Efros and B.I. Shklovskii *J. Phys. C: Solid State Phys.* **8**, L49 (1975).
253. I. Shlimak, M. Kaveh, R. Ussyshkin, V. Ginodman, S. D. Baranovskii, P. Thomas, H. Vaupel and R. W. van der Heijden *Phys. Rev. Lett.* **75** 4764 (1995).
254. S. R. Broadbent and J. M. Hammersley. Percolation processes I. Crystals and mazes. *Proc. Cam. Phil. Soc.*, **53**, 629 (1957).
255. G. Grimmett *Percolation.* Springer-Verlag, New York, 1989.
256. D. Stauffer and A. Aharony. *An Introduction to Percolation Theory*. Taylor and Francis, London, 2nd edition, 1992.
257. Adriana Moreo, Matthias Mayr, Adrian Feiguin, Seiji Yunoki, and Elbio Dagotto, *Phys. Rev. Lett.* **84**, 5568 (2000).
258. M. Ibarra and J. De Teresa *J. Magn. Magn. Mater.* **177–181**, 846 (1998).
259. Matthias Mayr, A. Morea, J. A. Verges, J. Arispe, A. Feiguin and E. Dagotto *Phys. Rev. Lett.* **86**, 135 (2001).
260. R. Raffaelle, H. U. Anderson, D. M. Sparlin and P. E. Parris *Phys. Rev. B* **43**, 7991 (1991).

261. M. Jaime, P. Lin, S. H. Chun, M. B. Salamon, P. Dorsey and M. Rubinstein *Phys. Rev. B* **60**, 1028 (1999).
262. J. Fontcuberta, B. Martinez, A. Seffar, S. Pinol, J.L. Garcia-Munoz and X. Obradors *Phys. Rev. Lett.***76**, 1122 (1996).
263. S. Bhattacharya, R. K. Mukherjee, B. K. Chaudhuri and H. D. Yang *Appl. Phys. Lett.* **82**, 4101 (2003).
264. R. Ang, Y. P. Sun, X. B. Zhu and W. H. Song *Solid State Commun.* **138**, 505 (2006).
R. Mahendiran, S. K. Tiwary, A. K. Raychaudhuri, T. V. Ramakrishnan, R. Mahesh, N. Rangavittal and C. N. R. Rao *Phys. Rev. B* **53**, 3348 (1996).
N. Gayathri, A. K. Raychaudhuri, S. K. Tiwary, R. Gundakaram, Anthony Arulraj, and C. N. R. Rao *Phys. Rev. B* **56**, 1345 (1997).
265. M. Viret, L. Ranno and J. M. D. Coey *Phys. Rev. B* **55**, 8067 (1997).
266. C. H. Lin, S. L. Young, H. Z. Chen, C. R. Ou, M. C. Kao, Lance Horng *J. Non-Cryst.Solids* **354**, 5290 (2008).
267. J. M. Liu, T. Yu, Q. Huang, J. Li, Z. X. Shen and C. K. Ong *J. Phys.: Condens. Matter* **14**, L141 (2002).
268. J. Li, Z. W. Li, C. K. Ong and D. N. Zheng *J. Phys.:Condens. Matter* **16**, 2839 (2004).
269. C. Krishnamoorthy, K. Sethupathi, V. Sankaranarayanan, R. Nirmala and S. K. Malik *J. Magn. Magn. Mater.* **308**, 28 (2007).
270. C. M. Varma *Phys. Rev. B* **54**, 7328 (1996).
271. L. Sheng, D. Y. Xing, D. N. Sheng and C. S. Ting *Phys. Rev.Lett.* **79**, 1710 (1997).
272. L. Sheng and C. S. Ting *Phys. Rev. B* **57**, 5265 (1998).
273. S. Ishihara and S. Maekawa *Phys. Rev.* B **62**, 5690 (2000).
274. S. Nakatsuji, V. Dobrosavljevic, D. Tanaskovic, M. Minakata, H. Fukazawa and Y. Maeno *Phys. Rev. Lett.* **93**, 146401 (2004).
275. P. W. Anderson *Phys. Rev.* **109**, 1492 (1958).
Qiming Li, Jun Zang, A. R. Bishop and C. M. Soukoulis *Phys. Rev. B* **56**, 4541 (1997).
Tal Schwartz, Guy Bartal, Shmuel Fishman and Mordechai Segev *Nature* **446**, 52 (2007).
276. Yoav Lahini, Assaf Avidan, Francesca Pozzi, Marc Sorel, Roberto Morandotti, Demetrios N. Christodoulides and Yaron Silberberg *Phys. Rev. Lett.* **100**, 013906 (2008)

Juliette Billy, Vincent Josse, Zhanchun Zuo, Alain Bernard, Ben Hambrecht, Pierre Lugan, David Clement,Laurent Sanchez-Palencia, Philippe Bouyer and Alain Aspect *Nature* **453**, 891 (2008).

277. E. Zacharias and R. Singh *Solid State Commun.* **93**, 135 (1995)
278. S. R. Sehlin, H. U. Anderson and D. M. Sparlin *Phys. Rev. B* **52**, 11681 (1995).
279. Bai-Mei Wu, Bo Li, and Wei-Hua Zhen, M. Ausloos, Ying-Lei Du, J. F. Fagnard and Ph. Vanderbemden *J. Appl. Phys.* **97**, 103908 (2005).
280. C. S. Hong, N. H. Hur, Y. N. Choi *Solid State Commun.* **133**, 531 (2005).
281. L. Morales, R. Allub, B. Alascio, A. Butera and A. Caneiro *Phys. Rev. B* **72**, 132413 (2005).
282. T. Sudyoadsuk, R. Suryanarayanan, P. Winotai and L.E. Wenger, *J.Magn. Magn. Mater.* **278**, 96 (2004).
283. M. Matsukawa, M. Chiba, E. Kikuchi, R. Suryanarayanan, M. Apostu, S. Nimori, K. Sugimoto, and N. Kobayashi, *Phys. Rev. B* **72**, 224422 (2005).
284. R. L. Zhang, W. H. Song, Y. Q. Ma, J. Yang, B. C. Zhao, Z. G. Sheng, J. M. Dai, and Y. P. Sun, *Phys. Rev. B* **70**, 224418 (2004).